

Yale University

EliScholar – A Digital Platform for Scholarly Publishing at Yale

Yale Graduate School of Arts and Sciences Dissertations

Spring 2021

Analyzing the Effect of Fuel Nitrogen on Soot Formation

Matthew Jacob Montgomery

Yale University Graduate School of Arts and Sciences, matthew.montgomery@yale.edu

Follow this and additional works at: https://elischolar.library.yale.edu/gsas_dissertations

Recommended Citation

Montgomery, Matthew Jacob, "Analyzing the Effect of Fuel Nitrogen on Soot Formation" (2021). *Yale Graduate School of Arts and Sciences Dissertations*. 244.

https://elischolar.library.yale.edu/gsas_dissertations/244

This Dissertation is brought to you for free and open access by EliScholar – A Digital Platform for Scholarly Publishing at Yale. It has been accepted for inclusion in Yale Graduate School of Arts and Sciences Dissertations by an authorized administrator of EliScholar – A Digital Platform for Scholarly Publishing at Yale. For more information, please contact elischolar@yale.edu.

Abstract

Analyzing the Effect of Fuel Nitrogen on Soot Formation

Matthew Jacob Montgomery

2021

In modern-day life, energy is primarily supplied by the combustion of carbon-containing fuels. As global economic and population growth occurs, the demand for energy, and consequently the amount of energy supplied by carbon-containing fuels, is predicted to increase. Despite overwhelming use of carbon-containing fuels, there are various human health, climate, and environmental issues related to combustion emissions like carbon dioxide (CO_2) and soot. To alleviate our dependence on fossil fuels while concomitantly minimizing the negative impacts of these pollutants, research into renewable fuels, engine geometries, and burning strategies is needed alongside advancements in renewable energy technologies. One strategy to reduce emissions is to change the fuel-type, which requires understanding the relationship between fuel structure and pollutant formation pathways.

The dominance of combustion in providing energy in the modern age, coupled with the drive to control harmful emissions from these systems, motivates the work presented in this dissertation. This thesis aims to elucidate the effect of fuel-nitrogen on soot formation, a subject receiving comparatively less attention than regular and oxygenated fuels. The effect of nitrogen on soot formation becomes relevant for diesel fuels with nitrogen-containing additives, as well as biomass or biomass-derived fuels, which can contain up to 30% nitrogen-containing compounds by dry weight. In addition, nations such as Korea, Japan, and Australia are exploring ammonia (NH_3) as a CO_2 -neutral fuel. Due to issues in stabilizing NH_3 -combustion, initial efforts look to enhance the stability of NH_3 -combustion by co-firing it with hydrocarbons. This doesn't completely eliminate CO_2 emissions, but it reduces them and serves as a stepping stone

to burning pure NH_3 /hydrogen. In these scenarios, soot formation can occur, and the influence of NH_3 on soot emissions becomes relevant.

In this work, various experimental and computational techniques were employed to study the influence of fuel-nitrogen on soot formation. To understand the chemical influence of fuel-nitrogen on soot formation, the sooting tendencies of 14 amines were measured. Sooting tendencies were quantified by re-scaling relative soot concentrations measured in fuel-doped methane flames into Yield Sooting Indices (YSIs). All amines had lower sooting tendencies than structurally analogous hydrocarbons, and the sooting tendencies of amines with the same chemical formula varied significantly. Calculations were performed to analyze decomposition pathways for three of the amines, revealing that trends in sooting tendency correlate with predicted primary decomposition products. The results suggest the suppressive effect of amines on soot formation may be due to carbon-nitrogen interactions which interfere with aromatic growth pathways.

While 2D simulations have been implemented to understand NH_3 oxidation and NO_x emissions from NH_3 -seeded hydrocarbon mixtures, few studies have analyzed the ability of chemical mechanisms to capture flame characteristics and soot formation in 2D atmospheric nonpremixed NH_3 - CH_4 flames with large ratios of NH_3 . To fill this gap, experiments were performed in nonpremixed NH_3 - CH_4 and N_2 - CH_4 co-flow flames with varying ratios of NH_3/N_2 to CH_4 , and compared to simulations. Experimentally, NH_3 had a strong chemical effect on suppressing soot formation, which is attributed to NH_3 -hydrocarbon interactions which reduce the formation of aromatics. While the model was able to capture the physical flame characteristics, it was unable to capture the inhibitive effect of NH_3 on soot. This highlights the need to identify and include nitrogen-hydrocarbon reactions relevant to soot formation in the underlying chemical mechanism.

For the first time, synchrotron X-ray fluorescence (XRF) and X-ray scattering (XRS) were employed to measure spatially-resolved temperatures and mixture fractions in sooting methane/air flames. Both techniques provide evidence that the flame physics are well-captured by the model, and suggest that issues in capturing the suppressive effect of NH_3 on soot is related to deficiencies in the kinetic mechanism. The XRF technique was shown to be insensitive to soot and compositional variations in the flame, and measured temperatures displayed excellent agreement with simulated temperatures. Simulated mixture fractions showed satisfactory agreement with mixture fractions determined by XRS, demonstrating the potential of this technique for probing mixing characteristics in sooting flames.

Lastly, YSIs were measured in partially-premixed flames, demonstrating that sooting tendency trends hold across a range of temperatures and air-to-fuel ratios relevant to soot formation. This suggests that the sooting tendency trends reported for the amines may also hold across these conditions. While a wide range of studies are reported in this thesis, they overlap, and help to strengthen our understanding of fuel-chemistry and soot formation. The work presented here is expected to aid in the development of models which describe nitrogen-hydrocarbon interactions, ultimately enabling the rational design of fuel-types and combustion geometries that mitigate pollutant formation.

Analyzing the Effect of Fuel Nitrogen on Soot Formation

A Dissertation
Presented to the Faculty of the Graduate School
Of
Yale University
In Candidacy for the Degree of
Doctor of Philosophy

by
Matthew Jacob Montgomery

Dissertation Directors: Lisa D. Pfefferle & Charles S. McEnally

June 2021

© 2021 by Matthew Jacob Montgomery

All rights reserved.

Contents

1	Introduction.....	1
1.1	Role of Fuels and Combustion in Society.....	1
1.2	Impact from Combustion Pollutants.....	4
1.2.1	Carbon Dioxide.....	4
1.2.2	Soot.....	5
1.2.3	Nitrogen Oxides.....	6
1.3	Importance of Nitrogen-Containing Compounds in Combustion.....	8
1.3.1	Nitrogen in biomass/coal.....	8
1.3.2	Ammonia as a Nitrogen-Containing Fuel.....	11
1.3.3	Other Nitrogen-Containing Compounds as Fuels/Fuel Additives.....	14
1.4	Dissertation Outline.....	15
2	Background on Soot Formation and Fuel Chemistry.....	18
2.1	Soot Formation Process.....	18
2.2	Influence of Fuel Structure on Soot Formation.....	21
2.2.1	Pure Hydrocarbons.....	21
2.2.2	Oxygen-Containing Compounds.....	23
2.2.3	Nitrogen-Containing Compounds.....	26
3	Sooting Tendencies of Nitrogen-Containing Hydrocarbons.....	29
3.1	Background.....	29

3.2	Experimental methods	30
3.2.1	Burner and flame details	30
3.2.2	Line-of-sight spectral radiance	34
3.2.3	Calculating YSI, and Its Advantages.....	34
3.2.4	Characterization of Soot Composition, Soot Emissivity, and Emission Spectrum from NHC-doped Flames	36
3.3	Results and Discussion	38
3.3.1	Validating the LSSR Diagnostic for Nitrogen-Containing Flames.....	38
3.3.2	Sooting Tendencies of Amines.....	44
3.3.3	Theoretical Insights into Sooting Tendencies of Amines, and Other Considerations.....	50
3.4	Conclusions	57
4	Influence of ammonia on flame characteristics and soot formation in nonpremixed methane/air flames	58
4.1	Background	58
4.2	Experimental methods	62
4.2.1	Burner details.....	62
4.2.2	Centerline temperature and flame height calculations.....	64
4.2.3	Lift-Off Heights and Experimental 2D CH*/NH ₂ * Profiles.....	67
4.2.4	Soot Volume Fraction Measurements.....	69
4.2.5	Species Measurements.....	71
4.3	Computational methods	73

4.3.1	Flow Solver and Flame Conditions.....	73
4.3.2	Chemical Kinetic Model	74
4.3.3	Radiation Model	76
4.4	Results and Discussion.....	77
4.4.1	Effect of NH ₃ on Temperature, Lift-Off Heights, and Flame Heights in Methane Flames	77
4.4.2	NH ₂ * and CH* Distributions in NH ₃ -CH ₄ Flames.....	84
4.4.3	Species Concentrations and Soot Volume Fractions.....	91
4.4.4	Discussion on Effect of NH ₃ on Soot Formation in CH ₄ Flames	99
4.5	Conclusions	102
5	Synchrotron X-ray Fluorescence Thermometry for Validating Combustion Models	104
5.1	Background/Motivation	104
5.2	Methodology	107
5.2.1	Theory Relating X-Ray Fluorescence Signal from Seeded Krypton Atoms to Physical Quantities	107
5.2.2	Burner and Flame Details.....	109
5.2.3	X-Ray Source.....	111
5.2.4	Computational Methods.....	112
5.3	Results and Discussion.....	113
5.3.1	Validation in a Non-Reacting N ₂ Jet.....	113
5.3.2	Uncertainties in a Co-Flow Flame	117

5.3.3	Spatially-Resolved Krypton Number Densities and Temperatures	122
5.4	Conclusions	128
6	Synchrotron X-ray Scattering as a Diagnostic for Measuring Mixture Fraction in Sooting Flames	129
6.1	Background.....	129
6.2	Methodology	131
6.2.1	Theory Relating X-Ray Scattering to Mixture Fraction.....	131
6.2.2	Burner and Flame Details.....	136
6.2.3	X-ray Source and Computational Methods	136
6.3	Results and Discussion.....	137
6.3.1	Mixture Fraction Results in a Methane/Air Flame	137
6.3.2	Preliminary Results in an Argon-diluted Methane/Air Flame	140
6.3.3	Uncertainties	142
6.4	Conclusions	144
7	Validating the applicability of YSI Under Different Temperatures and Air-to-Fuel Ratios.....	145
7.1	Background.....	145
7.2	Experimental methods	147
7.2.1	Burner and Flame Details.....	147
7.2.2	Methodology for Measuring Soot Concentrations	149
7.2.3	Calculation of YSI.....	151
7.3	Results and Discussion.....	151

7.3.1	YSIs Measured in Partially-Premixed Flames.....	151
7.4	Conclusions	156
8	Summary and Future Work	158
9	References	161

List of Figures

1-1: Difficult-to-decarbonize sectors.....	2
1-2: Historical data and projections for global primary energy consumption, by fuel.....	3
2-1: An overall schematic of the soot formation process.....	19
2-2: Elimination reactions for some oxygenates.....	25
3-1: Examples of primary, secondary, and tertiary amines analyzed in this study.....	29
3-2: Maximum LSSR Signal (relative to the undoped flame) from pyridine- and benzophenoneimine-doped flames versus concentration of dopant.....	33
3-3: LSSR Signal (relative to the average of the undoped flame) from undoped, toluene-, and benzophenoneimine-doped flames versus time.....	33
3-4: Diagram depicting the experimental setup for measuring relative soot concentrations.....	35
3-5: Measured YSI of <i>iso</i> -octane over 42 replications.....	35
3-6: XPS Spectra for soot collected from flames doped with different test compounds.....	40
3-7: XRF spectra from soot collected from doped methane flames.....	41
3-8: Blackness levels of soot from different NHC-doped CH ₄ flames vs. radial position in the flame.....	41
3-9: Radiative emission intensities from toluene- and <i>n</i> -butylamine-doped flames.....	43
3-10: YSIs compared to OESIs for 16 NHCs.....	44
3-11: YSI vs. Carbon-number for C ₄ and C ₆ amines.....	46
3-12: YSIs of C ₄ amines (top) and C ₆ amines (bottom) compared to the YSIs of structurally analogous hydrocarbons.....	47
3-13: YSIs of C ₄ amines (top) and C ₆ amines (bottom) compared to the YSIs of structurally analogous alcohols and ethers.....	50

3-14: Time evolution of the major intermediate products/radicals observed during the ReaxFF simulations at 1800 K, for DPA, DIPA, and DMBA.....	52
3-15: Primary decomposition products obtained from unimolecular decomposition of a) DPA, b) DIPA, and c) DMBA.....	54
3-16: Bimolecular H-abstraction reactions for DPA.....	55
3-17: Heat of Combustion vs YSI for select amines, and structurally analogous pure hydrocarbons and oxygenates.....	56
4-1: Simulated residence times of fuel molecules, for N ₂ -CH ₄ flames (left) and NH ₃ -CH ₄ flames (right)	63
4-2: Depiction of experimental setup for centerline temperature measurements.....	65
4-3: Picture of Type R Pt/13%-Rh thermocouple under an optical microscope.....	66
4-4: Simulated velocity information.....	66
4-5: Chart describing procedure for obtaining relative 2D CH*/NH ₂ * intensity profiles as β was varied, as well as relative radially-integrated centerline CH* intensities.....	68
4-6: Image showing the setup used for mass spectrometry measurements.....	72
4-7: Selected images of flames analyzed in this study. Top: N ₂ -CH ₄ flames, Bottom: NH ₃ -CH ₄ flames.....	78
4-8: Selected results for centerline temperatures vs. height-above burner (HAB) for N ₂ -CH ₄ flames (top row) and NH ₃ -CH ₄ flames (bottom row) with changes in β	78
4-9: Maximum centerline and adiabatic flame temperatures.....	79
4-10: Simulated centerline radiative heat losses vs. HAB, for the $\beta=0$ flame.....	80
4-11: Simulated gas phase radiative heat losses, for NH ₃ -CH ₄ flames.....	82
4-12: Experimental and simulated flame heights vs. β for N ₂ -CH ₄ flames (left) and NH ₃ -CH ₄ flames (right).....	83

4-13: Experimental and simulated lift-off heights vs. β for N_2 - CH_4 flames (left) and NH_3 - CH_4 flames (right)	83
4-14: Spatially resolved CH/CH^* profiles in N_2 - CH_4 flames.....	85
4-15: Spatially resolved CH/CH^* profiles in NH_3 - CH_4 flames.....	86
4-16: Radially integrated CH^* intensities/ CH concentrations.....	87
4-17: Spatially resolved NH_2/NH_2^* profiles in NH_3 - CH_4 flames.....	89
4-18: Spatially resolved NH_2/NH_2^* profiles in N_2 - CH_4 flames.....	90
4-19: Species profiles for select N_2 - CH_4 and NH_3 - CH_4 flames.....	92
4-20: Centerline C_2H_2 mole fractions vs height above the burner (HAB).....	92
4-21: Centerline C_6H_6 mole fractions vs HAB.....	93
4-22: 2D f_v distributions of N_2 - CH_4 flames and NH_3 - CH_4	95
4-23: Experimental soot temperatures corresponding to the f_v distributions in Figure 4-22.....	96
4-24: Simulated and experimental centerline f_v vs. HAB for both N_2 - and NH_3 - CH_4 flames.....	97
4-25: Adiabatic flame temperatures vs. β	98
4-26: Experimental and centerline temperature profiles for the $\beta=0.20$ N_2 - and NH_3 - CH_4 flames.....	98
4-27: Normalized centerline maximum C_2H_2 mole fraction (left column), C_6H_6 mole fraction (middle column), and f_v (right column) versus β	100
4-28: Experimental and simulated centerline mole fractions of CH_3CN	101
5-1: Experimental and simulated krypton number densities for a non-reacting, krypton-seeded N_2 -air co-flow jet.....	114
5-2: Simulated 2D Krypton Number Density Profiles for Perturbed and Unperturbed Krypton-Nitrogen Diffusivities, versus the measured profile.....	115
5-3: Simulated Krypton number densities and experimental Krypton number densities.....	116
5-4: Simulated 2D Pressures in the Nonpremixed CH_4 Flame Seeded with Krypton.....	117

5-5: Uncertainty in the experimental measurements due to variations in the krypton mole fraction.....	118
5-6: Measured detector as a function of photon energy, at various HABs in the flame.....	119
5-7: a) Radially-integrated soot volume fraction and transmitted beam intensity vs HAB b) 2D soot concentrations and scattering profiles.....	120
5-8: Random uncertainty in the experimental measurements attributable to photon Shot noise.....	121
5-9: Krypton number-densities in the CH ₄	123
5-10: Temperatures in the CH ₄ flame.....	124
5-11: Centerline temperatures in a methane/air diffusion flame seeded with krypton atoms.....	125
5-12: Radial profiles of near-burner temperatures, from HAB = 0.1 to 0.8 mm.....	126
6-1: Radial profiles of elastic and inelastic scattering signals at various heights in the CH ₄ /air flame.....	136
6-2: Experimental elastic-to-inelastic scattering ratios for the CH ₄ /air flame, at various heights above the burner surface (HABs)	137
6-3: Radial profiles of measured and simulated mixture fractions, at various heights in the flame.....	138
6-4: Centerline mixture fractions for the CH ₄ /air flame.....	139
6-5: Experimental elastic-to-inelastic scattering ratios for the Ar-diluted CH ₄ /air flame, at various heights above the burner surface (HABs)	140
6-6: Radial profiles of mixture fraction measured for the nonpremixed Ar-CH ₄ /air flame, at various heights above the burners.....	140
6-7: Theoretical curve used to map measured atomic carbon concentrations to mixture fraction, compared to the simulated results.....	141

6-8: Mixtures fractions determined at HAB = 1 mm in the CH ₄ /air flame, for varying values of F(x,z)/S(x,z)	142
7-1: Diagram depicting the color-ratio pyrometry experimental setup.....	148
7-2: Diagram depicting the line-of-sight spectral radiance (LSSR) setup.....	149
7-3: 2D Soot concentration profiles and radially integrated soot volume fractions vs. height above burner of doped methane flames.....	152
7-4: Soot concentration map of POSF 10264, demonstrating the range of conditions examined in this study.....	153
7-5: Reference YSI vs. experimentally measured YSI across various λ -values and adiabatic flame temperatures.....	154

List of Tables

1-1: Nitrogen-containing compounds commonly found in biomass.....	10
2-1: Some relevant hydrocarbon growth reactions leading to the formation of aromatics, and rate parameters in the range of flame temperatures.....	22
3-1: Details on the compounds used in the soot blackness measurements.....	31
3-2: Details on amines and nitrogen-containing hydrocarbons used for YSI measurements in this study.....	31
3-3: Details on YSIs and TSIs/OESIs, based on available smoke points in the literature.....	32
3-4: YSIs of 14 amines measured in this study.....	44
3-5: Bond-dissociation energies from DFT calculations, for the C ₆ H ₁₅ N isomers DPA, DIPA, and DMBA.....	53
4-1: Experimental values of β analyzed in this study, along with the corresponding flow rates used to generate nonpremixed NH ₃ -CH ₄ and N ₂ -CH ₄ flames.....	64
5-1: Experimental flow rates for gas mixtures analyzed in the XRF study.....	109
6-1: Atomic form factors, incoherent scattering functions, and other relevant atomic properties used in this study.....	134
6-2: Experimental flow rates for gas mixtures analyzed in the X-ray scattering study.....	135
6-3: Atomic form factors and incoherent scattering functions for other values of x	142
7-1: Dopant properties and flow parameters used for the partially-premixed flame studies.....	146

List of Publications

Some chapters of this dissertation have appeared/will appear in the following manuscripts:

- 1) Montgomery, Matthew J., et al. "Amines have lower sooting tendencies than analogous alkanes, alcohols, and ethers." *Combustion and Flame* 227 (2021): 335-345.
- 2) Kwon, Hyunguk, et al. "Reactive Molecular Dynamics Simulations and Quantum Chemistry Calculations To Investigate Soot-Relevant Reaction Pathways for Hexylamine Isomers." *The Journal of Physical Chemistry A* 124.21 (2020): 4290-4304.
- 3) Montgomery, Matthew J., et al. "The Influence of Ammonia on Flame Characteristics in Nonpremixed Ammonia/Methane Diffusion Flames." Submit to: *Combustion and Flame* (in preparation) (2021)
- 4) Montgomery, Matthew J., et al. "Effect of ammonia addition on suppressing soot formation in methane co-flow diffusion flames." *Proceedings of the Combustion Institute* (2020).
- 5) Montgomery, Matthew J., et al. "Two-dimensional temperature measurements in sooting methane/air co-flow flames using synchrotron X-ray fluorescence of seeded krypton atoms." Submit to: *Science* (in preparation) (2021)
- 6) Montgomery, Matthew J., et al. "Synchrotron X-Ray scattering measurements for obtaining mixture fractions in methane/air diffusion flames." Submit to: *Combustion and Flame* (in preparation) (2021)
- 7) Montgomery, Matthew J., et al. "Analyzing the robustness of the yield sooting index as a measure of sooting tendency." *Proceedings of the Combustion Institute* 37.1 (2019): 911-918.

Acknowledgements

The work presented in this thesis would not been possible without the efforts of many people.

I am incredibly thankful for my mentors, Prof. Lisa Pfefferle and Dr. Charles McEnally. They have provided me with excellent mentorship over the years, and I've had the opportunity to learn a number of different skills and contribute to a range of interesting and unique projects under their guidance. Without their amazing support, the work presented in this dissertation would never have come to fruition, and I would not be the researcher I am today.

I would also like to thank past and present members of the Pfefferle group. From the senior graduate students who showed me the ropes when I first arrived, to the fellow graduate students I've worked and grown with during my graduate studies, to the undergraduates and high school students it was a pleasure to mentor, we've made many memories together over the years that I will cherish the rest of my life. I could not have asked for a more amazing group to work with during my experience at Yale.

I would like to express gratitude to my committee members, Prof. Drew Gentner and Prof. Eric Altman. They have provided me with refreshing and useful feedback over the years, which has helped to shape and improve the research presented in this dissertation.

Many thanks are also due to the collaborators who made a large portion of this research possible. These include Hyunguk Kwon and Yuan Xuan (Penn State University), who performed the full 2D simulations of the nonpremixed flames which were experimentally studied. Seonah Kim and Brian Etz (National Renewable Energy Laboratory) performed quantum calculations, which were critical for providing theoretical insights into the decomposition processes for some of the compounds under study. Alan Kastengren (Advanced Photo Source, Argonne National Lab) and Rob Tranter and Travis Sikes (Chemical Sciences Division, Argonne National Lab) were

instrumental in planning and carrying out the synchrotron X-ray experiments presented in this thesis. Thanks are also due to Jochen Dreyer (Technical University of Denmark) and Junqing Zhu (Yale University), who helped with the color-ratio pyrometry and soot-sampling analyses. I would also like to acknowledge Dhrubajyoti Das (Yale University), who helped set up color-ratio pyrometry experiments for early studies. In addition, I would also like to acknowledge Dr. Min Li (Yale University), who provided extremely helpful insight for the XPS and XRF measurements. In addition, I would like to thank Tim Edwards (Wright-Patterson Air Force Base) for providing fuel samples for the YSI-robustness measurements.

I would also like to thank my mother Kim, father Dan, and sister Sarah. Without their love, sacrifice, and support over the years, I would not be who or where I am today.

Finally, this research would not have been possible without financial support. The work presented in this dissertation is supported by the National Science Foundation (NSF) under Grant no. CBET 1604983. This material is based upon work supported by the U.S. Department of Energy's Office of Energy Efficiency and Renewable Energy (EERE) under the Bioenergy Technologies Office (BETO) and Vehicle Technologies Office (VTO) Program Award Number DE-EE0007983. Use of the Advanced Photon Source was supported by the U. S. Department of Energy, Office of Science, Office of Basic Energy Sciences, under Contract No. DE-AC02-06CH11357. Data was collected on the X-ray Operations and Research beamline 7-BM at the Advanced Photon Source, Argonne National Laboratory. RST and TS acknowledge support from the U.S. Department of Energy, Office of Basic Energy Sciences, Division of Chemical Sciences, Geosciences, and Biosciences through Argonne National Laboratory. Argonne is a U.S. Department of Energy laboratory managed by UChicago Argonne, LLC, under contract DE-AC02-06CH11357

1 Introduction

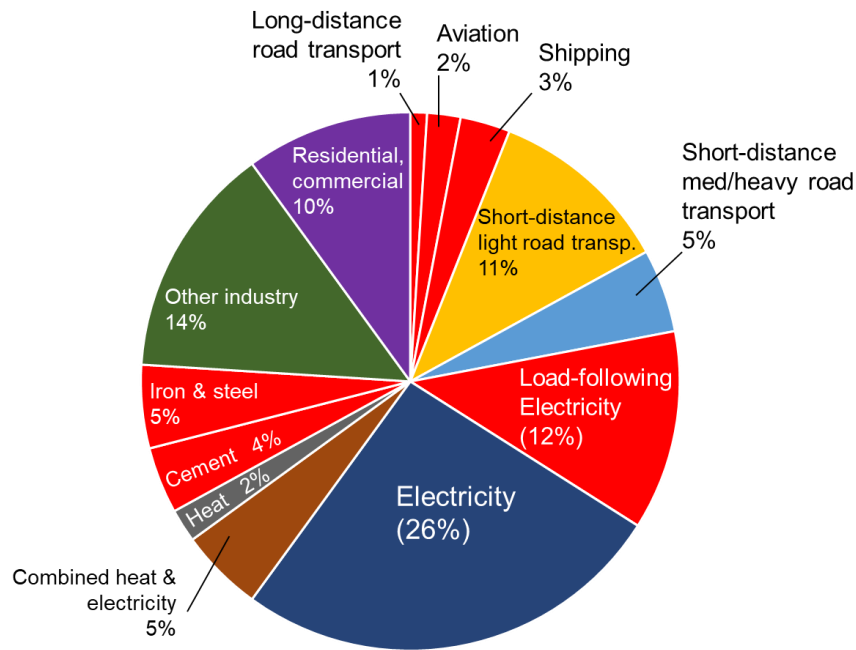
1.1 Role of Fuels and Combustion in Society

From 2015 to 2020, approximately 80% of U.S. energy consumption was supplied by petroleum, coal, and natural gas, while only 10-13% was supplied by renewable sources (1). In addition, of the projected top 10 crises facing humanity in the next 50 years, the need for alternative energy sources ranks number one (2). This is in part attributed to finite global fossil fuel reserves, as well to problems associated with emissions resulting from the combustion of these energy sources. These statements illustrate the large role of fossil-fuels and combustion systems for providing energy in the modern age, as well as the societal drive to alleviate our dependency on these fuel sources.

However, society currently depends on carbon-based fuels to provide energy for a wide variety of important processes, which hinders efforts to reduce our dependence on them. For instance, the industrial, transportation, and electric power sectors accounted for ~90% of total primary US energy consumption in 2020 (3). Within each of these sectors, gas, petroleum, and coal provided 60% to 95% of the total energy consumed (4). Despite the drive to develop renewable, carbon-neutral energy systems, the large dependency of these sectors on fossil fuels complicates transitioning to renewable energy sources.

This transition is also hindered by the fact that some sectors depend on processes where combustion of carbon-based fuels is the only viable solution at the moment. Shown in Figure 1-1 are the total CO₂ emissions from fossil fuel and industry sources in 2014 (5). The red pie slices show processes and sectors which are perceived as “difficult-to-decarbonize,” which accounted for over 25% of total CO₂ emissions in 2014. Renewable energy technologies such as solar and wind can more easily replace carbon-based fuels in areas such as residential heating and cooling, and for other residential/commercial purposes which have low power requirements. Cement is

perceived as difficult-to-decarbonize because the chemical processes required to manufacture it inherently release CO₂. Iron and steel manufacturing requires temperatures between 1100-1500°C, which is currently achieved by burning fossil fuels. Aviation, shipping, and long-distance road transport are considered difficult-to-decarbonize because these sectors have cargo and payload demands which require the gravimetric energy density afforded by liquid combustion fuels.



Global fossil fuel & industry emissions, 2014 (33.9 Gt CO₂)

Figure 1-1: Carbon dioxide emissions from various sectors, with “difficult-to-decarbonize” sectors given by red pie slices. Figure adapted from figure 2 in reference (5).

Because of the difficulty certain sectors face in transitioning to renewable energy sources, the use of fossil fuels is expected to continue for the next 50 to 100 years, and may even increase. To illustrate this point, shown in Figure 1-2 are historical and projected trends in global primary energy consumption, by fuel, from the US Energy Information Administration’s International Energy Outlook (EIA IEO) for 2020 (6). The projections from 2018 to 2050 assume certain rates of global economic and population growth, that current energy policies are implemented, and improvements to established energy technologies occur. Based on these projections, renewables are estimated to provide ~250 quadrillion Btu energy by 2050, more than 2.5 times the amount

they currently provide. Despite the projected increased use of renewable energy sources, the amount of energy supplied by liquid fuels, natural gas, and coal is expected to increase, providing ~615 quadrillion Btu of energy by 2050. This is compared to the ~500 quadrillion Btu supplied by these fuel sources in 2018. Therefore, if the use of combustion fuels is expected to continue into the near-future, then measures to combat emissions will be needed in addition to advancements in renewable energy sources.

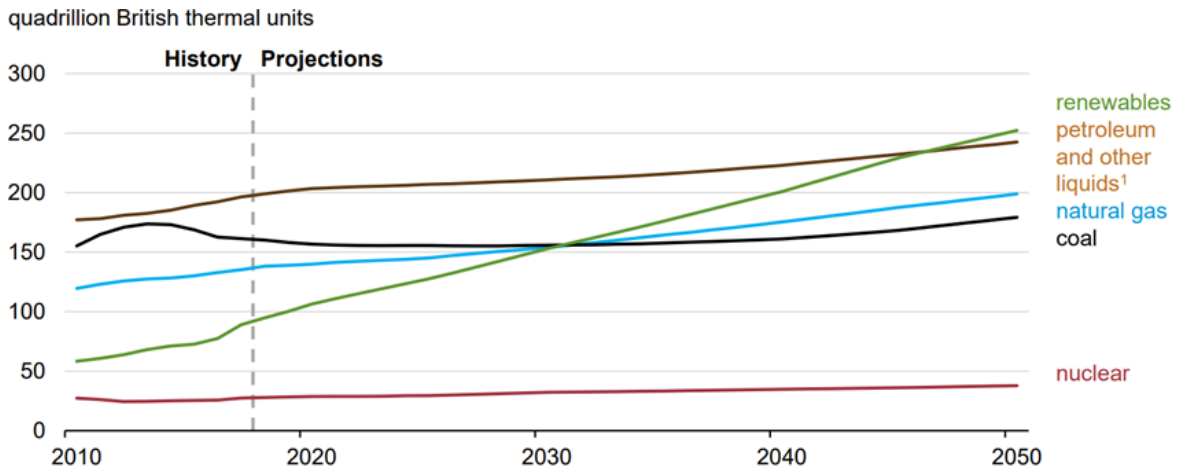


Figure 1-2: Historical data and projections for global primary energy consumption, by fuel. Figure taken from reference (6). ¹Includes biofuels

These reasons illustrate that combustion plays a large role in supplying energy in the modern age, and is likely to continue to for the next 50 to 100 years. This means that to alleviate dependence on fossil fuels while minimizing the impact of combustion emissions, research into renewable fuel types, engine geometries, and burning strategies is needed along with research into renewables. These efforts do not immediately eliminate reliance on combustion technologies, but do serve to eliminate dependence on fossil fuels over time. And while these efforts may not immediately curb the impact from combustion emissions, these efforts help to uncover fuel compositions and burning strategies which lead to reduced emissions. The dominance of combustion in providing energy in the modern age, coupled with the drive to understand and control harmful emissions from these systems, motivates the work presented in this dissertation.

1.2 Impact from Combustion Pollutants

Despite the fact that fossil fuels and combustion-based technologies supply most of the energy consumed in the US, there are a number of issues surrounding the emissions from these systems. Of these emissions, carbon dioxide (CO₂), soot, and nitrogen oxides (NO_x) can be considered some of the most important in terms of their negative impacts.

1.2.1 Carbon Dioxide

One of the most well-known and publicized emissions from combustion devices is CO₂. The formation of CO₂ occurs concomitantly with the formation of H₂O whenever any hydrocarbon undergoes complete combustion with O₂. In 2018, CO₂ emissions from fuel combustion reached a record-high of 33.5 GtCO₂, which has been driven by factors including population growth and global economic development (7).

The main concern driving policy to reduce CO₂ emissions is climate change. The radiative forcing, a measure of the incoming solar radiation versus infrared radiation emitted from the earth's surface, attributed to CO₂ is estimated at ~+1.6 to 2.0 W/m² (8, 9). This indicates that CO₂ has a positive warming effect on the climate. The warming effect of CO₂ occurs because of the "greenhouse effect", where infrared photons from the earth's surface are absorbed and re-emitted by CO₂, further heating the atmosphere rather than escaping to space (10-12). Climate models suggest that doubling of atmospheric CO₂ levels from pre-Industrial revolution levels (~280 ppm) is expected to contribute anywhere from +1.5 to 4.0 degrees of global warming (13), with some estimating even larger changes (14).

Due to these climate impacts, there are large efforts to reduce CO₂ emissions globally. Because the atmospheric lifetime of CO₂ is on the order of several hundred years (15), these measures would be preventative in nature and would have the largest impact generations from now. However, as mentioned in section 1.1, carbon-based fuels are expected to play a large role

in supplying energy in the coming decades. Along with research into renewables, this also necessitates research into combustion fuels and technologies which avoid or minimize the emission of CO₂, as well as into strategies for sequestering CO₂ and preventing its release to the atmosphere. This in part motivates the study of combustion fuels which lack carbon, including ammonia (NH₃).

1.2.2 Soot

One goal of this dissertation is to understand and ultimately control soot emissions from combustion sources. This is motivated by the growing body of evidence elucidating the negative impacts of soot on the environment and human health. Soot, also known as black carbon, is a byproduct from the incomplete combustion of carbon-containing fuels. The most important sources contributing to atmospheric soot emissions in the United States are transportation sources and open biomass-burning, which were responsible for more than ½-million tons and 85% of US black carbon emissions in 2005 (16).

Many studies have highlighted the negative health impacts related to soot emissions. These studies generally conclude that exposure to environmental soot is correlated with respiratory and cardiovascular diseases, as well as various types of cancer (17-19). The damaging health effects of soot may be explained by the generation of reactive oxygen species (ROS) at the particle surface (19, 20). The oxidative stress created by the generation of ROSs within the body could cause conditions such as inflammation and lung injury. While air quality standards focus on particulate matter with diameters generally smaller than 10 microns (PM₁₀) and 2.5 microns (PM_{2.5}), a growing body of research reveals that ultrafine soot particles (<100 nm) are markedly more toxic than larger particles, which could be due to a higher surface area and generation of ROSs (18, 21, 22). In addition, smaller particles are able to pass into the blood stream and through the blood-brain barrier, potentially increasing the risk smaller particles pose to human health (23-25). Soot also constitutes at least 10% of atmospheric particulate matter

pollution (26, 27), which was ranked as one of the top ten risk factors contributing to a reduced life expectancy in 2019 (28). The negative health effects associated with exposure to soot prompts investigation into methods for reducing these emissions from combustion sources.

Soot is also known to have an environmental impact. Studies suggest that black carbon has a positive direct radiative forcing effect of ranging from +0.3 to +0.71 W/m², with a total radiative forcing of +1.1 W/m² (8, 29). The total radiative forcing of soot is comparable to CH₄ (+0.86 W/m²) and may be second to only CO₂ (9). The direct radiative effect of soot is due to the direct absorption of sunlight, which reduces the amount of solar radiation that reaches the earth's surface and is emitted back to space. Soot also has indirect effects which warm the atmosphere, such as by changing the properties of ice and liquid clouds. Soot particles can act as nucleation sites for cloud formation, and can influence the number of liquid droplets, ice particle number, density and extent of clouds, and precipitation rates (8, 30). Soot can also deposit on reflective surfaces such as snow, which can melt the snow and reduce the amount of sunlight reflected from the earth's surface. These effects combine to contribute an estimated 0.5 to 1.0°C to surface warming (31). It has been suggested that to keep the global increase in temperature relative to pre-industrial conditions below 2°C by 2100, then in addition to CO₂ and CH₄ reductions, measures to reduce black carbon emissions are also needed (31, 32). It is worth noting that the atmospheric lifetime of soot particles is on the order of weeks to a month (8). Therefore, efforts to reduce soot emissions will have a more immediate, beneficial impact on climate compared to CO₂ and other measures.

1.2.3 Nitrogen Oxides

“Nitrogen oxide” (NO_x) emissions refer to the sum of NO, NO₂, and N₂O emitted from a particular source. NO_x emissions mainly occur when diatomic nitrogen in the air reacts with oxygen at high temperatures (known as “thermal NO_x”), but is also a common byproduct in the combustion of compounds containing fuel-nitrogen (known as “fuel-NO_x”) (33). NO_x can also

form from interactions between diatomic nitrogen and hydrocarbon-derived radicals during combustion (known as “prompt-NO_x”), but is usually negligible relative to other routes for forming NO_x. Most NO_x emissions in the US come from anthropogenic combustion sources (34), and 0.88 million tons of NO_x were emitted in the US in 2019 (35). NO_x emissions from on-road vehicles and nonroad vehicles/engines have accounted for more than 50% of total NO_x emissions in the US since 1999 (34).

Efforts to limit NO_x emissions are driven by their negative impact on human health and the environment. Previous studies show that exposure to NO_x is associated with increased cardiopulmonary and respiratory diseases, and may be linked with certain cancers (36). As an environmental pollutant, the health effect of NO_x could be due to its proclivity to form photochemical smog, resulting in dangerous ozone formation (37). Reactions of NO_x with atmospheric sulfur dioxide can result in the formation of acid rain (38). Coupled with these indirect effects, NO_x is also phytotoxic itself, and these factors combine to have harmful effects on ecosystems such as by inhibiting vegetative growth (39). In addition, N₂O is considered a greenhouse gas, with a radiative forcing of +0.17 W/m² (40).

While NO_x emissions in the US have been steadily declining (35), there is still work into finding better engine geometries and de-NO_x strategies which reduce these emissions. However, in efforts to achieve carbon neutrality by 2050, nations including Korea, Japan, and Australia have been exploring non-carbon combustion fuels such as NH₃ (41-43). In addition to burning pure NH₃, these efforts would also look to incorporate it into dual-fuel systems, and also as a hydrogen vector for burning pure hydrogen. If fuels containing nitrogen are to become prominent in the future, then potential fuel-NO_x emissions from these sources will need to be considered.

1.3 Importance of Nitrogen-Containing Compounds in Combustion

As alluded to in section 1.2, there is a drive to find fuel compositions that minimize or eliminate harmful combustion emissions. There is also a need to understand the combustion chemistry of different fuel types to enable accurate combustion modelling. While lots of studies have been devoted to understanding hydrocarbon and oxygenate combustion, comparatively less research has been devoted to studying the combustion of nitrogen-containing compounds. Fuel-nitrogen combustion chemistry becomes relevant in cases where fuel sources, such as biomass, are burned. In addition, nitrogen-containing compounds such as ammonia (NH_3) have received recent attention as potential green combustion fuels. Fuel-nitrogen can also be found naturally in coal and as additives in some fuels on the market (44-47). Since the focus of this dissertation relates to understanding the influence of fuel-nitrogen on combustion chemistry, the following sections review common sources for which fuel-nitrogen chemistry can be relevant.

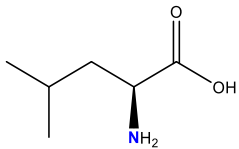
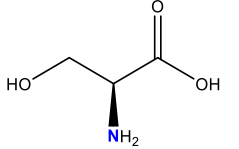
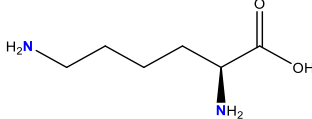
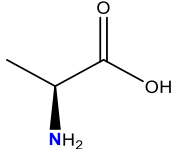
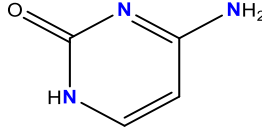
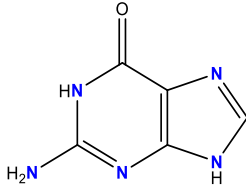
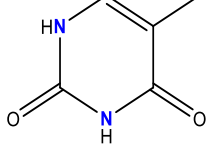
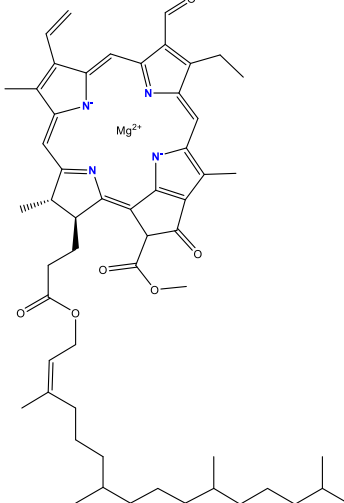
1.3.1 Nitrogen in biomass/coal

Biomass, which accounts for ~8–14% of the annual global energy consumption and is likely to increase, is burned widely in developing countries for uses such as cooking and household heating (48, 49). Solid fuels such as biomass and coal contain organically bound nitrogen. In coals, nitrogen is found as pyrrolic and pyridinic nitrogen (44). In biomass, nitrogen is also found in pyrrolic and pyridinic form, as well as in amino groups in proteins, DNAs, RNAs, chlorophylls, and other molecules. In particular, biomass can contain upwards of 30% nitrogen-containing molecules by dry weight (50-53), and between 0.1–12% nitrogen by elemental composition (54). Fuels derived from biomass, such as “bio-crude” or algae-derived oils, can contain elemental nitrogen on the order of 3–7% before upgrading, and can include nitrogenated species such as pyridines, indoles, amines, and amides (55-60). While the elemental mass fraction of nitrogen

in a given biomass or fuel may appear small, the mole fraction of nitrogen-containing compounds in the fuel is much larger since most of the atoms in the NHCs are not nitrogen. As will be shown in Section 3, the results of this study demonstrate that even a single nitrogen atom can measurably change the soot formation chemistry of a hydrocarbon. Table 1-1 shows some nitrogen-containing compounds found in biomass, along with the mass fraction of nitrogen in the compound's chemical structure. As an example, the table shows that a fuel containing only leucine would contain 10.7% nitrogen by elemental mass fraction yet would be composed of 100% nitrogen-containing molecules. Alanine and leucine are the most common amino acids in plants, comprising approximately 23-24% of the amino acid residues in plant proteins on average (61). Alanine, leucine, and other amino acids are characterized by the presence of amine groups in their chemical structure, making these functional groups ubiquitous in any biomass. Leafy green biomass tends to have a high content of chlorophyll, which has a porphyrin ring with four pyrrolic nitrogen atoms coordinated to a magnesium ion (see structures in Table 1-1).

Many studies have addressed the fate of fuel-bound nitrogen during coal and biomass combustion. For instance, fuel-nitrogen in coals tends to primarily end up as NO when fired under excess air, although NH₃ and HCN emissions can become more important for lower-ranking coals and under fuel-rich conditions (45). The relative importance of NH₃ and HCN emissions also depend on the nature of the coal, with more bituminous, volatile coals giving rise to higher concentrations of HCN than NH₃. The nature of biomass, as well as the chemical structure of nitrogen, has been shown to influence the distribution of NH₃, HCN, HNCO, and NO_x emissions from biomass gasification (62-64). Compared to coals, biomass contains more

Table 1-1: Nitrogen-containing compounds commonly found in biomass

Biomolecule	Formula	Molecular Structure	Percent N by Mass Fraction
L-Leucine (Amino acid)	$C_6H_{13}NO_2$		10.7%
L-Serine (Amino acid)	$C_3H_7NO_3$		13.3%
L-Lysine (Amino acid)	$C_6H_{14}N_2O_2$		19.2%
L-Alanine (Amino acid)	$C_3H_7NO_2$		15.7%
Cytosine (Nucleic Acid)	$C_4H_5N_3O$		37.8%
Guanine (Nucleic Acid)	$C_5H_5N_5O$		46.3%
Thymine (Nucleic Acid)	$C_5H_6N_2O_2$		22.2%
Chlorophyll b	$C_{55}H_{70}N_4O_6Mg$		6.2%

nitrogen in the form of amine sidechains, and therefore has a higher propensity to form NH_3 from fuel-nitrogen. The presence of oxygen in biomass is also thought to impact the fate of fuel-bound nitrogen. For example, oxygen-containing sidechains like amino groups and hydroxyls are thought to promote conversion of fuel-nitrogen to NH_3 compared to pyrrole and pyridinic groups (62, 65). Fundamental combustion studies of nitrogen-containing compounds like morpholine, diethylamine, and NH_3 have been performed in laboratory flames and shock tubes as model compounds for biomass combustion, and also demonstrate the importance of fuel chemistry on subsequent HCN , NH_3 , and NO_x distributions (66-69).

While lots of these studies focus on the fate of fuel-nitrogen during combustion, fewer studies have analyzed the influence of fuel-nitrogen on soot formation (discussed more in Section 2). Since carbon and nitrogen are both present in biomass, understanding their interaction and how it relates to soot formation may help to enable more robust and accurate modeling of biomass combustion, particularly when estimating particulate matter emissions or fire spread.

1.3.2 Ammonia as a Nitrogen-Containing Fuel

Ammonia has received increased attention as a fuel in the past decade. This is in part due to the fact that NH_3 does not contain carbon, and therefore produces no CO_2 emissions when burned. Ammonia also has the potential to be made from renewable sources. For instance, demonstration plants in places such as Port Lincoln, Australia promise to make 100% renewable NH_3 from electrolyzed water and nitrogen separated from the air (70). However, current methods for producing NH_3 are quite energy intensive, and account for ~1-2% of global CO_2 emissions annually. Much research is going into the development of methods for renewable ammonia synthesis (71-73), and nations such as Japan have already pledged to grow their NH_3 fuel demand by 2030 (41, 74).

The use of NH_3 as a combustion fuel is not a new concept. During World War II, diesel-shortages in Belgium prompted the development of the “omnibus,” which utilized a reciprocating engine fired by a dual mixture of NH_3 and coal (75). NASA developed the “North American X-15” plane in the 1960s, which ran on liquid NH_3 and O_2 , and also set a world record for the highest speed achieved by a manned aircraft (76). As a combustion fuel, ammonia has several attractive properties relative to other alternative green fuels like hydrogen. For instance, NH_3 only requires a pressure of 8 atm to liquify, whereas hydrogen requires several hundred times atmospheric pressure before it liquifies. In addition, there is already existing infrastructure for storing, transporting, and handling NH_3 that has been developed over the past 100 years, making NH_3 an easier fuel to transition to than hydrogen.

However, there are certain difficulties surrounding the adoption of NH_3 as a fuel. One issue surrounding ammonia combustion is its low flammability. This is in part related to the low flame speed of NH_3 . The laminar flame speed of a fuel mixture can be experimentally determined by measuring the rate at which the flame front travels for an outwardly propagating spherical flame (77). The flame speed of a fuel is related to the conditions under which it can undergo controlled combustion in an engine environment. Laminar burning velocities of premixed NH_3 /air mixtures range from ~ 2 cm/s at fuel-lean conditions (equivalence ratio $\phi = \sim 0.7$) to a maximum of ~ 7 cm/s at slightly fuel-rich conditions ($\phi = \sim 1.1$) (78). This is relatively low when compared to other fuels; as an example, CH_4 /air and H_2 /air mixtures have laminar burning velocities as high as 37 cm/s and 221 cm/s, respectively (79, 80). To increase the conditions over which NH_3 can be burned, one strategy is to increase its flame speed. This can be achieved by blending ammonia with fuels with higher flame speeds. By blending NH_3 with CH_4 , laminar burning velocities up to 25 cm/s have been achieved (81), and extends the conditions over which the fuel can be burned in a turbine (82). The enhanced stability of NH_3 -combustion through co-firing with hydrocarbons, along with the reduction in CO_2 emissions by replacing a portion of

the hydrocarbon with NH_3 , makes NH_3 /hydrocarbon mixtures attractive for achieving carbon neutrality. While blending NH_3 with hydrocarbons does not completely eliminate CO_2 emissions in the short-term, it reduces them and serves as a stepping-stone to burning pure NH_3 and hydrogen in the future.

Another issue surrounding the use of NH_3 as a fuel is that linked to NO_x emissions. Many studies are concerned with the fate of fuel-nitrogen from NH_3 combustion, and focus on strategies to reduce subsequent NO_x emissions (83, 84). While the thermodynamic products from NH_3 -combustion are H_2O and N_2 , kinetic factors can lead to the formation of NO_x . At low NH_3 -seeding concentrations (<1000 ppm) in nonpremixed CH_4 /air flames, it has been shown that NO outflow increases with NH_3 -seeding concentration (68). However, this occurs along with a decrease in the conversion efficiency of NH_3 to NO , which is attributed to an increase in reaction rates for which NO combines with other nitrogen species (NH , NH_2) to form N_2 . At these low concentrations, NO forms at early heights in the flame through the prompt mechanism, subsequently reacts with hydrocarbon radicals in fuel-rich regions to form species like HCN , and is then oxidized back to NO as it crosses the tip of the flame. For larger concentrations of NH_3 , studies on NO_x formation from turbines fueled by NH_3 and NH_3 /hydrocarbon mixtures demonstrate that NO_x is generally formed under fuel-lean conditions (82). Under fuel-rich conditions, unburnt NH_3 emissions can serve to reduce NO_x emissions via the selective catalytic reduction (SCR) process (82, 85). Relative to pure NH_3 , NH_3 / CH_4 mixtures may have a higher or lower propensity to form NO_x when fired in a microturbine, depending on the fraction of NH_3 in the primary fuel mixture (82, 85). Okafor et al. studied spherical NH_3 / CH_4 /air flames, and found that mixtures containing up to 40% NH_3 in the binary fuel mixture formed twice as much NO_x when compared to the pure NH_3 -air case (86).

Despite possible increased NO_x emissions by co-firing with hydrocarbons, recent efforts have shown that multi-stage combustion can be used to achieve reduced NO_x emissions from CH_4/NH_3 fuels relative to pure NH_3 (84). Single-stage combustion of $\text{CH}_4/\text{NH}_3/\text{air}$ mixtures in a swirl combustor was shown to emit up to 5000 ppmv of NO_x , twice that from NH_3/air mixtures (83). However, a rich-lean combustion strategy was implemented to lower emissions. The rich stage ensures low NO production, while the second stage mainly reduces NO through dilution effects. The higher flame speed of $\text{NH}_3/\text{CH}_4/\text{air}$ mixtures relative to NH_3/air is hypothesized to result in more efficient consumption of fuel during the first combustion stage, resulting in less unburned NH_3 and HCN which can be oxidized to NO during the lean stage. Using this strategy, NO_x emissions as low as 50 ppmv were achieved from $\text{CH}_4/\text{NH}_3/\text{air}$ mixtures without an SCR catalyst, compared to ~100 ppmv for NH_3/air mixtures. This was accompanied with next to no unburnt NH_3 or HCN emissions.

With increased interest in firing fuel mixtures of NH_3 and hydrocarbons, there is now the potential for CO_2 and soot emissions to occur when compared to pure NH_3 -combustion. In particular, while lots of work has been done to analyze the fate of fuel-nitrogen from NH_3 -combustion, fewer studies (described in section 2) have analyzed the influence of NH_3 on soot formation when fired with hydrocarbons. Therefore, one goal of this dissertation is to understand what effect NH_3 may have on soot formation in these scenarios.

1.3.3 Other Nitrogen-Containing Compounds as Fuels/Fuel Additives

Nitrogen-containing compounds can also be found in current combustion fuels. For instance, ethyl hexyl nitrate is used as a fuel additive in market diesels (47), and it along with various other alkyl nitrates have been studied as cetane boosters (87-90). These compounds decompose at lower temperatures than conventional diesel, release chain-initiating radicals, and in some cases result in exothermic heat release, which helps to shorten ignition delay times (91). Nitrogen-containing surfactants are also found in fuels on the market today, such as

in Shell's Nitrogen-Enriched gasolines, as a means to reduce carbon deposits formed in gasoline engines (46).

In addition, certain nitrogen-containing compounds have been examined as alternative fuels themselves (92). Urea has a gravimetric hydrogen content of 6.71 wt %, which can be used to power fuel cells and combustion engines. However, further development of catalysts is required for urea-based energy technologies. Ammonium-based molecules like ammonium carbonate (enthalpy of formation: could be viable as future fuels if NH_3 is used for capturing CO_2 at power plants, and has been used in fuel cells to generate comparable performance to NH_3 -fed fuel cells (93). Hydrazine (N_2H_4) and its derivatives are used as propellants in rocket combustors (94, 95), although there is work in finding safer alternatives (96). Ammonium salts, like ammonium nitrate and ammonium perchlorate, can be used as propellants, although research is looking into overcoming drawbacks such as low burning rates and negative emissions (97). Aqueous ammonium-nitrates, as well as aqueous ammonium hydroxide urea, have been evaluated as potential nontoxic alternatives for future chemical storage of renewable H_2 (98).

1.4 Dissertation Outline

Since there are discrepancies in our understanding of fuel-nitrogen chemistry on soot formation, this dissertation aims to fill in these knowledge gaps, as well as provide data for improving detailed numerical modeling. This dissertation is structured as follows:

- In **Section 2**, I provide a summary of the overall soot formation process, and give a brief review on the importance of fuel-structure on soot formation. Relevant literature related to the influence of fuel-nitrogen on soot formation is also discussed.
- In **Section 3**, I present measurements characterizing the chemical influence of amine functional groups on soot formation. The measurements are supplemented with theoretical simulations. On the whole, amines were found to offer lower sooting

tendencies than structurally-analogous hydrocarbons and oxygenates. Significant differences in sooting tendencies were observed among amines with the same chemical formula. Simulations support the measure trend in sooting tendencies for three of the amines, and suggest the inhibitory effect of amine groups on soot could be due to carbon-nitrogen interactions which compete with growth pathways to aromatics.

- In **Section 4**, I present results analyzing the influence of NH_3 -addition on the physical flame characteristics and soot formation pathways in nonpremixed CH_4 flames. The experimental results were compared to results based on either a literature nitrogen-chemistry mechanism, or general hydrocarbon-combustion mechanism. Experimentally, NH_3 was found to have a strong inhibitory effect on soot formation, which is attributed to carbon-nitrogen interactions which compete with aromatic formation pathways. While the nitrogen-chemistry mechanism performed best in capturing the physical flame characteristics of NH_3/CH_4 flames, both models were unable to capture the measured trends in soot formation. These studies highlight the need to identify and incorporate soot-relevant nitrogen-hydrocarbon reactions in underlying kinetic mechanisms.
- In **Sections 5 and 6**, I present results demonstrating the first application of synchrotron X-ray fluorescence (XRF) and X-ray scattering (XRS) for measuring spatially-resolved temperatures and mixture fractions in sooting CH_4/air diffusion flames. The XRF technique was shown to be insensitive to soot and compositional variations in the flame, and measured temperatures displayed excellent agreement with simulated temperatures. Mixture fractions determined with XRS also showed satisfactory agreement with simulated results, and was also extended to obtain mixture fractions in an argon-diluted CH_4 flame. Both sets of results together help judge the ability of the model to capture the physical characteristics of these systems. In particular, these

results support the idea that issues in simulating the effect of NH_3 on soot formation is due to deficiencies in the underlying kinetic mechanism, rather than with issues in the physical model.

- In **Section 7**, I present results analyzing the effect of partial-premixing on trends in sooting tendency. Since sooting tendency measurements are traditionally done in nonpremixed flame configurations, this analysis allows us to test if the results obtained under a particular set of conditions is robust and holds under a wider range of conditions. This helps to mimic conditions that may be experienced in a real engine environment, where temperature and air-fuel ratio are constantly changing. The results show that the trend in YSI is robust across a wide range of temperature and air-to-fuel ratios relevant to soot formation, and imply that the sooting tendency trends determined in **Section 3** may also hold under different conditions.
- Lastly, in **Section 8**, I summarize the major findings in this work, and provide comments on areas to explore in future studies.

2 Background on Soot Formation and Fuel Chemistry

Since the focus of this dissertation is on understanding the effect of fuel-nitrogen on soot formation, as well as to aid in the development of numerical methods for predicting emissions and other properties of fuel combustion, the following sections aim to provide a background in the overall processes involved with soot formation, with an emphasis on the varying effects of fuel structure on soot formation.

2.1 Soot Formation Process

When a hydrocarbon is completely burned with O_2 , the resulting products are only CO_2 and H_2O . However, in wildfires and practical combustion technologies such as internal combustion engines or turbines, incomplete combustion of the fuel molecules can result in the formation of soot molecules. Soot particles formed from these processes can range in size from tens of nanometers up to hundreds of nanometers (99). These particles can generally be considered to consist of randomly oriented carbon layers with varying degrees of graphitization, with studies demonstrating the presence of both amorphous and crystalline features in these particles (100, 101). The surface of soot particles may also contain various functional groups, including aliphatic, aromatic, carbonyl, and hydroxyl groups (102).

Soot formation is an entropically-driven process, since the endothermic formation of condensed phase carbon species is accompanied by the release of gas-phase species such as H_2 (103). The processes leading from fuel molecules to soot are quite complex, but can be simplified to a few major steps. Figure 2-1 shows an overall picture of the soot formation process. The generalized steps in the soot formation process involve (1) the decomposition of fuel molecules to produce small radicals which initiate combustion; (2) fuel decomposition products react to form larger hydrocarbons, single-ring aromatics, and polycyclic aromatic hydrocarbons (PAH); (3) reactions between PAH and other PAH/decomposition products lead to incipient

particle formation; (4) incipient soot particles react and undergo surface growth reactions to form clusters, which further agglomerate to form fractal clusters of soot particles; (5) in a nonpremixed system such as a diffusion flame, soot particles may either be emitted or oxidized as they cross the flame front and come into contact with oxygen-containing species.

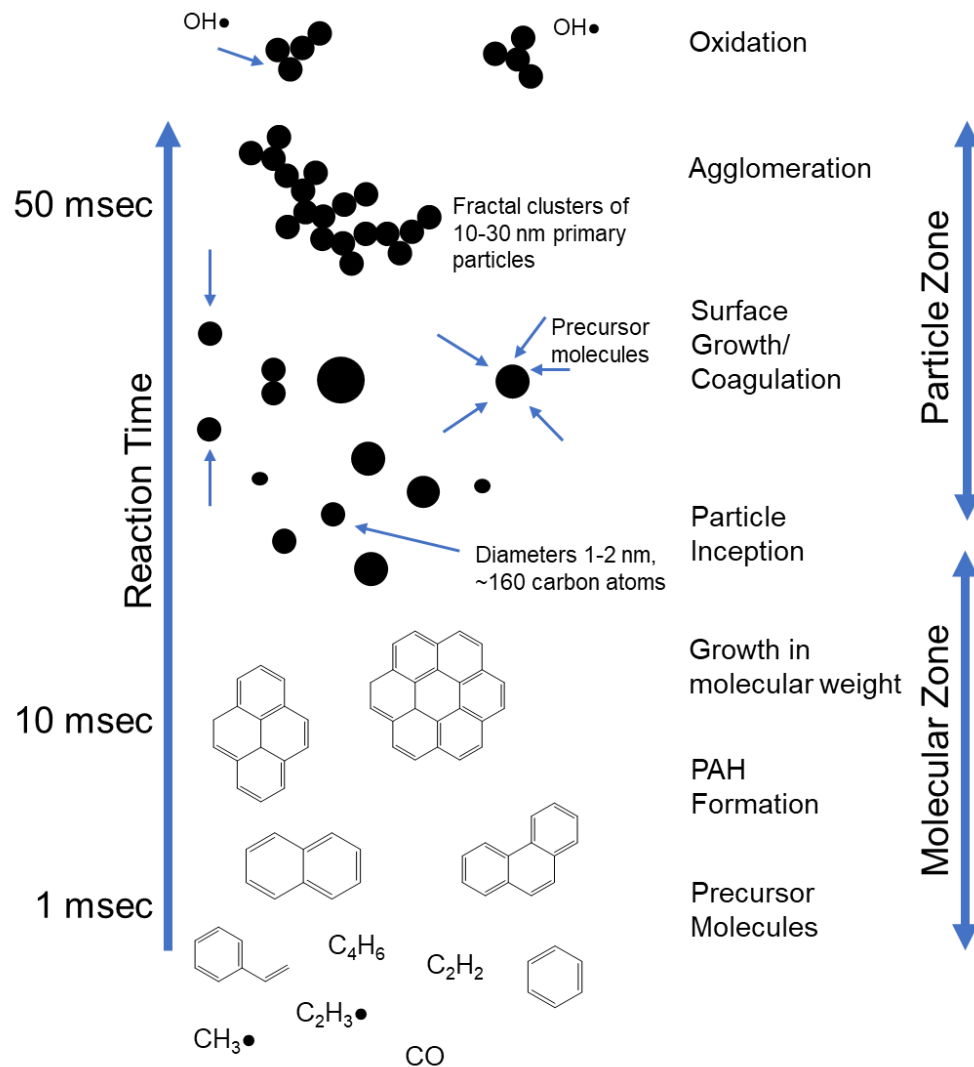


Figure 2-1: An overall schematic of the soot formation process. Figure adapted from data in (104), originally from (105).

The mode of combustion also has an impact on soot formation. Combustion of fuels can be placed into one of two categories: either “premixed” combustion or “nonpremixed” combustion. In premixed combustion, the fuel molecules are mixed with the oxidizer before burning. Premixed combustion is encountered in spark-ignition engines and gas stoves, and the

enhanced mixing of fuel and oxidizer before burning helps promote complete combustion. As the name implies, in nonpremixed combustion the fuel and oxidizer molecules are not mixed before reacting. A canonical example of nonpremixed combustion is the diffusion flame generated by a candle. Flames from wildfires are nonpremixed in nature, and diesel engines and gas turbines operate under nonpremixed conditions. In the case of nonpremixed combustion, fuel molecules have more time to decompose and react with one another before mixing with the oxidizer, which can result in growth to aromatics and subsequently soot. This means that, relative to premixed systems, nonpremixed systems may have a larger propensity to form and emit soot. Since most concern with soot emissions surrounds those derived from nonpremixed combustion sources (3, 16), the work in this dissertation focuses on soot formation in nonpremixed flame configurations.

In general, there are three influences of a fuel on soot formation. These include dilution, thermal, and chemical effects. Dilution influences (106) refer to mixing of one type of fuel with a primary fuel, which reduces the number of collisions that can occur between the primary fuel molecules. In the case of dilution with nonreactive gases, this has an inhibitive effect on soot formation (107). There are also thermal influences that a fuel can exert on soot formation processes. In addition to having dilution influences, inert gases blended into fuels act as a “sponge” to soak up heat released from combustion, exerting a thermal influence by lowering flame temperatures and reducing reactions rates which promote soot formation (106). Blending an inert into a fuel also leads to larger overall gas flow, and can lead to “wasted” energy since a non-reactive component is heated. The third influence of a fuel on soot formation are chemical effects, which will be discussed in the following sections.

2.2 Influence of Fuel Structure on Soot Formation

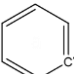
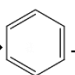
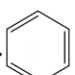
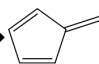
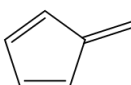
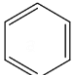
2.2.1 Pure Hydrocarbons

The influence of fuel structure on flame chemistry has been extensively studied for many hydrocarbons, including linear and branched alkanes, alkenes, and aromatic molecules. Early studies exploring the effect of fuel structure on soot formation used smoke point measurements for quantifying a fuel's chemical propensity to form soot. This measurement involves using a wick burner to generate a pure-fuel flame, and the smoke point is defined as the critical height of the flame just before smoking from the tip is observed (108-110). Fuels which have a larger tendency to form soot require a lower fuel flow rate, and hence lower flame height, to achieve the soot concentrations necessary for smoking, and therefore have correspondingly lower smoke points. Smoke points can be linearly re-scaled into a unitless index known as the threshold sooting index (TSI), which quantifies the relative propensity of different fuels to form soot. Various other indices, such as the Yield Sooting Index (YSI) (described in further detail in section 3) (111, 112) and Fuel-equivalent sooting index (FESI) (113, 114), have been developed to quantify sooting tendencies, and both indices involve quantifying relative differences in maximum soot concentrations between different fuel-doped flames. These studies generally show a higher sooting tendency for aromatic molecules relative to aliphatic compounds. This observation is attributed to the presence of benzenoid rings in the fuel structure, which tend to decompose into aromatic precursors that facilitate the formation of PAH and subsequently soot.

The results from these various studies also agree that the presence of carbon-branching increases a molecule's propensity to form soot. For fuel-doped nonpremixed methane flames, the rate-limiting step of soot formation tends to be the formation of the first aromatic ring (115, 116), and so structural features that promote the formation of decomposition products that more easily form benzene will have correspondingly larger sooting tendencies. A flavor of some

reactions leading to the formation of the first benzenoid ring are shown in Table 1-2, and demonstrate the range of C₂, C₃, and C₄ fragments that can react to form aromatic species. The relative importance of these pathways, as well as the many other pathways not shown, will change with varying fuel composition. For instance, in methane flames doped with heptane isomers, structure-dependent differences in the relative distributions of C₂, C₃, and C₄ species have been observed (115). The differences in the distribution of these products ultimately affected the benzene concentrations, which in turn was linearly correlated with soot volume fractions.

Table 2-1: Some relevant hydrocarbon growth reactions leading to the formation of aromatics, and rate parameters in the range of flame temperatures. Parameters were taken from NIST (117), and correspond to rate constants calculated as per $k(T)=A(T/T_{ref})^n \exp(-E_a/RT)$. Units for the A-factor are cm³ molecules⁻¹ s⁻¹

Reaction	Temp Range (K)	A	n	Activation Energy E _a (kJ/mole)	Ref.
(1) HC≡CH + HC≡C-CH=CH• → 	700-2500	347	-14.70	130	(118)
(2) HC≡CH + H ₂ C=CH-CH=CH• →  + H	400-1600	3.2E-13	1.18	15.63	(119)
(3) HC≡C-CH• + HC≡C-CH• → 	953-1262	1.47E-10	0.10	50.21	(120)
(4) HC≡C-CH• + H ₂ C=CH-CH ₂ • →  + 2H	700-2500	7.49E-05	-7.53	99.91	(121)
(5)  → 	1050-1150	7.59E-13	0	309	(122)

In certain cases, synergistic hydrocarbon-hydrocarbon interactions can occur which promote soot formation beyond the sum of the components. As an example, the influence of mixing methane, ethane, propane, and propene into ethylene counterflow diffusion flames has been studied (123-125). It was found that ethane and propane-addition had a large synergistic effect on increasing PAH and soot concentrations when co-fired with ethylene, while a minor

synergistic effect was observed with methane-addition. This was attributed to the increased production of the methyl radical ($\text{CH}_3\bullet$) relative to the baseline ethylene case, which led to an increased conversion of propyne (pC_3H_4) to propargyl (C_3H_3) via $\text{pC}_3\text{H}_4 + \text{CH}_3 \rightarrow \text{C}_3\text{H}_3 + \text{CH}_4$. The increased C_3H_3 levels then aid the formation of C_6H_6 and larger PAH species (126). Because the C-H bond in CH_4 is stronger than the C-C bonds in $\text{C}_2\text{H}_6/\text{C}_3\text{H}_8$ (124, 126), the latter species had larger propensities to undergo unimolecular decomposition and form $\text{CH}_3\bullet$, explaining the smaller synergistic effect of CH_4 -dilution. These various findings hint at the complex relationship between fuel structure and soot formation.

2.2.2 Oxygen-Containing Compounds

In general, oxygenated compounds have been found reduce soot, but placement of the oxygen-containing functional group in the molecule is important in determining whether soot formation is promoted or reduced (127-129). The soot-suppressing effects of oxygenates has been attributed to the idea that the C-O bonds in these molecules tend to be stronger than the C-C and C-H bonds, and so during thermal decomposition the C-O bond is maintained, leading to the formation of CO and subsequently CO_2 . This tends to sequester a carbon that could otherwise participate in soot formation (128). Various indices, such as the Oxygen-Extended Sooting Index (OESI) (129) and Yield Sooting Index (YSI) (127, 130), have been developed and used to capture the sooting tendencies of a wide range of biodiesels and oxygenated hydrocarbons.

Barrientos et al. measured the sooting tendencies of a range of oxygenated compounds, including esters, ethers, alcohols, aldehydes, and ketones (129). It was found that oxygenated functional groups generally had an inhibitive effect on soot formation relative to *n*-alkanes, although the degree of the effect depended on the functional group in question. Among mono-oxygenated functional groups, alcohols and aldehydes were found to have the lowest sooting tendencies on the whole, followed by ketones and then ethers. A group additivity model was

also developed, and revealed that as the oxygen-content of the functional group increases, its contribution towards reducing sooting tendency increases. These results highlight that not only the number of oxygen atoms, but also molecular structure, are important factors influencing the sooting tendencies of oxygenated fuels.

The sooting tendencies of a wide range of oxygenated hydrocarbons have also been characterized using the YSI (127, 130), and confirm the varying effects of oxygenated functional groups on soot formation. In some cases, a given oxygenated functional group was found to either promote or inhibit soot formation. For instance, secondary alcohols such as 2-butanol were found to have higher sooting tendencies than analogous primary alcohols and *n*-alkanes with the same carbon-number. This was attributed to the chemical structure of secondary alcohols, which makes it easier to participate in four-center elimination reactions (Fig. 2-1a) (130). In this case, the resulting products are H₂O and 2-butene; the oxygen atom does not sequester a carbon atom, and a four-carbon alkene is produced instead of smaller hydrocarbon radicals. Some alkyl esters also produced more soot than *n*-alkanes with the same carbon number, and were postulated to undergo six-center elimination reactions (Fig. 2-1b). For these cases, the oxygen atoms in the functional groups end up bonded to the same carbon, ending up ultimately as CO₂. This means the soot-reducing potential of these oxygenates is diminished, since each oxygen atom would bind one carbon atom in the ideal case. Oxygenated groups may also compete with other structural features towards inhibiting soot. For instance, differences in the sooting tendencies of unsaturated esters have been observed, which depend on factors such as the location of the carbonyl group with respect to the double bond (127). In some cases, the soot-reducing effect of the oxygenated group was outcompeted by the increase in soot formation afforded by the double bond. These studies show that the influence of oxygen on soot formation is not universal, further hinting at the complexities inherent in the soot formation mechanism.

In addition, a number of computational studies have been undertaken to understand the measured sooting tendencies of oxygenated compounds. Density functional theory (DFT) calculations have examined the chemical pathways responsible for the sooting tendencies of 1- and 2-phenylethanol (1PE and 2PE), as well as ethylphenol isomers (131, 132). 2PE was observed to have a higher sooting tendency than 1PE, which was explained by the location of the -OH group with respect to the aromatic ring. For 2PE, the alcohol group is two carbon positions removed from the benzenoid ring, and can be easily removed through dissociation or elimination reactions to yield aromatic hydrocarbon precursors (132). The alcohol group for 1PE had a larger tendency to remain attached to the aromatic ring, resulting in the formation of oxygenated aromatic precursors that competed with aromatic hydrocarbon formation pathways. DFT studies (131) on soot formation pathways from ethylphenol isomers demonstrate that the relative position of substituents connected to an aromatic ring influences their resulting sooting tendencies. 2-Ethylphenol (2EP) was measured to have a lower sooting tendency than 3-ethylphenol (3EP). The calculations revealed that the terminal C-C bond in the ethyl sidechains had the lowest bond dissociation energies (BDEs), and the *ortho* substitution in 2EP led to increased resonance stability of radical intermediates relative to the *meta* substitution in 3EP. The increased resonance stability for 2EP decomposition intermediates opened up pathways which led to the formation of oxygen-containing aromatics, explaining its lower sooting tendency.

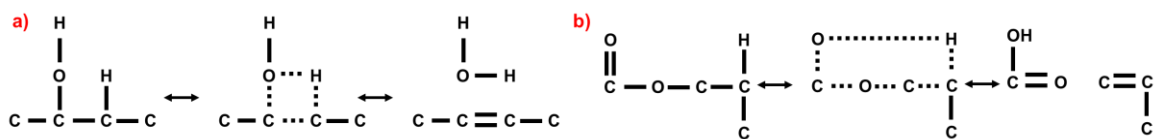


Figure 2-2: Elimination reactions for some oxygenates. a) Schematic for the four-center elimination reaction involving 2-butanol, b) Schematic for the six-center elimination involving the oxygenated groups of alkyl esters. Figures adapted from reference (130)

Full 2D numerical simulations of fuel-doped co-flow flames have been performed to predict the sooting tendencies of a range of bio-derived hydrocarbons and oxygenated compounds, including alcohols, ketones, furans, and esters (133). Great agreement was generally found between experimentally-determined sooting tendencies and numerically-predicted sooting tendencies, which allows for direct mechanistic insights into the relevant soot formation pathways for the different fuels. As a specific example, the model was able to explain the larger propensity of 2,5-dimethylfuran (2,5-DMF) to form soot relative to 2-methylfuran (2-MF). The model found that 2-MF primarily decomposed through a combination of H-atom migration and ring-opening reactions to produce smaller intermediates. Despite overestimating the sooting tendency of 2,5-DMF, the model found that the additional methyl group in 2,5-DMF opened up ring-expansion pathways to produce aromatic hydrocarbon intermediates which were not produced from 2-MF decomposition. These studies highlight how the decomposition processes for compounds with heteroatoms and similar chemical functionalities are not universal, and demonstrate the importance of considering fuel-structure on soot formation.

2.2.3 Nitrogen-Containing Compounds

While the sooting tendencies of hydrocarbons and oxygenated compounds have been studied extensively, very little has been reported on the sooting tendencies of compounds containing nitrogen. RA Hunt analyzed the sooting tendencies of 18 nitrogen-containing hydrocarbons (NHCs) relevant to petroleum and its distillates in 1953 by means of smoke point measurements (108). The effect of nitromethane, nitroethane, and nitropropane as fuel additives on soot formation were also analyzed across a variety of different devices (134), and had varying effects on soot formation depending on the combustion geometry. Other studies have explored the chemistry of small amines (e.g., NH_3 , dimethylamine, ethylamine, morpholine) during pyrolysis or combustion, but these do not focus on soot formation but rather emphasize the

conversion of fuel-bound nitrogen to species such as NO_x , NH_2 , HCN, and other small molecules (66, 67, 135-137).

In the case of mixing NH_3 with hydrocarbons such as CH_4 , soot formation becomes possible, and the influence of NH_3 on soot formation becomes relevant. Few studies before 2015 have addressed the influence of NH_3 on soot formation. Bockhorn *et al.* studied the influence of NH_3 on soot formation in flat premixed propane-oxygen flames (138). They seeded the flames with mixtures of N_2 and NH_3 up to 7.5% by volume and found that soot concentrations were reduced relative to analogous nitrogen additions. The decrease in soot concentrations from NH_3 was attributed primarily to the disruption of soot nuclei formation, but no specific pathways were identified. Another study by Haynes *et al.* (139) demonstrated that NH_3 addition up to 2% by mole in flat premixed ethylene/air flames has an inhibitive effect on soot concentrations, and they suggested this may be due to a quantitative sequestration of one fuel-carbon atom by NH_3 in the form of HCN. A study by Renard *et al.* (140) monitored hydrocarbon intermediates in low pressure flat premixed ethylene-oxygen-argon flames doped with up to 3% NH_3 by mole fraction. The authors found that NH_3 addition had only a slight impact on the C_2H_2 concentrations, while having a stronger influence on C_5 - C_{10} intermediates.

Since the conception of this thesis, recent interest in NH_3 /hydrocarbon mixtures for providing energy has prompted research into the effect of NH_3 on soot formation. In a recent study by Bennet *et al.*, laminar $\text{NH}_3/\text{C}_2\text{H}_4$ flames were studied (141). It was found that NH_3 -addition up to 25% by mole fraction reduced soot concentrations by 80%, compared to an analogous N_2 -diluted C_2H_4 flame. The authors used mass spectrometry to measure acetylene and benzene intermediates, and planar laser-induced fluorescence (LIF) to study the concentrations of multi-ring aromatic species. NH_3 -addition was concluded to have a small influence on C_2H_2 and C_6H_6 concentrations, but resulted in a pronounced decrease in 2-3 ring aromatic species. It was hypothesized that the inhibitive effect could be due to the formation of

reactive CN species which interfere with the growth of 2-3 ring PAH. Li et al. studied the influence of NH₃-addition on PAH concentrations in premixed ethylene stagnation flame, and noted a monotonic decrease in LIF intensities of multi-ring PAH (142). Based on a chemical kinetic analysis, it was hypothesized that the large H radical pool in NH₃-doped flames acts to chemically inhibit the formation of C₂H₂ and C₃H₃, in turn reducing the concentration of C₆H₆. The reduced C₂H₂ was also thought to interfere with carbon-addition reactions to larger PAH. Li et al. further studied the effect of NH₃-addition to premixed *n*-heptane stagnation flames (143). They observed a decrease in PAH formation, which was consistent with kinetic modeling results. The trend was attributed again to the large H radical pool derived from NH₃-addition, which inhibited C₂H₂/C₃H₃ growth pathways to C₆H₆. Soot formation has also been analyzed in turbulent nonpremixed NH₃/H₂/C₂H₄ flames (144). It was found that H₂-addition increased soot volume fractions, while NH₃-addition decreased them. Interestingly, NH₃-addition resulted in lower CH and OH intensities upstream of the soot formation region, while the intensities in downstream locations were unaffected by any of the diluents. While these studies generally show that NH₃ has a chemically inhibitive effect on soot formation, these studies also highlight the need for better model development to understand the exact mechanisms surrounding these observations.

3 Sooting Tendencies of Nitrogen-Containing Hydrocarbons

The contents of this chapter have been published previously in *Combustion and Flame*, and *The Journal of Physical Chemistry* (see “Publications” section prior to Chapter 1, entries 1. and 2.)

3.1 Background

While the sooting tendencies of regular hydrocarbons, oxygenates, and complex fuel mixtures have been well-studied, as was discussed in section 2, far less research has been devoted to analyzing the influence of fuel-nitrogen on soot formation. The effect of nitrogen on soot formation becomes relevant for diesel fuels with nitrogen-containing additives, as well as biomass or biomass-derived fuels, which can contain up to 30% nitrogen-containing compounds by dry weight.

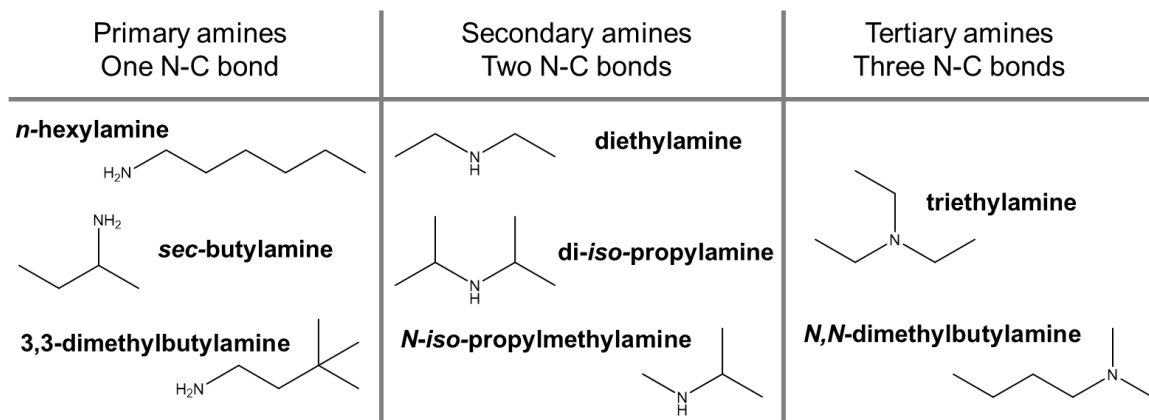


Figure 3-1: Examples of primary, secondary, and tertiary amines analyzed in this study. The feature that distinguishes these categories is the number of bonds between the nitrogen atom and carbon atoms.

To begin to understand the effect of fuel-nitrogen on soot formation, the sooting tendencies of isomeric alkyl amines were experimentally analyzed. Primary, secondary, and tertiary amines with varying substituents were considered for this study (Figure 3-1). Amines were chosen since these types of functional groups are common in biomass, and their study may prove useful for explaining soot formation processes from biomass and biomass-derived fuels.

The YSI was used to quantify relative sooting tendencies among the amines. YSIs of the amines were compared to those of structurally analogous hydrocarbons and oxygenates in order to assess the impact of amine groups and structure on sooting propensity. Soot composition, emission characteristics of the flame, and the emissivity of soot from flames doped with NHCs were also analyzed to ensure accuracy in the experimental sooting tendency measurements.

3.2 Experimental methods

In this work, the sooting tendencies of NHCs were quantified by doping a small amount of the test fuel into a nitrogen-diluted methane co-flow flame, measuring the luminous signal due to soot, and linearly rescaling the signal to YSI values (111, 145).

3.2.1 Burner and flame details

Atmospheric-pressure co-flow laminar non-premixed flames were generated with a Yale Coflow Burner (146): the fuel mixture – methane, nitrogen, and a dopant – flowed out of a 4.0 mm inner-diameter tube and reacted with secondary air that flowed from the annular region between this tube and a 76 mm inner-diameter tube. For a detailed burner description see ref. (147). The gaseous reactants flowed from 99.99+ % purity cylinders (methane, nitrogen) or a compressor (air). Electronic mass flow controllers (Omega FMA 5400/5500 series) actively governed the flow rates of these reactants and were calibrated with soap bubble meters for the specific process gases. The nominal flow rates of methane, nitrogen, and air at 296.4 K and 1 atm were fixed at 281, 112, and 50,000 cm³/min. The dopants were injected as liquids into the gaseous methane/nitrogen mixture by a syringe pump (KDS 100). The performance of this pump was characterized by measuring its linear rate-of-travel with calipers in place of a syringe; the pump was sufficiently accurate across the range of flow rates used in this study to contribute negligibly to uncertainties in the dopant mole fraction in the flame. The syringe pump flowrates at 296.4 K and 1 atm were calculated to produce a gas-phase flow rate of each dopant equal to 0.395

cm³/min, corresponding to a dopant mole fraction in the total methane/nitrogen/dopant fuel mixture of 1000 ppm. Tables 3-1 and 3-2 list the purities of the reactants, the densities used for calculating liquid-phase flow rates (148, 149), and the liquid-phase flow rates input to the syringe pump. Table 3-3 lists the YSIs, TSIs, and OESIs for which literature smoke points were available. The syringe needle entered the fuel line through a septum in a stainless-steel tee. Resistive tapes heated the fuel line to at least 90 °C, and the burner fuel tube to 170 °C, with the fuel tube temperature maintained to within ± 1 °C under PID control. As a result of this heating, the dopants vaporized rapidly upon injection and then were swept to the burner by the other fuel components (Figures 3-2 and 3-3).

Table 3-1: Details on the compounds used in the soot blackness measurements. Densities were obtained first from the Design Institute for Physical Properties (DIPPR) (148), secondarily from the CRC handbook (149), or lastly from the vendor, depending on the availability of information

Dopant	CAS No.	Purity	Mass Density (g/mL)	Flow Rate ^a (μl/hr)
1-Methylindole	603-76-9	97	1.0707 (CRC)	119.8
Benzophenoneimine	1013-88-3	95	1.0847 (CRC)	163.4
Heptanenitrile	629-08-3	98	0.8106 (CRC)	134.1
<i>n</i> -Hexylamine	111-26-2	99	0.7621 (DIPPR)	129.8
<i>N</i> -Methylpropionamide	1187-58-2	98	0.9310 (CRC)	91.5
Pyridine	110-86-1	99	0.9800 (DIPPR)	78.9
<i>tert</i> -Butyl nitrite	540-80-7	90	0.8670 (DIPPR)	116.3
1,8-Diazabicyclo[5.4.0]undec-7-ene	6674-22-2	98	1.0180 (Sigma)	146.2
Toluene	108-88-3	99	0.8655 (DIPPR)	104.1
<i>n</i> -Hexane	110-54-3	99	0.6576 (DIPPR)	128.1

^aLiquid-phase flow rates were calculated to ensure a constant gas-phase flow rate of 0.395 mL/min for all test compounds (corresponds to a dopant mole fraction of 1000 ppm in the fuel mixture at normal lab temperatures and pressures)

Table 3-2: Details on amines and nitrogen-containing hydrocarbons used for YSI measurements in this study. These compounds include those used for the YSI vs. OESI comparisons (Table 3-3/ Fig. 3-9). Densities were obtained first from DIPPR (148), secondarily from the CRC handbook (149), or lastly from the vendor, depending on the availability of the information (Table continued on next page)

Dopant	CAS No.	Purity	Mass Density, g/mL	Flow Rate ^a , μl/hr
<i>N,N</i> -Dimethylbutylamine	927-62-8	99	0.7178 (DIPPR)	137.8
Di- <i>iso</i> -propylamine	108-18-9	99.5	0.7146 (DIPPR)	138.5

3,3-Dimethylbutylamine	15673-00-4	97	0.7520 (Sigma)	131.6
<i>N</i> -Ethyl-butylamine	13360-63-9	98	0.7398 (CRC)	133.8
Dipropylamine	142-84-7	99	0.7388 (DIPPR)	133.9
1,3-Dimethylbutylamine	108-09-8	98	0.7170 (Sigma)	138.0
<i>n</i> -Hexylamine	111-26-2	99	0.7621 (DIPPR)	129.8
Triethylamine	121-44-8	99	0.7260 (DIPPR)	136.3
<i>tert</i> -Butylamine	75-64-9	99.5	0.6898 (DIPPR)	103.7
Diethylamine	109-89-7	99.5	0.7045 (DIPPR)	101.5
<i>n</i> -Butylamine	109-73-9	99.5	0.7365 (DIPPR)	97.1
<i>iso</i> -butylamine	78-81-9	99	0.7311 (DIPPR)	97.8
<i>N</i> - <i>iso</i> -Propylmethylamine	4747-21-1	98	0.7020 (Sigma)	101.9
<i>sec</i> -butylamine	13952-84-6	99	0.7216 (DIPPR)	99.1
Di- <i>n</i> -butylamine	111-92-2	99.5	0.7584 (DIPPR)	166.6
Tri- <i>n</i> -butylamine	102-82-9	99.5	0.7761 (DIPPR)	233.6
Aniline	62-53-3	99	1.0179 (DIPPR)	89.5
<i>o</i> -Toluidine	95-53-4	99	0.9959 (DIPPR)	105.2
<i>m</i> -Toluidine	108-44-1	99	0.9868 (DIPPR)	106.2
<i>n</i> -Butylaniline	1126-78-9	99	0.9323 (CRC)	156.5
Pyridine	110-86-1	99	0.9800 (DIPPR)	78.9
2-Methylpyridine	109-06-8	98	0.9415 (DIPPR)	96.7
3-Methylpyridine	108-99-6	99	0.9536 (DIPPR)	95.5
4-Methylpyridine	108-89-4	99	0.9518 (DIPPR)	95.7
Quinoline	91-22-5	98	1.0909 (DIPPR)	115.8
Quinaldine	91-63-4	95	1.0556 (DIPPR)	132.6

^a Liquid-phase flow rates were calculated to ensure a constant gas-phase flow rate of 0.395 mL/min all test compounds (corresponds to a dopant mole fraction of 1000 ppm in the primary fuel mixture at normal lab temperatures and pressures)
(continued on next page)

Table 3-3: Details on YSIs and TSIs/OESIs, based on available smoke points in the literature (108).

Dopant	YSI ^a	TSI/OESI ^b	Identifier in Fig. 3-3
Triethylamine	25.5	37.4/36.5	TEA
Diethylamine	13.2	36.3/35.1	DEA
<i>n</i> -Butylamine	15.0	36.2/35.1	nBA
<i>sec</i> -butylamine	18.1	35.6/34.5	sBA
Di- <i>n</i> -butylamine	31.3	40.3/39.7	DBA
Tri- <i>n</i> -butylamine	53.4	46.4/46.3	TBA
Aniline	84.6	86.8/77.8	ANL
<i>o</i> -Toluidine	105.2	105.5/96.3	oTD
<i>m</i> -Toluidine	119.6	119.3/108.5	mTD
<i>n</i> -Butylaniline	124.5	110.4/105.5	BAL
Pyridine	34.6	54.8/49.3	PYR
2-Methylpyridine	65.0	74.8/67.5	2MP
3-Methylpyridine	66.1	95.6/85.3	3MP
4-Methylpyridine	65.7	74.7/67.5	4MP
Quinoline	214.6	227.6/198.5	QNO
Quinaldine	311.2	139.4/125.5	QND

^a Measured in this study

^b Calculated based on smoke points from reference (108)

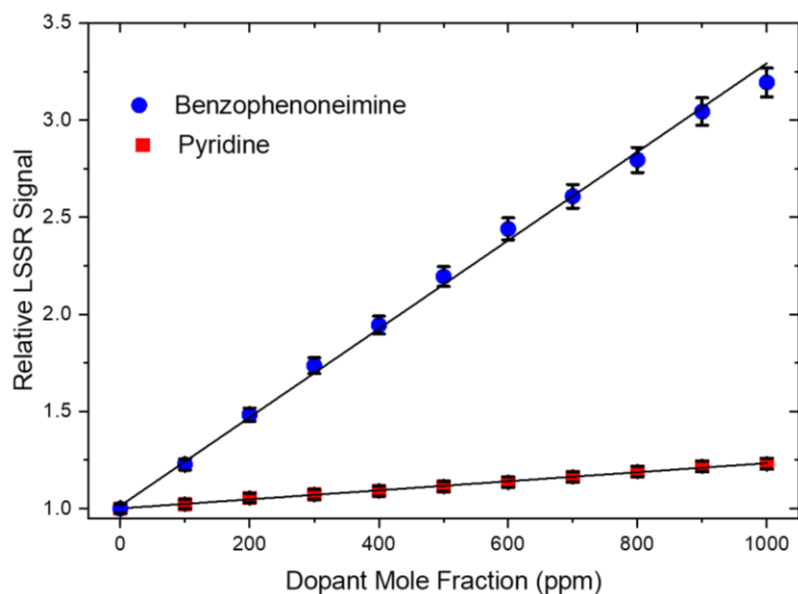


Figure 3-2: Maximum LSSR Signal (relative to the undoped flame) from pyridine- and benzophenoneimine-doped flames versus concentration of dopant. This figure demonstrates the linearity of the LSSR diagnostic in measuring the luminous signal from the nitrogen-containing compounds pyridine (lightly-sooting) and benzophenoneimine (heavily-sooting) up to 1000 ppm by mole fraction in the fuel stream. This linear behavior shows that all of the dopant is vaporizing and arriving at the flame. Lines represent linear least-squares fits to the data.

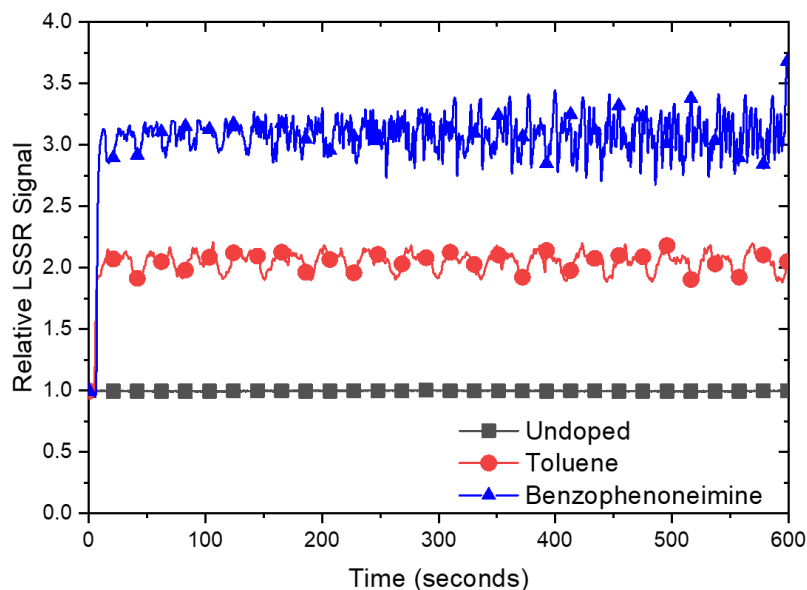


Figure 3-3: LSSR Signal (relative to the average of the undoped flame) from undoped, toluene-, and benzophenoneimine-doped flames versus time. This figure demonstrates that the dopant achieves adsorption/desorption equilibrium with the fuel line walls before the five-minute mark after the dopant is introduced to the base CH_4 flame. Oscillations in signals occur because of the syringe pump, and are largest for sootier dopants like benzophenoneimine, but cancel out because greater than 6 oscillation periods are averaged over the last five minutes of data acquisition. Markers are shown for every 100th data point.

3.2.2 Line-of-sight spectral radiance

In this work, line-of-sight spectral radiance (LSSR) at 660 nm was employed to measure relative soot concentrations. We include “line-of-sight” in the name of this technique because the depth-of-field of our detection system (~8 mm) is comparable to the flame diameter; thus, the measured signal is an integrated line-average of the spectral radiance from all flame locations along the detection system’s axis, rather than the signal from a single point. The LSSR signal was collected at the location of maximum soot (height-above-burner HAB = 44 mm), with 1 mm-spatial resolution in the vertical direction. This technique has been described previously (150) and YSIs measured with it agree well with those of spatially-resolved absolute soot measurement techniques such as color-ratio pyrometry (112). Figure 3-4 shows the experimental setup: (1) a UV silica window mounted in the chimney transmits light emitted by the flame to the rest of the measurement system; (2) a fused silica biconvex lens focusses some of this light onto a 1 mm diameter circular aperture with unity magnification; (3) an interference filter (Thorlabs FB660-10, 10 nm FWHM, $\lambda_{\text{center}} = 660 \pm 2$ nm) and an infrared-blocking filter (Schott KG2) isolate the portion of the light at 660 nm; and (4) a red-enhanced photomultiplier tube (PMT; Oriel 77348) detects it. An A/D converter (LeCroy LT342, 1 m Ω input impedance) samples the PMT output at 5 Hz. Each sample is an average of 50,000 8-bit readings recorded 2 μ sec apart.

3.2.3 Calculating YSI, and Its Advantages

As has been mentioned previously, the YSI measurement involves measurements of maximum soot concentrations in fuel-doped CH₄ flames. The intention of this measurement is to isolate the chemical influence of a dopant to form soot. The YSI measurement has the benefit that small concentrations of the test compound (1000 ppm) are doped into the base methane flame, so that thermal and dilution influences from the dopant are negligible. This means that

measurable differences in soot concentrations can be attributed to the chemical structure of the dopant, and the influence this has on the resulting decomposition products early in the flame.

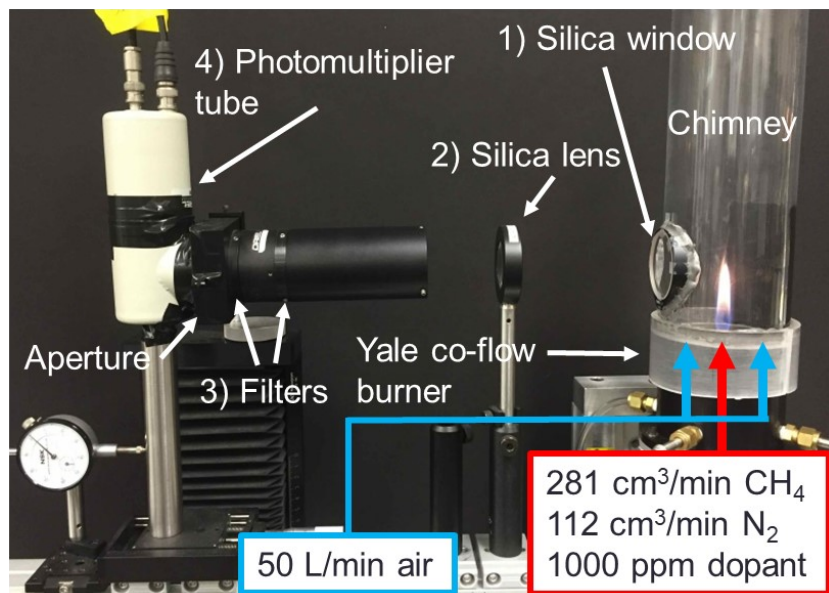


Figure 3-4: Diagram depicting the experimental setup for measuring relative soot concentrations

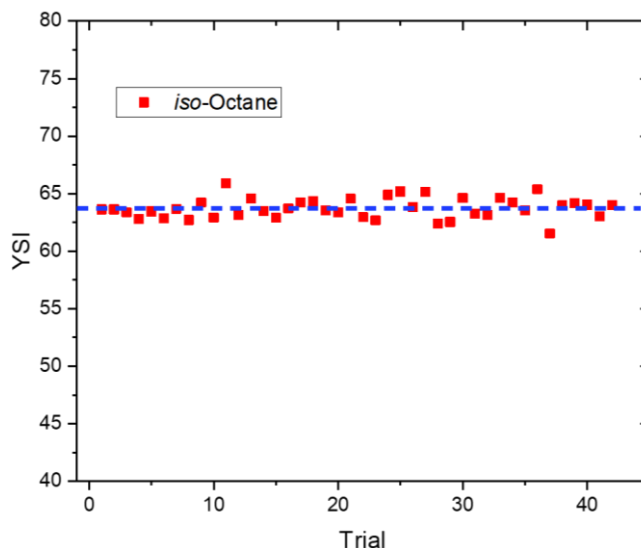


Figure 3-5: Measured YSI of *iso*-octane over 42 replications. With each set of YSI measurements, *iso*-octane was included as an internal standard, and 42 *iso*-octane YSIs were collected over the period of the experiments in this paper. This information was used to calculate the random error in the YSI measurement. Two standard deviations correspond to an uncertainty of $\pm 2.8\%$, and factoring in the systematic uncertainty arising from the density of the dopants, brings the total uncertainty of the YSI measurements in this paper to $\pm 5\%$. The dashed line denotes the average YSI of the 42 data points (which equals 63.7 ± 3.2). This value agrees to within 3.2% with the previously-measured value listed in the YSI Database (61.7) (111).

For this study, we converted LSSR signals into Yield Sooting Indices (YSIs) given by the following equation:

$$YSI_{TC} = (YSI_{TOL} - YSI_{HEP}) \times \frac{LSSR_{TC} - LSSR_{HEP}}{LSSR_{TOL} - LSSR_{HEP}} + YSI_{HEP} \quad (1)$$

where the subscripts TC, TOL, and HEP refer to the test compounds, toluene, and heptane (111, 145). The YSIs are additionally defined such that $YSI_{HEP}=36.0$ and $YSI_{TOL}=170.9$. This definition of YSI is consistent with a YSI database (111) that contains measurements for hundreds of other compounds.

To determine the random uncertainty of the measurements, *iso*-octane was included in each YSI test set as an internal standard. Its YSI was measured 42 times in total and the uncertainty (two standard deviations) was $\pm 3\%$ (Fig. 3-5). The primary source of systematic error is uncertainty in the density of the dopants, which is estimated to be $\pm 2\%$. Errors due to changes in flame temperature and flame shape are assumed to be negligible since the adiabatic flame temperatures and flame heights for the doped flames only vary by 1.5 K and 0.4 mm (151). Altogether, there is an estimated $\pm 5\%$ uncertainty in the measured YSIs.

3.2.4 Characterization of Soot Composition, Soot Emissivity, and Emission Spectrum from NHC-doped Flames

The calculation of YSI from the measured luminous signals depends on the soot optical properties, which may change with the addition of nitrogen into the test compound. To test if differences exist between the properties of soot particles between regular hydrocarbon-doped flames and flames doped with NHCs, we thermophoretically collected soot and characterized it using X-ray photoelectron spectroscopy (XPS), X-ray fluorescence (XRF), and soot blackness measurements. In addition, *in-situ* flame emission measurements were also employed.

The soot used for characterization was collected using a thermophoretic deposition technique (152), in which a spatula tip containing a white paper target is pneumatically inserted and retracted from the flame for an exposure time of 600 ms; this exposure time is short enough

so that the paper target does not react or change optical properties where the measurements were performed (153, 154). For XPS, XRF, and soot blackness measurements, soot was collected at a HAB of 44 mm. To ensure complete optical blockage on the paper target by soot, 40 exposures were taken. For soot blackness measurements, the dopant concentration was set to the same value as for YSI measurements (1000 ppm). For XPS/XRF measurements, the dopant concentration was intentionally increased to 10,000 ppm to increase the odds of incorporating nitrogen into the collected soot.

XPS spectra were analyzed on soot samples for three nitrogen-containing hydrocarbons, quinaldine, pyridine, and 1-methyl indole, based on the hypothesis that they would be the most likely to produce nitrogen-containing soot because they contain pyridinic nitrogen. Soot samples from toluene-doped flames were collected and analyzed for reference. The concentration of the dopant in the base methane flame was increased to 10,000 ppm for these sets of experiments. Spectra were collected using a monochromatic 1486.7 eV Al K α X-ray source on a PHI VersaProbe II X-ray Photoelectron Spectrometer (0.47 eV system resolution). The energy scale was calibrated using Cu 2p $_{3/2}$ (932.67 eV) and Au 4f $_{7/2}$ (84.00 eV) peaks on a clean copper plate and a clean gold foil, respectively. Soot samples collected on the paper target were cut and placed on double-sided tape. For the survey scan, high power (200u50W15kV), 188 eV Pass Energy and 0.800 eV step size were used. Data analysis was performed in CasaXPS.

X-Ray Fluorescence was used to corroborate the results from XPS, and to see if elevated nitrogen concentrations could be detected in the soot samples relative to nitrogen-levels in the paper target. Since XPS is a surface sensitive technique, it will identify nitrogenated species on the surface of the soot with very good sensitivity. The XRF technique probes the bulk of the soot particles, and gives insight into the bulk nitrogen content of the soot samples. Two soot samples (one each for quinaldine and 1-methyl indole) were analyzed, along with a region of the paper target untouched by soot, using a Rigaku ZSX Primus II XRF Spectrometer. The Wavelength Dispersive X-ray

Fluorescence (WDXRF) spectrometer adopts a Rh K- α source with a beam energy of 20.2161 keV, corresponding to an X-ray wavelength of 0.6147 Å.

Because the LSSR method depends on collecting the luminous soot signal at 660 nm, interference from emission bands from nitrogen-containing species becomes possible with the introduction of nitrogen-containing dopants into the flame, and may introduce error into the sooting tendency measurements. To confirm that introducing amines to the flame did not result in emission that interfered with our optical diagnostics, a Mightex HRS-BD1-025 Spectrometer was used to capture the emission spectrum of flames doped with either 1000 ppm of toluene or *n*-butylamine from 550-650 nm. The detector was positioned at the circumference of the burner, 22 mm above the burner surface. The exposure was set to 5 seconds and the collected signal was averaged over 1000 frames.

Table 3-1 lists the names of the dopants, consisting of NHCs and pure hydrocarbons, that were analyzed for the soot blackness measurements. For these experiments, the dopant concentration in the flame was 1000 ppm. Here, soot particles were thermophoretically collected as described above, and photographs of the targets were captured using Adobe Lightroom CC. Photos were saved in .DNG format, and the gray-scale of individual pixels at 1 mm above the bottom edge of the target were analyzed using the program ImageJ (155, 156). Here, blackness is defined as 0 when the gray-scale value of a certain pixel from an 8-bit image is 255 (i.e. pure white) and 1 when the gray-scale value is 0 (i.e. pure black).

3.3 Results and Discussion

The aim of this study was to characterize the sooting tendencies of isomeric C₄ and C₆ amines. We begin by providing evidence that validates the YSI diagnostic in flames doped with NHCs, and then we present the measured YSIs for the amines.

3.3.1 Validating the LSSR Diagnostic for Nitrogen-Containing Flames

Although the LSSR method worked well in our past studies (145, 150), it has only been applied to flames doped with regular hydrocarbons and oxygenates. Four pieces of evidence

were collected during this study to demonstrate that it is also suitable for measuring the sooting tendencies of nitrogen-containing compounds:

(1) XPS measurements showed that, within the detection limit of the instrument ($\sim 1\%$ by atomic concentration), nitrogen was not present on the surface of soot particles sampled from NHC-doped flames. Since the LSSR technique depends on the soot radiative properties at flame temperatures, the results might have changed if nitrogen had been present near the surface of the soot. It is assumed that any presence or lack of nitrogen in the thermophoretically-sampled soot would also hold *in-situ* at flame temperatures. XPS measurements on soot collected from flames doped with the NHCs pyridine, quinaldine, and 1-methylindole were compared to the measurements of soot collected from a toluene-doped flame. These NHCs were chosen because they have nitrogen-containing aromatic rings; thus, it was hypothesized that these compounds would be more likely to yield nitrogen-containing soot. For doped flames used to collect soot for XPS and XRF analyses, the dopant concentration was increased from 1,000 ppm to 10,000 ppm to increase the chances that nitrogen is incorporated into the collected soot. It is further assumed that the elemental composition of the soot particles is not affected by this increase in dopant concentration. The XPS results (Fig. 3-6) show that only carbon and oxygen could be detected on the surface of the soot samples; nitrogen was not detected in any samples.

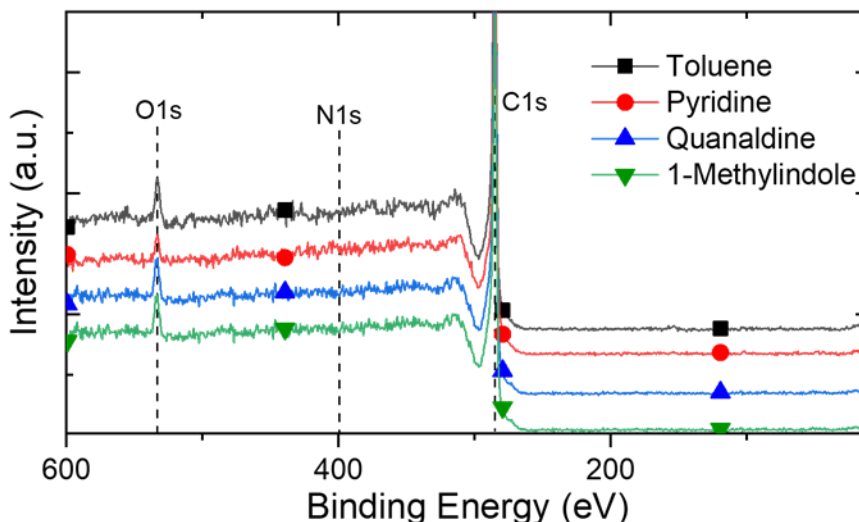


Figure 3-6: XPS Spectra for soot collected from flames doped with different test compounds, which are differentiated by different marker symbols. The spectra are vertically offset, and markers are shown for every 200th datapoint

These results were supplemented with an XRF analysis of the soot from the quinaldine and 1-methylindole-doped flames (Figure 3-7), which provides further evidence that nitrogen is not incorporated into the volume of soot in significant quantities.

(2) Soot “blackness” measurements suggested negligible changes in the emissivity of thermophoretically-deposited soot particles as test compounds varied. Soot from flames doped with several NHCs and toluene was deposited by thermophoretic sampling (152) on to white paper targets until an optically thick layer was formed. The blackness of the soot layers relative to the white paper target was measured by taking a visible light photo of the target after deposition. The blackness of soot particles was defined on a scale from 0 to 1, where 0 and 1 correspond to the whitest and blackest colors detectable by the camera. The NHC-doped flames generated soot with blackness values that were slightly less than one (0.94 to 0.97) and were indistinguishable from those in the toluene- and *n*-hexane-doped flames (Fig. 3-8). It should be noted that these data were analyzed at room temperature, while the LSSR signal is determined at flame temperatures, and it is assumed that any similarities/differences in the emissivity of the room-temperature soot will hold at flame temperatures as well.

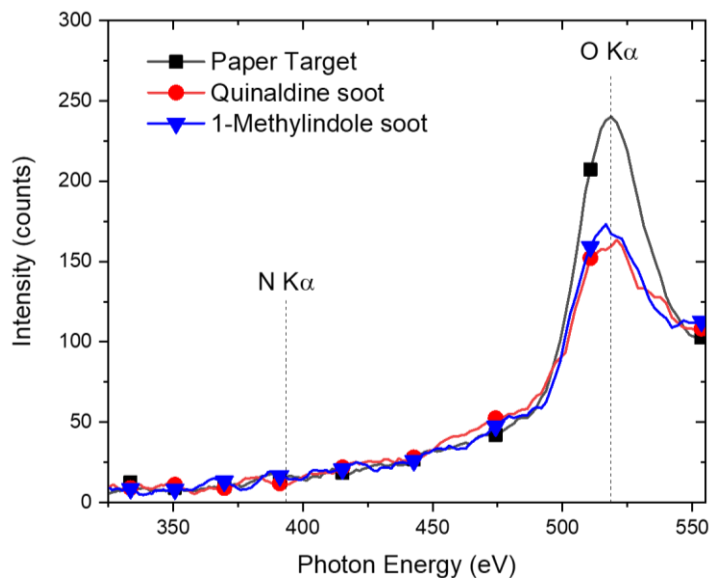


Figure 3-7: XRF spectra from soot collected from doped methane flames. Higher levels of oxygen were found on the bare paper target relative to the paper target covered with soot, but nitrogen was equally undetectable in the paper target and soot samples. This demonstrates that nitrogen is not being incorporated into the bulk of the soot in significant quantities. Markers are shown for every 20th data point

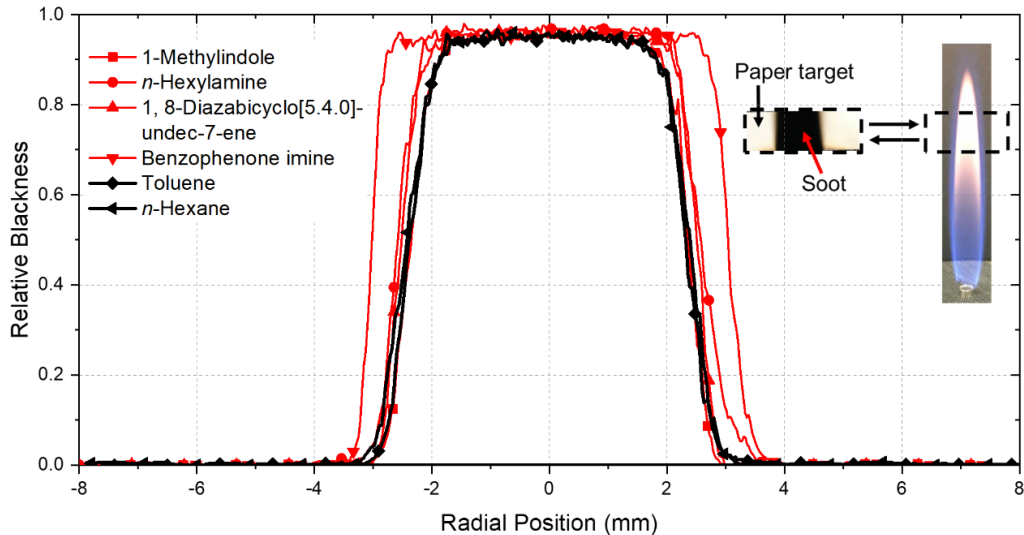


Figure 3-8: Blackness levels of soot from different NHC-doped CH₄ flames vs. radial position in the flame at HAB/L_f=0.89 (HAB= height-above-burner, L_f= flame height calculated from ref (157)). Inset: Image of the paper target covered with soot, along with a photo of the flame, showing the location where soot was collected. NHCs are denoted in red, while pure hydrocarbons are denoted in black. Markers are shown for every 30th data point.

(3) Measurements of the emission spectrum (i.e. from the flame at flame temperatures) reveal that while NHCs may lead to chemiluminescence from NH_2 and other species (158), none of these bands interfere with the LSSR diagnostic at 660 nm. Figure 3-9 compares the emission spectra of flames doped with *n*-butylamine and toluene. For these measurements, the dopant concentration was set to 1000 ppm. It is evident that any new spectral lines introduced near 660 nm in the *n*-butylamine doped flames are negligible relative to the broadband blackbody emission from soot. The larger intensity of the toluene-doped flame occurs because toluene (YSI=170.9) has a higher sooting tendency than *n*-butylamine (YSI=15.0) as shown in Section 3.2. These measurements are intended to provide information on chemiluminescent emissions that may interfere with the diagnostic at 660 nm rather than measure soot properties, but it should be noted that the intensity-ratios for the two doped flames was observed to vary with wavelength. While this observation may be related to etaloning phenomena and the efficiency of the detector at different wavelengths, it may also indicate variations in the Ångstrom exponent for soot between the two flames (159). Such variations could potentially cause YSIs measured at other detection wavelengths to vary from those measured at 660 nm. However, due to the low soot-loading/optically-thin nature of the flames, and coupled with the results from (1), (2), and (4), it is expected that such variations would not significantly influence the measured YSIs.

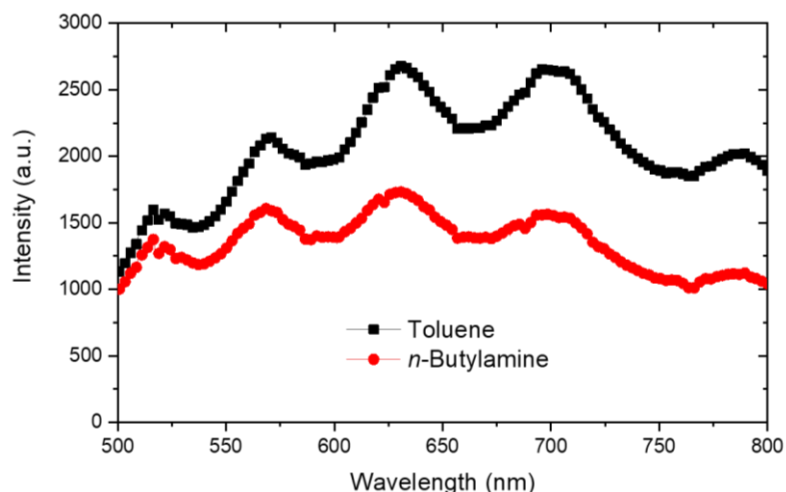


Figure 3-9: Radiative emission intensities from toluene- and *n*-butylamine-doped flames at wavelengths from 500 nm to 800 nm. The observed signal is due to the blackbody radiation from soot particles; the oscillatory behavior and local minima in the plots are due to etaloning phenomena intrinsic to the detector. Markers are shown for every 10th data point.

(4) The LSSR-based YSIs measured in this study agree with earlier smoke point measurements (108). To enable a direct comparison, the smoke point data was converted to oxygen-extended sooting indices (OESIs) (129). The OESI of a test compound TC is defined as:

$$\text{OESI}_{\text{TC}} = A \cdot S_{\text{ox}} / \text{SP} + B \quad (2)$$

$$S_{\text{ox}} = h/4 + c - o/2 \quad (3)$$

where S_{ox} is the number of moles of O_2 required to stoichiometrically combust one mole of the TC, SP is the smoke point, and the TC is assumed to have the formula $\text{C}_c\text{H}_h\text{O}_o\text{N}_n$. In eqn. (3), it is assumed that the fuel-nitrogen is converted to N_2 . For this comparison, the parameters A and B were chosen such that the OESI of *n*-heptane and toluene matched the YSI endpoint values of 36.0 and 170.9. OESI is similar to the threshold sooting index (TSI) (160), but it normalizes the SP to S_{ox} instead of molecular weight, which makes it more applicable to TCs that contain oxygen (129); this is the first time it has been applied, to our knowledge, to nitrogen-containing molecules. Good agreement was found between OESI and YSI for 15 out of the 16 compounds, with an R^2 of 0.964 (Fig. 3-10). YSI indicates a much higher sooting tendency than the smoke point data for quinaldine (QND; rightmost data in the figure). Since QND is a methyl-substituted version of QNO, we expect it to soot more and therefore we attribute this

discrepancy to error in the measured smoke point. Overall, the good agreement between YSI and the smoke point results from (108) provides evidence that the YSI results are not affected by changes in the soot due to the presence of nitrogen in the dopants.

Despite the limited number of data points to use for comparison, the good linear agreement between OESI and YSI, as well as the previous characterization results discussed in (1)-(3), indicates the LSSR diagnostic is suitable for measuring the sooting tendencies of NHCs.

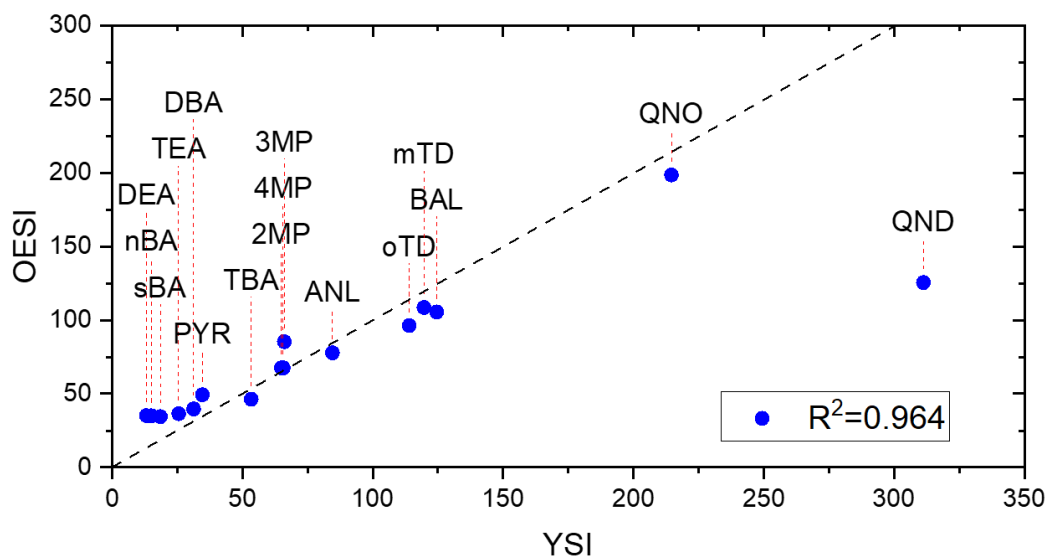


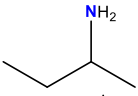
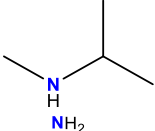
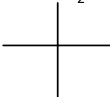
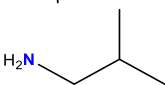
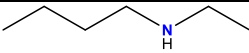
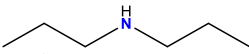
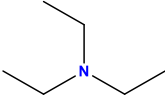
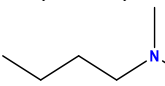
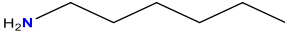
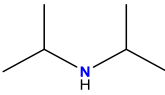
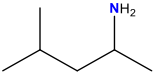
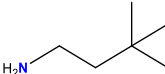
Figure 3-10: YSIs compared to OESIs for 16 NHCs. OESIs were calculated using smoke point data from (108) such that $OESI(n\text{-heptane})=36.0$ and $OESI(\text{toluene})=170.9$. The line $y=x$ is denoted by a dashed line. Reference identifiers correspond to entries in Tables 3-3 and 3-4. R^2 values were calculated without including the QND data point.

3.3.2 Sooting Tendencies of Amines

In this study, sooting tendencies were measured for 14 saturated primary, secondary, and tertiary amines. Table 3-4 lists the results.

Table 3-4: YSIs of 14 amines measured in this study (table continued on next page)

Dopant	Identifier*	Molecular Formula	Structure	YSI (+/-5%)
C4 Amines				
Diethylamine	DEA	$C_4H_{11}N$		13.2
n-Butylamine	nBA	$C_4H_{11}N$		15.0

<i>sec</i> -Butylamine	sBA	C ₄ H ₁₁ N		18.1
<i>N</i> - <i>iso</i> -Propylmethylamine	iMA	C ₄ H ₁₁ N		18.6
<i>tert</i> -Butylamine	tBA	C ₄ H ₁₁ N		21.1
<i>iso</i> -Butylamine	iBA	C ₄ H ₁₁ N		23.4
C6 Amines				
<i>N</i> -Ethylbutylamine	NEB	C ₆ H ₁₅ N		22.1
Dipropylamine	dPA	C ₆ H ₁₅ N		22.5
Triethylamine	TEA	C ₆ H ₁₅ N		25.5
<i>N,N</i> -Dimethylbutylamine	NDB	C ₆ H ₁₅ N		26.1
<i>n</i> -Hexylamine	nHA	C ₆ H ₁₅ N		26.6
Di- <i>iso</i> -propylamine	dIA	C ₆ H ₁₅ N		32.0
1,3-Dimethylbutylamine	13A	C ₆ H ₁₅ N		37.9
3,3-Dimethylbutylamine	33A	C ₆ H ₁₅ N		40.8

*Corresponds to identifiers used in Figure 3-10, and/or in the text

Figure 3-11 displays the YSIs of the saturated and unsaturated amines versus carbon-number, along with the YSIs of branched and *n*-alkanes plotted for comparison. The YSIs measured in this study span a range of 13.2 to 23.4 for the C₄ amines, while those for C₆ species span a range from 22.5 to 40.8. These large ranges show that the specific isomeric structure clearly influences the sooting tendency of amines. For example, the variation among the C₆ amines is equal to the change due to carbon-number from *n*-butane to *n*-octane. Most of the saturated amines were observed to have sooting tendencies lower than the *n*-alkane with the same carbon-number, although a handful of compounds had a higher sooting tendency.

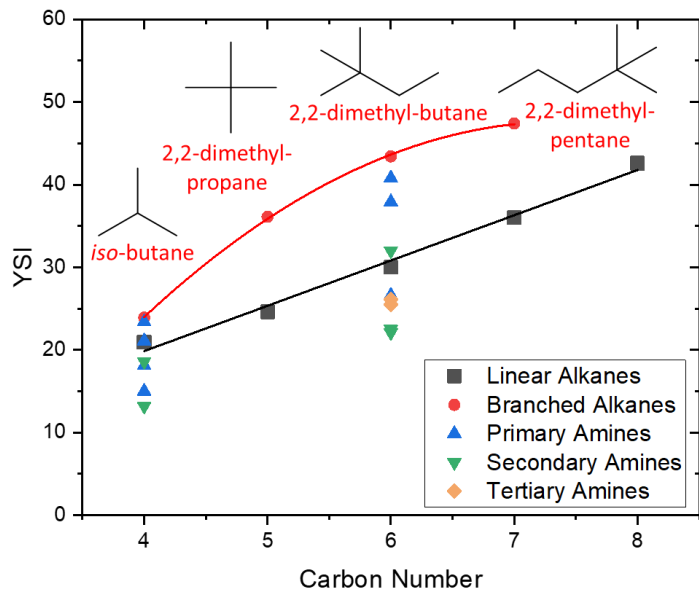


Figure 3-11: YSI vs. Carbon-number for C₄ and C₆ amines. Linear alkanes and some branched alkanes are plotted for comparison, with best-fit lines drawn through the corresponding alkane data. The YSIs of the branched and *n*-alkanes are measured values taken from (111), except those for *n*-butane, *iso*-butane, and 2,2-dimethylpropane, which were estimated using the group additivity model from ref. (145).

Since increased carbon-branching in alkanes increases their YSI (111, 145), the presence of carbon-branching in some amines may explain why they have higher YSIs than the *n*-alkane with the same carbon-number. To better understand the effect of amine groups on sooting tendency, we compared the YSIs of amines to those of structurally-analogous regular hydrocarbons with similar heats of combustion. The requirement that the pure amine and pure hydrocarbon have similar heats of combustion dictates keeping the carbon-number the same between the amine and the comparative hydrocarbon, since carbon and hydrogen contribute significantly to the heat of combustion while nitrogen mostly does not (161). This is opposed to keeping the number of polyvalent atoms the same between the amine and the regular hydrocarbon, which would mean the amine would contain one less carbon atom than the comparative hydrocarbon. Structurally analogous hydrocarbons were heuristically chosen so that they reflect the carbon-branching in the amine chemical structure. When compared in this way, the NHCs were all measured to have a lower sooting tendency than the corresponding

hydrocarbon (Fig. 3-12), even though the C6 amines 3,3-dimethylbutylamine and 1,3-dimethylbutylamine had greater sooting tendencies than the C7 *n*-alkane.

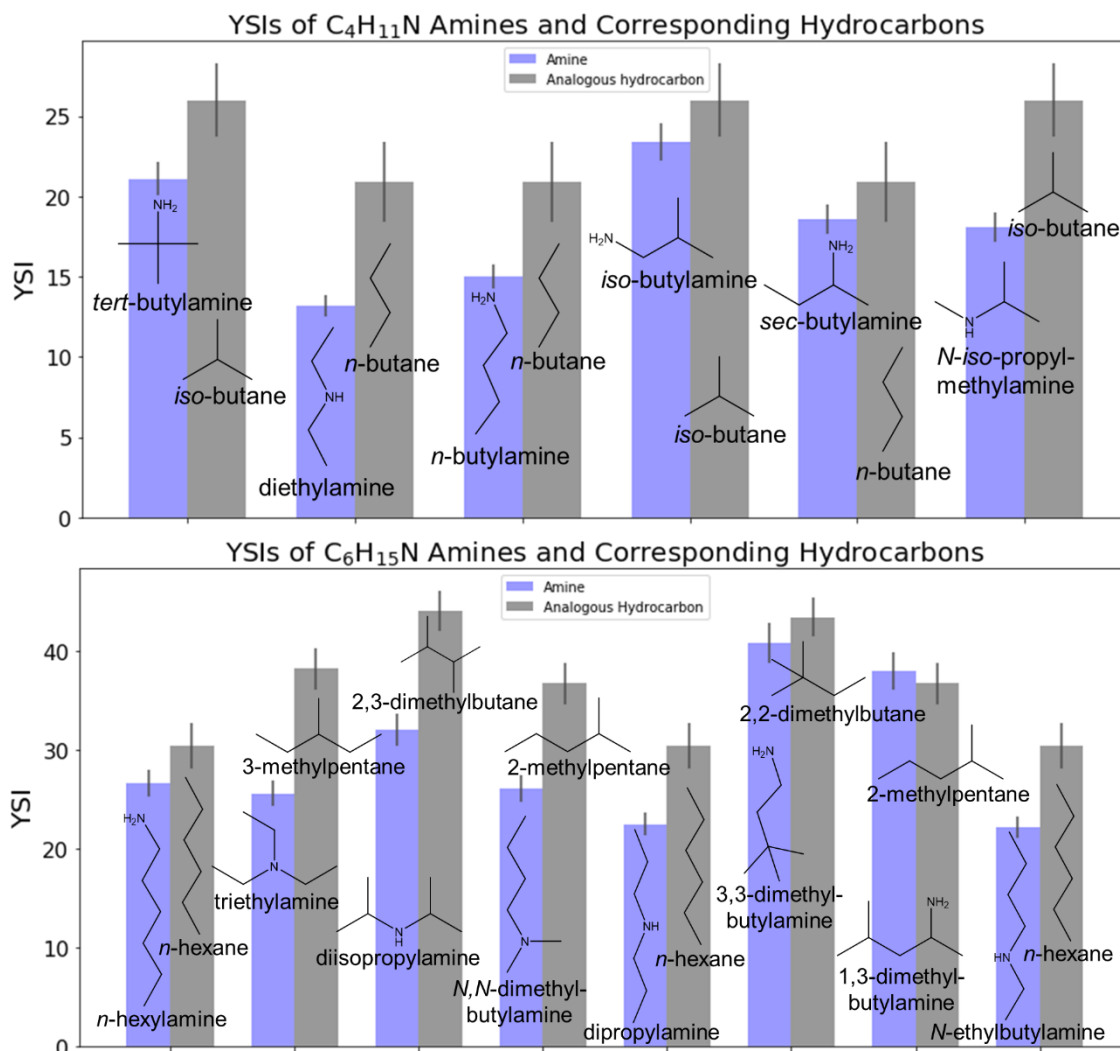


Figure 3-12: YSIs of C₄ amines (top) and C₆ amines (bottom) compared to the YSIs of structurally analogous hydrocarbons. The YSIs of the regular hydrocarbons are measured values taken from (111), except for those for *iso*-butane and *n*-butane, which were estimated using the group additivity model from ref. (145).

Several trends were observed in the dependence of sooting tendency on chemical structure for this particular set of C₄ and C₆ amines (Fig. 3-12):

- Linear primary amines (i.e. *n*-butylamine, *n*-hexylamine) have higher sooting tendencies than the isomeric secondary amines with linear alkyl substituents (i.e. diethylamine, *N*-ethylbutylamine, dipropylamine).

- The secondary amines dipropylamine and *N*-ethylbutylamine have similar YSIs, suggesting that the location of amine groups within the linear hydrocarbon structure negligibly impacts sooting tendency. More secondary amines would need to be studied to confirm this trend.
- Secondary amines with branched alkyl substituents (i.e. *N*-*iso*-propylmethylamine, di-*iso*-propylamine), show a sooting tendency larger than the corresponding linear primary amine (i.e. *n*-butylamine, *n*-hexylamine). This trend is the opposite of the one observed for linear secondary amines.
- The tertiary amines (i.e. triethylamine, *N,N*-dimethylbutylamine) have YSIs slightly lower than the primary amine *n*-hexylamine.
- Among the C6 tertiary amines, the arrangement of linear substituents on the nitrogen (i.e. triethylamine vs *N,N*-dimethylbutylamine) has a negligible effect on the sooting tendency of the compound. This agrees with the trend in YSI among the secondary linear amines in bullet point 2, further suggesting that the location of the amine group within structures that lack carbon-branching has a negligible impact on the sooting tendencies between two compounds so long as they have the same carbon-number.
- For primary amines, the placement of the amine group in the NHC is also observed to impact the sooting tendency of the fuel. For example, placing an -NH₂ group on a secondary carbon increases the sooting tendency relative to a primary carbon (i.e. *sec*-butylamine vs. *n*-butylamine). However, this effect is reversed for the primary amines containing carbon-branching (i.e. *tert*-butylamine, *iso*-butylamine). In this case, placing the -NH₂ on the tertiary carbon in *tert*-butylamine lowers the sooting tendency relative to placement on a primary carbon. More compounds need to be studied to confirm these particular trends.
- Compounds with carbon-branching (i.e. *tert*-butylamine, *iso*-butylamine) have larger YSIs than analogous compounds that lack carbon branching (i.e., *n*-butylamine). This

observation is consistent with previous studies, which demonstrate that carbon-branching generally increases YSI (111, 130, 145, 162).

Another method of assessing the sooting tendency of NHCs is to compare them to their oxygenated counterparts (alcohols and ethers). This allows for the evaluation of the impact of nitrogen-containing functional groups on sooting propensity relative to oxygen-containing functional groups. It should be noted that oxygenated analogues for tertiary amines (triethylamine, *N,N*-dimethylbutylamine) do not exist, but these are among the least sooty of the amines. But for all other saturated amines with oxygenated analogues, when compared in this way it is clear that amine functional groups lower the sooting tendency of a fuel compared to oxygen-containing groups (Fig. 3-13). Several observations are noteworthy:

- All amines examined in this study soot less than their oxygenated counterparts, although in some case the differences are less than the uncertainties in the measurements.
- The largest reduction in sooting tendency occurs between *n*-butylamine and *n*-butanol, with the amine group providing a YSI-decrease of 7.0 relative to the alcohol group. However, the magnitude of this reduction is reduced in the case of *n*-hexylamine (YSI=26.6) and *n*-hexanol (YSI=30.0), suggesting that as carbon-number increases the impact of -NH₂ groups on sooting propensity relative to -OH groups becomes smaller.
- The second-largest reduction in sooting tendency afforded by an amine group occurs between *tert*-butylamine and *tert*-butanol, which reduces YSI by 6.4. The smallest change occurs between 3,3-dimethyl-1-butylamine and 3,3-dimethyl-1-butanol, with YSIs of 40.7 and 40.9, respectively. By comparing the YSIs of 3,3-dimethylbutylamine and *tert*-butylamine, it appears that the farther the -NH₂ group is from a tertiary carbon, the less of an impact it has on reducing the sooting tendency relative to -OH groups.

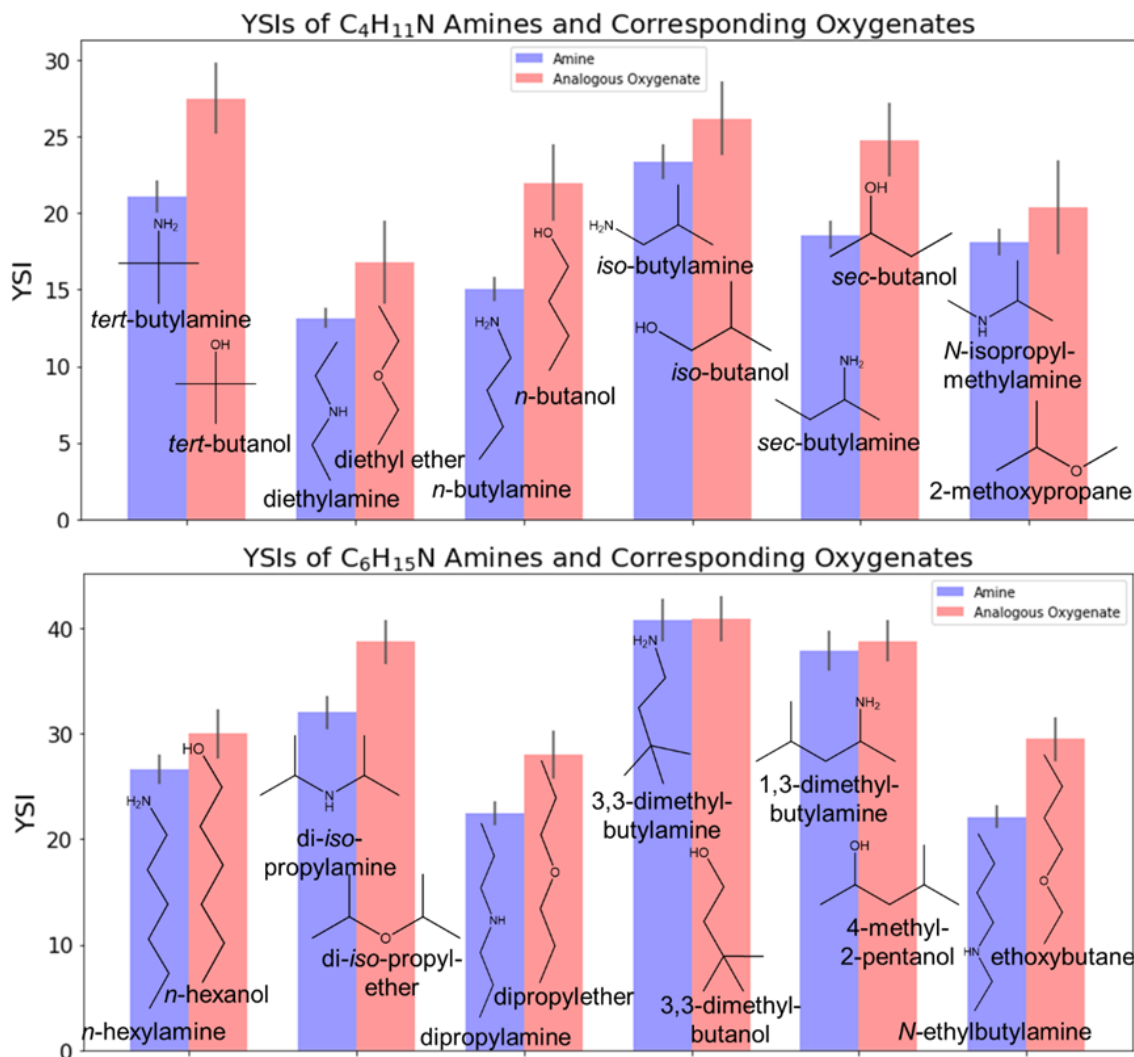


Figure 3-13: YSIs of C₄ amines (top) and C₆ amines (bottom) compared to the YSIs of structurally analogous alcohols and ethers. The YSIs of the alcohols and ethers are measured values taken from (111), except for 2-methoxypropane, which was estimated using the group additivity model from ref. (145).

3.3.3 Theoretical Insights into Sooting Tendencies of Amines, and Other Considerations

To explain the measured sooting tendencies of the amines, follow-up simulations were performed on three of the C₆ amines. Three hexylamine isomers were chosen: dipropylamine (DPA, YSI=22.5), diisopropylamine (DIPA, YSI=32.0), and 3,3-dimethylbutylamine (DMBA, YSI=40.8). The decomposition products were analyzed with Reactive Force Field (ReaxFF) molecular dynamics (MD) simulations and DFT simulations (163).

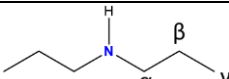
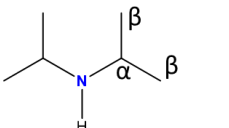
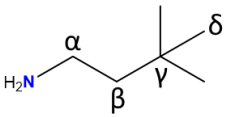
The structures, as well as the bond dissociation energies calculated via DFT, are shown in Table 3-5. A description of the computational methods can be found in ref. (163). For all three compounds, the weakest bonds were found to be the C^α-C^β, followed by the N-C^α bond. The weakest C-H bond was also found at the C^α position for all compounds. This suggests that initiation reactions will involve N-C^α or C^α-C^β bond fissions, or hydrogen abstractions from the C^α position. By tracing out decomposition pathways for the amines by considering dissociation of the weakest bond and assuming β-scissions are the fastest dissociations (116), the major stable decomposition products for DPA, DIPA, and DMBA are obtained as C₂H₄, C₃H₆, and C₄H₈, respectively. This is consistent with the trend that YSI(DPA) < YSI(DIPA) < YSI(DMBA).

A detailed description of ReaxFF MD simulations can be found in (164, 165). Briefly, ReaxFF MD simulations define atomic and molecular interactions through the concept of “bond order,” which defines the connectivity between atoms based on bond, angle, and torsion terms, as well as interatomic distances. Coulombic and van der Waals interactions, which don’t depend on connectivity, are calculated between every pair of atoms. To simulate bond formation and breaking, the bond order is updated every iteration of the simulation. This allows full simulations of chemically reactive systems to be performed, and has the added benefit that simulations can be performed on compounds for which no detailed kinetic mechanisms exist. This is particularly useful for the C₆ amines under question. To mimic the combustion environment in the YSI flame, *NVT*-MD simulations were first performed for 280 CH₄ and 160 O₂ molecules. This mimics the equivalence ratio ($\phi=3.5$) in the region of soot formation for the YSI flame (166). Then, 42 fuel molecules were randomly inserted into the mixture, and a second *NVT*-MD simulation was performed. From this, information on the decomposition products could be extracted.

Figure 3-14 shows the results for the time history of the major decomposition products of DPA, DIPA, and DMBA at 1800 K. The major decomposition products for DPA, DIPA, and DMBA

are C₂H₄, C₃H₆, and C₄H₈, respectively, which is consistent with the previous pathway analysis that considers dissociation of the weakest bonds. Additionally, a number of nitrogen-containing hydrocarbons were observed at the end of the simulation. For DPA, DIPA, and DMBA, the major

Table 3-5: Bond-dissociation energies from DFT calculations, for the C₆H₁₅N isomers DPA, DIPA, and DMBA. The two weakest bonds are highlighted in red. All values are in kcal/mol. Data adapted from (163).

	N-H	N-C ^α	C ^α -C ^β	C ^β -C ^γ	C ^γ -C ^δ	C ^α -H	C ^β -H	C ^γ -H	C ^δ -H
 Dipropylamine (DPA, YSI=)	91.2	82.2	79.6	86.7	-	89.4	96.4	98.8	-
 Diisopropylamine (DIPA, YSI=)	91.5	80.1	79.8	-	-	87.9	99.0	-	-
 3,3-dimethylbutyl- amine (DMBA, YSI=)	96.8	82.7	80.2	84.2	85.1	89.0	96.8	-	99.4

nitrogen-containing species that formed were the *N*-methylmethanimine radical (C₂H₄N•), acetonitrile (C₂H₃N), and methanimine (CH₃N), respectively. These results suggest that the lower sooting tendencies of nitrogenated hydrocarbons relative to pure hydrocarbons and oxygenates may be due to carbon-nitrogen interactions, which reduces the flux of carbon able to participate in the formation of aromatic species. The observation that DMBA forms compounds in which the nitrogen atom only sequesters one or two carbons could also help explain the higher sooting tendency of DMBA relative to DIPA and DPA.

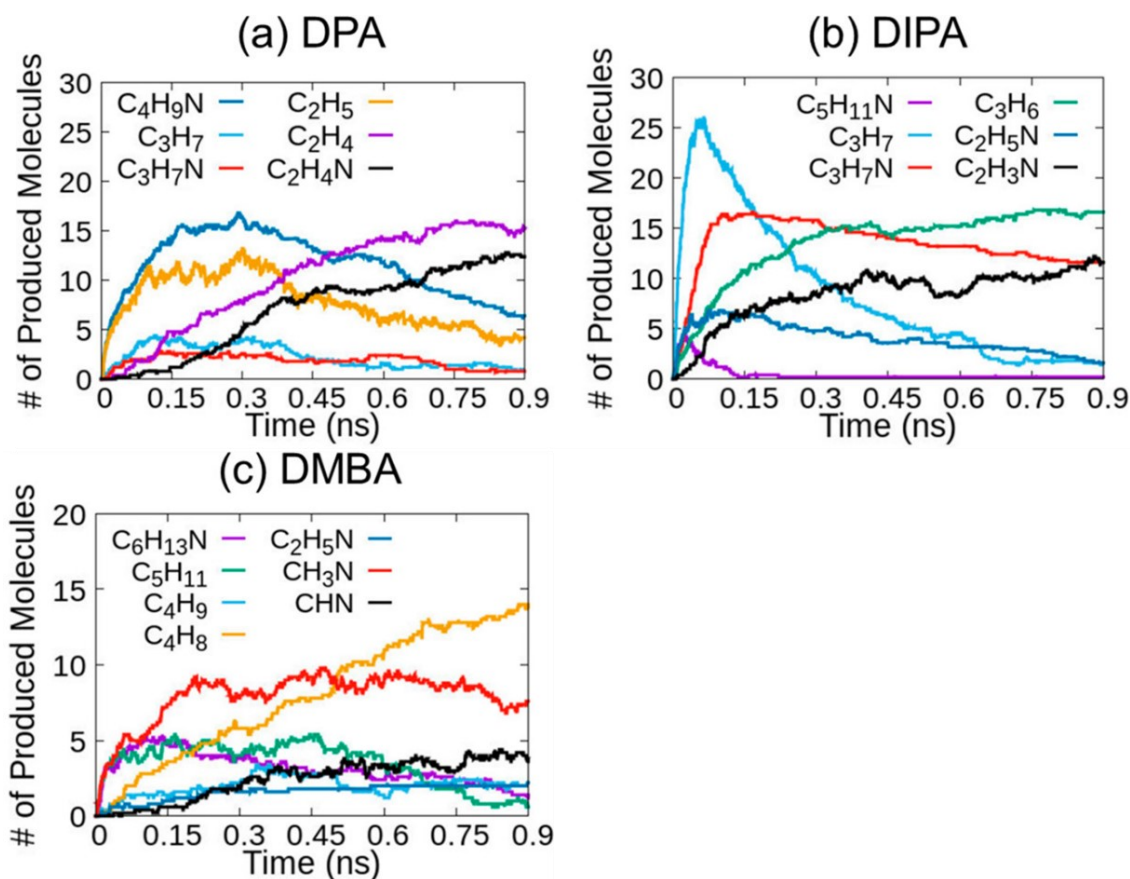


Figure 3-14: Time evolution of the major intermediate products/radicals observed during the ReaxFF simulations at 1800 K, for a) DPA, b) DIPA, c) DMBA

To support the ReaxFF calculations, the major decomposition pathways were also analyzed with DFT. Shown in Figures 3-15 are unimolecular decomposition products obtained from considering H-atom migrations. For DMBA and DPA, the lowest-energy unimolecular pathways were determined as N-C α bond fission (68.5 kcal/mol and 67.9 kcal/mole, respectively). In the case of DMBA, this results in the formation of ammonia, ethylene, and isobutene (Fig. 3-15c, reaction i). For DPA, this results in the formation of propene and NH₃ (Fig. 3-15a, reaction i). For DPA, the two most stable radicals formed by bimolecular H-abstractions were shown to result in C₂ species, which will convert to C₂H₄ (Fig. 3-16). In the case of DIPA, there were multiple competing unimolecular pathways, resulting in either propene or an azetidine intermediate which further decomposes to C₂/C₃ species (Fig. 3-15b, reaction i and ii). The H-abstraction pathways for DIPA and DMBA (not shown) show that decomposition of the

most stable radicals result in the formation of primarily C₃ or C₄ products, respectively. These results are in agreement with the ReaxFF results, which show that the carbon-number of the primary decomposition product increases in the order of DPA→DIPA→DMBA, and explain the trend in sooting tendencies of these isomers. The DFT simulations also show evidence of carbon-nitrogen interactions which could interfere with aromatic formation pathways, potentially explaining the lower sooting tendencies of amines relative to hydrocarbons/oxygenates (Fig. 3-11, 3-12).

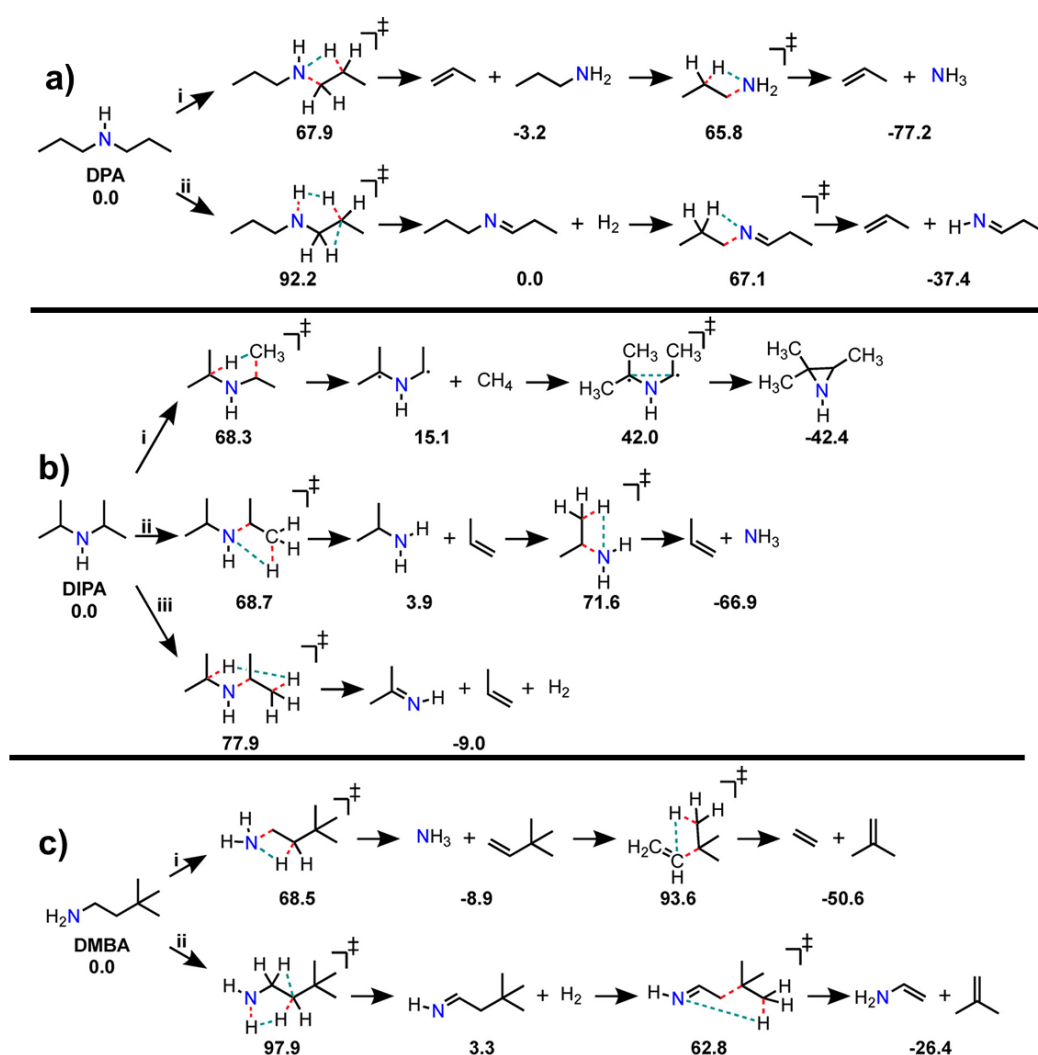


Figure 3-15: Primary decomposition products obtained from unimolecular decomposition of a) DPA, b) DIPA, and c) DMBA. For transition state structures, the red dashed lines represent bond breaking, and teal lines represent bond formation. All energies are Gibbs free energies, calculated using composite G4 theory at 1800 K. Units are kcal/mol relative to DPA/DIPA/DMBA. Figure adapted from (163)

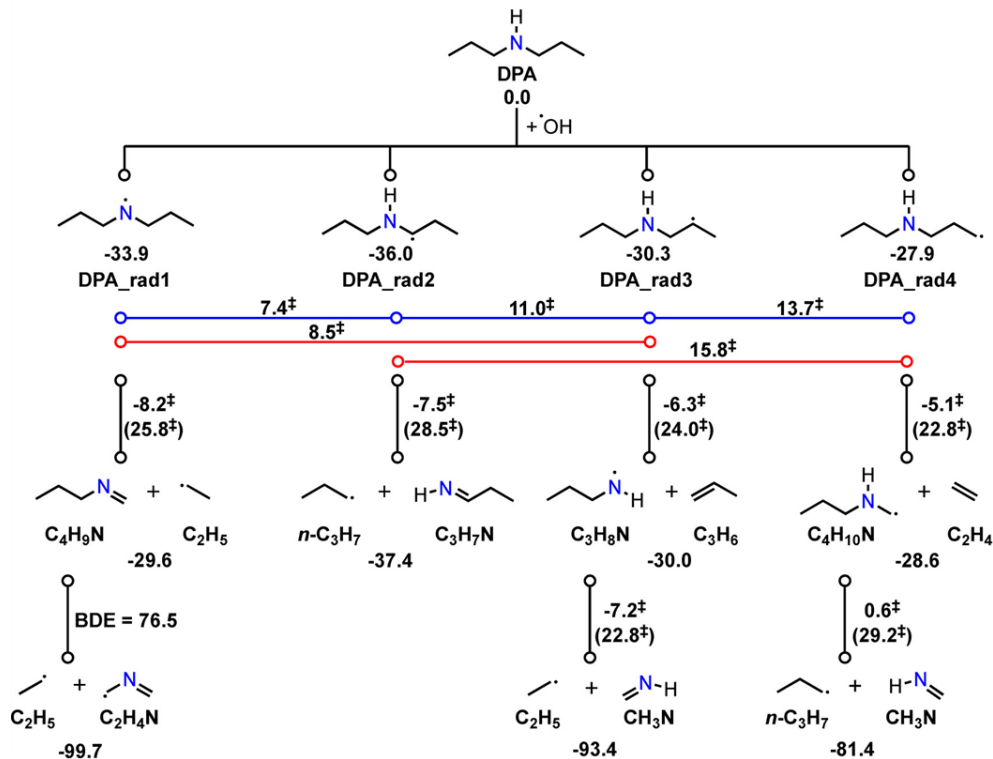


Figure 3-16: Bimolecular H-abstraction reactions for DPA. Blue and red horizontal lines represent [1,2] H-shift and [1,3] H-shift rearrangements. All energies are Gibbs free energies, calculated using composite G₄ theory at 1800 K. Units are kcal/mol relative to DPA. Energies in parenthesis are not normalized to DPA. Figure adapted from (163)

If nitrogen-containing compounds are to become fuels in the future, or used as additives for reducing soot formation, several criteria need to be considered. One such criterion is the energy content of the fuel. The higher heating value (HHV) and lower heating value (LHV) of a fuel are typically used to describe the energy content of a fuel, depending on whether water is condensed (HHV) or not condensed (LHV) through the course of a combustion reaction. These values depend on the heat of combustion (HoC) of the fuel, and the heat of vaporization of water in the case of LHV. Schmidt-Rohr (161) showed that the HoC of a generic fuel C_cH_hO_oN_n can be predicted from elemental composition within ±3% by the formula

$$\text{HoC} \approx -417 \text{ kJ/mol} \times (c + 0.3h - 0.5o) \quad (4)$$

It is interesting that the HoC is reduced if oxygen is present, but it is also noteworthy that the HoC does not depend on nitrogen. In this case, nitrogen-containing hydrocarbons should have similar heats of combustion to analogous hydrocarbons, and a higher HoC than analogous oxygenates. This idea is expressed in Figure 3-17, with HoC shown in units of kJ/L. As far as soot emissions and energy content is concerned, the “best” fuel would have a low YSI and high HoC, which would correspond to compounds found nearer to the upper-left corner of Figure 3-17. It can be seen that most of the amines are found left of the pure hydrocarbons and generally above the oxygenated hydrocarbons, best fitting the aforementioned criteria. From this standpoint, nitrogen-containing compounds may be attractive as an alternative to conventional fuels because of a similar energy content to hydrocarbons while having the potential to lower soot emissions below that of oxygenates.

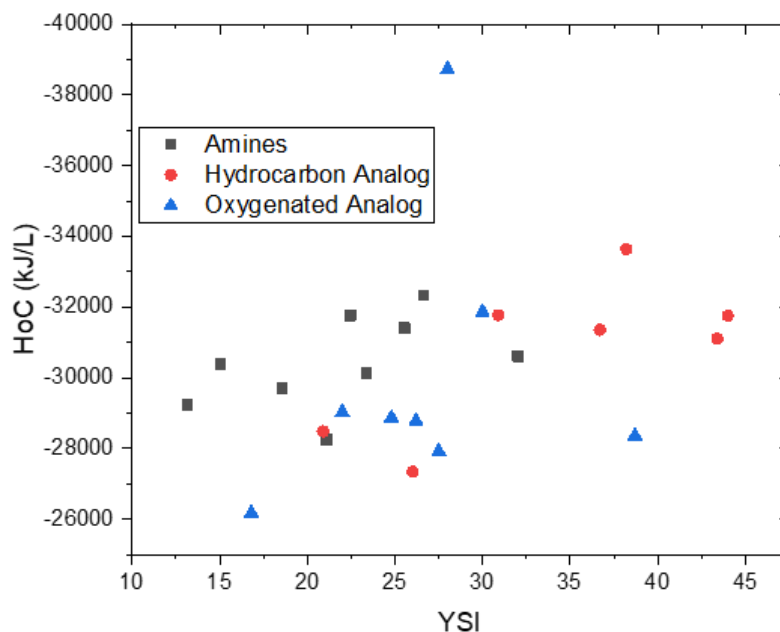


Figure 3-17: Heat of Combustion vs YSI for select amines, and structurally analogous pure hydrocarbons and oxygenates. Heats of combustion were obtained from NIST (167).

There are further considerations when choosing a fuel for a particular application, such as the fuel’s vapor pressure, volatility, cetane/octane number, and other properties. One of the more salient concerns with fuels containing nitrogen is the potential for increased NO_x emissions, which could limit the applicability of these compounds as fuels. Should liquid

nitrogen-containing compounds promote NO_x formation, a discussion on whether their reduction in sooting tendency outweighs their propensity to form NO_x may be necessary. Much more research into the properties of different nitrogen-containing compounds and the conversion of different nitrogen functionalities into NO_x are needed, however, if nitrogen-containing compounds are to be used as fuels in the future.

3.4 Conclusions

In this work, the YSIs of 14 alkyl amines were determined. It was found that line-of-sight spectral radiance is a suitable technique for measuring sooting tendencies of nitrogen-containing hydrocarbons, with negligible error introduced due to the presence of nitrogen in the test compound. The YSIs of amines on the whole were found to be lower than structurally analogous hydrocarbons and oxygenates. Secondary amines with linear alkyl substituents were observed to have the lowest sooting tendency. Simulations were performed to analyze decomposition pathways for three $\text{C}_6\text{H}_{15}\text{N}$ isomers with varying YSIs (dipropylamine, diisopropylamine, and 3,3-dimethylbutylamine), and show that their YSIs correlate with the size of each compound's primary decomposition products. The simulations also suggest that the suppressive effect of amine groups on soot formation relative to analogous ethers and oxygenates could be explained by carbon-nitrogen interactions which compete with growth pathways to aromatics. Overall, while amines may promote NO_x formation, they have lower sooting tendencies and higher heats of combustion than oxygenates and therefore may be attractive as bio-derived fuels in the future.

4 Influence of ammonia on flame characteristics and soot formation in nonpremixed methane/air flames

Parts of this chapter are from manuscripts under preparation, or have been published previously in The Proceedings of the Combustion Institute, (see “Publications” section prior to Chapter 1, entries 3. and 4.)

4.1 Background

To meet global energy demands in a sustainable and environmentally benign manner, replacing conventional fossil fuels with renewable combustion fuels and other energy sources is necessary. One compound analyzed as a potential “green” combustion fuel is ammonia (NH_3), as it can be generated from processes utilizing renewable energy, yields only N_2 and H_2O when burned to completion, liquifies more easily than hydrogen, and utilizes existing infrastructure for its large-scale handling (168).

The realization of combustion technologies utilizing NH_3 as a fuel are hindered by a variety of issues, including difficulties in stabilizing NH_3 -combustion. This issue in part arises from the low burning velocity of NH_3 . Indeed, the unstretched laminar burning velocities S_L (a unique type of flame speed) of NH_3 -air premixed flames range from ~ 2 cm/s at fuel-lean conditions (equivalence ratio $\phi \sim 0.7$) to a maximum of ~ 7 cm/s at slightly fuel-rich conditions ($\phi \sim 1.1$) (78). This is much lower relative to the laminar burning velocities of hydrogen/air mixtures ($S_L \sim 250$ cm/s at $\phi \sim 1.1$) (79) and well-known hydrocarbon mixtures, such as ethylene/air ($S_L \sim 65$ cm/s $\phi \sim 1.1$) (169), methane/air ($S_L \sim 37$ cm/s at $\phi \sim 1.1$) (80), and acetylene/air ($S_L \sim 140$ cm/s at $\phi \sim 1.0$) (170). Other issues surrounding NH_3 combustion involve the narrow flammability range for NH_3 in air ($\sim 16\%$ to 30%) (171) and high minimum autoignition temperature of NH_3 ($\sim 650^\circ\text{C}$) (172).

Strategies for stabilizing NH_3 combustion over a wider range of conditions have been developed in recent years. To enhance the combustion of NH_3 /air flames, researchers have

looked at blending NH_3 with hydrocarbons such as methane. This results in flames with higher burning velocities afforded by the hydrocarbon (81) as well as an increase in heat release rates in the flame, as the lower heating value (LHV) of NH_3 (18.6 MJ/kg) is less than half of the LHV for hydrocarbons including CH_4 (46.4 MJ/kg) (168). The higher flame speed afforded by the hydrocarbon results in NH_3/CH_4 mixtures with higher flame speeds, and are thus able to maintain stable combustion across a larger range of equivalence ratios, fuel flow rates, etc. For instance, Okafor et al. (81) have studied the laminar burning velocities of NH_3/CH_4 mixtures, demonstrating that laminar burning velocities could be enhanced up to ~ 25 cm/s at $\phi = \sim 1.1$ for NH_3/CH_4 blends composed of 21% $\text{NH}_3/79\%$ CH_4 by mole fraction. More recently, turbulent burning velocities in high-pressure premixed $\text{NH}_3\text{-CH}_4\text{-air}$ blends have been studied, demonstrating that the ratio of turbulent to unstretched laminar burning velocities (S_T and S_L , respectively) decreases as the ratio of NH_3 in the base fuel increases.

The enhancement of NH_3 -combustion, as well as reduced emissions relative to the pure hydrocarbon, afforded by blending with fuels like CH_4 , makes these mixtures attractive as a next step towards carbon-free combustion. However, to develop clean technologies which efficiently co-fire CH_4 along with NH_3 , mechanisms accurately describing the interactions between NH_3 and CH_4 are necessary. Therefore, various studies have been undertaken on NH_3/CH_4 flames to reconcile experimental findings with chemical mechanisms and simulations. While lots of studies have focused on flame characteristics and NO_x/CO_2 emissions from the co-firing of NH_3/CH_4 flames, very few studies have looked at the effect of NH_3 on soot formation. If technologies that co-fire hydrocarbons along with NH_3 are to become prominent in the future, being able to accurately assess soot emissions along with other emissions from these devices will be necessary for improving their development and mitigating these issues. A review of recent literature which studies the effect of NH_3 on soot formation can be found in section 2.2.3.

Mechanisms containing ammonia oxidation pathways have already been used in 2D simulations of ammonia-seeded methane flames. For instance, Sullivan et al. numerically studied NH_3 -conversion and NO_x formation in laminar nonpremixed CH_4 /air flames seeded with NH_3 , demonstrating that a higher percentage of NH_3 is converted to N_2 as more NH_3 is added to the primary fuel mixture (68). Grcar et al. compared 2D simulations of a plug-flow model to experimental data on heavily nitrogen-diluted mixtures containing 1000 ppm CH_4 and 300 ppm NH_3 in the base fuel, showing that the formation of N_2 or NO as NH_3 -oxidation products is sensitive to mixing (173). Other work experimentally and numerically studied NO_x emissions from premixed CH_4 /air flames doped with up to 1400 ppm NH_3 on a Taran-type burner (174), demonstrating that the employed mechanism could adequately describe NO formation across a wide range of temperatures.

While these studies tend to focus on NO_x emissions and show that the mechanisms are able to satisfactorily predict NO emissions in environments with ppm-levels of NH_3 , most mechanisms and simulations have not been tested or optimized for other conditions and applications, such as for describing soot formation or in systems where NH_3 is present well-beyond the ppm-level. As mentioned earlier, the laminar burning velocities of NH_3 / CH_4 flames have been studied (81), and subsequently validated against multiple mechanisms employing NH_3 chemistry. Many mechanisms with a focus on ammonia interactions were tested, and while features like species concentrations could be captured accurately, burning velocities were largely overpredicted. The Tian mechanism (175) was found to underestimate unstretched laminar burning velocities in these blends. This was attributed to reactions involving the formyl radical HCO . The Mendiara mechanism (176), which contains 97 species, 779 reactions, and emphasizes interactions between CO_2 and N-containing radicals and between amines and hydrocarbons, was found to over-predict laminar burning velocities (81). The GRI Mech 3.0 was found to predict burning velocities of the examined NH_3 / CH_4 mixtures well, but may not work well for some NH_3

mixtures as it does not contain important NH_3 oxidation reactions that become relevant in NH_3 -rich conditions (81). One-dimensional numerical studies of the co-firing of NH_3 and CH_4 have been undertaken (177) to try and develop reduced mechanisms from the Konnov Mechanism (178) which can replicate experimental results, including ignition delay times and species concentrations. While the full Konnov mechanism and other reduced mechanisms were able to accurately reproduce NO mole fractions from laminar flames and ignition delay times in gas turbines, all mechanisms overpredicted CO mole fractions from laminar flames and ignition delay times obtained from shock tube studies. These studies highlight that while progress is being made in describing and understanding NH_3/CH_4 combustion, there are still areas where chemical mechanisms can be improved. Phenomena not apparent under low NH_3 concentrations of may exhibit greater influence in $\text{NH}_3\text{-CH}_4$ blends with larger fractions of NH_3 , necessitating mechanisms that can satisfactorily capture NH_3 -hydrocarbon interactions across a wide range of NH_3 concentrations.

The present studies aim to analyze the ability of mechanisms employing ammonia chemistry to capture the flame characteristics of nonpremixed $\text{NH}_3\text{-CH}_4$ co-flow flames with up to 50% NH_3 by volume, as well as their ability to capture ammonia-hydrocarbon interactions relevant to soot formation. To this end, experimentally-determined centerline temperatures, flame lengths, and lift-off heights in atmospheric nonpremixed co-flow flames with varying ratios of NH_3 to CH_4 were compared to computational simulations employing the mechanism developed by Glarborg et al. (179) or the GRI mechanism (180). The results were also compared against data on $\text{N}_2\text{-CH}_4$ flames. To gain an idea of the effectiveness of the chemical mechanisms in describing basic chemistry in NH_3/CH_4 blends, spatially-resolved relative CH^* and NH_2^* signals were experimentally determined and compared to the trends in simulated 2D CH/NH_2 profiles as β was varied. Additionally, soot volume fraction distributions and important precursors for soot formation, including acetylene (C_2H_2) and benzene (C_6H_6), were measured. The concentrations

of these precursors were predicted using the Glarborg mechanism (179) and compared to the measured trends as a function of NH₃/N₂-dilution. Since the Glarborg mechanism (179) does not include any hydrocarbons larger than C₂H₂, we incorporated hydrocarbon growth reactions from C₂H₂ up to naphthalene taken from (181) into the mechanism.

4.2 Experimental methods

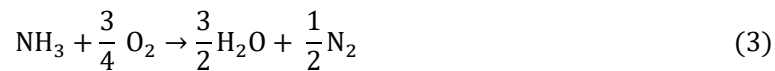
4.2.1 Burner details

Atmospheric-pressure co-flow laminar diffusion flames of N₂-CH₄ or NH₃-CH₄ were generated with a Yale Coflow Burner (182), as described in section 3.2. All reactants flowed from 99.99%+ purity cylinders or a compressor (air). Omega FMA 5400/5500 series mass flow controllers were used to control the flowrates of the gaseous reactants. Flow controllers were calibrated for the specific process gases except for NH₃ gas; a conversion factor was applied to a flow controller calibrated with N₂.

The ratios of N₂ or NH₃ to CH₄ were varied according to the parameter β , which is defined as:

$$\beta = \frac{Q_x}{Q_x + Q_{\text{CH}_4}} \quad (1)$$

where Q_{CH_4} is the volumetric flow rate of methane, Q_x denotes the volumetric flow rate of species x in the fuel mixture, where $x = \text{N}_2$ or NH₃. β was also varied in a way such that the stoichiometric oxygen requirement for burning the fuel mixture was held constant at 660 mL/min O₂. This requirement was based on the following chemical equations for CH₄ and NH₃ combustion:



From these equations and the definition of β , the flow rates for process gasses are determined by the following equations (4), for $\text{NH}_3\text{-CH}_4$ flames, and (5), for $\text{N}_2\text{-CH}_4$ flames:

$$\frac{3}{4}Q_{\text{NH}_3} + 2Q_{\text{CH}_4} = 660, \quad (\text{mL}/\text{min}) \quad (4)$$

$$2Q_{\text{CH}_4} = 660 \quad (\text{mL}/\text{min}) \quad (5)$$

This requirement was chosen so that the flame heights are similar, to the first order, as the ratio of NH_3 or N_2 to CH_4 is varied (157). This requirement should also keep residence times of reactants fairly similar as ratios of process gasses are changed, which simulated centerline residence times confirm (Figure 4-1). Values of β from 0 to 0.50 were experimentally analyzed for both sets of fuel mixtures, with experimental flow rates given in Table 1. This limit was chosen because the experimental $\text{NH}_3\text{-CH}_4$ flames would become unstable and blow out between $\beta=0.50$ to 0.55. No heating was supplied to the burner or fuel lines for all experiments.

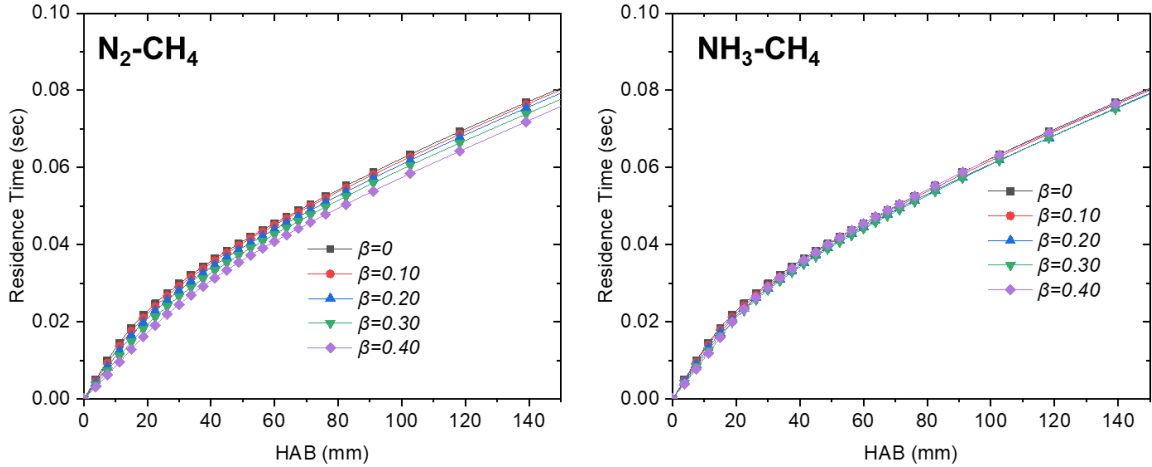


Figure 4-1: Simulated residence times of fuel molecules, for $\text{N}_2\text{-CH}_4$ flames (left) and $\text{NH}_3\text{-CH}_4$ flames (right). The Glarborg mechanism (described in section 4.3.2) was used to determine the residence times of fuel molecules along the centerline. These figures demonstrate that the residence time of fuel molecules are similar, to the first order, between flames as β is varied

Table 4-1: Experimental values of β analyzed in this study, along with the corresponding flow rates used to generate nonpremixed NH₃-CH₄ and N₂-CH₄ flames.

β	NH ₃ -CH ₄ Flames		N ₂ -CH ₄ Flames	
	NH ₃ flow rate (mL/min)	CH ₄ flow rate (mL/min)	N ₂ flow rate (mL/min)	CH ₄ flow rate (mL/min)
0	0	330	0	330
0.05	17.0	323.6	17.4	330
0.10	35.2	316.8	36.7	330
0.15	54.6	309.5	58.2	330
0.20	75.4	301.7	82.5	330
0.25	97.8	293.3	110	330
0.30	121.8	284.3	141.4	330
0.35	147.8	274.6	177.7	330
0.40	176	264	220	330
0.45	206.6	252.5	270	330
0.50	240	240	330	330

4.2.2 Centerline temperature and flame height calculations

Centerline temperatures were measured using a Type R Pt/Rh-13% thermocouple (wire diameter=0.005 in). A depiction of the thermocouple setup is shown in Figure 4-2. The thermocouple bead was aligned to the centerline of the flames by measuring radial temperature profiles near the tip of the flame and determining the position of axial symmetry. Each of the data points along the centerline of the flames corresponds to the average of 1000 samples, sampled at 1250 samples/s, of the differential voltage between the flame thermocouple and an identical thermocouple in an ice bath. The burner was scanned along the centerline starting from either the base or tip of the flame, with endpoints being 90mm and 2mm HAB, at a rate of 0.353 mm/s, for each flame condition. This was done to determine the regions along the centerline where temperature data is unreliable due to soot deposition or lift-off phenomena. Data was acquired using an NIDAQ board (NI USB-6210, 16 bit, 250 kS/s). The thermocouple response was then converted to temperature using the NIST polynomials for Type R thermocouples (183). Flame heights were determined from the experimental centerline temperature data, and were defined as the height-above-burner (HAB) where the maximum centerline temperature occurs.

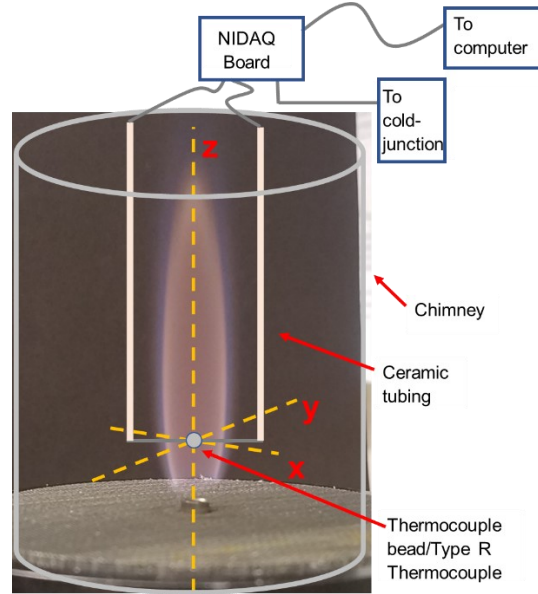


Figure 4-2: Depiction of experimental setup for centerline temperature measurements.

The radiation correction to the junction temperatures was based on previous work (184). The radiation correction to the thermocouple measurements was adopted from (184). The following equation was used to find the gas-phase temperature along the centerline:

$$\epsilon_j \sigma T_j^4 = (k_{g0} \text{Nu}_j / 2d_j)(T_g^2 - T_j^2) \quad (6)$$

where ϵ_j is the junction emissivity (value of 0.2433 used for Pt/Rh-10%, which is similar in composition to the Pt/Rh-13% thermocouple used in this study, from ref. (185)), σ is the Stefan Boltzmann constant, T_j is the measured junction temperature, d_j is the junction diameter (measured to be 3.53E-4 m, Fig. 4-3), and T_g is the desired gas temperature. The Nusselt number Nu_j was approximated according to the low-Peclet number expansion for spherical geometries described in (186). The term k_{g0} , defined as $k_{g0} \equiv k_g / T_g$, is assumed to be constant and was taken from (184) as 6.54E-5 W/m²*K². The value of the dynamic viscosity of nitrogen at 1700 K was used for calculations. The constant-pressure heat capacity of air was calculated using heat capacity values for O₂ and N₂ at 1700 K. The density and thermal conductivity of nitrogen at 1700K was also used for the fluid density and thermal conductivity. The values for the aforementioned

thermophysical properties were obtained from the NIST online chemistry database (187). The velocities used in the radiation correction were extracted from CFD simulations using the Glarborg mechanism (Fig. 4-4a) and applied for the temperatures displayed in Figure 4-8. For the maximum centerline temperature values plotted against β in Figure 4-9, the value of the velocity at the location of maximum temperature along the centerline predicted by the Glarborg mechanism for a given β were analyzed and found to hover around 2.2 m/s (Fig. 4-4b). Therefore, this value of the velocity was used to obtain the experimentally-determined maximum temperature values.

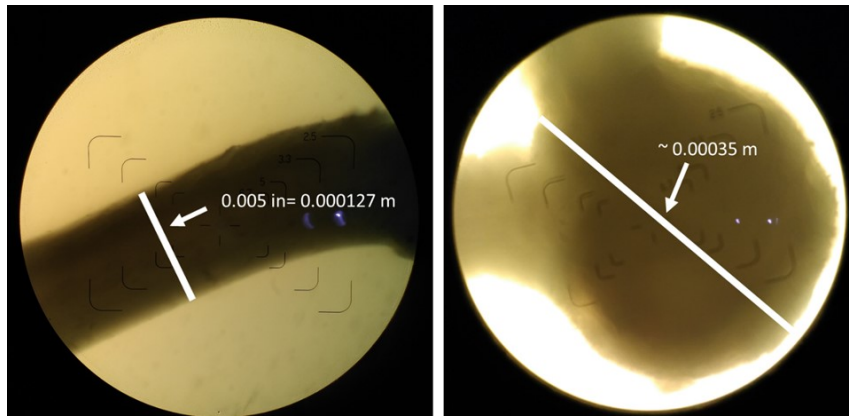


Figure 4-3: Picture of Type R Pt/13%-Rh thermocouple under an optical microscope. The image on the left shows the thermocouple wire, which is reported by the manufacturer (Omega) to be 0.005”=0.127 mm. Using this value for the wire diameter, the diameter of the probe was determined to be ~0.353 mm. This value was used for the junction diameter d_j for the radiation correction to centerline temperatures.

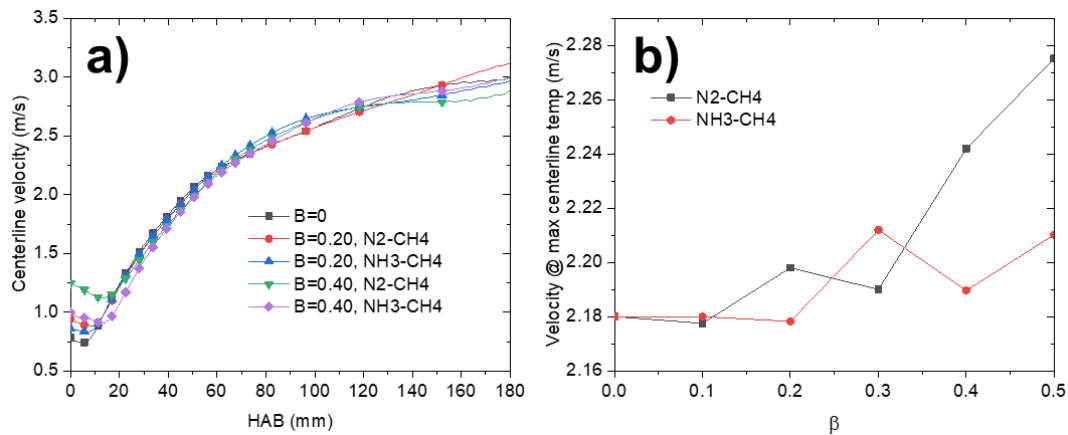


Figure 4-4: Simulated velocity information a) Velocity profiles obtained from the Glarborg mechanism, shown for the $\beta=0, 0.20,$ and 0.40 flames, b) Simulated centerline velocities at the location of maximum temperature plotted against β , for both N_2-CH_4 and NH_3-CH_4 flames.

4.2.3 Lift-Off Heights and Experimental 2D CH*/NH₂* Profiles

For this study, experimental lift-off heights were defined as the centerline HAB where the maximum CH* chemiluminescence occurs. This definition has been shown to yield good agreement with simulated maximum CH values in past studies on laminar N₂-CH₄ co-flow diffusion flames (188). Lift-off heights were obtained by imaging the CH* chemiluminescence emitted from the flames. A camera (Moto E5 Supra model XT1924-6, 1440 x 720 pixels) was used to image the flames through a 430 nm bandpass filter (ThorLabs, FWHM= 10 nm) to capture the visible chemiluminescence from the flames due to the CH* band. The radially integrated CH* signal was then determined using the program ImageJ (155), from which a lift-off height could be extracted. The setup for these experiments is depicted in Figure 4-5.

Before the flames are imaged, the camera is held in a fixed position, the camera focus is fixed on the $\beta=0$ flame without any filters, and then the 430 nm filter is placed in front of the camera. Then, flow rates are varied to achieve the $\beta=0.50$ NH₃-CH₄ flame condition, and the exposure on the camera is fixed so that as much signal as possible through the 430 nm filter is achieved. This is because the emission from CH* or NH₂* at high values of β is much weaker than the soot emission at lower values of β , and so this ensures that signal due to CH*/NH₂* positioned at lower HAB does not saturate the camera as different flames are imaged. After the exposure was fixed relative to the $\beta=0.50$ NH₃-CH₄ flame, one image through each filter was then taken, across varying β in both N₂-CH₄ and NH₃-CH₄ flames. The images through the 430 nm filter were also directly analyzed in ImageJ (156) to obtain radially-integrated centerline CH* intensities, from which lift-off heights could be extracted (experimental results for $\beta=0$, 0.10, 0.20, and 0.30 are shown in Fig. 4-14).

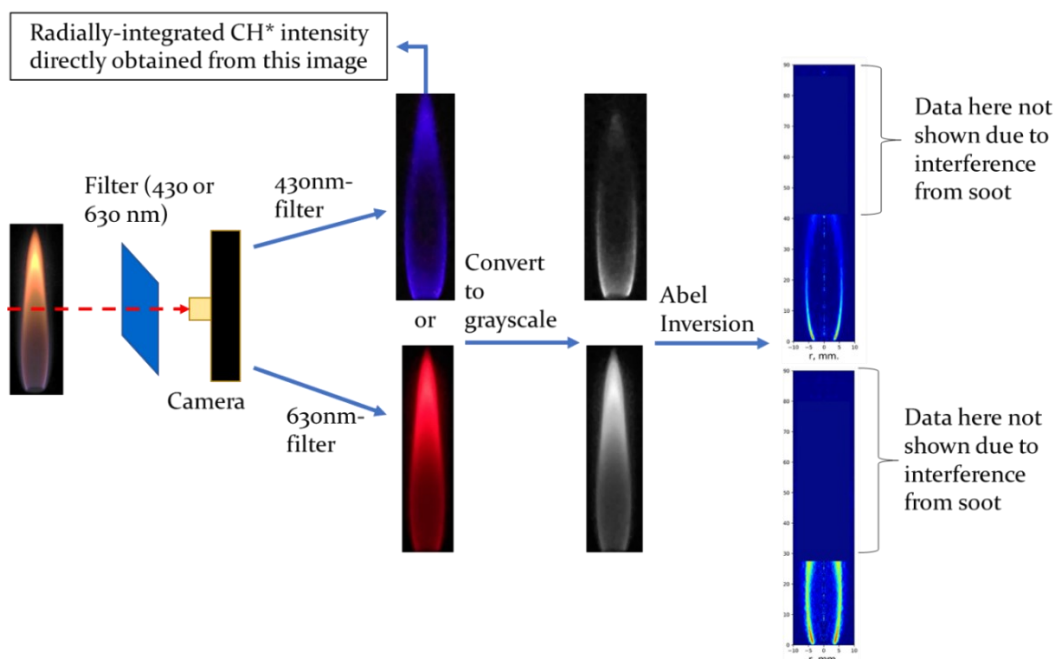


Figure 4-5: Chart describing procedure for obtaining relative 2D $\text{CH}^*/\text{NH}_2^*$ intensity profiles as β was varied, as well as relative radially-integrated centerline CH^* intensities.

Spatially-resolved CH^* and NH_2^* profiles were obtained in a similar manner. These profiles can be compared to CH and NH_2 profiles from 2D flame simulations. Since NH_2 participates in a number of important chain-branching and terminating reactions (33, 179), this comparison should give an indication of the effectiveness of the mechanisms to capture ammonia chemistry accurately. Since lift-off heights are tied to concentrations of radicals such as H , OH , and O , analyzing the CH^* and NH_2^* profiles should also help elucidate whether the influence of NH_3 or N_2 on lift-off heights is tied to chemistry involving these species. To obtain the spatially-resolved relative $\text{CH}^*/\text{NH}_2^*$ chemiluminescence signals in the flames, an Abel inversion (189, 190) was performed on the images of the $\text{CH}^*/\text{NH}_2^*$ chemiluminescence emitted from the flames. A procedure similar to obtaining the CH^* signal described in the previous paragraph was used to image the NH_2^* chemiluminescence, but a 630 nm bandpass filter (Thorlabs, FWHM= 10 nm) was used instead of a 430 nm filter. This chemiluminescence corresponds to the NH_2 α -band (158) and 630 nm was chosen as it was well-separated from other spectral bands present in the flame. For all of the images, the exposure and focus were held

constant as different flames were imaged. For both the CH* and NH₂* photos, the exposure was set and fixed so that as much signal as possible from the $\beta=0.50$ NH₃-CH₄ flame through the 430 nm-filter was captured. Once the exposure was fixed based on the $\beta=0.50$ NH₃-CH₄ flame, images of each flame condition were then taken through each filter. Since the exposure is held constant as the flames are imaged, this means changes in the signal captured by the camera reflects relative changes in the CH* or NH₂* chemiluminescence as β changes. The flame images were converted to grayscale versions in ImageJ, and the Abel inversion of the grayscale images was performed using a Basis Set Expansion (BASEX) method developed specifically for co-flow laminar flames (191). Experimental and simulated 2D profiles were normalized so that trends in CH(*)/NH₂(*) as β varied could be compared between the experiments and simulations. The CH* intensity profiles were normalized by the maximum CH* signal in the $\beta=0$ flame, while the CH concentration profiles were normalized to the maximum CH concentration simulated for the $\beta=0$ flame. The NH₂* and NH₂ profiles were normalized by the average of the maximum 99.8th percentile of either NH₂* signal or NH₂ concentration in the $\beta=0.50$ NH₃-CH₄ flame.

4.2.4 Soot Volume Fraction Measurements

Spatially-resolved soot temperatures and soot volume fractions (f_v) in the flames were obtained with color-ratio pyrometry (CRP). This technique utilizes the emissions from radiating soot particles and Planck's law to infer soot temperatures, and subsequently f_v distributions (192). Flames with values of β up to 0.20 were analyzed using this technique, since soot emission in NH₃-CH₄ flames beyond this value became negligible relative to chemiluminescent emissions from CH and NH₂. The experimental setup consisted of a D90 Nikon camera (2848 x 4288 pixels), which captured images of the flames through a Schott BG7 Filter. The spectral response of the camera has been characterized previously (192). The spatial resolution in the plane of the flame was 56.9 pixels/mm.

To obtain R/G/B intensity distributions of the flame cross-section from the recorded 2D projections, the FLiPPID (Fitting the Line-of-sight Projection of a Predefined Intensity Distribution) methodology was used for the inverse Abel transform (189). Briefly, this method predefines a parametric function for the radial light intensity distribution inside the flame and fits its forward Abel transform to the experimentally observed light intensity. This fitting procedure is repeated for each horizontal pixel line and each color channel. Advantages of FLiPPID over other Abel inversion methods are that it avoids noise amplification towards the axis of symmetry as well as unphysical negative light intensities. This allows a better comparison of experimental centerline values to simulations, which is important in the current flames where f_v peaks on the centerline. Reference (189) provides more details on FLiPPID.

The Abel-inverted R/G/B signals obtained from the FLiPPID methodology were then converted to spatially-resolved soot temperatures and subsequently soot-volume fraction distributions. A Type-S thermocouple was used for calibrating the optical system as described in (193). The f_v calculations were adopted from (194). Soot emissivity and the dimensionless extinction coefficient (K_{ext}) were assumed to be $\lambda^{-1.38}$ (192) and 8.6 (195), respectively. CRP measurements of f_v with these values of soot emissivity and K_{ext} have been used to measure variations in maximum f_v in $\text{N}_2\text{-CH}_4$ flames similar to the ones under study (193), and analogous measurements in C_2H_4 diffusion flames have shown good agreement with other diagnostics which measure soot volume fraction such as laser-induced incandescence (LII) (192). The largest source of systematic uncertainty in the measurements comes from assuming uniform soot optical properties throughout the flame (196, 197), which may not be a valid assumption particularly low in the flame and on the inner edge of the soot distribution, where soot concentrations are low and the particles are not yet fully carbonized. It is also assumed that soot particles formed from $\text{NH}_3\text{-CH}_4$ and $\text{N}_2\text{-CH}_4$ flames have the same optical properties. Interferences due to light scattering or emission from excited state NH_2 were negligible relative

to uncertainty in the soot optical properties. Uncertainty in centerline temperatures for all N₂-CH₄ flames and for NH₃-CH₄ flames with values of β up to 0.10 are expected to be the greater of 2.5% or 50 K, with uncertainties in f_v values of +100%/-50%. The soot temperatures for all flames except the $\beta=0.20$ NH₃-CH₄ case were computed based on an average of the temperatures obtained from each color-ratio. For the $\beta=0.20$ NH₃-CH₄ flame, soot concentrations were low (max = 0.02 ppm), and interferences from chemiluminescence were experienced, predominantly through the blue channel. Therefore, the reported f_v profiles for this flame were computed based on temperatures calculated from the red-green color ratio. Unphysically high temperatures were found at lower positions in some flames due to uncertainties stemming from low soot concentrations and differences in the optical properties of soot formed in these regions. Nonetheless, uncertainty in soot temperatures for the region of the flame where the maximum f_v occurs (~55 to 60 mm height-above burner HAB) are estimated to be 5%, since relatively mature soot was located in this region, increasing the validity of the soot emissivity model. Due to low soot concentrations and increased signal from chemiluminescence, the absolute error in centerline f_v values for the $\beta=0.20$ NH₃-CH₄ flame is +500%/-50%. Overall relative uncertainties in f_v from flame-to-flame are estimated to be $\pm 10\%$.

4.2.5 Species Measurements

Centerline mole fractions of major species were analyzed using on-line electron impact mass spectrometry (198, 199). A diagram depicting the probe and general setup is shown in Figure 4-6. A quartz microprobe with an internal pressure of 1-3 torr was used to sample gases from the centerline of the flames. The probe had an outer diameter of 9 mm and came to a tapered end with an orifice ~200 μm in diameter. The gas sampling through the probe tip accompanied by the large pressure drop leads to volumetric expansion and cooling of the reaction products. The species profiles obtained via this technique agree well with non-perturbative methods such as Raman scattering, as well as with simulations (198). The quenched reaction products were then

delivered to a Stanford Research Systems RGA100 mass spectrometer under high vacuum. To increase the rate at which the gases reached steady-state with the sampling system walls as the probe was moved, these walls were heated to 60 °C using a PID temperature controller.

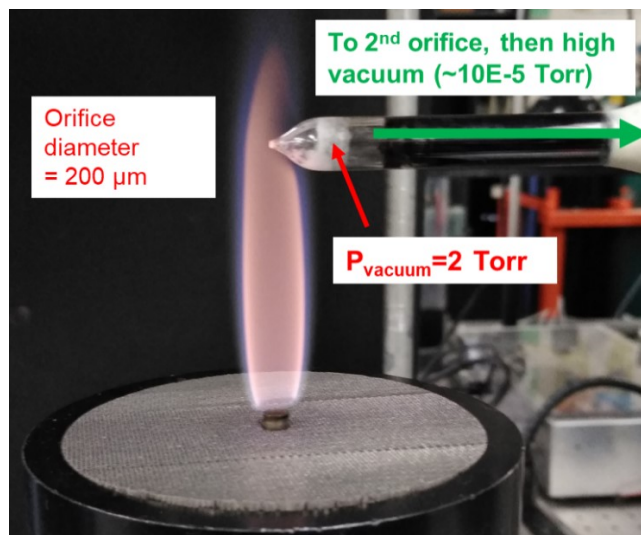


Figure 4-6: Image showing the general setup used for mass spectrometry measurements.

At each height in the flame, the ion current of relevant ion channels for species of interest were recorded over time, typically over 100 seconds. Each reported data point corresponds to an average over at least 60 seconds of the collected signals after they had reached a steady state, except for regions where soot-clogging of the orifice occurred; in these cases, the data corresponds to an average of 10-50 seconds of collected signals depending on the severity of soot-clogging. The number density of each species in the mixture was determined from the ion current, transmission/detector factors, fragmentation factors, and ion gauge sensitivities derived from (200). Then the mole fraction of each species was calculated as the number density of that species divided by the total number density of all measured species. The inability to measure all species in the flame leads to an underprediction of the total number density, which is estimated to contribute 0 to +8% error in the hydrocarbon-rich region of the flame. Fragmentation factors were either measured directly (N_2 , CH_4 , CO_2 , NH_3 , H_2O , C_2H_2) or obtained from NIST (C_6H_6) (201). Error for the C_2H_2 mole fractions from overlap with C_2H_2

fragments produced by other species (C_2H_4 , C_2H_6) is estimated, based on simulated data (Fig. S1), to be 0 to +7%. Uncertainty in C_6H_6 mole fractions is expected to be ± 100 ppm. Uncertainty in flow rates, spatial position in the flame, and ion gauge sensitivities is estimated to contribute another $\pm 15\%$ error to species measurements.

4.3 Computational methods

One goal of this dissertation is to help develop better computational fluid dynamic (CFD) models for predicting combustion phenomena from NH_3 - CH_4 co-combustion. For the results reported in sections 4.4.1 and 4.4.2, we test the ability of two chemical kinetic models to capture the NH_3/CH_4 flame chemistry: the GRI mechanism, and the Glarborg mechanism. For the results reported in sections 4.4.3 and 4.4.4, we test only the ability of the Glarborg mechanism to capture trends in soot concentrations and precursors. Because of a lack of reactions describing the interaction of NH_3 with larger hydrocarbons, an additional reaction scheme was included to model hydrocarbon growth from C_2 species up to naphthalene for these studies.

4.3.1 Flow Solver and Flame Conditions

The NGA code (202) is used for 2D detailed simulations of laminar co-flow diffusion flames. The NGA solver uses staggered variables and allows for accurate, robust, and flexible simulations of both laminar and turbulent reactive flows in complex geometries and has been applied in a wide range of test problems (166, 181, 203). The species mass fractions and temperature are transported using the BQUICK scheme, which ensures that the physical bounds of appropriate quantities are numerically preserved throughout the simulation without adding significant artificial diffusion (204). A recently-developed computationally efficient, semi-implicit, iterative method is used for the time-integration of chemical source terms for the transport equations of gas-phase species. This method has been shown to be free of lagging errors, as efficient as an explicit time-integration per time step, and capable of using large, stable

time-step sizes (205). These numerical methods guarantee globally second-order accuracy in both space and time (205).

The co-flow laminar non-premixed flames of N_2 - CH_4 or NH_3 - CH_4 are generated with a Yale Co-flow Burner (182) in the simulation, as in the experiment. Inlet operating conditions such as flow rate, temperature, fuel compositions are the same as in the experiment. Detailed 2D simulations of the flames are performed using a domain of 25 cm (radial) \times 70 cm (axial) with a grid of 150 \times 160. Uniform mesh is used around the burner exit, and the grid is gradually stretched in both radial and axial directions away from the burner exit.

4.3.2 Chemical Kinetic Model

To capture the flame characteristics of NH_3 - CH_4 and N_2 - CH_4 flames through reacting flow simulations, chemical models that well-describe combustion chemistry of NH_3 and CH_4 are required. A chemical model with well-optimized and reasonable size, recently proposed by Glarborg et al. (179), is employed in this study. The kinetic model containing 147 species and 2764 reactions (forward and backward reactions counted separately) is developed based on work on nitrogen chemistry published over the last four decades, and includes the chemistry of C1-C2 hydrocarbons, amines, cyanides, and small hydrocarbon/nitrogen interactions (179). It has been extensively tested and validated against a wide range of experimental data, including results from laminar flames at low and atmospheric pressure, from shock tube experiments, and from jet-stirred reactors (179). In particular, the ability of this model has been verified against significant reactions for this study, such as oxidation of NH_3 , small hydrocarbons, and CH_4 doped with NH_3 . Detailed validations can be found in a paper by Glarborg et al. (179).

As mentioned before, the kinetic model by Glarborg et al only contains up to C2 hydrocarbons, therefore, soot formation is not considered in simulations with the kinetic model reported in sections 4.4.1 and 4.4.2. To our best knowledge, simulating the soot formation in

CH₄/NH₃ flames is quite challenging, since there is no chemical kinetic model which can describe co-firing of ammonia and large hydrocarbons accurately. The effect of gas-phase radiation and radiative heat losses from soot particles were studied independently, and detailed in the following sections. These soot and radiation models have been applied in laminar sooting flame simulations, where they accurately predict measured soot volume fractions (typically within a factor of 2) (166, 203, 206).

To investigate effects of radiation from soot (reported in section 4.4.1, figures 4-9 and 4-10), we additionally generate a methane flame ($\beta = 0$) with a reduced finite-rate chemistry model. The model originally developed in (207, 208) was reduced from 85 species and 1903 reactions (forward and backward reactions counted separately) to 47 species and 290 reactions using a multi-step approach combining automatic and manual chemistry reduction. Briefly, aromatic species larger than naphthalene and their corresponding chemical reactions were first eliminated manually, since the formation of naphthalene is regarded as the rate-determining step in the formation of larger polycyclic aromatic hydrocarbons (PAHs). The resulting chemical model was further reduced automatically using the DRGEP method (209). A manual reduction was finally performed to lump isomers and their corresponding reactions based on a thorough reaction flux analysis. The chemical model has been validated and used in multiple sooting flame simulations (205, 210-212). More details about the chemistry reduction procedure and chemical model validation can be found in (210).

For the results reported in sections 4.4.3 and 4.4.4, an additional kinetic mechanism and soot model were included. Since the Glarborg mechanism does not include any hydrocarbons larger than C₂H₂, we incorporated hydrocarbon growth reactions from C₂H₂ up to naphthalene taken from (181) into the mechanism. We did not include any interactions between the added hydrocarbons and nitrogen-containing species. The final kinetic mechanism contains 170 species and 2907 reactions (forward and backward reactions counted separately). The soot

model, taken from (213, 214), using a bi-variate approach based on the total volume and surface area, is employed in the current work. The soot model includes the contributions from soot nucleation, coagulation, condensation, surface growth, and oxidation to the evolution of the soot population, and more details can be found in (213, 214).

4.3.3 Radiation Model

Radiative heat losses from the gas-phase mixture has an important impact on flame structure, species distribution, and soot emissions (215-217), and these effects are accounted for by using an optically thin grey gas model that has been derived from the RADCAL model (218). The optically thin medium assumption is reasonable for the laminar flames considered in this work (218, 219). In this model, CO₂, H₂O, CH₄ and CO are regarded as radiating species. The rate of heat loss per unit volume due to radiation is expressed as follows (218, 219),

$$\dot{q}_{rad} = -4\sigma \sum_i p_i a_{p_i} (T^4 - T_\infty^4) \quad (6)$$

where σ is the Stefan-Boltzmann constant, p_i is the partial pressure of species i , a_{p_i} is the Plank mean absorption coefficient of species i , and T and T_∞ are the local flame and ambient temperatures, respectively.

The broadband-integrated soot radiative intensity as described in (181, 220) is used to calculate the radiative heat losses from soot particles, \dot{q}_{soot} . The final expression for the heat losses due to soot radiation is,

$$\dot{q}_{soot}(T) = 4a\sigma f_v T^4, \quad (7)$$

where $a \cong 1862T$, is the spectrally-integrated soot emissivity, which gives a better asymptotic behavior at around 1700 K, the temperature at which soot particles are generally formed (220). In the above equation, f_v is the local soot volume fraction and T is the local flame temperature.

4.4 Results and Discussion

4.4.1 Effect of NH₃ on Temperature, Lift-Off Heights, and Flame Heights in Methane Flames

In this study, nonpremixed diffusion flames of N₂-CH₄ and NH₃-CH₄ were examined. Images of the flames generated with the fuel mixtures, ranging in β from 0 to 0.40, are shown in Figure 4-7. It is clear from these images that the soot luminosity decreases much more rapidly for the NH₃-CH₄ flames relative to the N₂-CH₄ flames as β increases. An orange color distinct from soot emission becomes more visible in the NH₃-CH₄ flames at higher values of β . This is attributed to the NH₂* chemiluminescence (158).

To test the ability of the mechanisms in capturing physical phenomena in laminar NH₃-CH₄ flames, experimental centerline temperatures were compared to centerline temperatures from 2D CFD simulations employing the GRI and Glarborg mechanisms (179, 180). Selected results are shown in Figure 4-8 for three values of β , for both sets of flame conditions. Both the GRI and Glarborg mechanisms match the experimental N₂-CH₄ centerline flame temperatures very well. Both mechanisms are able to accurately reproduce experimentally observed temperatures in the $\beta=0.20$ NH₃-CH₄ flame. For mixtures with larger ratios of ammonia, temperature profiles determined with the Glarborg mechanism agree better with the experimental measurements. The temperature profiles determined with the GRI mechanism at higher β are shifted to higher HAB. This is attributed to the tendency of the GRI mechanism to overpredict lift-off heights in NH₃-CH₄ flames, discussed further on, causing absolute positions of the centerline temperatures to disagree with the experiments. Overall, both mechanisms are able to match experimental centerline temperatures when employed in 2D simulations, although absolute positions may not agree in flames with larger ratios of NH₃ due to lift-off phenomena.

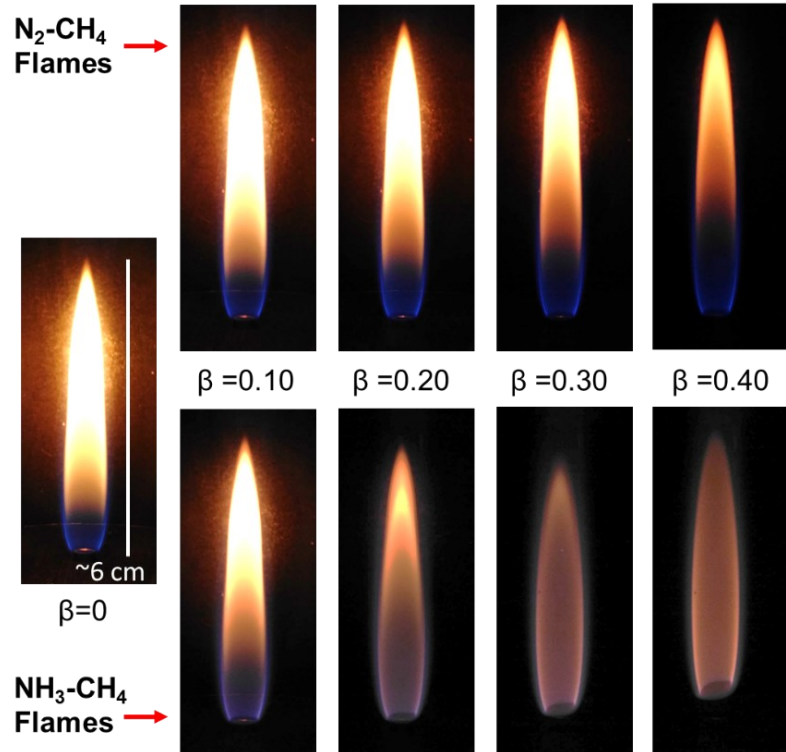


Figure 4-7: Selected images of flames analyzed in this study. Top: N_2 - CH_4 flames, Bottom: NH_3 - CH_4 flames

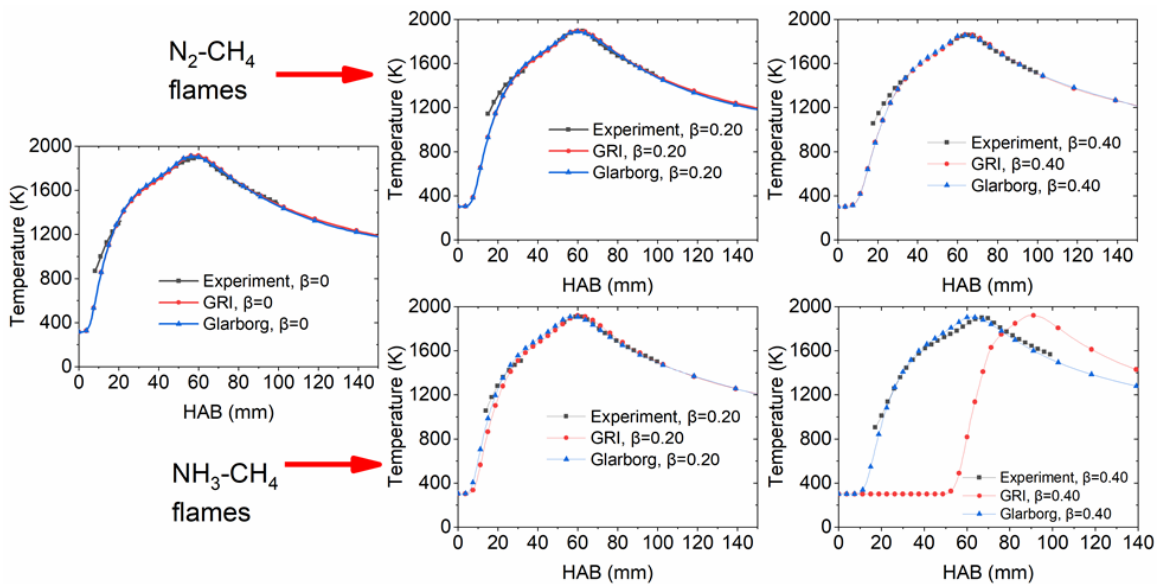


Figure 4-8: Selected results for centerline temperatures vs. height-above burner (HAB) for N_2 - CH_4 flames (top row) and NH_3 - CH_4 flames (bottom row) with changes in β . Every 10th datapoint is shown with markers, with straight lines connecting each individual datapoint to its nearest neighbor

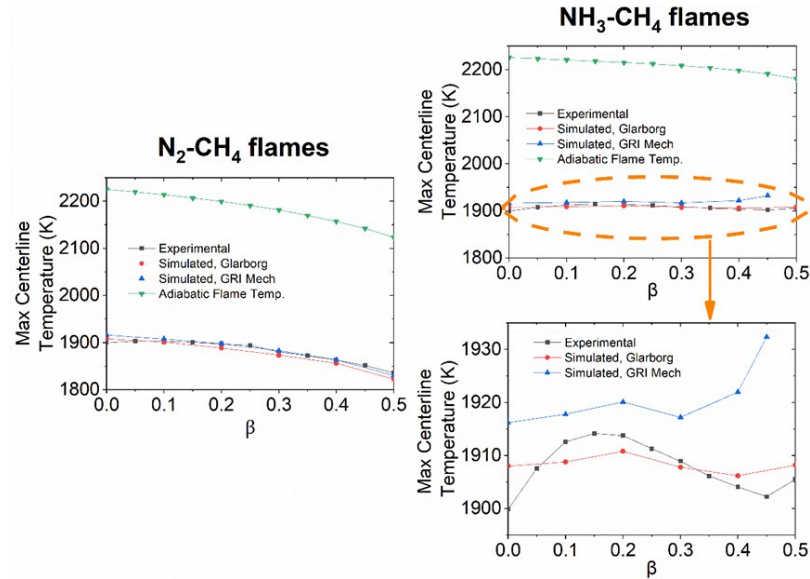


Figure 4-9: Maximum centerline and adiabatic flame temperatures. Top row- Maximum experimental and simulated centerline temperatures vs. β for N₂-CH₄ flames (left) and NH₃-CH₄ flames (right). Adiabatic flame temperatures were calculated using the NASA CEA code (221), and are shown for comparison. Each datapoint is designated with a marker, with straight lines connecting adjacent datapoints, Bottom right: Zoomed-in graph of maximum centerline temperatures in NH₃-CH₄ flames

To analyze trends in flame temperature with changes in β , experimental and simulated maximum centerline temperatures for various values of β were compared, showing good agreement (Fig. 4-9). A monotonic decrease in the maximum flame temperature with an increase in β was observed in both sets of N₂-CH₄ flame simulations. The simulated trends also match the trends in the adiabatic flame temperatures T_{ad} with varying β . This reflects how addition of inert nitrogen decreases the flame temperature by diluting the heat release of methane. For both the N₂-CH₄ and NH₃-CH₄ flames at a given β , lower simulated and experimental maximum centerline temperatures were obtained relative to the calculated T_{ad} due to the non-adiabaticity of the flame. However, a slight increase in the maximum centerline flame temperatures was experimentally observed from $\beta=0$ to $\beta=0.10$ for the N₂-CH₄ flames. After $\beta=0.10$, the observed maximum centerline temperatures monotonically decreased.

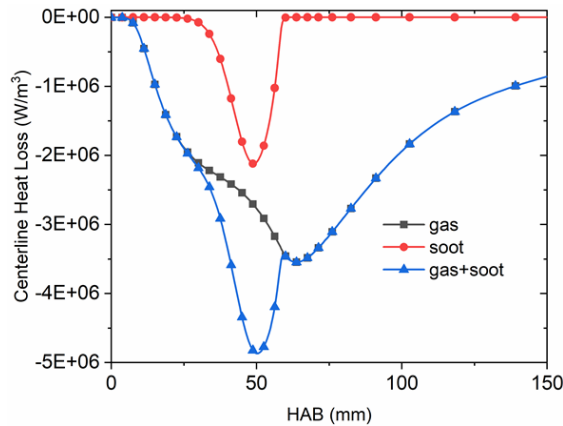


Figure 4-10: Simulated centerline radiative heat losses vs. HAB, for the $\beta=0$ flame. The gas phase contribution was calculated based on the Glarborg mechanism species profiles. Every 15th datapoint is shown with markers, with straight lines connecting each individual datapoint to its nearest neighbor

This initial increase in maximum flame temperature is attributed to soot radiation, which is present in the experiments but is difficult to capture in the simulations for higher ratios of NH_3 . To support this idea, the effect of soot radiation was computationally investigated in the $\beta=0$ flame using a reduced chemical model to capture soot radiation (Fig. 4-10). The contribution of soot radiation to the centerline heat losses was found to only be significant from HAB ~25 mm to ~60mm. In the region where the maximum centerline temperature is located, from HAB=50 to 60 mm, the total gas+soot contribution to the radiative heat loss is anywhere from 1.2 to ~2 times higher than the gas phase contribution only. This effect will be most significant in the $\beta=0$ flame, and will decrease upon increasing β since soot luminosity consequently decreases (see Fig. 4-7). The decrease in soot concentration will lead to less radiative heat transfer, thereby initially causing an increase in the flame temperature. At larger ratios of fuel nitrogen, the soot is present in low concentrations, and so the effect of soot radiation on the flame temperature becomes negligible.

For the $\text{NH}_3\text{-CH}_4$ flames, trends in the experimental maximum centerline temperatures were captured by the simulations (Fig. 4-9). The experiments and simulations reveal that the maximum flame temperatures remain rather steady relative to the $\text{N}_2\text{-CH}_4$ flames as β varies.

Upon closer inspection (Fig 4-9, bottom row), there is non-monotonic behavior in the maximum flame temperature as β increases, which is captured by both experiments and simulations. From $\beta=0$ to $\beta=0.15$, the experimental maximum temperature was observed to increase. Then the observed maximum flame temperature decreases from $\beta=0.15$ to 0.45, and increases again from $\beta=0.45$ to 0.50.

The increase in the experimental flame temperature from $\beta=0$ to $\beta=0.15$ (~15K) is attributed primarily to a decrease in radiative heat losses. Because there are no mechanisms that describe the interaction of NH_3 with larger hydrocarbons, the computational model implemented for the current results was unable to capture radiative heat losses due to soot in $\text{NH}_3\text{-CH}_4$ flames. As β increases for $\text{NH}_3\text{-CH}_4$ flames, the moles of water in the products increases, while the moles of CO_2 and CH_4 decrease (see equations 1-4). Therefore, the initial increase in simulated maximum centerline temperatures from $\beta=0$ to $\beta=0.15$ (~5 K) may be a result of decreasing gas-phase radiation. To explore this concept, gas-phase radiative heat losses were calculated for $\text{NH}_3\text{-CH}_4$ flames from $\beta=0$ to 0.40 (Fig. 4-11). In the region from $\text{HAB}=50$ mm to 60 mm, where the maximum temperature occurs, centerline gas phase radiative heat losses were indeed found to decrease as β increases. However, the decrease in gas phase radiation with increasing β (Fig. 4-11) has a smaller effect on radiative heat losses than the effect of including a radiative soot model in the simulations for low- β flames (Fig. 4-10). This slight decrease in centerline gas-phase radiative losses with addition of NH_3 , coupled with the lack of soot radiation in the model, explains the increase in simulated temperatures from $\beta=0$ to 0.20, and also why a larger increase in experimental maximum centerline temperatures was observed compared to the simulations in this range of β . From $\beta=0.20$ to 0.40, the decrease in maximum flame temperature is attributed to the slightly lower heat release afforded by NH_3 -addition (see T_{ad} calculations, Fig. 4-9). From $\beta=0.45$ to 0.50, the flame becomes lifted and stabilized far from the burner surface. The larger lift-off height could allow for more premixing of the reactants

before combustion and will also result in less heat transfer to the fuel tube and burner surface, explaining the increase in temperature.

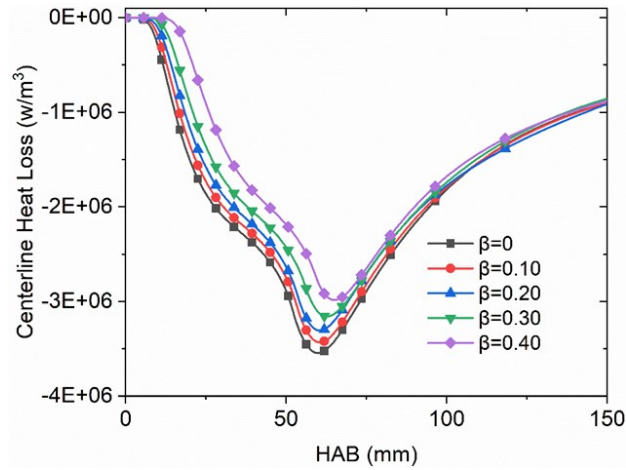


Figure 4-11: Simulated gas phase radiative heat losses, for $\text{NH}_3\text{-CH}_4$ flames. Every 15th datapoint is shown with markers, with straight lines connecting each individual datapoint to its nearest neighbor

Experimental and simulated values of the flame heights and lift-off heights were determined, and are shown in Figures 4-12 and 4-13, respectively. Experimentally, the $\text{NH}_3\text{-CH}_4$ flames were found to have significantly larger flame and lift-off heights than the $\text{N}_2\text{-CH}_4$ flames at higher values of β . While both mechanisms predicted stable lift-off in the $\text{NH}_3\text{-CH}_4$ flames, only the GRI mechanism was able to capture the experimentally observed trend in lift-off between the $\text{N}_2\text{-}$ and $\text{NH}_3\text{-CH}_4$ flames. Good agreement was found between the experimental and simulated $\text{N}_2\text{-CH}_4$ flame and lift-off heights for both mechanisms. For the $\text{NH}_3\text{-CH}_4$ flames, good agreement between experimental and simulated lift-off heights were observed from $\beta=0$ to $\beta=0.20$. However, experimental lift-off heights and those predicted with the GRI mechanism begin to diverge at $\beta=0.20$. Focusing on the absolute values, better agreement with measured lift-off heights was found with the Glarborg mechanism, which satisfactorily predicted lift-off heights up to $\beta=0.40$. It should be noted that, experimentally, blow-out in the $\text{N}_2\text{-CH}_4$ flames was observed at values of β greater than 0.63, while the $\text{NH}_3\text{-CH}_4$ flames blew out between $\beta=0.50$ to 0.55. For the GRI mechanism, the $\text{NH}_3\text{-CH}_4$ flames were predicted to become unstable

and blow out between $\beta=0.45$ to 0.50 , while the Glarborg mechanism predicted blow-out above $\beta=0.70$. Blow-out was predicted in the N_2 - CH_4 flames between $\beta=0.60$ to 0.65 in both sets of simulations.

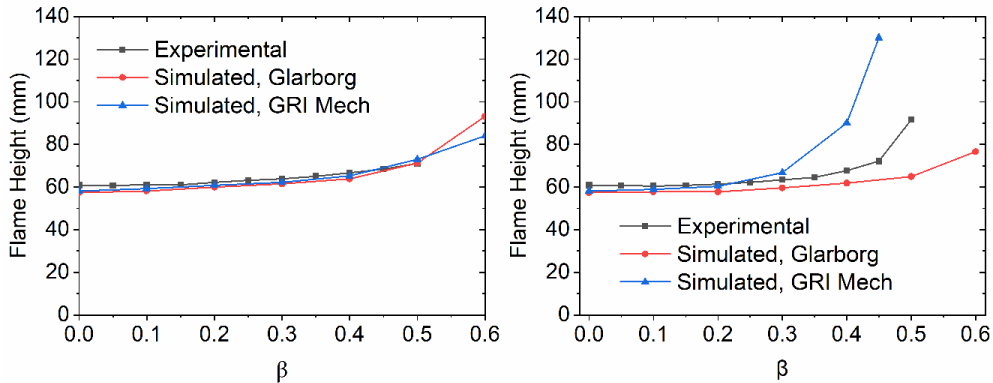


Figure 4-12: Experimental and simulated flame heights vs. β for N_2 - CH_4 flames (left) and NH_3 - CH_4 flames (right). Each datapoint is designated with a marker, with straight lines connecting adjacent datapoints

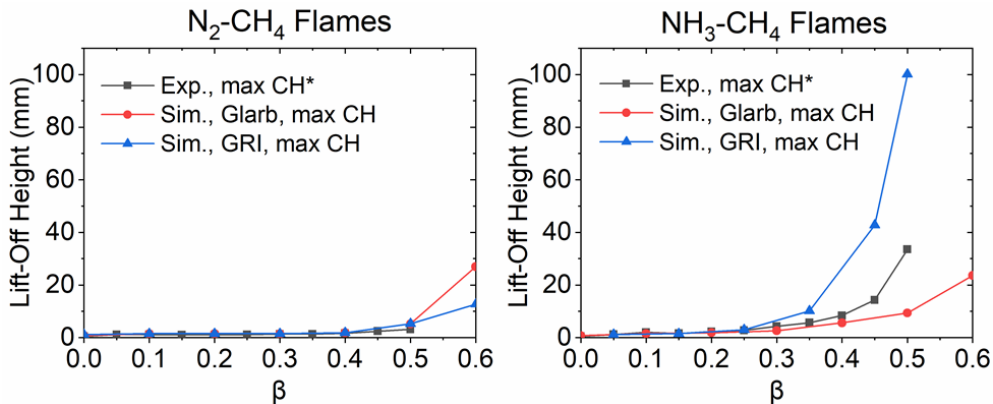


Figure 4-13: Experimental and simulated lift-off heights vs. β for N_2 - CH_4 flames (left) and NH_3 - CH_4 flames (right). Each datapoint is designated with a marker, with straight lines connecting adjacent datapoints

The observation that the trends in blow-out between the N_2 - and NH_3 - CH_4 flames were predicted correctly by the GRI mechanism, as well as the overprediction in the stable blow-out limit in the NH_3 - CH_4 flames by the Glarborg mechanism, is consistent with past studies on NH_3 - CH_4 burning velocities. Okafor et al. compared the ability of the GRI mechanism and other mechanisms developed for capturing ammonia combustion to predict experimental laminar burning velocities, a parameter that influences flame stability and lift-off, in NH_3 - CH_4 mixtures (81). They found that the GRI mechanism satisfactorily captured the flame speeds for blends of

CH₄ and NH₃, despite lacking important reactions relevant to flame speed and NO formation in ammonia flames. The chemical mechanisms based on ammonia chemistry in their study did not satisfactorily reproduce experimental laminar burning velocities across all conditions, with most overestimating the values. However, the Tian mechanism (175) was found to underpredict experimental laminar burning velocities. This was attributed to a dominance of radical-consuming reactions involving HCO, which are prevalent under the conditions the Tian mechanism was validated (4 kPa) but not at higher pressures.

4.4.2 NH₂* and CH* Distributions in NH₃-CH₄ Flames

To analyze how the distribution of CH and NH₂ in the flames varied with β , relative 2D CH* and NH₂* distributions in the flames were experimentally determined. These profiles are compared to the CH and NH₂ profiles predicted using each mechanism to give an indication of how accurate the mechanisms are in capturing basic methane and ammonia chemistry, as well as trends in the profiles as β is varied. The 2D CH/CH* profiles for the N₂-CH₄ and NH₃-CH₄ flames are shown in Figures 4-14 and 4-15, respectively. Radially integrated CH*/CH profiles are also shown in Figure 4-16. For the N₂-CH₄ flames, it is clear that the CH* chemiluminescence is present and exists in a thin shell around the flame (Fig. 4-14). This thin shell of CH* gets weaker as it extends towards the tip of the flame. These results are consistent with past studies on CH* chemiluminescence in laminar N₂-CH₄ flames (188). The relative radially integrated CH* signal, normalized to the fraction of CH₄ in the fuel mixture, increases as β increases (Fig. 4-16). These trends were all captured in the 2D CH profiles and radially-integrated centerline CH profiles predicted using both the GRI and Glarborg mechanisms, for N₂-CH₄ flames. Compared to the N₂-CH₄ flames, the thin shell of CH* in the NH₃-CH₄ flames is less intense for a given value of β (Fig. 4-15). At larger ratios of NH₃, almost no CH* chemiluminescence can be experimentally observed, a factor that is also reflected in the low simulated CH intensities. Unlike the N₂-CH₄

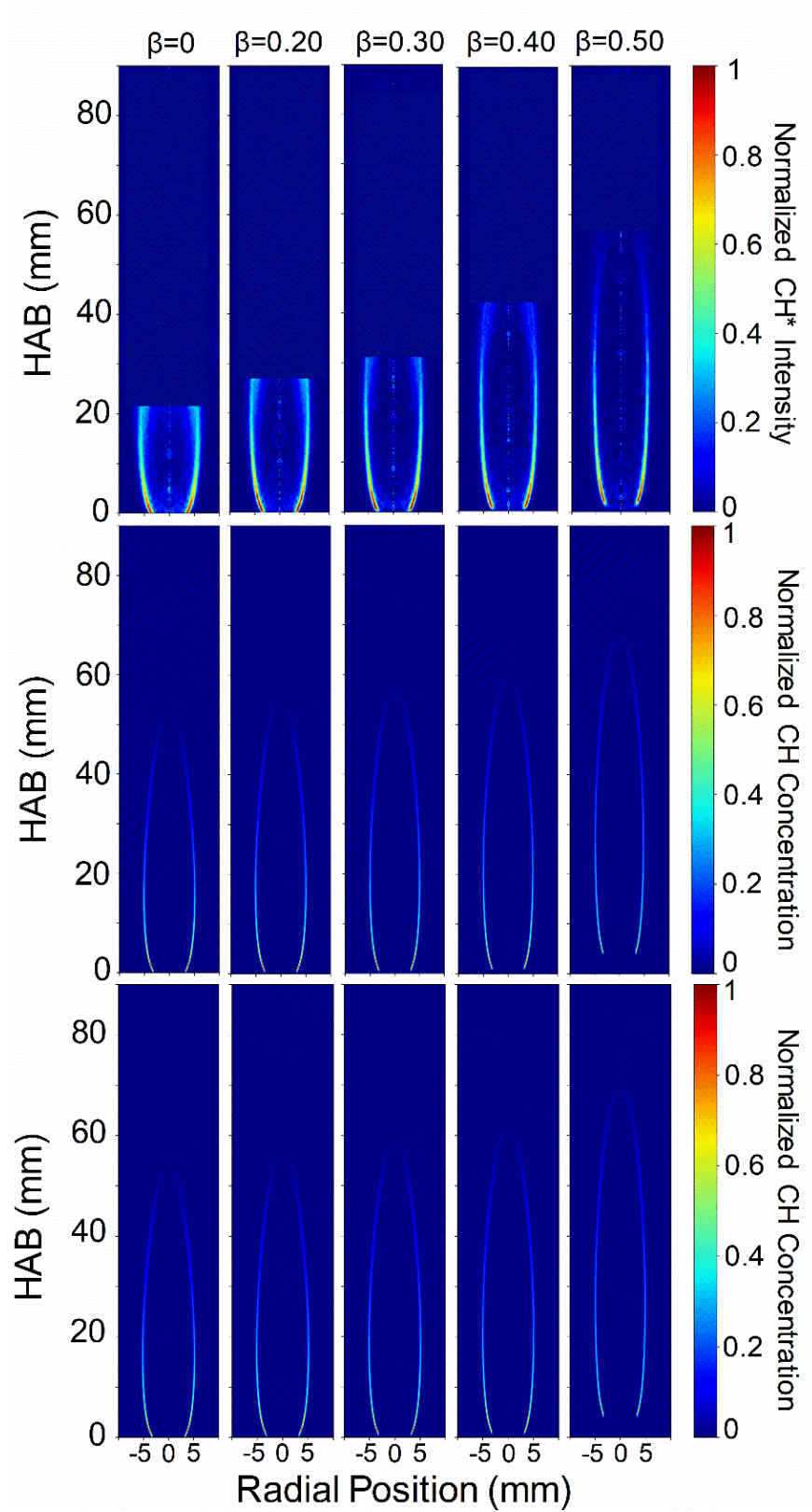


Figure 4-14: Spatially resolved CH/CH* profiles in N_2 - CH_4 flames a) Experimentally-determined CH* signal, normalized b) Simulated CH concentration using the Glarborg mechanism, normalized c) Simulated CH concentrations using GRI mech, normalized

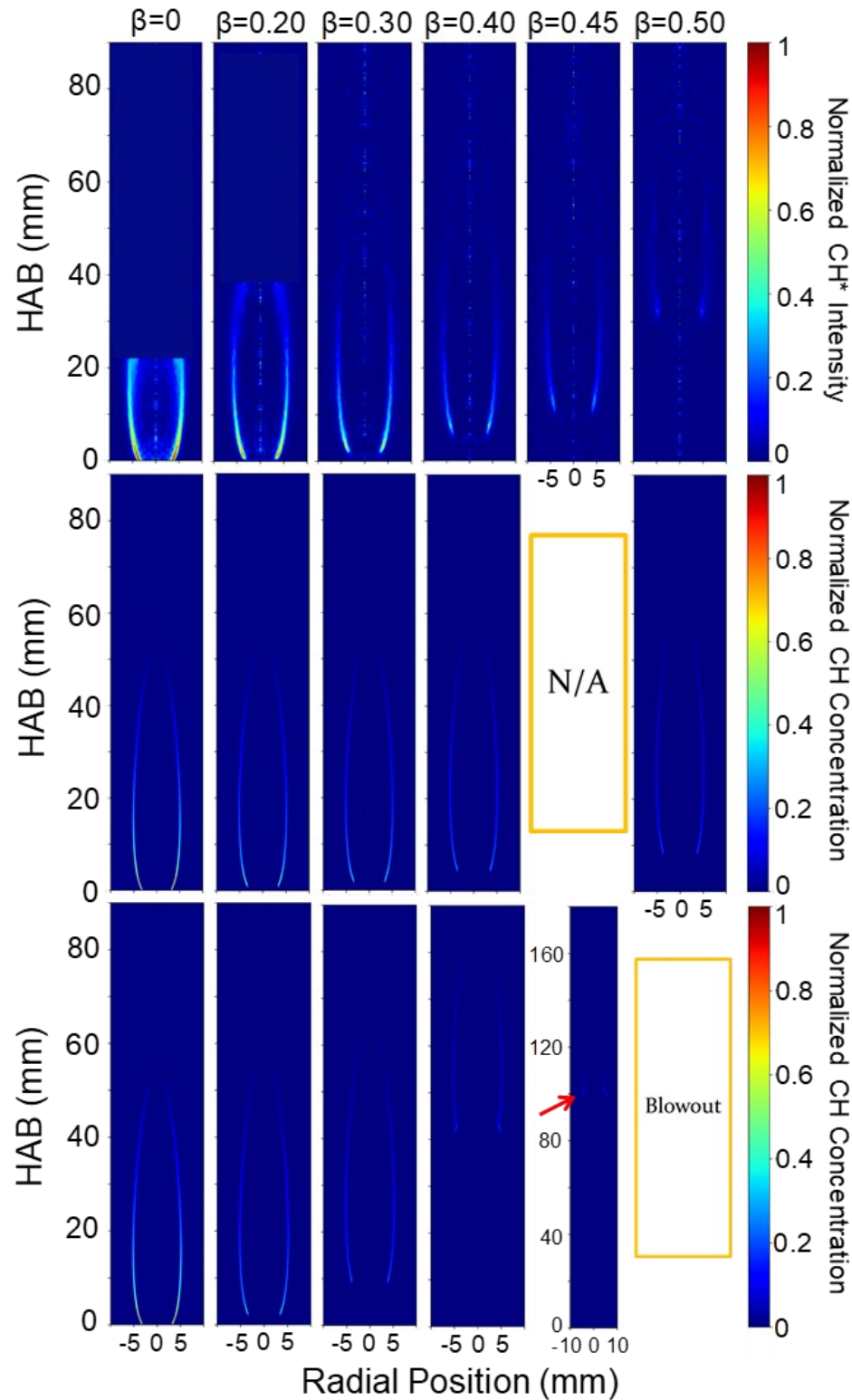


Figure 4-15: Spatially resolved CH/CH* profiles in NH₃-CH₄ flames Top row: Experimentally-determined CH* signal, normalized. Middle row: Simulated CH concentration using the Glarborg mechanism, normalized Bottom row: Simulated CH concentrations using GRI mech, normalized

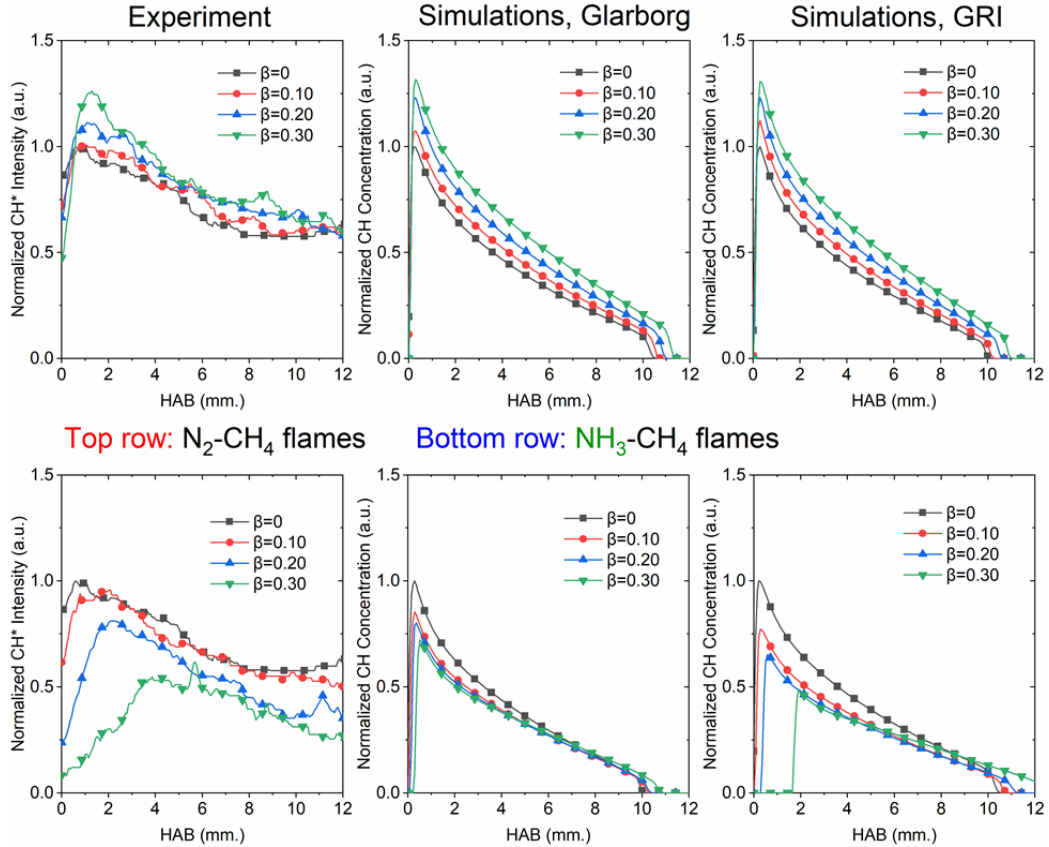


Figure 4-16: Radially integrated CH^* intensities/ CH concentrations. Plots were normalized to the fraction of CH_4 in the primary fuel mixture (i.e. $1 - \beta$)

flames, the relative radially integrated CH^* signal decreases as β increases for the NH_3 - CH_4 flames. These trends were also captured in the CH profiles by the GRI and Glarborg mechanisms. The decrease in CH^*/CH observed with additions of NH_3 compared to the increase observed for N_2 -additions may indicate that NH_3 is interfering with CH formation and/or consumption pathways. For instance, sequestration of fuel carbon, which may otherwise participate in these reactions, in the form of HCN could explain this observation. The main discrepancy between the simulated and experimental CH^*/CH profiles is the absolute location of the CH/CH^* , which is attributed to differences in simulated and experimental lift-off heights. However, differences in CH/CH^* profiles as β changes are captured by both mechanisms, while the shape of the CH^* profiles is best predicted by the Glarborg mechanism.

Figure 4-17 shows the 2D $\text{NH}_2^*/\text{NH}_2$ profiles for the $\text{NH}_3\text{-CH}_4$ flames. The 2D $\text{NH}_2^*/\text{NH}_2$ profiles for the $\text{N}_2\text{-CH}_4$ flames are shown in Figure 4-18. Comparing the flame and lift-off heights based on the shape of the $\text{NH}_2^*/\text{NH}_2$ profiles from Figures 4-17 and 4-18, it is easy to distinguish that the $\text{NH}_3\text{-CH}_4$ flames have significantly higher flame and lift-off heights than the $\text{N}_2\text{-CH}_4$ flames. This is consistent with the flame heights based on experimental centerline temperature measurements and lift-off heights obtained from CH^*/CH data. From Figure 4-17, it is evident that the NH_2^* is also located in a thin shell around the flame. Unlike the CH^* chemiluminescence, however, NH_2^* chemiluminescence was observed to extend further towards the tip of the flame. For higher ratios of NH_3 , the NH_2^* chemiluminescence at higher HAB was found in a spread-out region about the centerline. Both sets of simulations show similar trends, with NH_2 being located primarily in a thin shell around the flame. At larger ratios of NH_3 , both sets of simulations show a more smeared distribution of NH_2 towards tip of the flame. Similar to the CH^*/CH profiles, however, the NH_2 profiles predicted by the Glarborg mechanism better match the shape of the experimental NH_2^* profiles than those predicted with the GRI mechanism. This result is not surprising, as the Glarborg mechanism was developed to predict NO emissions, with special focus on fuel-nitrogen chemistry like that of NH_3 . The GRI mechanism, however, was intended to model natural gas combustion as opposed to NH_3 combustion, and pays more attention to N_2 than other fuel-nitrogen chemistry.

It should be noted that the formation of a tribrachial flame structure was experimentally observed towards the base of the flames in the NH_2^* profiles (Fig. 4-17), beginning to appear at $\beta=0.30$ and becoming prominent at $\beta=0.50$. The formation of a tribrachial flame structure was also predicted by both mechanisms and was observed at $\beta=0.20$ in both cases. However, the GRI mechanism predicts a significantly more prominent tribrachial structure as β increases relative to the Glarborg mechanism. These features evident in the 2D NH_2

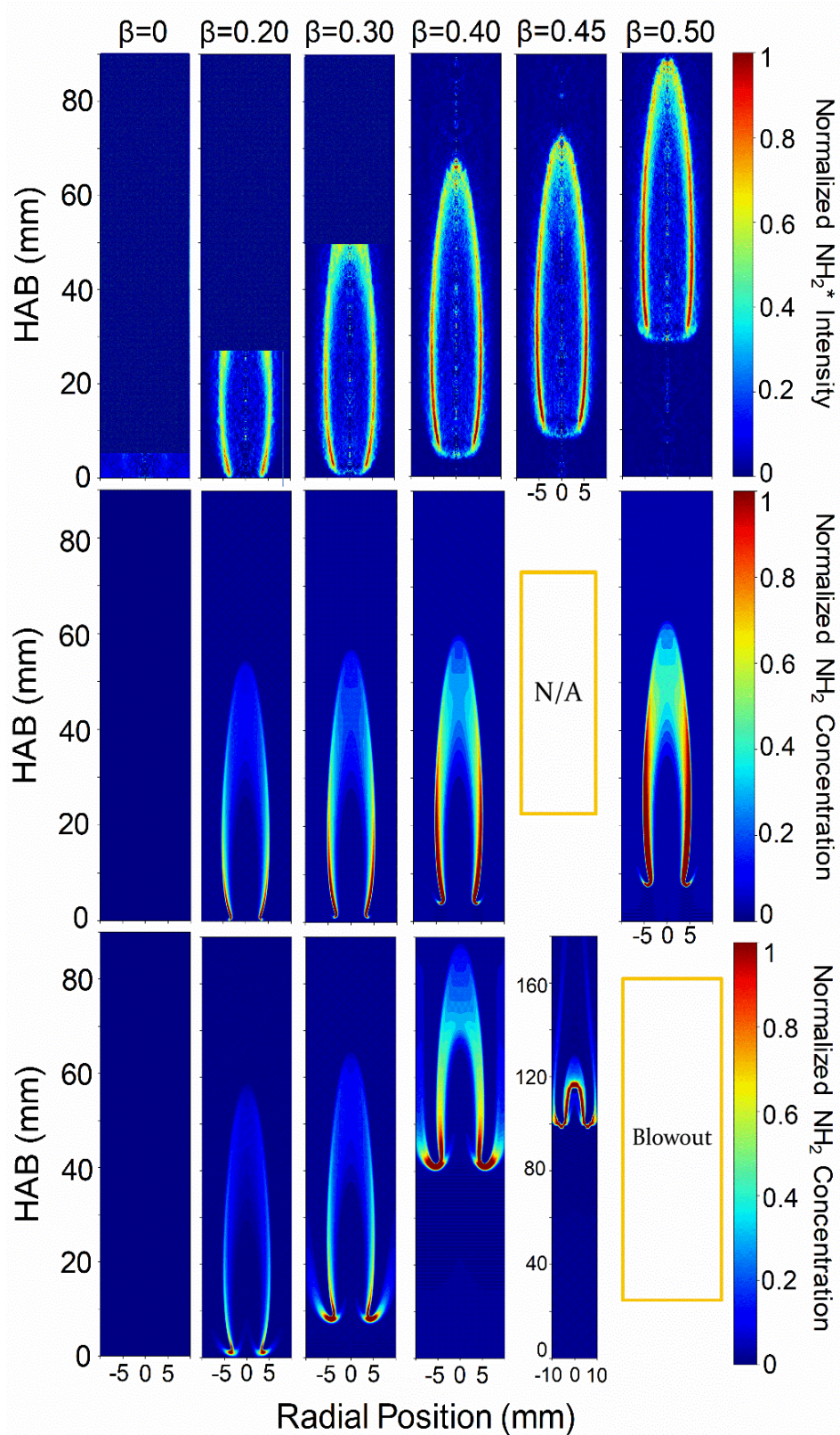


Figure 4-17: Spatially resolved $\text{NH}_2/\text{NH}_2^*$ profiles in $\text{NH}_3\text{-CH}_4$ flames. Top row: Experimentally-determined relative NH_2^* signal. Middle row: Simulated relative NH_2 concentration using the Garborg mechanism. Bottom row: Simulated relative NH_2 concentrations using GRI mech.

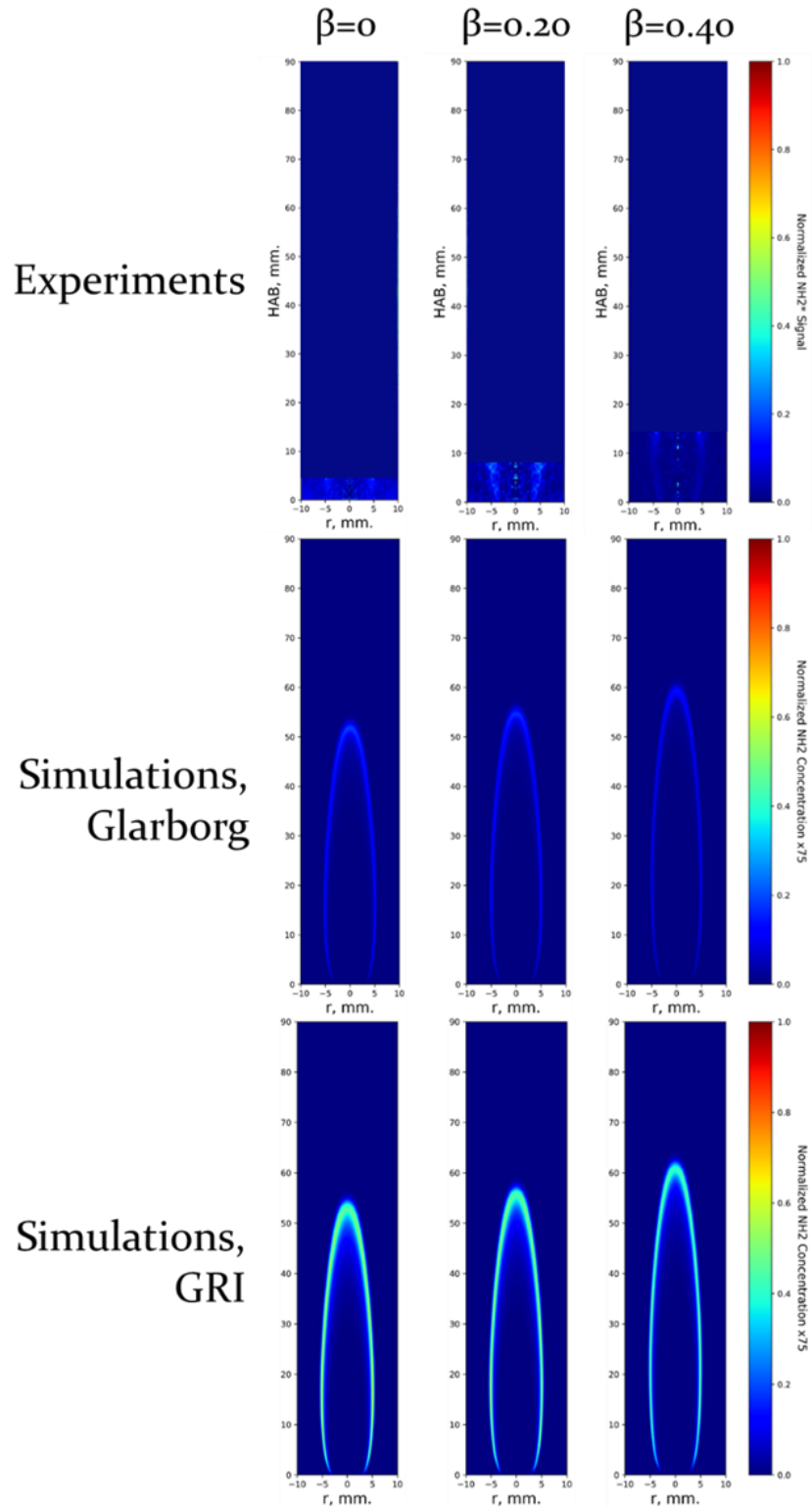


Figure 4-18: Spatially resolved $\text{NH}_2/\text{NH}_2^*$ profiles in $\text{N}_2\text{-CH}_4$ flames a) Experimentally-determined NH_2^* signal, normalized b) Simulated NH_2 concentration using the Glarborg mechanism, normalized c) Simulated NH_2 concentrations using GRI mech, normalized. Note that the relative signals in simulations have been multiplied by 75 in order to visualize the NH_2 in the image plots

profiles predicted by the Glarborg mechanism are comparable in size and shape to those observed in the experimental NH_2^* profiles, giving further support to the accuracy of the Glarborg mechanism in capturing complex flame characteristics in atmospheric co-flow nonpremixed ammonia-methane flames.

4.4.3 Species Concentrations and Soot Volume Fractions

The main objective of this study was to explore the effect of NH_3 addition on soot formation in CH_4 flames, and to determine the ability of the current kinetic models to reproduce these effects. The Glarborg mechanism was used for the model predictions presented in this section, based on its performance in capturing NH_3/CH_4 flame characteristics from the previous sections. As described in section 4.3.2, the Glarborg mechanism does not include any hydrocarbons larger than C_2H_2 , and therefore we incorporated hydrocarbon growth reactions from C_2H_2 up to naphthalene, taken from (181), as well as a soot model, into the mechanism. Major species (CH_4 , NH_3 , N_2 , H_2O , CO_2) were measured to test the agreement of the simulations with the experiments. Figure 4-19 displays centerline mole fraction profiles for these species. The experimental and simulated species profiles agree with one another, and measured mole fractions of $\text{N}_2/\text{NH}_3/\text{CH}_4$ near the burner surface agree with the reactant concentrations expected for each β . This demonstrates that the general flame characteristics are well-predicted by the model. It should be noted that the measured N_2 mole fractions are slightly elevated at low HAB, as the measurement is unable to distinguish between N_2 and CO ($m=28$ amu).

To analyze the effect of NH_3 on the formation of soot precursors, we measured the centerline mole fractions of acetylene (C_2H_2), an important reactant involved in the formation of higher hydrocarbons, soot nuclei and surface growth (222). Figure 4-20 shows the measured and simulated C_2H_2 mole fractions, for both $\text{N}_2\text{-CH}_4$ and $\text{NH}_3\text{-CH}_4$ flames. The peak C_2H_2 mole fractions become smaller and shift to higher HAB with addition of either N_2 or NH_3 . For a given

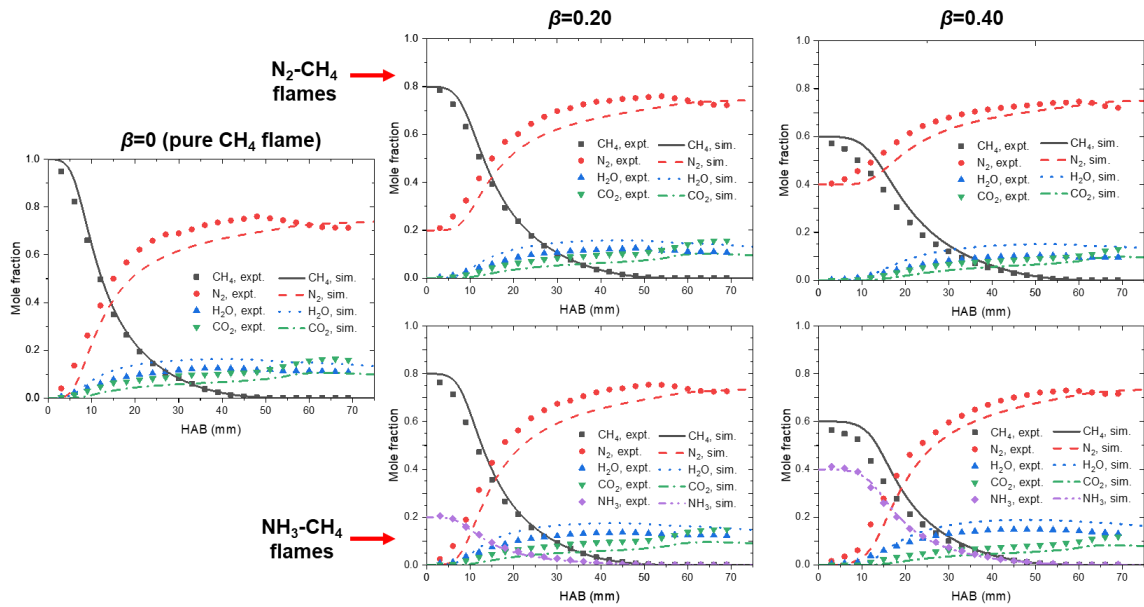


Figure 4-19: Species profiles for select N_2 - CH_4 and NH_3 - CH_4 flames.

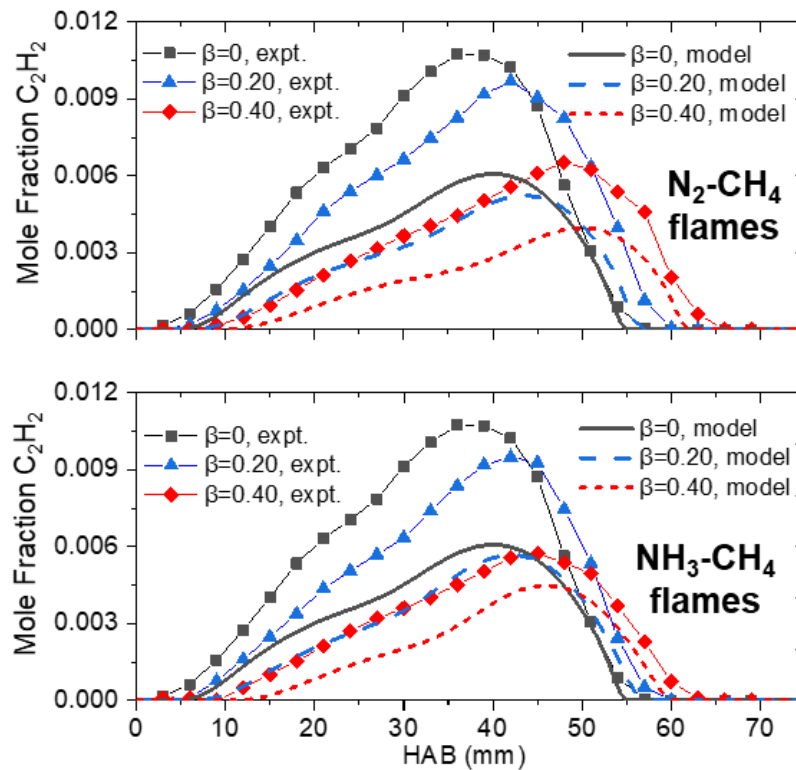


Figure 4-20: Centerline C_2H_2 mole fractions vs height above the burner (HAB). The HAB was defined relative to the exit of the fuel tube. Experiments: Markers+lines; Simulations: Lines only.

value of β there is good agreement between the location of experimental and simulated peak C_2H_2 mole fractions. However, the predicted absolute C_2H_2 mole fractions are 2x lower than the measured values. This difference is in part attributed to experimental interferences from other

hydrocarbon fragments and underestimation of the total gas pressure, resulting in larger C_2H_2 mole fractions (overestimated at most by +30% based on simulated data). However, this doesn't fully explain the discrepancy and hints at issues in hydrocarbon growth chemistry from C_2H_2 . The shift of peak C_2H_2 to higher HAB is attributed to an increase in the flame height with N_2 or NH_3 additions. This is supported by the position of the peak centerline mole fraction of CO_2 (Fig. 4-19), a marker of the stoichiometric flame height, which shifts to higher HAB with an increase in β . The simulations show similar decreases in the overall C_2H_2 profiles with additions of either N_2 or NH_3 to the base CH_4 fuel, with N_2 additions leading to slightly lower peak C_2H_2 maxima than NH_3 additions at larger blending ratios. Experimentally, however, the trend was reversed. These dependences in peak C_2H_2 concentrations with variations in β are explored in Section 4.4.4. Overall, NH_3 and N_2 additions were found to reduce C_2H_2 mole fractions and shift the location of the maximum centerline C_2H_2 to higher HAB, trends that are captured both in the simulations and measurements.

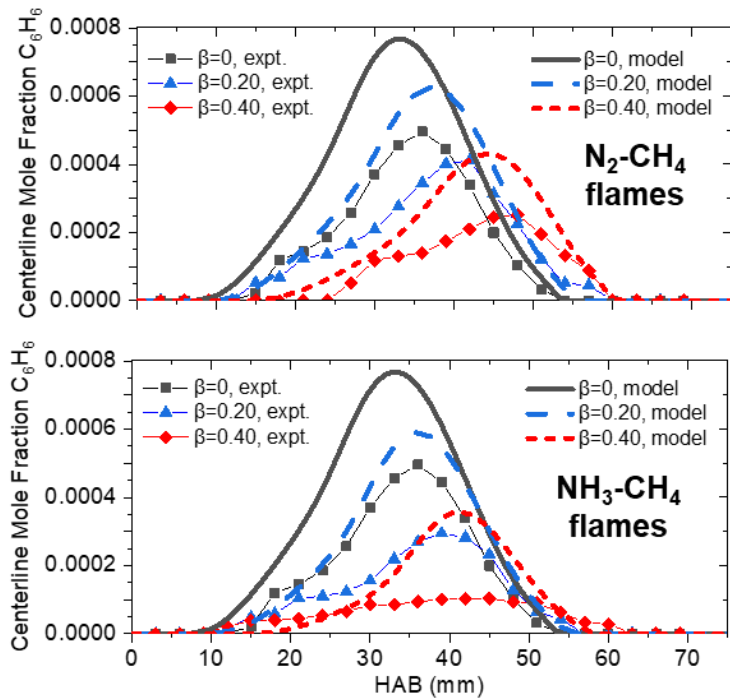


Figure 4-21: Centerline C_6H_6 mole fractions vs HAB. Experiments: Markers+lines; Simulations: Lines only

Benzene (C_6H_6) is a building block for polyaromatic hydrocarbons, and C_6H_6 formation has been shown to correlate to maximum soot concentrations in nonpremixed undoped and doped N_2 -diluted CH_4 flames similar to the flames under study (115). The centerline C_6H_6 profiles in the flames are displayed in Figure 4-21. With additions of N_2 or NH_3 to the base CH_4 -flame, the peak C_6H_6 decreases and shifts to higher HAB, which is analogous to the trends observed in the C_2H_2 centerline profiles. Interesting to note is that the simulated peak C_6H_6 mole fractions decrease with increasing β , with N_2 and NH_3 additions yielding similar decreases in peak C_6H_6 levels. Experimentally, NH_3 additions were found to have a stronger suppressive effect on peak C_6H_6 levels. It should be noted that predicted C_6H_6 mole fractions are 1.3 to 2x higher than those that were measured. This trend is attributed to the simplified reaction scheme from C_2H_2 to C_6H_6 in the chemical mechanism, which may overconsume C_2H_2 and subsequently overestimate C_6H_6 levels. The relationship between peak C_6H_6 concentrations and β are discussed in Section 4.4.4.

To compare the effect of NH_3 and N_2 additions on soot formation in CH_4 flames, f_v distributions in N_2 - CH_4 and NH_3 - CH_4 flames with values of β up to 0.20 were determined. This is a narrower range of β than for the species measurements because soot was negligible in NH_3 - CH_4 flames beyond $\beta > 0.20$. The f_v distributions (Fig. 4-22) were obtained using the FLiPPID methodology, which results in centerline data with less artifacts than in our earlier CRP results (197). Corresponding temperature distributions and centerline f_v plots are shown in Figure 4-23 and 4-24. The heights between the simulated and experimental soot profiles differ by ~10%. These discrepancies are attributed to uncertainties in the experimental flowrates, uncertainties in the thermal boundary conditions for the simulations, and deficiencies in the chemical mechanism. Nonetheless, the overall magnitudes in soot volume fractions are largely matched between the experiments and simulations, giving confidence in the model for analyzing trends in soot concentrations with N_2 or NH_3 dilution.

For the $\beta=0$ CH₄ flame, the measured maximum f_v was located along the centerline (between 50 to 60 mm HAB), consistent with previous findings in CH₄-air flames (223). Focusing on this region, then it is clear that adding either N₂ or NH₃ to the flame lowers overall soot

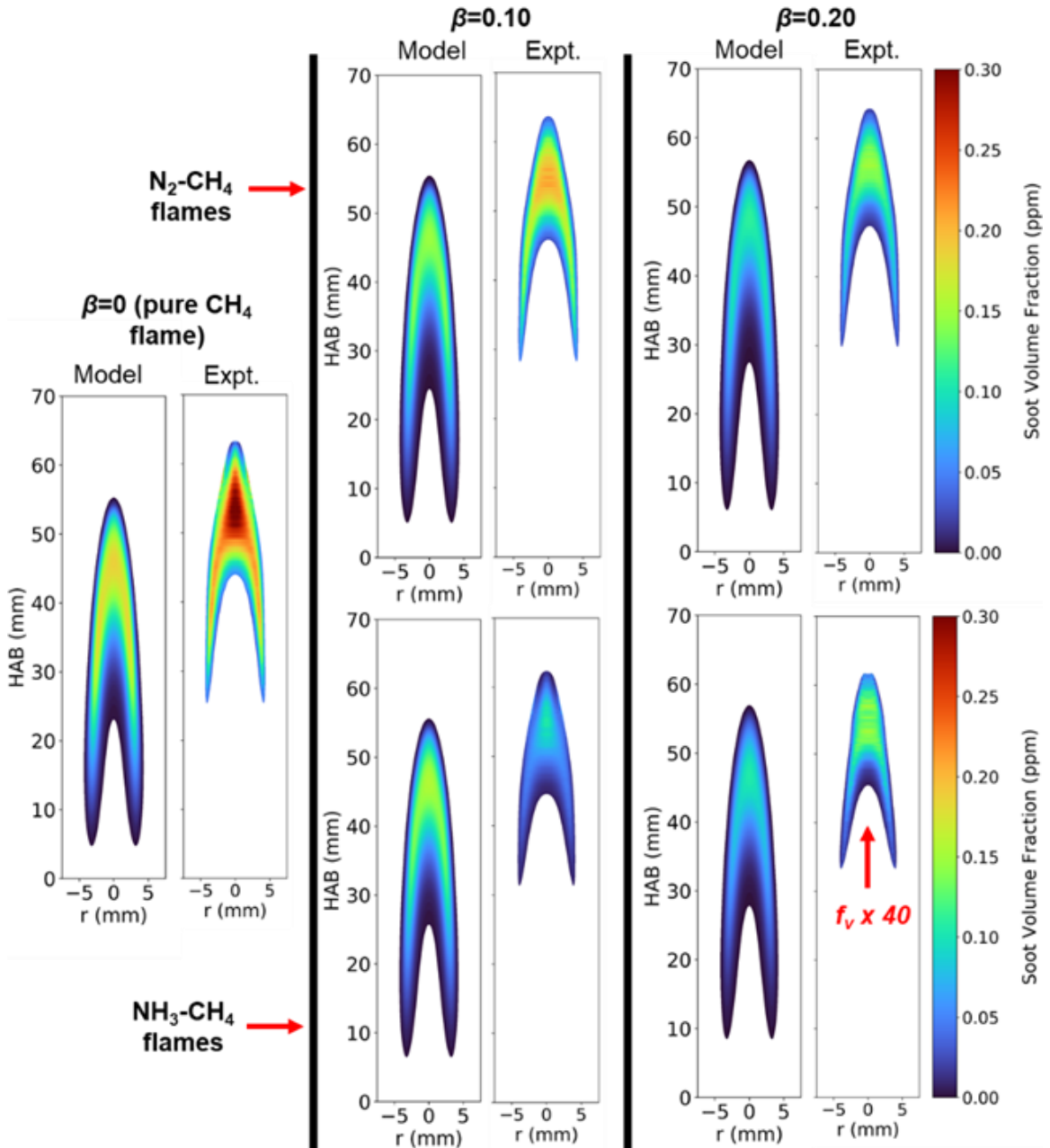


Figure 4-22: 2D f_v distributions of N₂-CH₄ flames and NH₃-CH₄. The f_v values for the $\beta=0.20$ NH₃-CH₄ flame are multiplied by 40 to make the f_v distribution visible.

concentrations. For the $\beta=0.20$ N_2 - CH_4 flames, f_v values in this region decrease by 2x relative to the $\beta=0$ flame. In the NH_3 - CH_4 flames, the soot concentration decreases by 3x by $\beta=0.10$, and drops below 0.01 ppm by $\beta=0.20$. The f_v values for the $\beta=0.20$ NH_3 - CH_4 flame are multiplied by 40 to make the f_v distribution visible. Addition of inert gases like N_2 to a flame lowers the

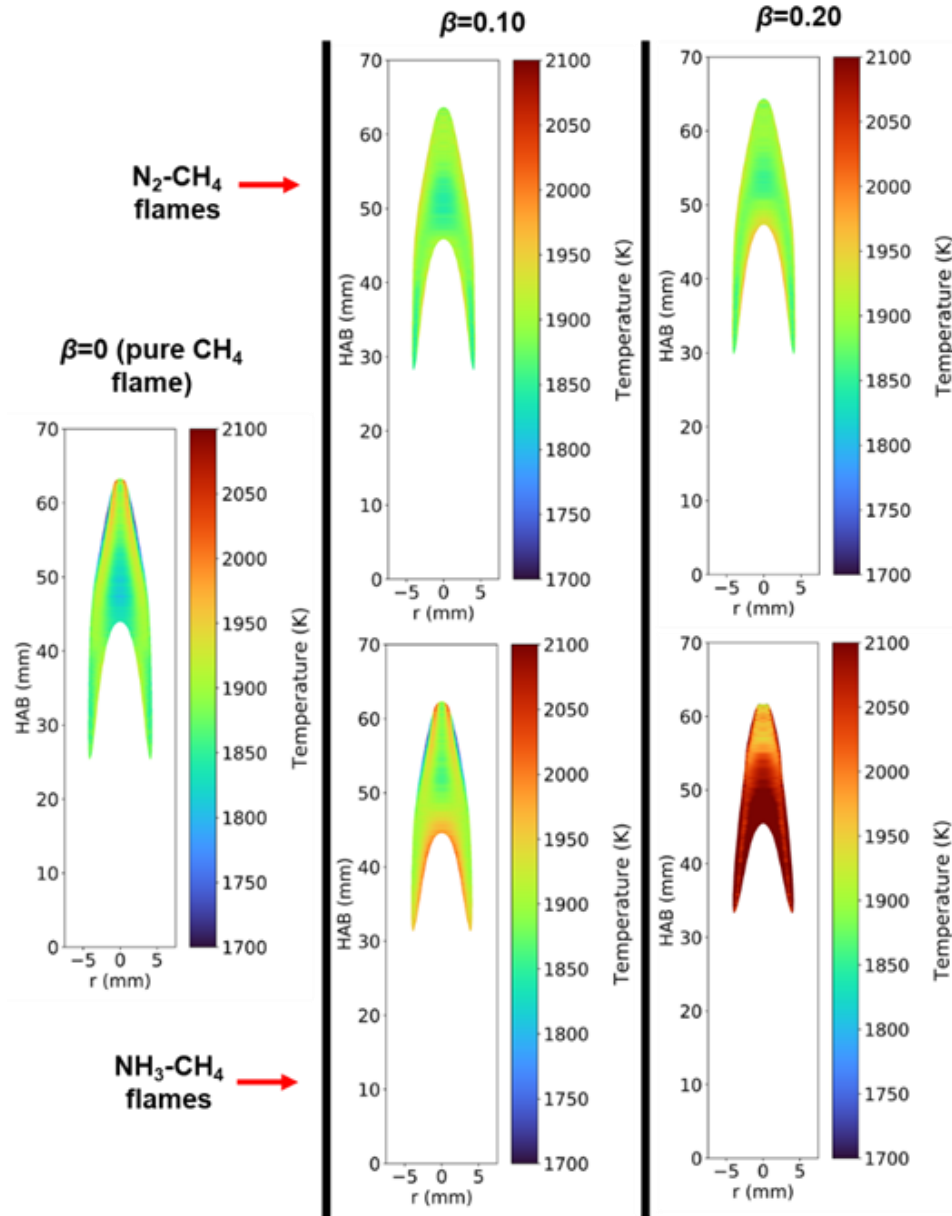


Figure 4-23: Experimental soot temperatures corresponding to the f_v distributions in Figure 4-22. The artificially high temperatures for the $\beta=0.20$ NH_3 - CH_4 flame are attributed to changes in soot optical properties, which invalidate assumptions present in the soot emissivity model for generating the temperature look-up table. Nonetheless, overall errors in f_v in the region of soot formation from HAB 55 to 60 mm is expected to be +500%/-50%.

adiabatic flame temperature, which consequently decreases the rate of hydrocarbon growth and soot formation processes (106, 107). It also dilutes the fuel mixture, reducing the frequency of collisions of the fuel and its products. Compared to N_2 , addition of NH_3 to the flame has a smaller thermal effect (Figs. 4-25, 4-26) and the same dilution effect for a given β . Therefore, the observation that the NH_3 - CH_4 flames have lower overall f_v than N_2 - CH_4 flames for a given β demonstrates a strong chemical influence of NH_3 on suppressing soot formation.

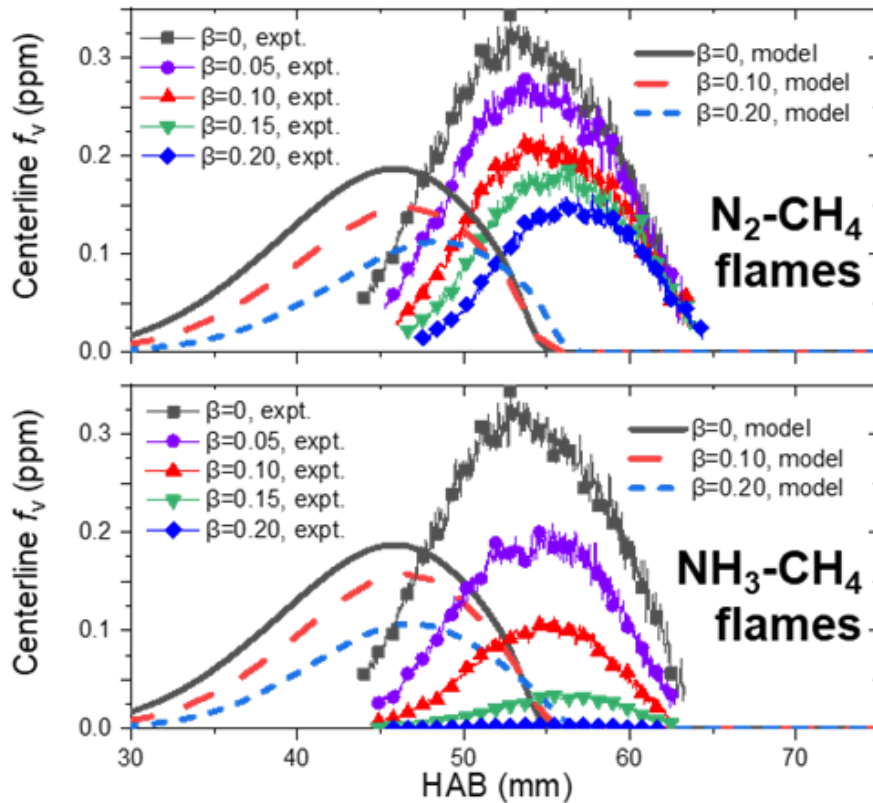


Figure 4-24: Simulated and experimental centerline f_v vs. HAB for both N_2 - and NH_3 - CH_4 flames. For experimental data, every 50th data point is designated with a marker. Values of maximum centerline f_v used for the analysis in Figure 4 are derived from these plots

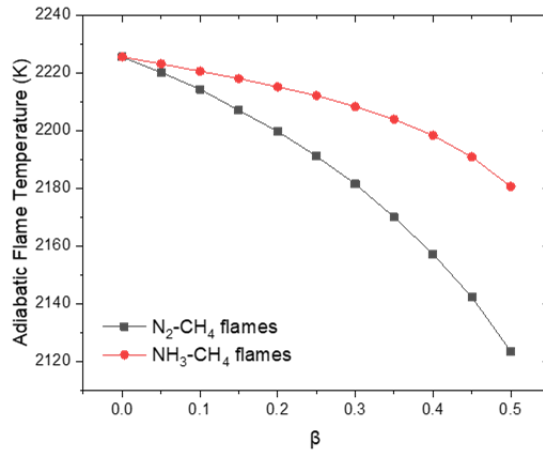


Figure 4-25: Adiabatic flame temperatures vs. β . Adiabatic flame temperatures were calculated using the online NASA Chemical Equilibrium with Applications Software (221).

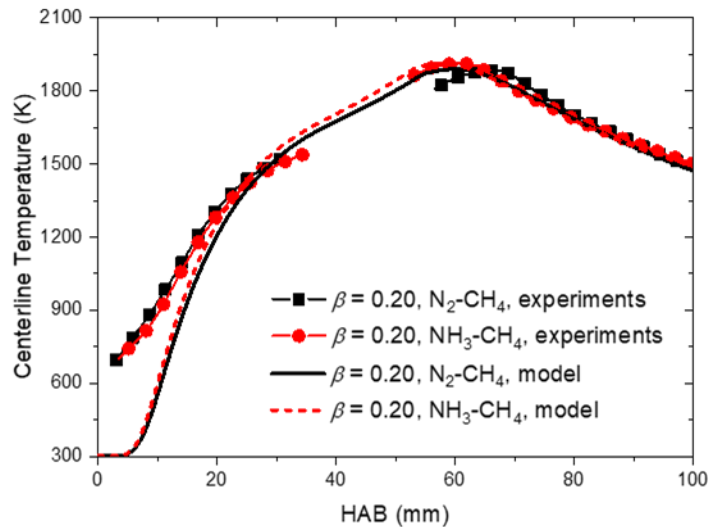


Figure 4-26: Experimental and centerline temperature profiles for the $\beta=0.20$ N_2 - and NH_3 - CH_4 flames. Measured temperatures were obtained using a Type R thermocouple (224). For both experimental and simulated data, every 10th datapoint is designated with a marker. Some experimental datapoints are missing due to interference from soot deposition. Heat conduction to the thermocouple bead resulted in larger uncertainty in datapoints from HAB = 2 to 15 mm.

The simulations show similar trends in the f_v distribution for the N_2 - CH_4 flames, although soot was found to occur closer to the burner surface than was measured. It has been shown that young soot particles, which have different optical properties than mature soot, can be detected with thermocouple-based diagnostics closer to the burner surface relative to some optical setups (184). It should be noted that the entire flame is imaged with the CRP diagnostic so that the maximum soot concentrations are captured. Measuring the lowest soot concentrations and soot of varying maturities thus requires special optical techniques with a larger dynamic range

than CRP, such as combined LII/cavity ring-down extinction measurements (225), but this is outside the scope of this study. Therefore, the model and experimental differences in the location of soot inception is attributed to CRP being sensitive to only fully carbonized mature soot, whereas the simulation results include freshly nucleated, young soot. Simulated f_v profiles for the $\text{NH}_3\text{-CH}_4$ flames predicted decreases in f_v similar to the $\text{N}_2\text{-CH}_4$ model results, although were largely unable to match measured trends. It should be noted that fuel-nitrogen interactions with hydrocarbons larger than C_2H_2 were not in the underlying mechanism, but growth reactions from C_2H_2 up to naphthalene were considered in the soot model, partly explaining the observed differences in measured and predicted f_v values. It should be noted that the simulated C_6H_6 values were larger than the measured values, while predicted soot concentrations for the $\text{N}_2\text{-CH}_4$ flame were lower than those that were measured. While beyond the scope of this study, this observation may suggest that investigation of the reactions from C_6H_6 to incipient soot is needed to accurately capture the magnitude of soot concentrations.

4.4.4 Discussion on Effect of NH_3 on Soot Formation in CH_4 Flames

To further analyze the agreement between the experiments and simulations in capturing relative differences in the concentrations of soot and soot precursors as β varied, Figure 4-27 plots the maximum centerline C_2H_2 , C_6H_6 , and soot concentrations for each β normalized to the corresponding maxima in the $\beta=0$ flame. Thus, this analysis tests the ability of the simulations to capture relative differences in mole fractions and f_v values as β varies, even though the absolute experimental and simulated values may disagree for a given value of β . The better the agreement between the normalized experimental and simulated curves in Fig. 4-27, then the better the simulations match experimentally observed differences in maximum centerline C_2H_2 , C_6H_6 , or soot levels with variations in β .

For the $\text{N}_2\text{-CH}_4$ flames, the simulations satisfactorily matched the measured relative differences in the maximum C_2H_2 and C_6H_6 mole fractions as β varied up to 0.40. For $\text{N}_2\text{-CH}_4$

flames, the measured differences in maximum centerline f_v values were found to be more sensitive to variations in β than the simulations predicted. For the $\text{NH}_3\text{-CH}_4$ flames, the measured and predicted relative maximum C_2H_2 levels begin to diverge at $\beta=0.20$, with simulations predicting smaller decreases with NH_3 additions than were experimentally observed. For the $\beta=0.40$ $\text{NH}_3\text{-CH}_4$ flame, the simulations predict a 1.3x decrease in the maximum centerline C_2H_2 mole fraction relative to the $\beta=0$ CH_4 flame, while a 1.8x decrease is experimentally observed. The disagreement in the measured and simulated differences in maximum centerline C_6H_6 mole fractions with variations in β , however, is larger than that observed in the C_2H_2 mole fractions. The simulations predict that the maximum centerline C_6H_6 mole fraction in the $\beta=0.40$ $\text{NH}_3\text{-CH}_4$ flame is reduced by a factor of 2 relative to the $\beta=0$ flame, while a five-fold reduction was experimentally observed. It should be noted that N_2 addition to

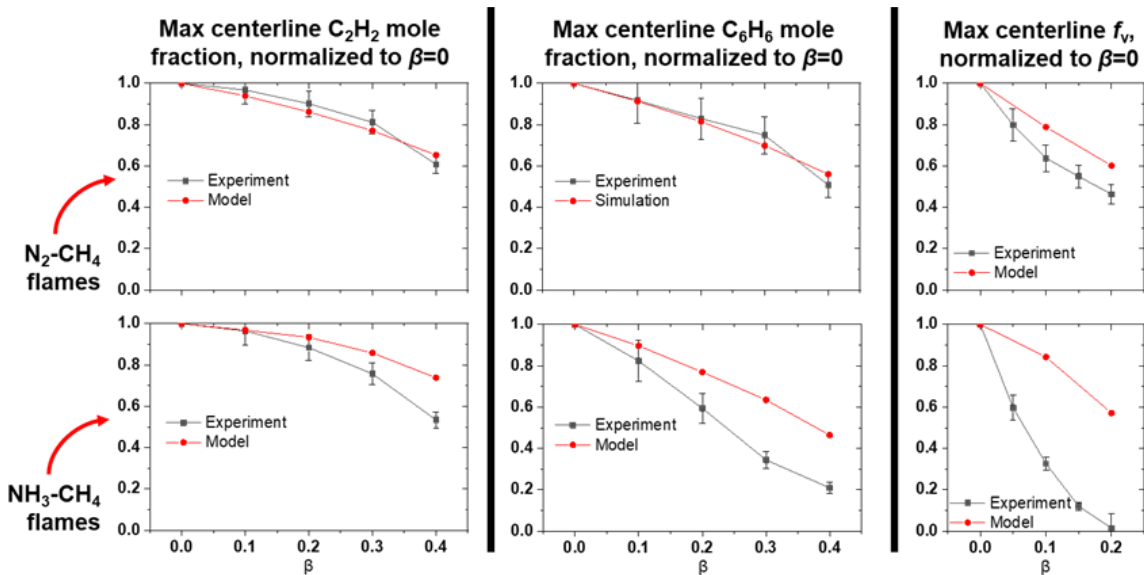


Figure 4-27: Normalized centerline maximum C_2H_2 mole fraction (left column), C_6H_6 mole fraction (middle column), and f_v (right column) versus β . Values for maximum centerline f_v were derived from the plots in Figs. 4-18, 4-19, and 4-22.

the flame lowers C_6H_6 concentrations through dilution and thermal influences, so the observation that NH_3 lowers C_6H_6 concentrations more than similar N_2 additions suggests a chemical influence of NH_3 on C_6H_6 formation rates. Since absolute C_2H_2 levels were found to only slightly differ between $\text{N}_2\text{-CH}_4$ and $\text{NH}_3\text{-CH}_4$ flames at a given β , this implies that NH_3 could

potentially affect C_6H_6 formation by interfering with the pathways of other precursors to C_6H_6 , such as C_3H_3 or C_4H_6 (226, 227). This could additionally explain the disagreement between experimental and simulated C_6H_6 profiles, since the chemical mechanism employed in this study does not contain nitrogen-hydrocarbon reactions with hydrocarbon species from C_2H_2 to C_6H_6 derived from the soot model.

The simulated and experimentally observed differences in maximum centerline f_v with variations of β disagree even more markedly for the NH_3-CH_4 flames. Even as low as $\beta=0.10$, the simulated maximum centerline f_v was predicted to decrease by a factor of 1.2 relative to the $\beta=0$ flame, while a 3x decrease was measured. The analogous reductions in the $\beta=0.10$ N_2-CH_4 flame were found to be 1.3x and 1.6x for the simulations and experiments, respectively. It should be noted that the difference between predicted and measured centerline maximum values is expected to increase for larger chemical species. This is because their formation is sensitive to reactions between smaller species, and uncertainties in temperatures and predicting smaller hydrocarbons compound for larger hydrocarbons.

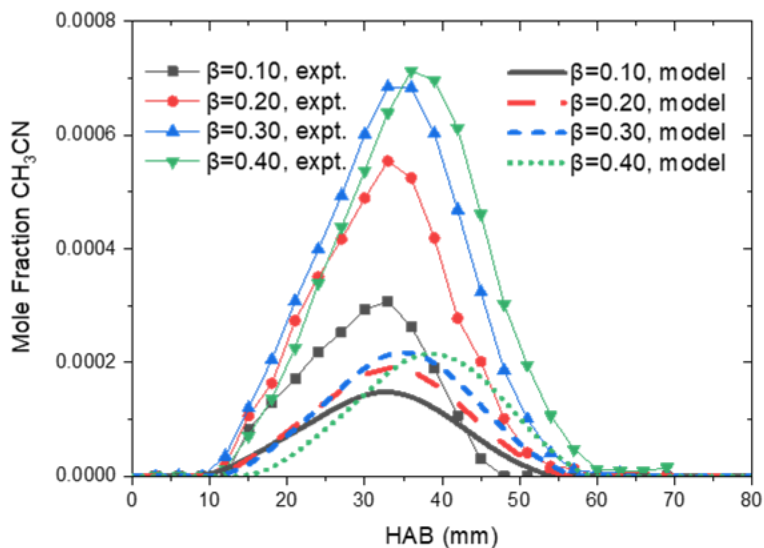


Figure 4-28: Experimental and simulated centerline mole fractions of CH_3CN . These plots demonstrate that fuel-nitrogen interactions with hydrocarbons within the flame are occurring.

These comparisons suggest that the simulations are able to adequately capture trends in the concentrations of soot and important soot precursors with variations in β for N_2 - CH_4 flames, but perform less than ideally for predicting similar trends in NH_3 - CH_4 flames. The disagreement between simulated and experimental centerline C_6H_6 and f_v profiles can be attributed to a lack of reactions in the detailed chemical mechanism describing the interaction of fuel- NH_3 with higher hydrocarbons. It should be noted that the formation of acetonitrile (CH_3CN) was observed in NH_3 - CH_4 flames (Fig. 4-28), indicating nitrogen-hydrocarbon interactions are indeed occurring. These results taken together imply there are fuel-nitrogen reactions relevant to soot formation in NH_3 - CH_4 flames that are missing from the underlying chemical model. For future models to accurately predict particulate emissions from systems that co-fire NH_3 and hydrocarbons, these reactions should be identified and included.

4.5 Conclusions

In this work, it was shown that NH_3 strongly suppresses soot concentrations, which is likely through chemical interactions with carbon that compete with aromatic growth pathways. Nonpremixed axisymmetric NH_3 - CH_4 and N_2 - CH_4 co-flow flames were experimentally and numerically studied, and trends in centerline temperatures agreed well with both sets of simulations, although temperatures predicted with the Glarborg mechanism better matched experimental profiles at larger ratio of NH_3 to CH_4 . NH_3 - CH_4 flames were found to have significantly larger lift-off and flame heights than N_2 - CH_4 flames at higher ratios of fuel NH_3/N_2 . While this trend was captured by simulations employing the GRI mechanism, absolute lift-off and flame heights were best predicted by the Glarborg mechanism. Trends in 2D CH profiles predicted by both mechanisms agreed well with experimental trends in CH^* chemiluminescence. Trends and shapes of the NH_2^* chemiluminescence profiles were best matched by the Glarborg mechanism. A model based on the Glarborg mechanism was able to capture changes in C_2H_2 , C_6H_6 , and f_v with increasing N_2 -addition to the fuel, but was unable to

fully match measured trends in $\text{NH}_3\text{-CH}_4$ flames. This disagreement is attributed to a lack of chemical pathways in the underlying mechanism that describe the interaction of NH_3 and its decomposition products with C_3 or greater hydrocarbons.

5 Synchrotron X-ray Fluorescence Thermometry for Validating Combustion Models

Parts of this chapter are from manuscripts under preparation (see “Publications” section prior to Chapter 1, entry 5)

The results presented in Sections 5 and 6 intend to demonstrate new X-ray techniques that can probe physical quantities in these flames. The data generated from these techniques can be directly compared to simulations in order to judge how well the model is capturing phenomena such as temperature and mixing. The results in Section 4 suggest that the disagreement between model predictions and measurements are related to the underlying mechanism’s ability to capture nitrogen-hydrocarbon interactions relevant to soot formation, and so these measurements help rule out the possibility that the disagreement between model predictions and measurements are due to issues in capturing the flame physics, and is indeed related to reactions missing in the underlying kinetic mechanism. While the results presented in these sections are for flames lacking N_2/NH_3 , they still provide useful validation targets for testing CFD models, and these techniques could be extended to flames containing N_2/NH_3 in future work.

5.1 Background/Motivation

X-ray techniques have been used extensively to characterize solid samples and have played a role in many Nobel Prizes awarded in chemistry, physics, and medicine (228). X-ray measurements in gas phase environments such as flames are more challenging since the density is orders of magnitude lower, especially at high temperatures. However, these difficulties are being overcome by the availability of intense x-ray sources, such as synchrotrons (229), and gas-phase measurements are becoming increasingly feasible. Frank et al. have used X-ray absorption to measure CH_4 and CO concentrations in nonpremixed flames (230). Sakurai et al. have used

Compton Scattering to measure temperature in Bunsen burner flames (231). Hansen et al. used x-ray fluorescence (XRF) of krypton atoms to examine probe disturbances in molecular beam sampling from low-pressure premixed flames (232). X-ray radiography measurements have also been applied to understanding the relationships between nozzle geometry and diesel spray characteristics (233). In this study we apply the same technique to measure temperatures in nonpremixed co-flow methane/air flames.

X-rays are electromagnetic radiation with wavelengths of 10 to 200 pm and corresponding energies of 6 to 120 keV (234). They have several interesting properties for combustion diagnostics (e.g. density and temperature measurements) (235, 236):

1. Index of refraction close to 1, so they scatter weakly at phase boundaries and do not suffer from beam steering due to temperature gradients in combusting flow fields.
2. Weak interaction with light atoms typically found in combustion systems (e.g. C, H, O, N), so they are well-suited for studies with heavier tracer elements, such as krypton.
3. X-ray absorption predominantly is caused by interactions with core electrons, making absorption and fluorescence measurements generally sensitive to individual elements rather than molecular structure
4. X-rays can be focused to a small spot size (on order of microns) at long working distances (hundreds of mm), allowing for good spatial resolution

In this study we utilize these properties, using the same technique as Kastengren et al. (233), to measure temperatures in nonpremixed co-flow methane/air flames. Temperature is an important state variable that is a driver of combustion reactions, including those involved in the formation of pollutants such as soot. Temperature is also an important boundary condition to capture accurately, as predictions of PAH and soot concentrations can be sensitive to uncertainties in inlet conditions (182). To study physical properties such as density and spatial temperature variations in reacting flows, krypton can be seeded at the same mole fractions into

fuel and oxidizer streams of a reacting flow, and synchrotron radiation can be used to excite the Kr atoms. The radiation will primarily interact with the core-shell electrons of the Kr atoms, resulting in $K\alpha$ X-ray fluorescence. Because krypton is inert, it does not participate in any chemical reactions and therefore behaves as a tracer species, and distributes evenly throughout the flame. If the krypton mole fraction and pressure are constant throughout the flow, then the krypton XRF signal is proportional to the gas density, and hence temperature via the ideal gas law.

This technique has many benefits, including that the Kr fluorescent event, with a lifetime of 170 attoseconds (237), is about 6 orders of magnitude faster than the collisional period between reactants. Because C, H, O, and N have low mass attenuation coefficients relative to Kr, the incident beam and resulting Kr $K\alpha$ signal experience little attenuation from soot or compositional variations (238). The krypton $K\alpha$ fluorescence signal at 12.6 keV is also well-separated spectrally from other interferences, including other Kr emission lines (239), elastic scattering, Compton scattering, blackbody radiation from soot particles, and potential X-ray emission lines from elements like C, H, O, and N. This complements thermometry techniques such as two-line krypton planar laser-induced fluorescence, which has been applied in measuring temperatures in ethylene diffusion flames (240) but experiences interferences of up to 200 K in sooting regions of the flames.

The present implementation of synchrotron-based XRF thermometry requires a steady flow to allow sufficient data acquisition time ($\sim 1s$) at each location and cannot currently be used for measuring temperatures in turbulent flows. This method also requires the use of a synchrotron radiation source, but these facilities are numerous and acquiring beam time is increasingly feasible through general user proposal submissions (241). Other work has employed X-ray tomography in laminar flames seeded with Kr tracer gas using benchtop X-ray sources (242), demonstrating the potential for X-ray based combustion diagnostics to be applied in a benchtop

setting. Point-data is collected with the XRF technique reported here, yielding micron-order resolution but makes acquiring 2D sets of data longer than other Kr-based thermometry techniques (242).

The specific burner geometry used in this work is one that has been chosen by the ISFW as a canonical configuration for testing numerical models of soot formation, and researchers around the world are performing complementary measurements and simulations in this burner (112, 243-247). Nonpremixed nitrogen-diluted methane/air diffusion flames generated from this burner are also being used to characterize the sooting propensities and reaction pathways of advanced biofuels (127, 130, 162, 248). In that work 1000 ppm of the test biofuel is added to the fuel stream and the sooting tendency is determined from the soot concentration in the resulting flame. Numerical simulations of the sooting tendency are performed to validate detailed chemical kinetic mechanisms for the biofuels (132, 133, 150, 249). This information then informs the rational selection of advanced biofuel components which, among other properties, offer lower sooting tendencies than conventional diesels. Since soot formation reactions are sensitive to variations in temperature, a model should be able to capture physical characteristics of a system before being employed for predicting other phenomena. In this work, we stringently test the ability of the CFD simulations to predict temperature through validation using the synchrotron XRF measurements.

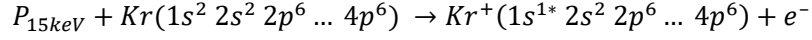
5.2 Methodology

5.2.1 Theory Relating X-Ray Fluorescence Signal from Seeded Krypton Atoms to Physical Quantities

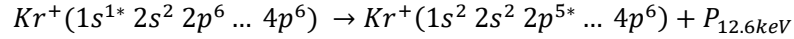
Temperature was measured via the following steps: (1) krypton was doped into both reactant streams of the flame at an initial mole fraction $X_{\text{Kr},o} = 0.023$; (2) the krypton number density n_{Kr} was measured throughout the flame by XRF; (3) the temperature T was determined by the ideal gas law and the assumption that $X_{\text{Kr}} = X_{\text{Kr},o}$ throughout the flame; (4) the measured

T was compared to simulated T ; (5) the validated simulation was used to estimate the uncertainties in T due to the assumption that $X_{Kr} = X_{Kr,o}$.

XRF as implemented in this study is a two-step process. First a 15 keV photon from the incident X-ray beam is absorbed by a krypton atom and ionizes it to a core-hole ion



The ionization predominantly occurs at the 1s electrons, and not the valence 4p electrons, because the incident photon energy slightly exceeds the binding energy for the 1s electrons (14.3 keV) (250). The core-hole ion that is formed quickly stabilizes by relaxation of a 2p electron into the 1s hole and emission of a 12.6 keV photon to conserve energy



The detection of these fluorescent photons $P_{12.6keV}$ is the goal of these experiments. The measured signal $S(x, y)$ collected from a position x, y in an axisymmetric 2D flow is related to the number of fluorescence photons $P_{12.6keV}$ captured by the detector, and can be given by:

$$S(x, y) = \eta_d \left(\frac{\Omega}{4\pi} \right) (1 - F_{abs}) Y_f \Delta t \Delta x \pi R_p^2 \sigma \phi n_{Kr}(x, y) \quad (1)$$

where η_d is the detector efficiency, Ω is the solid angle viewed by the detector, F_{abs} is the fraction of fluorescence photons directed towards the detector that are absorbed before reaching it, Y_f is the fluorescence yield, Δt is the measurement time, Δx is the detector field of view along the beam propagation direction, R_p is the radius of the incident beam, σ is the absorption cross section, ϕ is the incident photon flux, and n_{Kr} is the krypton number-density. For a given experimental geometry (described further in section 2.2/2.3), constant measurement time, and assuming the measurement is insensitive to compositional variations in the flame, the terms $\eta_d \left(\frac{\Omega}{4\pi} \right) (1 - F_{abs}) Y_f \Delta t \Delta x \pi R_p^2 \sigma$ can be considered a calibration constant c , and thus we can write the signal $S(x, y)$ as:

$$S(x, y) = c\phi n_{Kr}(x, y) = c\phi X_{Kr(x,y)} \left(\frac{N}{V}\right)_{x,y} \quad (2)$$

where $X_{Kr(x,y)}$ is the krypton mole fraction at position x,y in the flow, and $\left(\frac{N}{V}\right)_{x,y}$ is the fluid density at position x,y . If the mole fraction of krypton and the pressure in the flow are constant, then the signal can be re-written using the ideal-gas law to obtain spatially-resolved temperatures:

$$S(x, y) = c\phi X_{Kr,ref} \left(\frac{N}{V}\right)_{x,y} = c\phi X_{Kr,ref} \frac{P_{ref}}{T(x, y)k_B} \quad (3)$$

Furthermore, if a reference signal $S(ref)$ is collected at a place in the flow with known temperature T_{ref} , the temperature can be further simplified as:

$$T(x, y) = \frac{S(ref)}{S(x, y)} * T_{ref} \quad (4)$$

If the temperature remains constant rather than the krypton mole fraction, then the spatial krypton number densities can be calculated as:

$$X_{Kr(x,y)} \left(\frac{N}{V}\right)_{x,y} = \frac{S(x, y)}{S(ref)} X_{Kr,ref} \left(\frac{N}{V}\right)_{ref} = \frac{S(x, y)}{S(ref)} X_{Kr,ref} \left(\frac{P_{ref}}{T_{ref}k_B}\right) \quad (5)$$

where $S(ref)$ is a signal collected in a place with known mole fraction $X_{Kr,ref}$, and constant pressure and temperature P_{ref} and T_{ref} .

5.2.2 Burner and Flame Details

In this study, a non-reacting cold-flow N₂ jet and an atmospheric-pressure nonpremixed CH₄ flame were generated with a Yale co-flow burner (18, 33). Flow rates and Initial Krypton mole fractions are shown In Table 5-1. The krypton mole fractions were chosen to ensure sufficient signal while keeping the collection time reasonable. For all experiments, the reactants either flowed from 99.99%+ purity cylinders (fuel-CH₄, fuel-Kr, and oxidizer-Krypton), an air compressor (oxidizer-air), or a house liquid nitrogen supply (fuel-N₂). The flow rates of fuel-N₂,

fuel-CH₄, oxidizer-Kr, and oxidizer-air were controlled with FMA5400/5500 Omega thermal mass flow controllers that were directly calibrated with the corresponding process gas. The fuel-Kr flow rate was controlled with an MKS Series 1179A thermal mass flow controller. For the flame experiments, a chimney made of Kapton tape (5 mil) was used to minimize perturbations due to stray air currents.

For the non-reacting cold flow N₂ jet, krypton was doped into the fuel-N₂ stream at an initial mole fraction of $X_{Kr,o}=0.029$, while the oxidizer-Kr mole fraction was set to 0. This permits the diffusion of fuel krypton into the surrounding oxidizer, which can be studied by measuring the Krypton number-density at various points in the flow-field with XRF. These measurements in a non-reacting flow can then be compared to simulated Kr number densities to assess the suitability/accuracy of the diffusive properties used for krypton in the 2D simulations.

Table 5-1: Experimental flow rates for gas mixtures analyzed in the XRF study

Non-reacting N₂ jet						
Fuel				Oxidizer		
N₂ (mL/min)	CH₄ (mL/min)	Kr (mL/min)	X_{Kr,fuel}	Air (L/min)	Kr (mL/min)	X_{Kr,ox}
330	0	10.0	0.029	50.0	0	0
Atmospheric nonpremixed CH₄ flame						
Fuel				Oxidizer		
N₂ (mL/min)	CH₄ (mL/min)	Kr (mL/min)	X_{Kr,fuel}	Air (L/min)	Kr (mL/min)	X_{Kr,ox}
0	330	8.0	0.0237	50.0	1206.9	0.0236

For the atmospheric nonpremixed CH₄ flame, Kr was seeded into both the fuel and oxidizer streams at the same initial mole fractions (<±1% variation). This requirement ensures that the mole fraction of Kr is constant throughout the flame, to within +2%/-3% (see section 5.2.1), so that the measured XRF signal is proportional to Krypton number-density. Using the ideal gas law, a temperature can then be computed from the measured Kr number-densities.

Uncertainties in measured temperatures due to phenomena such as non-uniform pressure or Kr mole fractions throughout the flame are discussed further on in section 5.3.2.

5.2.3 X-Ray Source

The experiments were conducted at the 7-BM beamline of the Advanced Photon Source (APS) at Argonne National Laboratory. The emission from the APS bending magnet x-ray source was filtered using a double multilayer monochromator, resulting in an X-ray beam at 15.0 keV nominal photon energy ($\Delta E/E = 1.0\%$). This beam was focused with a pair of Kirkpatrick-Baez focusing mirrors (260 mm optical length) to a focal spot $4 \times 6 \mu\text{m}$ in size FWHM, with a beam divergence of less than 2 mrad in both directions. The burner was placed such that the center of the burner was at the same z (x-ray beam propagation direction) position as the focal point.

Three x-ray detectors were used in this work. A diamond photodiode (55 μm thickness) was used upstream of the focusing mirrors to monitor the incoming beam intensity. Downstream of the burner, a silicon PIN diode (300 μm thickness) was used to monitor the transmitted X-ray intensity. The signals from both photodiodes were amplified with transimpedance amplifiers and ported to voltage-to-frequency converters for readout. The X-ray emission spectra were recorded with a silicon drift diode (SDD) energy dispersive X-ray detector (490 μm thickness). This detector was coupled to a digital x-ray pulse processor, providing a spectrum of the emitted X-rays. The detector was placed at 90° to the incident x-ray beam in the horizontal plane, taking advantage of the polarization of the x-ray beam to minimize the amount of x-ray scattering seen by the detector.

If used without other optics, the SDD would sense x-rays from a wide solid angle. To perform 3D resolved fluorescence measurements, a polycapillary X-ray optic (100 mm focal length) was coupled to the detector in front of the SDD. The polycapillary effectively restricts X-rays from reaching the detector unless they originate from a small, well-defined region of the domain. The detector was positioned using a 3-axis positioning platform so the polycapillary

focal region coincided with the X-ray beam focus. The polycapillary focal region was roughly Gaussian with a size of 270 μm FWHM at 15 keV. Accounting for the dependence of focal spot size on energy, the effective probe volume size of these measurements is 4 x 6 x 320 μm , with the largest dimension in the X-ray beam propagation direction.

To collect fluorescence data, the burner was moved using a precision x,y-positioning platform through a raster pattern. At each measurement location, the incident X-ray intensity, transmitted X-ray intensity, and x-ray emission were measured for 1 s. The 2D raster scan was used to build 2D maps of the flowfield at various flow conditions.

Several steps were required to process these data. The incident and transmitted X-ray intensity were used to determine the attenuation of the beam in the flame. For each spectrum, a spectral region of interest containing the Kr $K\alpha$ peak was defined. The Kr $K\alpha$ photon counts were corrected for detector dead time effects, changes in incident beam intensity, and attenuation of the incident x-ray beam. Signal trapping effects were calculated to be quite minor, and hence no correction for signal trapping was made.

5.2.4 Computational Methods

The NGA code (34), an unsteady flow solver, was used to perform the 2D detailed simulations of the co-flow diffusion flame and non-reacting N_2 jet. The scalar equations were discretized using the BQUICK scheme, which ensures that the physical bounds of appropriate quantities are numerically preserved throughout the simulation without adding significant artificial diffusion (35). A recently-developed computationally efficient, semi-implicit, iterative method is used for the time-integration of chemical source terms for the transport equations of gas-phase species (36). The chemical model used in this work was constructed based on the chemical model developed in (37, 38). The original chemical model (37, 38) containing 171 species and 1878 reactions (forward and backward reactions counted separately) has been extensively tested and validated in laminar diffusion flames (30, 39, 40), however, it does not

contain Kr as inert gas. Therefore, the thermodynamic and transport properties of Kr were taken from (41, 42), and were incorporated into the chemical model. In Section 5.3.1, the reliability of the Kr properties incorporated are validated in the non-reacting N₂ jet. For all simulations, a refined and uniform mesh was used around the burner exit where the main chemical reactions and diffusion processes occur. The mesh was gradually stretched in both radial and axial directions away from the burner exit to reduce the computational cost. The thermal boundary conditions for the fuel and oxidizer were taken as T=298 K. The inlet flow conditions and burner geometry used for the current simulations are described in Section 5.2.2.

5.3 Results and Discussion

5.3.1 Validation in a Non-Reacting N₂ Jet

The goal for analyzing the nonreacting N₂ jet seeded with krypton was to obtain measurements which depend on the diffusive properties of krypton, and could therefore be used to assess the suitability of the physical parameters (e.g. mass diffusivity) used for krypton in the simulations. Because the oxidizer was seeded with no krypton, diffusion of krypton from the fuel stream into the surrounding oxidizer occurred and could be studied through synchrotron XRF. Furthermore, because the temperature is constant in the non-reacting flow, the krypton number-densities could be calculated from the measured krypton K- α fluorescent signal using equation (5) (section 2.1). In this case, the reference signal was collected slightly above the fuel tube exit (height-above-burner (HAB) of 0.2 mm), where the temperature, pressure, and krypton mole fraction were taken as 298 K, 996 mbar, and $X_{Kr,ref}=0.0294$.

A depiction of the flow setup, along with the experimentally-measured and simulated krypton number-densities are displayed in Figure 5-1. The krypton number-densities are largest above the fuel tube surface, as expected. The krypton number-density decreases along the centerline, reaching 50% of the initial number-density between 50-60 mm HAB. At higher HAB,

oxidizer-air diffuses to the centerline where the oxygen concentration is low, while krypton diffuses away from the centerline in the radial direction toward the co-flow lacking Kr (Figure 1a), explaining the observed decrease in the krypton-number density along the centerline. Incredible agreement was found between the simulated and experimental profiles, with both showing the Kr number density decreasing at similar rates along the centerline at higher HAB. One notable difference between the simulations and experiments is that the simulated krypton number densities near the centerline were slightly higher than those measured experimentally. If the difference is attributable to uncertainty in the mass diffusivity properties of krypton, then this would imply slower mass diffusivity of krypton in the simulations compared to the experimental diffusivity. Overall, the profiles exhibit great agreement, demonstrating the model is able to capture the physical characteristics of the flows.

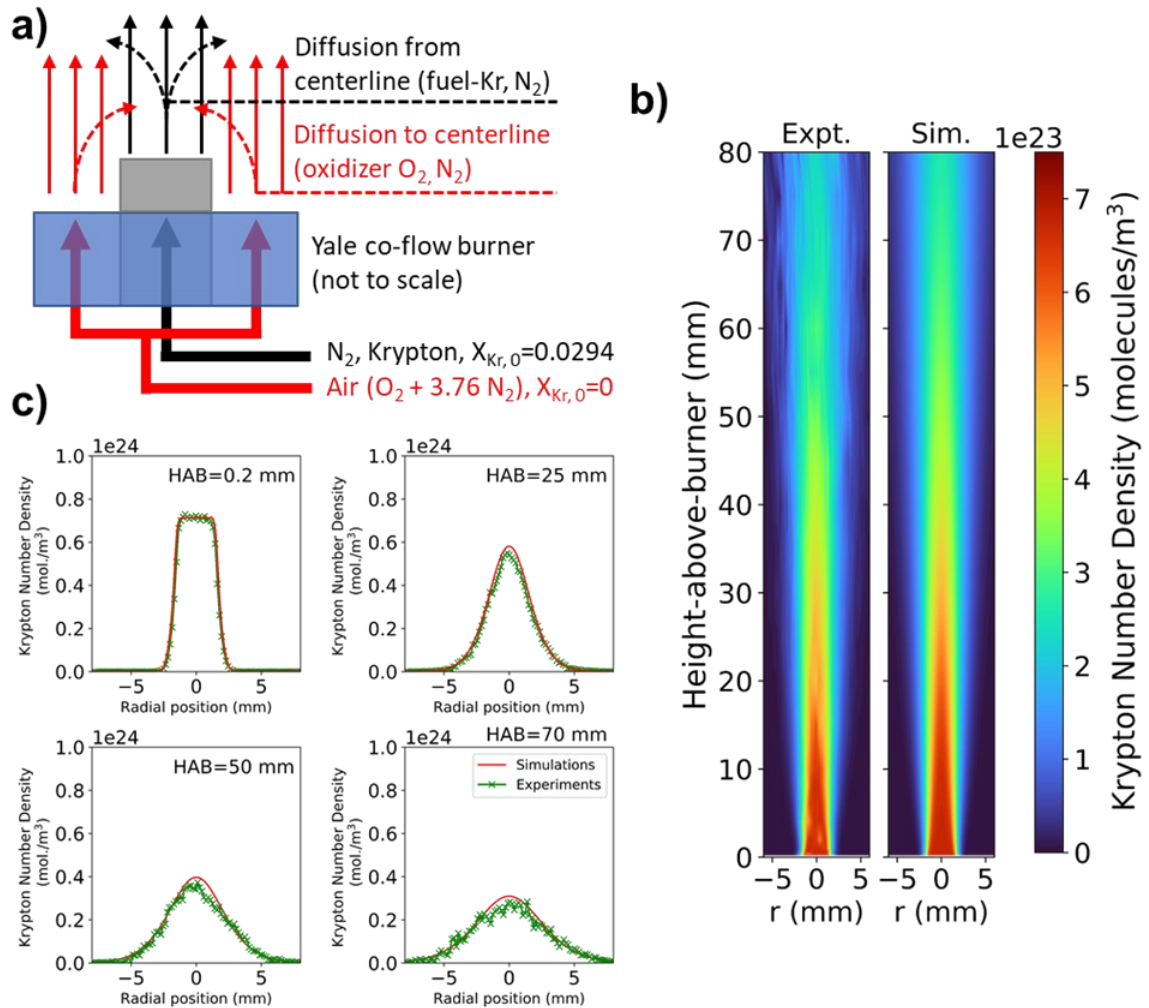


Figure 5-1: Experimental and simulated krypton number densities for a non-reacting, krypton-seeded N₂-air co-flow jet. A) Diagram depicting the flow setup b) Experimental and simulated 2D Krypton number-density profiles c) Krypton number-densities vs. radial position, at various heights in the flame

To investigate how the diffusive properties of krypton influence the krypton number density, nonreacting flows were also simulated with $\pm 5\%$ perturbations to the diffusion coefficient for krypton in nitrogen. This seemed to be a reasonable method for comparison, as the majority of the fuel and oxidizer streams were composed of N₂ (97% and 78%, respectively). Comparisons of the perturbed 2D profiles to the nonperturbed case and experiments are shown in Figure 5-2, and representative radial comparisons are shown in Figure 5-3. Differences were most pronounced near the centerline and at higher HAB. The simulated and experimental

profiles quickly converged to similar values at radial positions farther from the centerline. The effect of diffusivity was found to be largest towards the tip of the flame, where differences between the +5% and -5% cases were ~5-7%. For reference, there was a 6.6% maximum difference between the two scenarios at an HAB=70 mm. The experimental and simulated results show good agreement at low HAB. Slightly lower Kr number densities were measured at

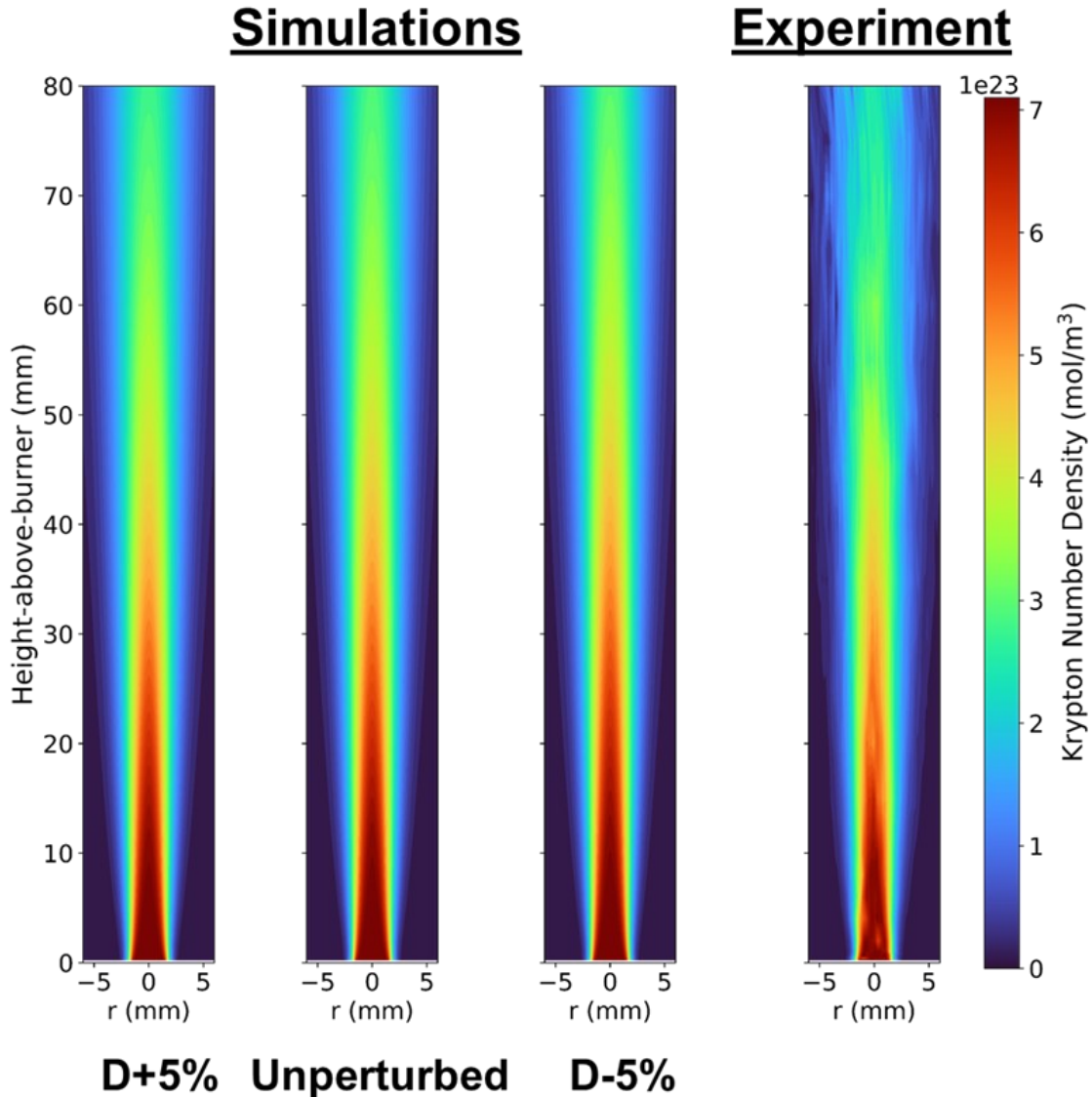


Figure 5-2: Simulated 2D Krypton Number Density Profiles for Perturbed and Unperturbed Krypton-Nitrogen Diffusivities, versus the measured profile.

higher HAB than were predicted by the simulations. This could indicate that other factors, such as random noise during signal-collection and preferential species diffusion, are introducing

uncertainty into the experimental measurements in these regions of the flow. Altogether, the results suggest that the model is accurately capturing the diffusive properties of krypton, and will also be suitable for addressing uncertainties caused by variations in the krypton mole fraction.

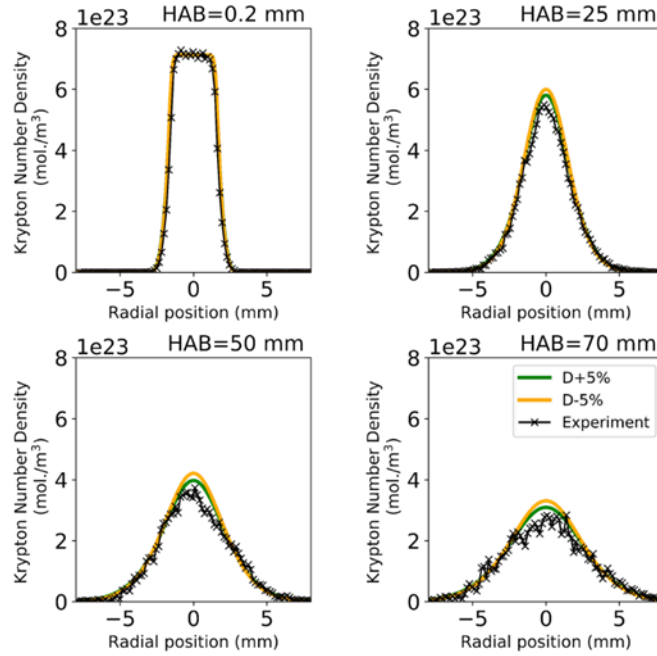


Figure 5-3: Simulated Krypton number densities and experimental Krypton number densities. The simulated profiles were calculated for $\pm 5\%$ perturbations to the mass diffusivity of Krypton into nitrogen (denoted D+5% and D-5%)

5.3.2 Uncertainties in a Co-Flow Flame

In the following section, the various assumptions and uncertainties present in the experimental measurements are analyzed. These include the assumptions that the krypton mole fraction and pressure are constant, that the fluorescent signal is well-separated from other emission lines or interferences due to soot, and random uncertainty during signal collection.

(1) Uncertainty due to non-Uniformities in Krypton Mole Fraction

Two assumptions lumped into this analysis are that the krypton mole fraction and pressure are constant throughout the flame. To address these uncertainties, the simulated pressure and krypton mole fraction profiles were computed based on the experimental conditions for the nonpremixed CH_4 flame seeded with krypton. The simulated 2D pressure profiles (Fig. 5-4)

reveal that the pressure varies at most by $4.9 \times 10^{-4}\%$ and mainly as a function of HAB. The krypton

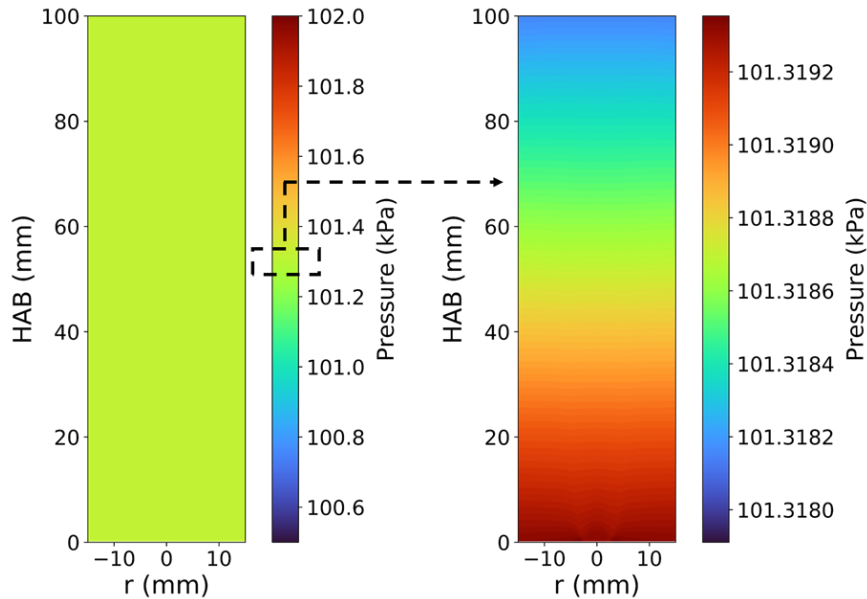


Figure 5-4: Simulated 2D Pressures in the Nonpremixed CH₄ Flame Seeded with Krypton

mole fraction variations and differences from the assumed value are shown in Figure 5-5. The krypton mole fractions were found to vary from 2.3% to 2.4%. The largest differences in the simulated mole fraction versus the fuel-Kr mole fraction is towards the tip of the flame and in the wings. The simulated mole fraction of krypton mole fractions was found to be larger than the assumed value towards the tip of the flame. This is attributed to the preferential diffusion of comparatively light combustion species away from the centerline compared to krypton. The lower mole fraction of krypton in the wings of the flame could be due to initial fuel decomposition and non-equimolar reactions which dilute the krypton in these regions. Based on these variations, this is expected to cause uncertainties of -3% up to +2% in the measured temperatures, which would correspond to an uncertainty of -60 /+40 K at 2000 K.

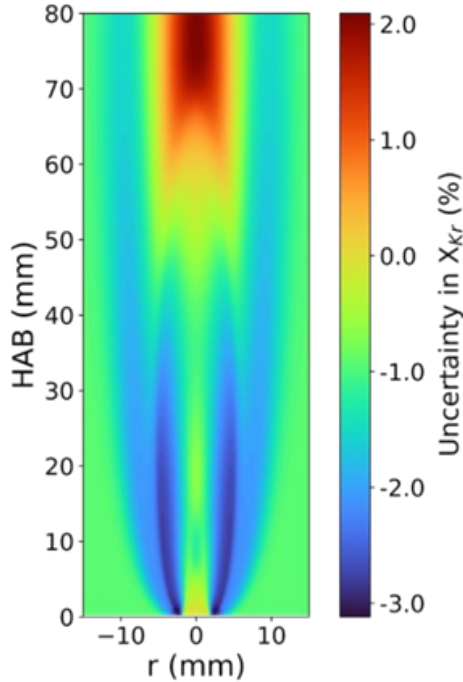


Figure 5-5: Uncertainty in the experimental measurements due to variations in the krypton mole fraction. The uncertainty was calculated based on the simulated krypton mole fractions

(2) Uncertainty due to soot and other interferences

Another assumption lumped into the experimental measurements is that the collected signal is coming only from krypton K- α photons, and that the detection of these photons is insensitive to the presence of soot and compositional variations in the flame. Figure 5-6 shows the measured detector signal as a function of photon energy at locations in the flame with and without soot. A peak is observed at 12.6 keV, which is due to the absorption of 15 keV photons by krypton atoms seeded in the flow and their subsequent emission of fluorescent photons. This peak is actually a doublet, but is difficult to visualize given the limited spectral resolution of the SDD. Another peak is also observed at 14.1 keV, corresponding to the weaker Kr K- β fluorescent transition. This peak is well-separated from the peak centered at 12.6 keV. For 15 keV incident photon energies, the Compton Energy peak for scattering would occur roughly at 14.57 keV (251), and it is clear from these results that any scattering is weak and not interfering with the signal at 12.6 keV.

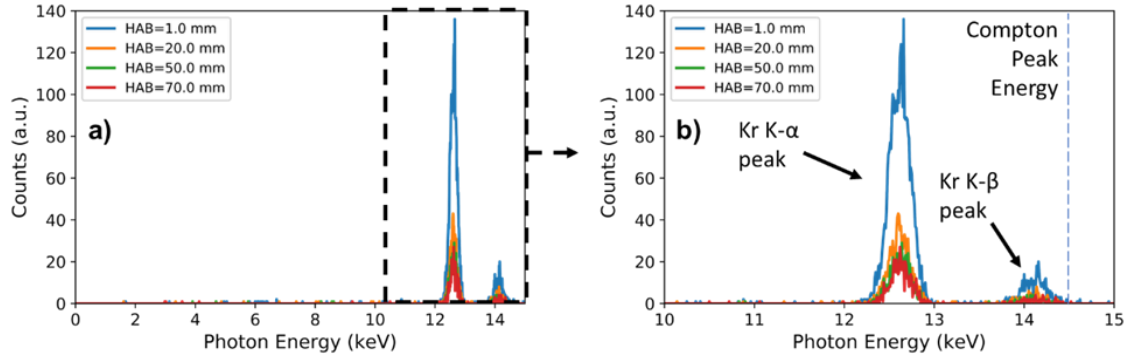


Figure 5-6: Measured detector as a function of photon energy, at various HABs in the flame. The incident photon energy was 15 keV. Figure 4a) shows the entire spectrum from 0 to 15 keV, while figure 4b) shows the region of the spectrum from 10 to 15 keV where the fluorescent signal was detected.

Shown in Figure 5-7 are the transmitted beam intensity and the radially integrated soot volume fraction profiles along the height of the flame. There was no significant difference in the transmitted beam intensity along the centerline, despite the soot volume fraction changing as the HAB varied (Fig. 5-7a). Given a constant incident beam intensity, these results suggest soot does not interfere with the absorption of incident 15 keV photons. In Figure 5-7c, the 2D scattering signal in the flame is shown, along with a plot showing the 2D soot concentrations for reference (Fig. 5-7b). The scattering signal is lowest towards the centerline of the flame, but gets larger towards the oxidizer side of the flame. The major contribution to the scattering signal is expected to be the Compton (inelastic) scattering, which itself is proportional to the electron density and hence temperature inside the flame (231). Thus, the larger scattering signal in the oxidizer region relative to the fuel is explained by the larger electron density found in the colder oxidizer region compared to the flame. By comparing the 2D soot concentrations to the scattering profile, it can be seen that the scattering signal inside the flame is unaffected by the presence of soot. Based on these results, it can be concluded that the measurement is free from interference due to soot in these nonpremixed CH_4 flames, and the measured signal is well-separated from any other types of interferences.

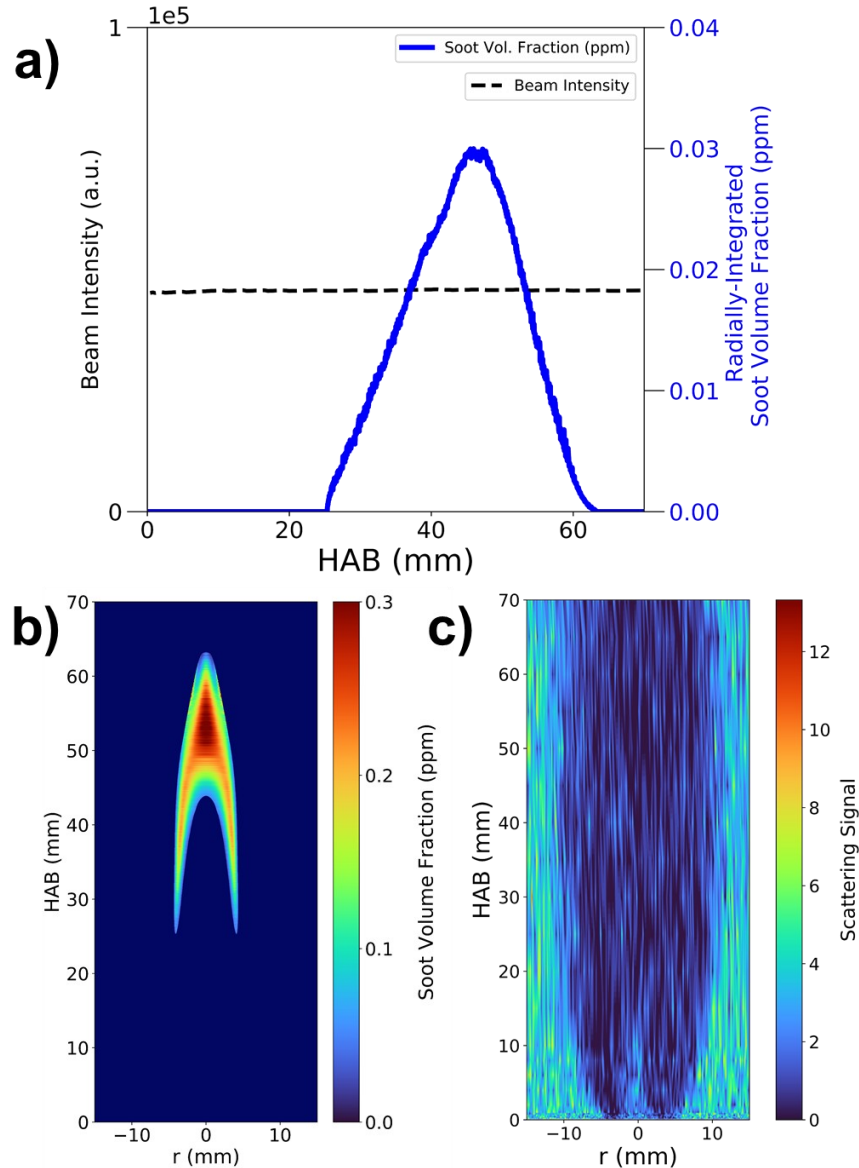


Figure 5-7: a) Radially-integrated soot volume fraction and transmitted beam intensity vs HAB b) 2D soot concentrations from ref. (224), for the same methane flame under study except without seeded krypton atoms, c) scattering profile in the Kr-seeded CH_4 flame

(3) Random Uncertainty

Additionally, the counting time for collecting fluorescent photons influences the resulting accuracy. Photon-counting processes can be modelled as a Poisson distribution, in which the signal-to-noise ratio (SNR) scales with \sqrt{n} , where n is the number of collected photons (252). Using $1/\sqrt{n}$ as a measure of the random uncertainty in the measurement, shown in Figure 5-8 is a plot of the percent-error attributable to Shot noise. The results show that the Shot noise is

responsible for 2% to 4.9% uncertainty in the measured signal. The uncertainty is largest in the wings and towards the tip of the flame, where the temperatures were highest and thus the collected signal was lowest. It should be noted that a detection time of 1 s was used for the two-dimensional temperature measurements, and so the random uncertainty in the measurements could be further reduced by increasing the photon-collection time.

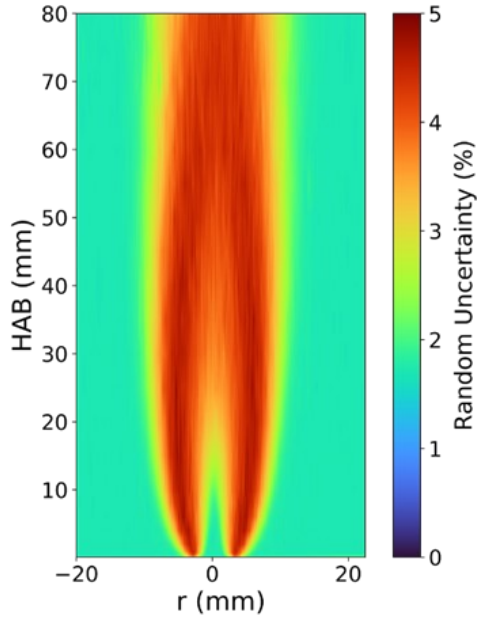


Figure 5-8: Random uncertainty in the experimental measurements attributable to photon Shot noise.

Based on these considerations, it is concluded that the main uncertainties governing the accuracy of the temperature measurements are due to 1) the assumption that the krypton mole fraction is constant throughout the flame and 2) the acquisition time for collecting the data. Based on the uncertainty introduced by variations in X_{Kr} ($\pm 1\%$ down to/up to $-3\%/+2\%$) and two standard deviations of the random uncertainty ($\sim 2-5\%$) we estimate a minimum (maximum) uncertainty of $-5\%/+5\%$ ($-13\%/+12\%$) in measured 2D temperatures. The minimum (maximum) uncertainty in the centerline measurements are estimated at $<\pm 1\%$ ($\pm 4\%$).

5.3.3 Spatially-Resolved Krypton Number Densities and Temperatures

Spatially-resolved krypton number-densities and temperatures were measured in a sooting methane/air co-flow diffusion flame seeded with krypton. The experimentally-measured

krypton number densities are displayed in Figure 5-9, along with the simulated profiles. The experimental and simulated temperatures are shown in Figure 5-10. Experimental and simulated radial plots at various HABs are also shown in each figure for comparison. The experimental 2D profiles show that the technique was able to successfully capture the shape of the flame, and had sufficient resolution to resolve sharp gradients in krypton number-densities and temperatures. The experimentally-measured profiles show outstanding agreement with the simulated results, demonstrating that the XRF technique was successful in retrieving temperatures in both sooting and non-sooting regions of the flame. It should also be noted that gas temperatures were obtained at HAB values as low as 100 microns. The radial plots reveal that the largest differences between the experimental and simulated values occur along the wings of the flame, and towards the centerline at higher HAB-values. This observation is due to the minor variations in the krypton mole fraction, as well as the high temperatures encountered in these regions of the flame, which results in a lower collected fluorescent signal and subsequently larger uncertainty from photon Shot noise.

Experimental and simulated centerline temperature profiles are shown in Figure 5-11. For these measurements, the collection time was increased from 1 s to 5 s. The centerline temperatures, as well as 2D temperature profiles, reveal that the gases along the centerline remain at room temperature until reactions begin to occur at ~10 mm HAB. The temperature then begins to increase at this point along the centerline, until the temperature peaks between ~60 to 70 mm HAB. This trend is also accurately predicted by the simulations. The predicted peak centerline temperature also matches well with the measured value, agreeing within <1.8%. It should be noted that above HAB=55 mm, minor noise is visible in the measured temperatures. This is attributable to uncertainty introduced by unavoidable temperature fluctuations/flickering in the flame at these regions, and could be better-resolved with a longer detection time.

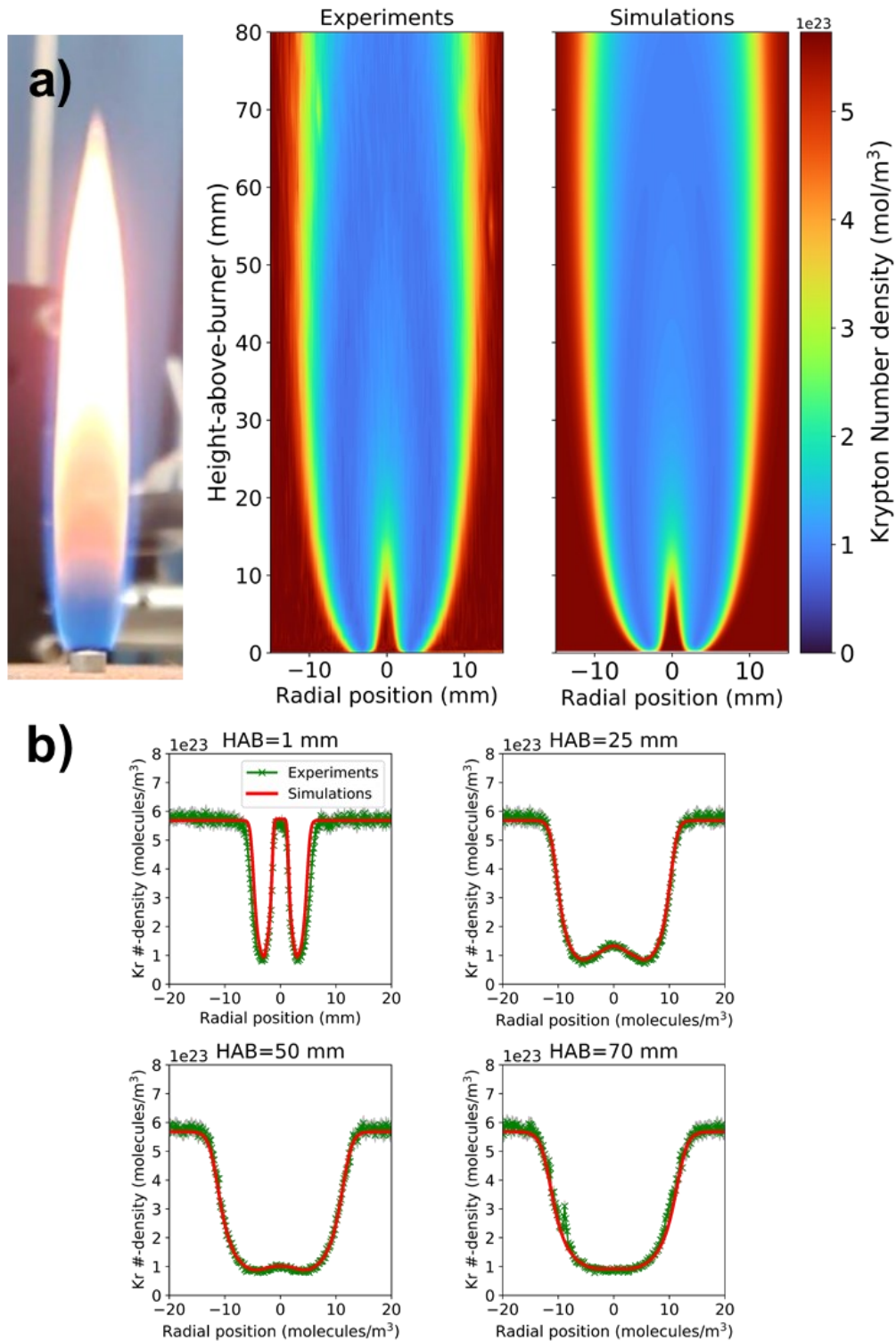


Figure 5-9: Krypton number-densities in the CH₄ flame a) Experimental and simulated two-dimensional krypton number density profiles in a sooting methane/air diffusion flame. An image of the flame is shown, to approximate scale. b) Radial profiles of the krypton number densities, at various heights in the flame. Error bars for the measurements are represented by the gray shaded regions.

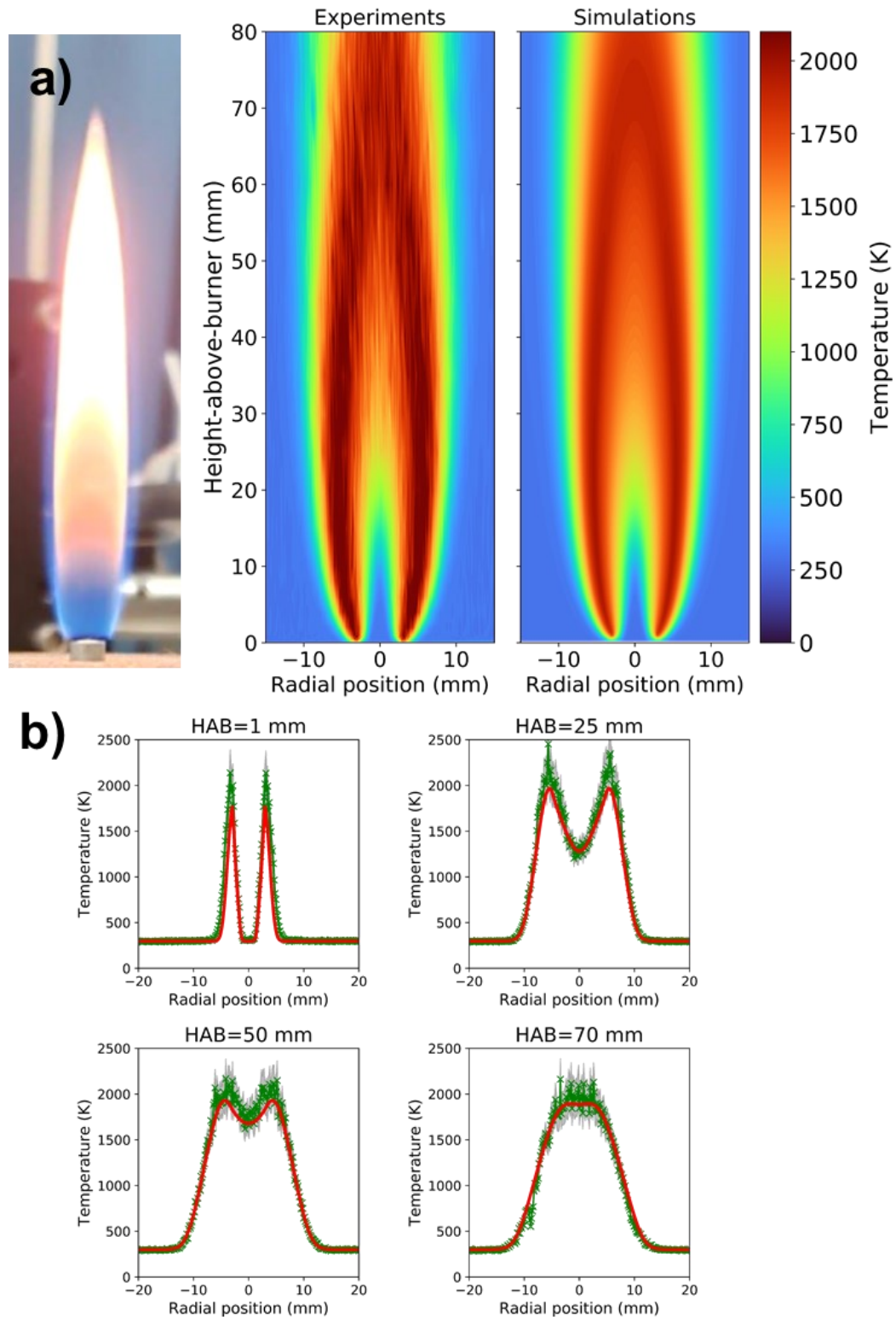


Figure 5-10: Temperatures in the CH_4 flame a) Experimental and simulated two-dimensional temperature profiles in a sooting methane/air diffusion flame. An image of the flame is shown, to approximate scale. b) Radial profiles of the temperatures, at various heights in the flame. Errors bars for the measurements are represented by the gray shaded regions.

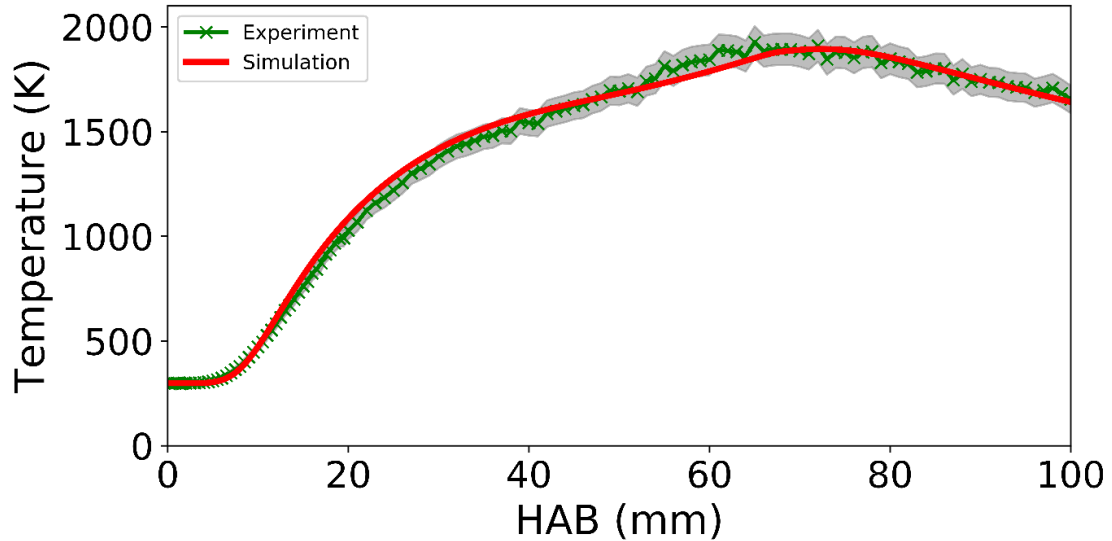


Figure 5-11: Centerline temperatures in a methane/air diffusion flame seeded with krypton atoms. The detection time for these experiments was 5 s. Errors bars for the measurements are represented by the gray shaded regions.

In combustion modelling of laminar flames, thermal boundary conditions are required as inputs, and have been assumed to be ambient temperature in past cases (182, 253-256) due to experimental difficulties in carrying out these measurements. Recent boundary condition thermometry measurements in diffusion flames using co-flow burners like the one under study, however, suggest that this may not be an accurate assumption (257). Accurately capturing thermal boundary conditions is important because uncertainties in these initial conditions can influence modelling results, such as predictions for peak flame temperature, flame shape, and emissions like soot concentrations (182, 256).

The XRF technique was able to measure flame temperatures as low as 100 microns above the burner surface. Previous studies have found that thermal boundary conditions measured with a thermocouple at an HAB of 100 microns strongly correlate with boundary conditions determined at the burner surface with phosphor thermometry (257). Based on this, it seems reasonable to conclude that the temperatures measured with the XRF technique at an HAB of 100 microns are correlated with those found at or near the burner surface. Likewise, temperatures predicted by the simulations at these near-burner HABs would be expected to

depend strongly on the thermal boundary conditions. By comparing the near-burner temperatures determined with XRF to the predicted values, one can gauge the accuracy of the thermal boundary conditions input to the simulations.

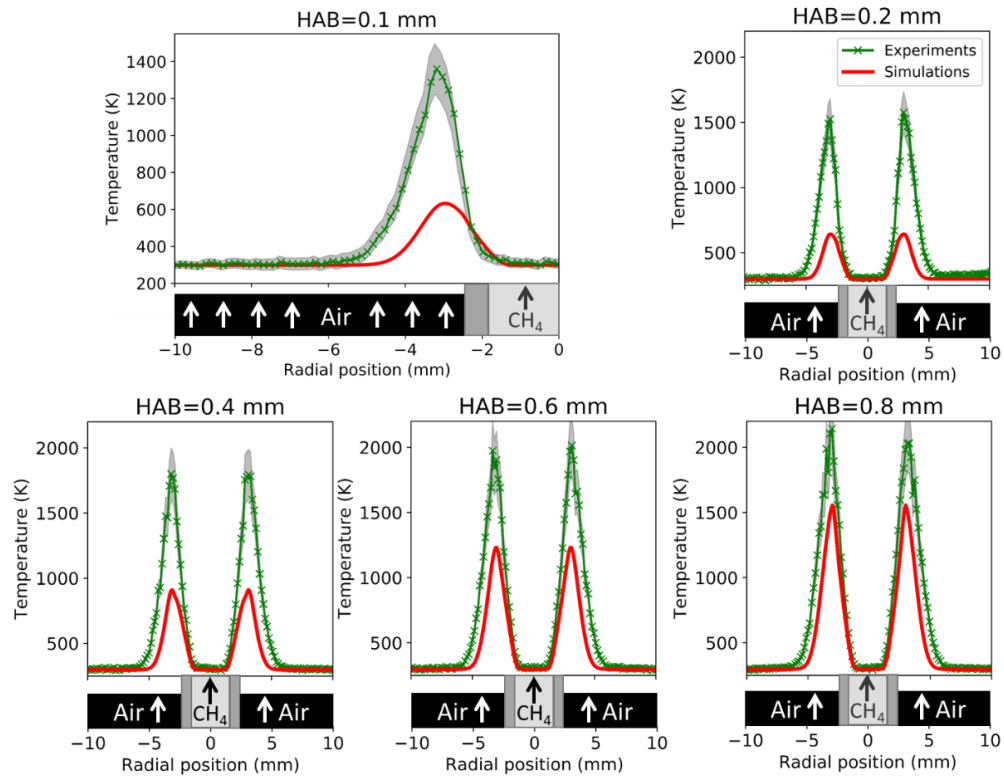


Figure 5-12: Radial profiles of near-burner temperatures, from HAB = 0.1 to 0.8 mm. Depictions of the burner/fuel tube are shown, to approximate scale in the radial direction. Errors bars for the measurements are represented by the gray shaded regions.

Radial plots of the near-burner temperatures measured with this technique are compared to the simulated temperatures in Figure 5-12. For this study, it should be noted that the thermal boundary conditions were taken as $T=298$ K in both the fuel and oxidizer. The measured and simulated profiles both show that the temperature peaks in the wings of the flames at a radial position of ± 3 mm, and increases rapidly as the HAB increases. The measured temperatures agree well with the predicted temperatures in the farther co-flow regions and right above the fuel tube, and reveal that the areas above the edge of the fuel tube are not at room temperature. The measured temperatures in the wings of the flame were found to be >100 K higher than those predicted by the simulations, which in part is attributable to experimental uncertainty.

However, the large differences that are evident at low HAB may suggest that the thermal boundary conditions are not accurately captured, and may require further experimental investigation to measure correctly. Despite the disagreement observed in near-burner temperatures, the simulated and experimental temperatures quickly converge at higher HAB (Figs. 5-10 and 5-11), and the overall flame shapes are well-matched.

5.4 Conclusions

In this work, the accuracy of 3D-resolved synchrotron X-ray fluorescence for measuring temperatures in sooting flames has been tested for the first time. The technique was validated in a non-reacting nitrogen jet, and it was found that the main uncertainties influencing the accuracy of the technique are those related to variations in the krypton mole fraction, as well as random uncertainty caused by Shot noise. The technique was found to be insensitive to the presence of soot, and was able to retrieve krypton number densities and temperatures in both non-sooting and sooting regions of the flame. The technique was also able to resolve sharp gradients in these variables, over a wide dynamic range. The simulated krypton number densities and temperatures were in overall great agreement with the measured values, with the largest disagreements observed in the wings near the burner surface. Near-burner temperatures were also retrieved and used to judge the suitability of the thermal boundary conditions used in the simulations. The results demonstrate the accuracy of this thermometry technique for sooting flames and its utility for validating predictive combustion models. These results also provide further evidence that the issues presented in Section 4 are attributed to the underlying chemical mechanism, as opposed to issues in capturing the flame physics.

6 Synchrotron X-ray Scattering as a Diagnostic for Measuring Mixture Fraction in Sooting Flames

Parts of this chapter are from manuscripts under preparation (see “Publications” section prior to Chapter 1, entry 6)

As was mentioned at the beginning of Section 5, the following section describes an X-ray technique for measuring physical quantities in nonpremixed flames, and can be directly compared to simulations to judge how well these phenomena are being captured. The following section reports on the use of X-ray scattering for obtaining information on fuel and oxidizer mixing in the flame. While the results presented here are for flames lacking N_2/NH_3 , they still provide useful validation targets for testing CFD models, and help ensure the model is capturing fundamental physics of the flame properly.

6.1 Background

In combustion studies, mixture fraction is an important variable that contains information on the local fuel-to-air equivalence ratio, and can be used to track the flame front, as well as to help determine other quantities such as scalar dissipation rates and reaction-progress variables. Mixture fraction is defined as the local mass fraction of all atoms in a region that is derived from the fuel stream, and is normalized in such a way that the mixture fraction in the oxidizer and fuel streams are 0 and 1. Given increasing concern over soot emissions from combustion systems (8, 28, 258, 259), there is pressure to develop fuels, burning strategies, and engine geometries that eliminate soot. To this end, experimental and computational researchers around the world have been developing diagnostics and computational tools to aid the development of these technologies. Experimental measurements studying the influence of mixture fraction on turbulent and laminar nonpremixed combustion (260-267) can be used to validate predictive models and ensure these parameters are captured accurately.

Experimental efforts to measure mixture fraction typically involve the use of UV/visible photons, and may require multiple scalar measurements. For instance, mixture fraction measurements have been obtained in laminar nonpremixed flames using a combination of depolarized and polarized Rayleigh scattering along with CO LIF (268). The depolarized and polarized Rayleigh signals yield information on the fuel concentration, while CO LIF provides higher sensitivity in regions where the Rayleigh signal is low. Raman scattering has been employed to measure major species concentrations in nonpremixed flames (269), and can be combined with Rayleigh thermometry measurements to calculate mixture fractions (270). High-speed laser-imaging techniques have also been developed to measure mixture fractions in nonreacting turbulent flows (266), but stability of certain tracers like acetone makes its use in reacting flows limited. Two-line laser-induced fluorescence (LIF) measurements have overcome this issue by using an inert tracer such as krypton (262, 265), however suffer from interferences in sooting regions of flames.

While gas-phase measurements using X-rays are challenging due to the low densities encountered, these difficulties are being overcome with the availability of intense X-ray sources, including synchrotrons. X-ray measurements, including inelastic scattering, absorption, and tomography, have been used to characterize major species, temperatures, and flow structures in gas-phase systems (230-232, 235, 242). X-ray fluorescence measurements using seeded argon and krypton atoms have also been used to measure mixture fractions in co-flow jet flames (260). To our knowledge, X-ray scattering has never been used to obtain mixture fraction measurements in reacting flows. X-rays have particular advantages compared to techniques which rely on UV/visible light, including that the high-energy X-rays interact primarily with individual atoms rather than molecules as a whole (235). This is beneficial for measuring properties that depend on atomic composition rather than molecular composition, such as mixture fraction. The index of refraction for X-rays is also very close to one (236), so that there is little scattering at phase

boundaries, such as between soot particles and gas molecules. This makes X-ray scattering an intriguing technique for overcoming issues with interferences from particles that UV/visible techniques may face. The X-ray scattering technique reported here, however, requires a steady flow because point-data with micron-order resolution is collected, and cannot be used in turbulent flows. This also makes acquiring 2D sets of longer than other one-shot mixture fraction imaging techniques (262, 265, 266).

Herein, we report on the use of synchrotron X-ray scattering to obtain mixture fractions in nonpremixed methane/air co-flow flames. The specific burner used for these experiments has been chosen as an official geometry for testing numerical combustion models (112). Among other studies, flames generated with this burner are being used to characterize and validate sooting tendencies and reaction pathways of advanced biofuels (127, 130, 133, 166, 193, 248, 249). The technique is first demonstrated in a nonpremixed CH₄/air flame generated with this burner, and further extended to an argon-diluted CH₄/air flame. Simulations are performed, and compared to the experimental measurements to judge the uncertainties in the X-ray scattering measurements

6.2 Methodology

6.2.1 Theory Relating X-Ray Scattering to Mixture Fraction

Mixture fractions were measured via the following steps: (1) The elastic and inelastic synchrotron X-ray scattering signals were measured at different points in a nonpremixed CH₄/air diffusion flame; (2) The ratio of the elastic to inelastic signal was obtained; (3) The ratio of the scattering signals was used to calculate the atomic percentage of carbon at a particular location, from which mixture fraction could be retrieved.

X-ray scattering as implemented in this study involves two types of scattering events (271, 272). An incident photon at 15 keV is directed to a particular position in the flame, and can

either elastically or inelastically scatter off of the atoms at this position. In the case of elastic scattering, the X-ray interacts with the electron cloud surrounding the atom, and the atom emits radiation at the same energy. In the case of inelastic scattering events, known as Compton scattering, the X-ray interacts with individual electrons of the atom, resulting in momentum and energy transfer between the incident photon and electrons. The detection of these elastically and inelastically scattered photons is the goal of these experiments. For atoms, the atomic cross sections for elastic and inelastic scattering can be given by:

$$\frac{d_a\sigma}{d\Omega_{elastic}} = \left(\frac{d_e\sigma}{d\Omega}\right)_{Thomson} F^2(x, z) \quad (1)$$

$$\frac{d_a\sigma}{d\Omega_{inelastic}} = \left(\frac{d_e\sigma}{d\Omega}\right)_{KN} S(x, z) \quad (2)$$

where $(d_e\sigma/d\Omega)_{Thomson}$ and $(d_e\sigma/d\Omega)_{KN}$ are the Thomson and Klein-Nishina electron cross-sections, $F(x,z)$ is the atomic form factor, and $S(x,z)$ is the incoherent scattering function. The functions $F(x,z)$ and $S(x,z)$ range from 0 up to Z , and correct the cross-sections for the fact that an electron is bound to a particular type of atom governed by its atomic number Z . The functions also depend on the momentum transfer x , given by

$$x = \frac{\text{Sin}(\theta/2)}{\lambda} \quad (3)$$

where θ is the scattering angle and λ is the wavelength of the incident beam. For a given experimental setup, the signal from elastically (S_{el}) or inelastically (S_{inel}) scattered photons measured by a detector can be given by:

$$S_{el} = e^{\mu(E_0)L_i} \times \left(\frac{d_e\sigma}{d\Omega}\right)_{Thomson} F^2(x, z) \times \Delta\Omega\Delta LN_0 n_{at} \times e^{\mu(E_0)L_s} \quad (4)$$

$$S_{inel} = e^{\mu(E_0)L_i} \times \left(\frac{d_e\sigma}{d\Omega}\right)_{KN} S(x, z) \times \Delta\Omega\Delta LN_0 n_{at} \times e^{\mu(E')L_s} \quad (5)$$

where N_0 is the number of incident photons, n_{at} is the number of atoms per unit volume, μ is the attenuation coefficient, $\Delta\Omega$ is the solid angle of the detector seen from the probe volume,

ΔL is the length of the sample volume in the direction of the incident beam, E_o (E') is the incident (scattered) photon energy, and L_i (L_s) is the path length along the incident (scattered) beams. If the elastic and inelastic signals are measured under the same experimental conditions, then the ratio of the two signals can be taken to obtain:

$$\frac{S_{el}}{S_{inel}} = \frac{\left(\frac{d_e\sigma}{d\Omega}\right)_{Thomson} F^2(x, z) \times e^{\mu(E_o)L_s}}{\left(\frac{d_e\sigma}{d\Omega}\right)_{KN} S(x, z) \times e^{\mu(E')L_s}} \quad (6)$$

Note that the ratio does not depend on the temperature in the probe volume. If θ and E_o are chosen such that the scattered photon energy is close to the incident photon energy, the quantities $e^{\mu(E_o)L_s}$ and $e^{\mu(E')L_s}$ are roughly similar, so that the ratio can be simplified to:

$$\frac{S_{el}}{S_{inel}} = \frac{\left(\frac{d_e\sigma}{d\Omega}\right)_{Thomson} F^2(x, z)}{\left(\frac{d_e\sigma}{d\Omega}\right)_{KN} S(x, z)} \quad (7)$$

Furthermore, the above equation can be generalized to mixtures containing multiple elements by assuming the form factor and incoherent scattering function of the mixture is represented by a linear combination of the atomic $F(x, z)/S(x, z)$, weighted by their atomic percentage α_i^{at} in the mixture:

$$\frac{S_{el}}{S_{inel}} = \frac{\left(\frac{d_e\sigma}{d\Omega}\right)_{Thomson} F^2(x, z)}{\left(\frac{d_e\sigma}{d\Omega}\right)_{KN} S(x, z)} = c * \frac{\sum_i \alpha_i^{at} F^2(x, z_i)}{\sum_i \alpha_i^{at} S(x, z_i)} \quad (8)$$

Thus, for a certain experimental setup, the elastic-to-inelastic scattering ratio depends only on the atomic composition. The values for $F(x, z_i)$ and $S(x, z_i)$ used in this study were taken from reference (271) for $x=1.0$, which is close to the value of $x=1.05$ used in this study ($\theta=120^\circ$, $E_o=15$ keV), and are displayed in Table 6-1. The constant c can be determined by measuring the scattering ratio in a region with known atomic composition. To obtain mixture fractions from equation (8), further constraints need to be imposed on the values of α_i^{at} , which are determined

by the particular flow setup. For a nonpremixed pure methane flame using air (assumed to be composed of only nitrogen, oxygen, and argon) as oxidizer, these constraints include:

$$\alpha_{Ar}^{at} + \alpha_O^{at} + \alpha_N^{at} = 1 - \alpha_C^{at} - \alpha_H^{at} \quad (9)$$

$$\alpha_H^{at} = 4\alpha_C^{at} \quad (10)$$

$$\alpha_N^{at} = \alpha_N^{ox}(1 - \alpha_C^{at} - \alpha_H^{at}) = \alpha_N^{ox}(1 - 5\alpha_C^{at}) \quad (11)$$

$$\alpha_O^{at} = \alpha_O^{ox}(1 - \alpha_C^{at} - \alpha_H^{at}) = \alpha_O^{ox}(1 - 5\alpha_C^{at}) \quad (12)$$

$$\alpha_{Ar}^{at} = \alpha_{Ar}^{ox}(1 - \alpha_C^{at} - \alpha_H^{at}) = \alpha_{Ar}^{ox}(1 - 5\alpha_C^{at}) \quad (13)$$

where α_i^{at} is the atomic percentage of species *i* at a particular location in the flame, and α_i^{ox} is the known atomic percentage of species *i* in the oxidizer. These constraints assume no preferential diffusion of lighter atoms in the flame, so that the atomic ratios of certain atoms are dictated by the fuel and oxidizer compositions. Constraints (9)-(13) can be used to solve equation (8) for α_C^{at} as a function of S_{el}/S_{inel} . Solving these equations using Mathematica (273) leads to the following expression:

$$\alpha_C^{at} = \frac{c * 1.183 * 10^{27} - 4.284 * 10^{27} * S_{el}/S_{inel}}{c * 5.076 * 10^{27} + 1.508 * 10^{28} * S_{el}/S_{inel}} \quad (14)$$

From these values of α_C^{at} obtained from the ratios S_{el}/S_{inel} , the mixture fraction for the pure CH₄/air flame is calculated as:

$$\begin{aligned} MF &= \frac{\alpha_C^{at} * M_C + \alpha_H^{at} * M_H}{\alpha_C^{at} * M_C + \alpha_H^{at} * M_H + \alpha_N^{at} * M_N + \alpha_O^{at} * M_O + \alpha_{Ar}^{at} * M_{Ar}} \quad (15) \\ &= \frac{\alpha_C^{at} * M_C + 4\alpha_C^{at} * M_H}{\alpha_C^{at} * M_C + 4\alpha_C^{at} * M_H + \alpha_N^{ox}(1 - 5\alpha_C^{at}) * M_N + \alpha_O^{ox}(1 - 5\alpha_C^{at}) * M_O + \alpha_{Ar}^{ox}(1 - 5\alpha_C^{at}) * M_{Ar}} \end{aligned}$$

where M_i is the atomic mass of element *i*. Constraints (9)-(13) and equation (14) can be modified to accommodate mixture fraction measurements in flows with other fuel/oxidizer compositions.

Table 6-1: Atomic form factors, incoherent scattering functions, and other relevant atomic properties used in this study. Values for F(x,z) and S(x,z) come from reference (271) , for x=1.0

Element	Atomic Number Z	Atomic mass (amu)	Atomic Form Factor F(x,Z)	Incoherent Scattering Function S(x,Z)
Hydrogen	1	1.008	0.0068811	0.99995
Carbon	6	12.011	1.1121	5.3485
Nitrogen	7	14.007	1.2620	6.1130
Oxygen	8	15.999	1.3763	6.9010
Argon	18	39.948	4.4433	13.629

For the argon-diluted methane flames, equations (9) thru (13) need to be modified to account for the addition of another element to the fuel, as well as for the fact that argon is present in both the oxidizer and fuel streams. The volume ratio of Ar to CH₄ in the fuel is 1:1, so that we have:

$$\alpha_{Ar}^{at,ox} + \alpha_O^{at} + \alpha_N^{at} = 1 - \alpha_C^{at} - \alpha_H^{at} - \alpha_{Ar}^{at,f} \quad (16)$$

$$\alpha_H^{at} = 4\alpha_C^{at} \quad (17)$$

$$\alpha_{Ar}^{at,f} = \alpha_C^{at} \quad (18)$$

$$\alpha_O^{at} = \alpha_O^{ox}(1 - \alpha_C^{at} - \alpha_H^{at} - \alpha_{Ar}^{at,f}) = \alpha_O^{ox}(1 - 6\alpha_C^{at}) \quad (19)$$

$$\alpha_N^{at} = \alpha_N^{ox}(1 - \alpha_C^{at} - \alpha_H^{at} - \alpha_{Ar}^{at,f}) = \alpha_N^{ox}(1 - 6\alpha_C^{at}) \quad (20)$$

$$\alpha_{Ar}^{at,ox} = \alpha_{Ar}^{ox}(1 - \alpha_C^{at} - \alpha_H^{at} - \alpha_{Ar}^{at,f}) = \alpha_{Ar}^{ox}(1 - 6\alpha_C^{at}) \quad (21)$$

where $\alpha_{Ar}^{at,f}$ and $\alpha_{Ar}^{at,ox}$ are the local atomic concentrations of argon derived from the fuel and oxidizer. Solving (8) using constraints (16) thru (21) yields:

$$\alpha_C^{at} = \frac{-c * 1.568 * 10^{36} - 5.680 * 10^{36} * S_{el}/S_{inel}}{c * 9.461 * 10^{27} + 1.341 * 10^{37} * S_{el}/S_{inel}} \quad (22)$$

For the argon-diluted methane flame, the corresponding expression for mixture fraction is given as:

$$MF = \frac{\alpha_C^{at} * M_C + \alpha_H^{at} * M_H + \alpha_{Ar}^{at,f} * M_{Ar}}{\alpha_C^{at} * M_C + \alpha_H^{at} * M_H + \alpha_N^{at} * M_N + \alpha_O^{at} * M_O + \alpha_{Ar}^{at} * M_{Ar}} \quad (23)$$

$$= \frac{\alpha_C^{at} * M_C + 4\alpha_C^{at} * M_H + \alpha_{Ar}^{at,f} * M_{Ar}}{\alpha_C^{at} * M_C + 4\alpha_C^{at} * M_H + \alpha_N^{ox}(1 - 6\alpha_C^{at}) * M_N + \alpha_O^{ox}(1 - 6\alpha_C^{at}) * M_O + (\alpha_{Ar}^{ox} + \alpha_{Ar}^{at,f})(1 - 6\alpha_C^{at}) * M_{Ar}}$$

6.2.2 Burner and Flame Details

In this study, nonpremixed flames containing methane as the base fuel were generated with a Yale co-flow burner (112). The flow rates used in this study are detailed in Table 1. For all experiments, the reactants either flowed from 99.99%+ purity cylinders (fuel-CH₄, fuel-Ar), or an air compressor (oxidizer-air). The flow rates of fuel-CH₄, fuel-Ar, and oxidizer-air were controlled with FMA5400/5500 Omega thermal mass flow controllers. A chimney made of Kapton tape (5 mil) surrounded the flame, and served to minimize perturbations due to stray air currents.

Table 6-2: Experimental flow rates for gas mixtures analyzed in the X-ray scattering study

Atmospheric nonpremixed CH₄ flame		
Fuel		Oxidizer
CH₄ (mL/min)		Air (L/min)
330		50.0

Atmospheric nonpremixed Ar/CH₄ Flame		
Fuel		Oxidizer
CH₄ (mL/min)	Ar (mL/min)	Air (L/min)
165	165	50.0

6.2.3 X-ray Source and Computational Methods

The X-ray source implemented in this work is the same as that for the XRF work, and is described in more detail in section 5.2.3. The main difference for these measurements is that the detector was placed at 120° to the incident x-ray beam in the horizontal plane, instead of 90° as was used for the XRF measurements to enhance the X-ray scattering signal measured by the detector. The computational methods are also the same as were implemented for the XRF work, and are described in more detail in section 5.2.4.

6.3 Results and Discussion

6.3.1 Mixture Fraction Results in a Methane/Air Flame

To obtain mixture fractions, synchrotron X-ray scattering measurements were first taken at varying positions in the flame. Radial profiles of the elastic and inelastic scattering signals at varying heights in the nonpremixed CH₄/air flame are shown in Figure 6-1. The inelastic scattering signal was found to be stronger than the elastic scattering signal for all positions analyzed. It should be noted that the angle of the detector was set to $\theta=120^\circ$ and the incident photon energy was 15 keV, corresponding to a momentum transfer of $x=1.05$ (equation 3). For x near these values, each $S(x,z_i)$ is larger than the corresponding $F(x,z_i)$ (Table 6-3) (271), so that the inelastic scattering cross section is larger than that for elastic scattering (equation (1) and (2)). Both the elastic and inelastic scattering signals varied with the radial position, with the largest differences observed at earlier HAB. The signals obtained at farther radial positions

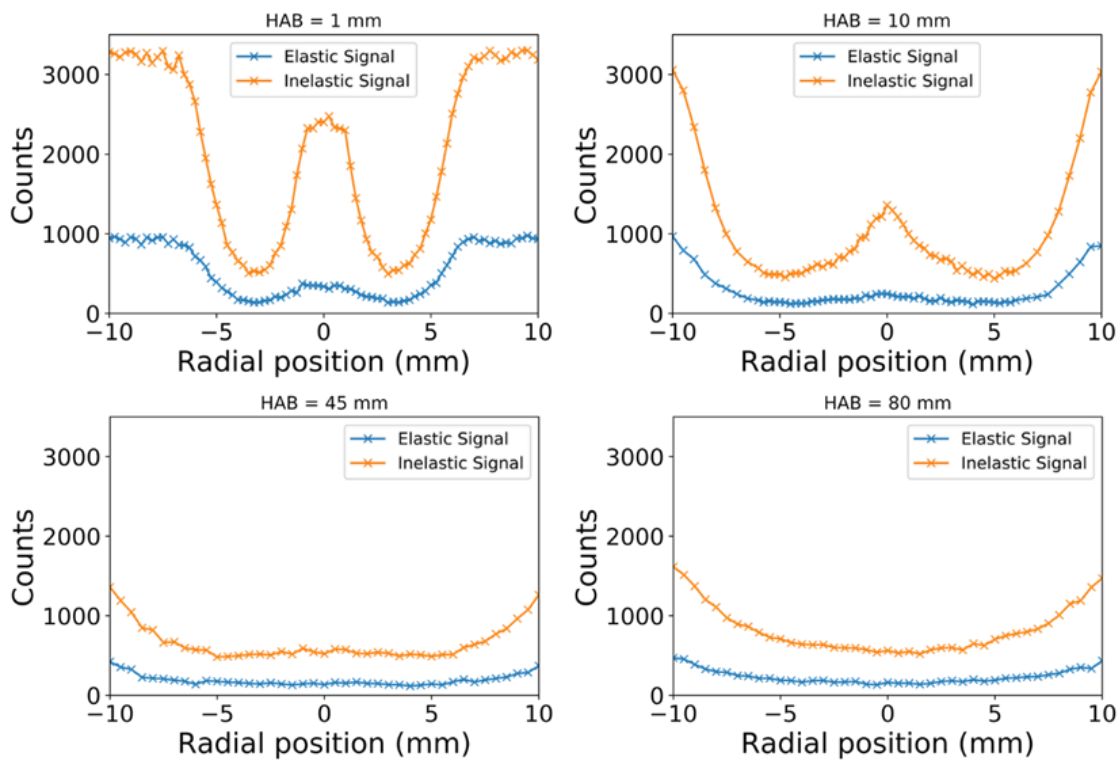


Figure 6-1: Radial profiles of elastic and inelastic scattering signals at various heights in the CH₄/air flame.

correspond to the oxidizer region of the flame, and was found to be larger than the signals near the centerline. The lowest signals were retrieved from the wings of the flame ($r=\pm 3$ mm). The observation that the scattering signal is larger at farther radial positions than near the centerline can be attributed to the higher electron density found in the oxidizer relative to the fuel stream. The electron density is also proportional to temperature (231), and so the high temperatures encountered in the wings of the flames is responsible for the lower observed signals. Using $1/\sqrt{n}$ as a measure of the uncertainty in the photon-detection process (252), where n is the number of collected photons, we estimate that the random error in the calculated elastic-to-inelastic ratios is $\pm 13\%$ in the wings of the flame, and $\pm 5\%$ in oxidizer regions.

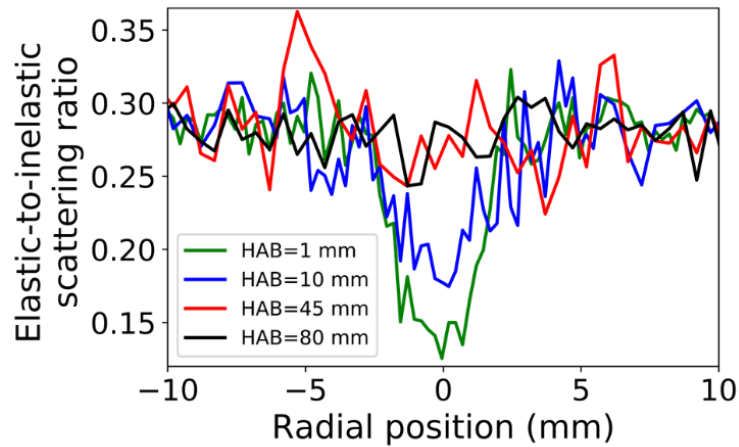


Figure 6-2: Experimental elastic-to-inelastic scattering ratios for CH_4/air , at various heights above the burner surface (HABs).

The elastic-to-inelastic ratios were determined (Fig. 6-2), and it is clear that from the ratio of the signals that the temperature-dependencies evident in Figure 6-1 cancel out, leaving the ratio to only vary as a function of local atomic composition. From this, the mixture fractions could be calculated as per equation (14). Radial plots of the mixture fractions determined from the experimental scattering measurements are shown in figure 6-3, along with simulated profiles for comparison. The simulations show that mixture fractions near the centerline generally decrease as the HAB increases, which is attributed to increased mixing between the fuel and oxidizer at higher HAB. This trend is also captured in the experimental measurements. The peak

mixture fraction and overall shape of the radial profiles are well matched at earlier HAB; however, noise in the measurement is large at higher HAB such that no conclusions can be drawn from these plots. A centerline plot of the experimental and simulated mixture fractions is displayed in figure 6-4. The simulations show that the fuel doesn't mix with the oxidizer until \sim HAB=10 mm, at which point the mixture fraction begins to decrease along the centerline. The experimental mixture fractions also exhibit this trend, and the shape of the overall centerline curve is in satisfactory agreement with the simulations. Uncertainty that is present in the experimental measurements, attributed to Shot noise, could be reduced through longer photo-collection times. This could help to resolve features such as the stoichiometric mixture fraction ($Z_{st}=0.055$ for nonpremixed CH_4/air flames) (274).

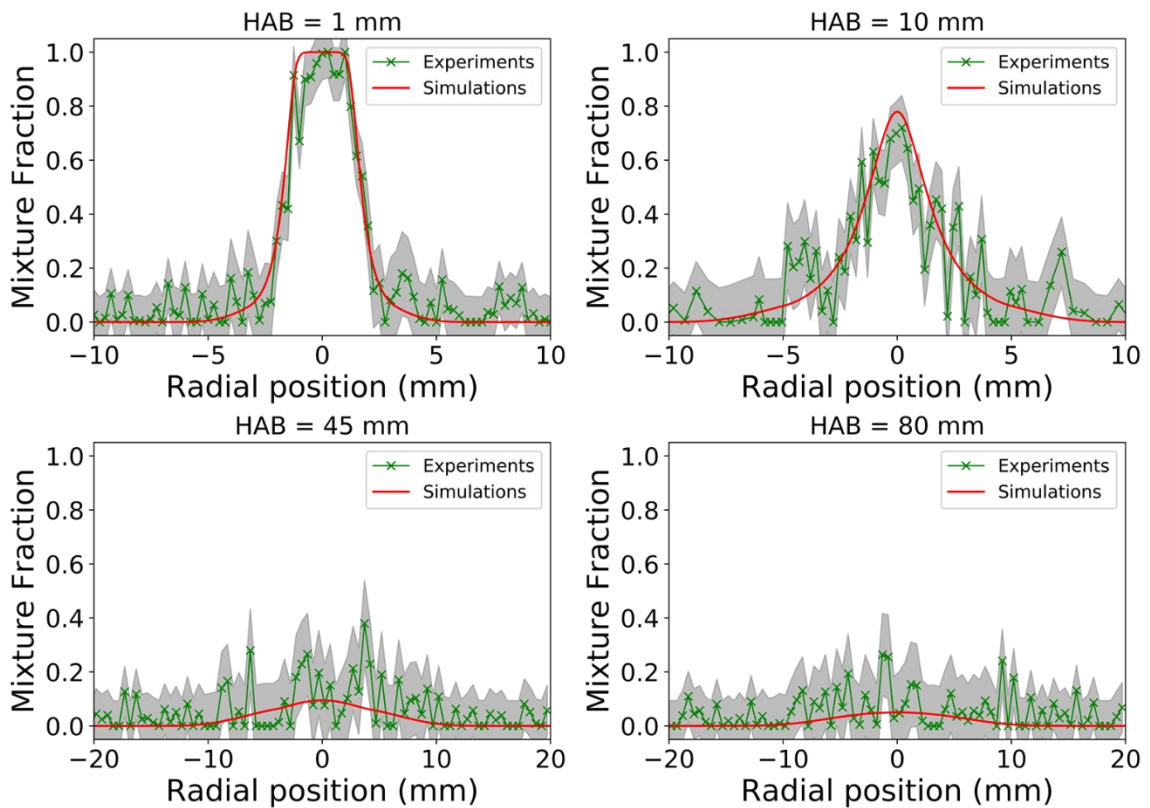


Figure 6-3: Radial profiles of measured and simulated mixture fractions, at various heights in the flame. Uncertainties, based on two standard deviations of the photon Shot noise and uncertainty in atomic form factors/incoherent scattering functions, are represented by the gray shaded regions

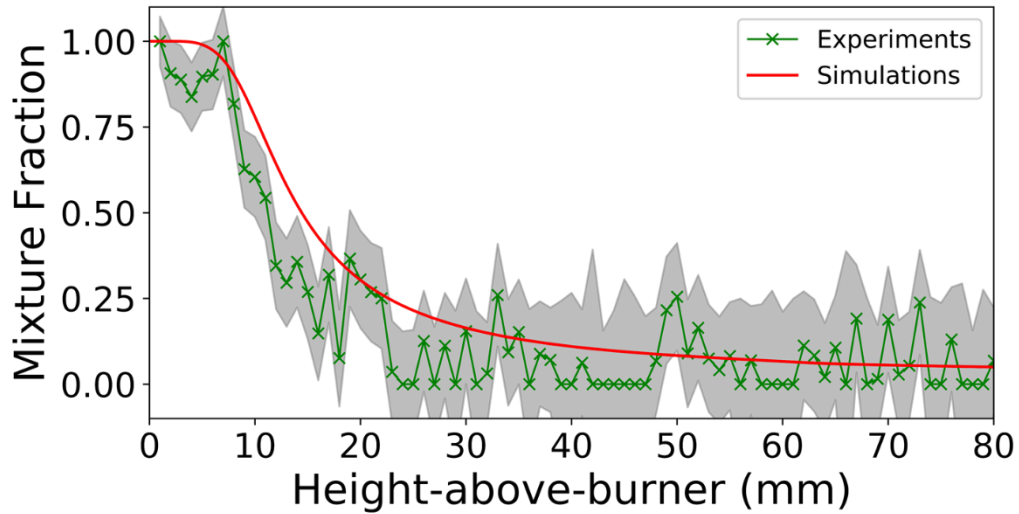


Figure 6-4: Centerline mixture fractions for the CH₄/air flame. Uncertainties, based on two standard deviations of the photon Shot noise and uncertainty in atomic form factors/incoherent scattering functions, are represented by the gray shaded regions

6.3.2 Preliminary Results in an Argon-diluted Methane/Air Flame

Preliminary measurements were also obtained in an argon-diluted methane/air flame. The elastic-to-inelastic ratios determined at various heights in this flame are displayed in Figure 6-5. Similar to the results in Figure 6-2, it is again clear that any temperature-dependence of the signals cancel when taking their ratios. Unlike the scattering ratios observed in Figure 6-2, however, the scattering ratio in the fuel region was higher than that observed in the oxidizer. This reflects the addition of argon to the fuel stream, which interacts more strongly with incident X-rays than C, H, O, and N atoms. The change in scattering cross-section induced by diluting the fuel with argon has the combined effect of increasing the scattering ratio relative to pure CH₄ and air mixtures.

Mixture fractions in the Ar/CH₄ flame are reported in Figure 6-6, at HAB values of 1 mm and 5 mm. The simulated and measured mixture fractions at these heights show excellent agreement. Compared to the results in Figure 6-3, there is less scatter in the experimental measurements, which is particularly evident by comparing mixture fractions in the co-flow regions. Since there is a much smaller difference in the scattering ratio between the fuel and

oxidizer in the pure CH₄ flame (Fig. 6-3) relative to the Ar-diluted flame (Fig. 6-5), uncertainty in scattering ratios may lead to larger uncertainties in mixture fractions obtained for the pure CH₄ flame relative to the Ar-CH₄ flame. This may explain the lower noise in mixture fractions measured for the Ar-diluted flame relative to the pure CH₄ flame. While the simulations and measurements show good agreement at early heights in the flame, further work is required to test the agreement at higher HAB. Nonetheless, the results presented here and in the previous section suggest that XRS can be used to obtain mixture fraction measurements from nonpremixed flame configurations.

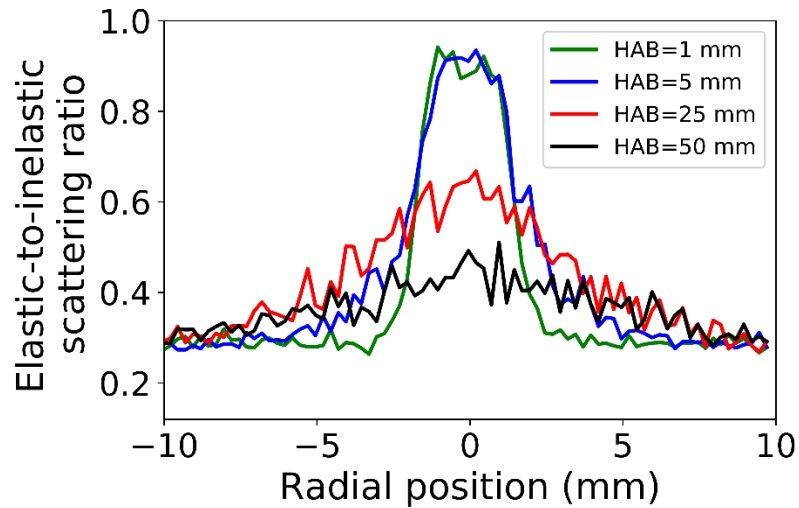


Figure 6-5: Experimental elastic-to-inelastic scattering ratios for the Ar-diluted CH₄/air flame, at various heights above the burner surface (HABs).

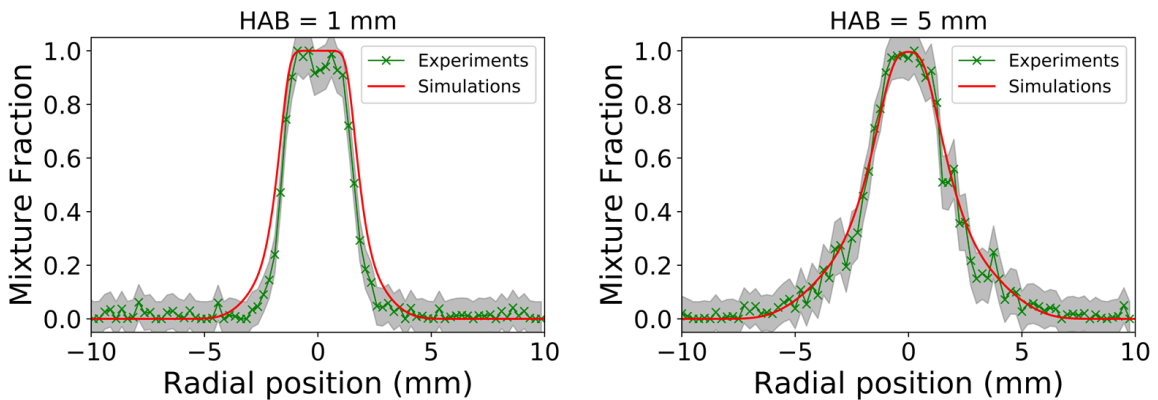


Figure 6-6: Radial profiles of mixture fraction measured for the nonpremixed Ar-CH₄/air flame, at various heights above the burners

6.3.3 Uncertainties

One source of error in the experimental calculations is the assumption that there is no preferential diffusion of lighter atoms occurring in the flame. Shown in figure 6-7 is a plot of the atomic carbon concentrations versus mixture fraction, calculated using equation (14). A scatter plot of the simulated atomic carbon concentrations and mixture fractions are also shown. Since the simulations capture effects due to preferential species diffusion, this comparison allows us to judge how much uncertainty is present in the experimental assumptions in equation (14). The results show that the simulated mixture fractions fall tightly around the theoretical curve used to map measured atomic carbon concentrations to mixture fraction. Based on these results, the experimental assumption of no preferential diffusion of lighter atoms is expected to introduce negligible uncertainty relative to other sources of error.

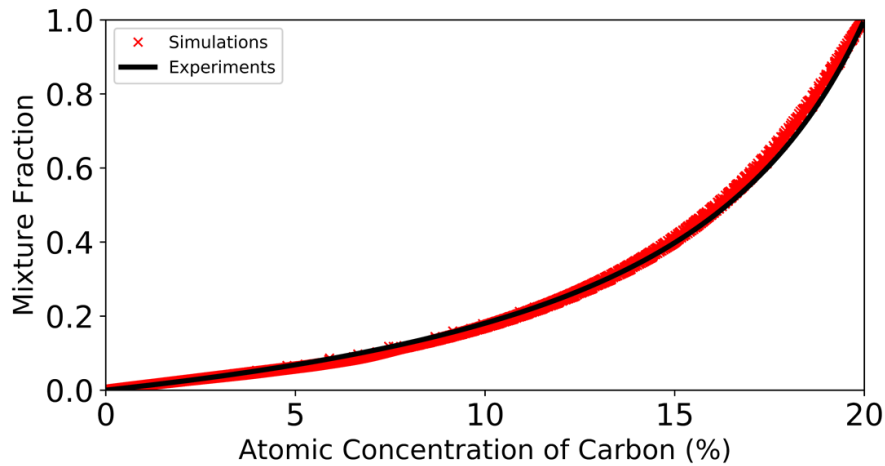


Figure 6-7: Theoretical curve used to map measured atomic carbon concentrations to mixture fraction, compared to the simulated results.

There is also uncertainty inherent in the use of atomic form factors and incoherent scattering functions used in this study. The values for $F(x,z)$ and $S(x,z)$ come from reference (271) for a momentum transfer of $x=1.0$, which is close to the value of $x=1.05$ used in this study. To try and ascertain the degree to which the form factors and incoherent scattering functions influence the results, the mixture fractions were also calculated using $F(x,z)$ and $S(x,z)$ for $x=0.9$

Table 6-3: Atomic form factors and incoherent scattering functions for other values of x . Values were obtained from reference (271)

Element	Atomic Number Z	$x=0.90$		$x=1.0$		$x=1.25$	
		F(x,z)	S(x,z)	F(x,z)	S(x,z)	F(x,z)	S(x,z)
Hydrogen	1	0.010091	0.99990	0.0068811	0.99995	0.0029947	0.99999
Carbon	6	1.2165	5.2085	1.1121	5.3485	0.86482	5.6153
Nitrogen	7	1.3521	5.9680	1.2620	6.1130	1.0456	6.4571
Oxygen	8	1.4623	6.7750	1.3763	6.9010	1.1820	7.2159
Argon	18	5.0165	13.061	4.4433	13.629	3.2318	14.4745

and $x=1.25$ (Table 6-3). The results show that the overall mixture fraction profiles are largely unaffected when calculated using $F(x,z)/S(x,z)$ values for $x=0.90$ and $x=1.0$ (Fig.6-8). When calculated using values for $x=1.25$, the absolute values of the mixture fraction are calculated to be ~ 0.1 higher in the oxidizer and ~ 0.1 lower near the centerline relative to the $x=0.90/x=1.0$ cases. Since $x=1.0$ is only $\sim 5\%$ different than the value used in this study, the absolute error in mixture fractions from using form factors for values of $x=1.0$ is expected to be smaller than ± 0.1 .

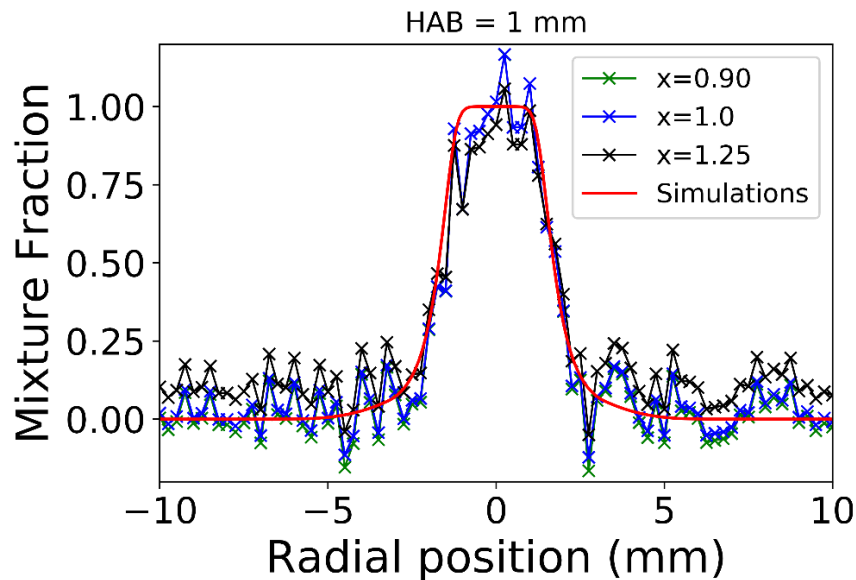


Figure 6-8: Mixtures fractions determined at HAB = 1 mm in the CH_4/air flame, for varying values of $F(x,z)/S(x,z)$.

Other possible sources of error in the experimental measurements include uncertainties due to fluctuations in flow rates, uncertainties due to unavoidable temperature/spatial

fluctuations in the flame, and uncertainty introduced from assuming the incident X-rays interact with molecules as if they were mixtures of independent atoms (see equation 8). These sources of uncertainty are still under consideration, and are currently being investigated.

6.4 Conclusions

In this work, the use of X-ray scattering as a diagnostic for probing mixture fractions in sooting methane/air diffusion flames was tested for the first time. Mixture fractions in a pure CH₄/air flame were measured with this technique, and showed satisfactory agreement with simulated results. Preliminary mixture fraction measurements were also obtained in an argon-diluted CH₄ flame, and showed excellent agreement with mixture fractions determined by the simulations. While uncertainties in the experimental measurements still need to be addressed, these results provide evidence that X-ray scattering can potentially be applied to retrieve spatially-resolved mixture fraction measurements in nonpremixed flame configurations. With further development, the data generated by this technique could provide stringent validation targets for predictive combustion models.

7 Validating the applicability of YSI Under Different Temperatures and Air-to-Fuel Ratios

The contents of this chapter have been published previously in The Proceedings of the Combustion Institute (see “Publications” section prior to Chapter 1, entry 7)

The results presented in the following section are intended to extend the applicability of the YSI to partially-premixed flames. As was described in Section 3, the YSI is determined by doping a nonpremixed flame with a small concentration of a test compound. In partially-premixed combustion, as might be encountered in a gasoline direct injection engine, the fuel is mixed with oxidizer before burning. While the results presented here only focus on hydrocarbons, they may give insight into whether the measured trends in YSIs from section 3 hold under partially-premixed cases. If nitrogen-containing compounds/ NH_3 are used as future fuels, then an understanding of their sooting tendencies in premixed situations may be required.

7.1 Background

One issue with most sooting tendency measurements is that they are performed under a very limited set of flame conditions, whereas in real devices parameters such as the air-to-fuel equivalence ratio (λ) and characteristic temperature vary significantly (275, 276). This calls into question the applicability of these sooting tendency measures in the development of combustion technologies, since sooting indices determined under one set of these parameters may not extend to another set of conditions. For instance, the smoke point of a fuel is a measure of sooting tendency that is based on experiments performed in a wick lamp, and it is difficult to assess the effect of partial premixing or temperature changes because the wick lamps traditionally used in these measurements (110) do not allow these parameters to be systematically varied.

For sooting indices to be used in applications such as developing surrogate fuels aimed at accurately capturing the sooting tendency of a real fuel or in aiding the transition to cleaner engines and fuels, robust measures that can accurately describe the sooting behavior of fuels across a wide range of combustion conditions are necessary. The objective of this research is therefore to assess whether YSI is consistent across a range of combustion conditions relevant to soot formation in a series of doped nonpremixed and partially premixed flames. The combustion conditions varied in this work include λ and the adiabatic flame temperature T_{ad} . The fuels tested include three cyclic hydrocarbons and three jet fuels. The cyclic hydrocarbons were methylcyclopentane, cyclohexane, and cyclohexene. They were chosen based on the hypothesis that their sooting behavior would be particularly sensitive to changes in λ since their chemical consumption mechanisms involve competition between ring-breaking unimolecular dissociation reactions and ring-preserving abstraction reactions with O_2 (277, 278). The jet fuels were practical fuel samples obtained from Wright-Patterson Air Force Base and were used to examine the impact of changing flame conditions on the sooting behavior of real fuels.

7.2 Experimental methods

7.2.1 Burner and Flame Details

Atmospheric-pressure coflow laminar premixed flames were generated with a Yale Coflow Burner (147): the fuel mixture – methane, nitrogen, primary air, and a dopant – flowed from 99.99+ % purity cylinders (methane, nitrogen) or a compressor (air). Electronic mass flow controllers (MKS 1179A and 1559A, Omega 5514) actively governed the flowrates of these reactants and were calibrated with soap bubble meters for the specific process gases. The dopants examined were either pure cyclic hydrocarbons (methyl cyclopentane, cyclohexane, and cyclohexene) or jet fuels (POSF 4658, POSF 10264, and POSF 10289) (Table 7-1). Their YSI values have been previously characterized (130, 162). The dopants were injected into the gaseous methane/nitrogen/air mixture by a syringe pump (KDS 100). The performance of this pump was characterized by measuring its linear rate-of-travel with calipers in place of a syringe; the pump was sufficiently accurate across the range of flowrates used in this study to contribute negligibly to uncertainties in the dopant mass fraction in the flame. The syringe needle entered the fuel line through a septum in a stainless-steel tee. Resistive tapes heated the fuel line and the burner fuel tube to 175 °C, with the fuel tube temperature maintained to within ± 1 °C under PID control;

Table 7-1: Dopant properties and flow parameters used for the partially-premixed flame studies

Test Compounds	Formula	Mol. Wt	Flow ($\mu\text{l/hr}$) ^a	YSI
Cyclohexane	C ₆ H ₁₂	84.2	122	19.1 ^b
Cyclohexene	C ₆ H ₁₀	82.1	117	21.7 ^b
Methylcyclopentane	C ₆ H ₁₂	84.1	127	30.9 ^b
POSF 10264	C _{10.8} H _{21.6} ^c	151.5	124	49.6 ^d
POSF 4658	C _{10.2} H _{19.9} ^e	142	120	75.5 ^d
POSF 10289	C _{11.9} H _{22.6} ^c	165.7	117	86.9 ^d
n-hexane	C ₆ H ₁₄	86.2	144	0
Benzene	C ₆ H ₆	78.1	108	100

^a Liquid phase flow rate of compound dispensed from syringe pump

^b Obtained from Ref. (130) on a mole basis

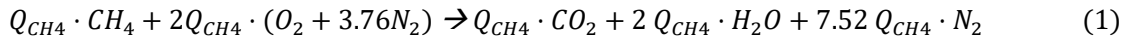
^c Obtained from Ref. (279)

^d Obtained from Ref. (280) on a mass basis

^e Obtained from Ref. (281)

given this heating the dopants vaporized rapidly upon injection and then were swept to the burner by the other fuel components (see Figs. 3-2 and 3-3).

The nominal flow rates of methane and secondary air were chosen such that the volumetric flow rate of methane $Q_m = 282$ mL/min and volumetric flow of secondary air $Q_{air} = 50,000$ mL/min. The flow rates of the dopants were chosen such that the mass fraction of dopant in the total dopant + methane base fuel mixture was $Y_{dop}=0.85\%$. The volumetric flow rate of the primary nitrogen Q_{N_2} and primary air Q_{pa} were independently varied to explore different flame temperatures and air-to-fuel equivalence ratios (λ), respectively. λ is defined as $\lambda = AFR_{Actual}/AFR_{Stoichiometric}$, where $AFR=Q_{air}/Q_{fuel}$ denotes the volumetric air-to-fuel ratio. Q_{pa} was calculated to achieve a chosen λ according to the chemical equation:



for the stoichiometric case. Then the air-to-fuel equivalence ratio becomes:

$$\lambda = \frac{Q_{pa}/Q_{CH_4}}{9.52 Q_{CH_4}/Q_{CH_4}} = \frac{Q_{pa}}{9.52 Q_{CH_4}} \quad (2)$$

and we define Q_{pa} as $Q_{pa}=9.52 \lambda \cdot Q_{CH_4}$. Though the λ values examined in this study are small ($\lambda = 0, 0.02, \text{ and } 0.04$), this range goes from a completely nonpremixed methane flame to a flame that is sufficiently partially premixed such that the soot concentrations are at the detection limit. Adiabatic flame temperatures were calculated using the NASA CEA program (221). Though actual flame temperatures are lower than the adiabatic flame temperature, this calculation captures the relative differences in flame temperatures induced by changes in the nitrogen dilution levels in the fuel.

7.2.2 Methodology for Measuring Soot Concentrations

Color-ratio pyrometry

We measured absolute maximum soot concentrations using color-ratio pyrometry. Detailed descriptions of this technique are available in the literature (192, 193). Radiative emissions from soot in a doped flame are imaged by a digital camera, then spatial maps of the soot volume fraction f_v distribution in the flame are generated. The maximum soot concentration in these f_v distributions are used in determining the YSI of a dopant fuel. Figure 7-1 shows the experimental setup: (1) an anodized aluminum chimney with a transparency film window minimizes backscattering and allows light from the flame to be imaged; (2) a Schott BG-7 filter permits the transmission of light in the 400 to 700 nm range and provides a better balance between the red, green, and blue intensities from the flame (192); (3) a Nikon D90 consumer camera captures light from the flame that is transmitted through the filter and is subsequently saved in the camera's .NEF 12-bit compressed raw format. For each dopant, 100 flame images were captured over a 600 second period, demosaiced using OMA (282), and then the reconstruction procedure and following temperature and soot calculations were performed using Python code.

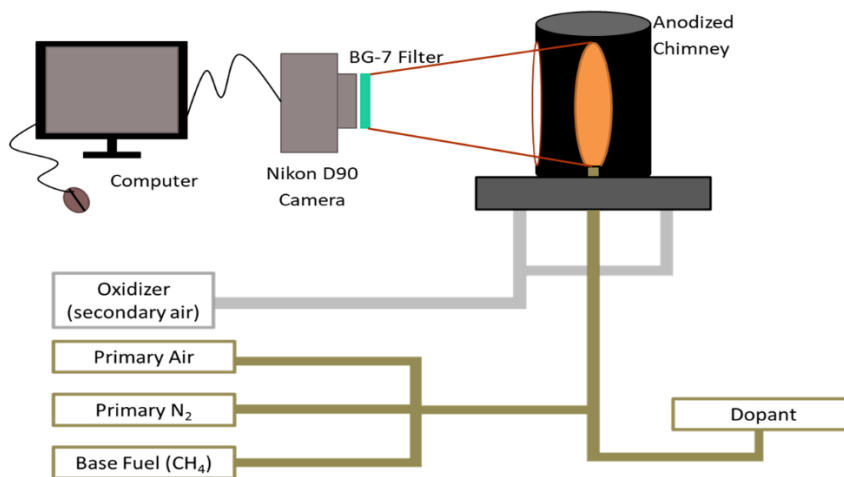


Figure 7-1: Diagram depicting the color-ratio pyrometry experimental setup

Line-of-sight spectral radiance

To validate our results across different experimental methods for determining sooting tendency, line-of-sight spectral radiance (LSSR) at 660 nm was employed to measure relative soot concentrations. In this method the integrated radiant signal from soot particles along a path through the centerline of the flame is measured. We include “line-of-sight” in the name of this technique because the depth-of-field of our detection system (~8 mm) is comparable to the flame diameter; thus the measured radiance comes from all flame locations along the detection system’s axis, not from a single point.

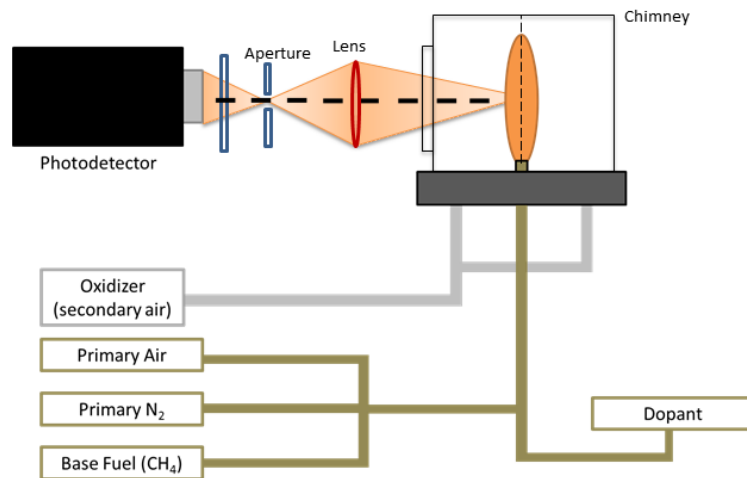


Figure 7-2: Diagram depicting the line-of-sight spectral radiance (LSSR) setup

Figure 7-2 shows the basic experimental setup: (1) a UV silica window mounted in the chimney transmits light emitted by the flame to the rest of the measurement system; (2) a fused silica biconvex lens focusses some of this light onto a 1 mm diameter circular aperture with unity magnification; (3) an interference filter (Thorlabs FB660-10, 10 nm FWHM, $\lambda_{\text{center}} = 660 \pm 2 \text{ nm}$) and an infrared-blocking filter (Schott KG2) isolate the portion of this light at 660 nm; and (4) a red-enhanced photomultiplier tube (PMT; Oriel 77348) detects it. An A/D converter (LeCroy LT342, 1 m Ω input impedance) samples the PMT output at 5 Hz. Each sample is an average of 50,000 8-bit readings recorded 2 μsec apart. The noise in the measurements is negligible compared to other sources of experimental error, including uncertainty arising from assuming

uniformity in temperature and soot volume fraction distributions for different dopants under a particular set of dilution levels and in the density of the dopants ($\pm 2\%$). Random noise in the measurements becomes negligible because >1000 data points are averaged over 5 minutes (random error less than $\pm 0.33\%$).

7.2.3 Calculation of YSI

There are many ways to define the YSI, depending upon the choice of reference compounds used. For this study, we have defined the YSI as follows:

$$\text{YSI}(i) = A * M(i) + B \quad (3)$$

$$\text{YSI}(\text{n-hexane}) = 0 \quad (4)$$

$$\text{YSI}(\text{benzene}) = 100 \quad (5)$$

where $\text{YSI}(i)$ denotes the YSI of species i , and $M(i)$ is the experimentally measured maximum concentration of soot in a methane-based flame doped with species i . A and B are constants chosen to satisfy Eqs. 4 and 5, and depend on the technique used to evaluate maximum soot concentrations. Benzene and n-hexane were chosen as the reference compounds because they sufficiently span the range of sooting tendencies of the fuels examined, and were the reference compounds used to determine the literature YSI values of the compounds and fuels under study.

7.3 Results and Discussion

7.3.1 YSIs Measured in Partially-Premixed Flames

In this study, we evaluated the maximum peak soot volume fraction for nonpremixed and partially premixed methane flames doped with three cyclic hydrocarbons and three jet fuels under nine different flame conditions which span a range of adiabatic flame temperatures and λ values. For a subset of conditions $(T_{\text{ad}}, \lambda) = (2224 \text{ K}, 0), (2224 \text{ K}, 0.02), (2224 \text{ K}, 0.04), (2185 \text{ K}, 0.02)$, the maximum soot concentrations were arbitrarily evaluated via color-ratio pyrometry using the “peak-region” method. In this method, local soot volume fractions f_v in the regions of

the flame with f_v above the 90th percentile are averaged; this average is used as the representative peak soot volume fraction $f_{v,max}$ in the flame. This has been shown to be a robust method of quantifying the peak soot levels in similar flames (145). Since YSI is based upon relative differences in sooting tendency between different doped flames, the near-peak method yields a measure of sooting level relevant for determining YSI.

For the remaining five flame conditions, the LSSR technique was used to measure the relative differences in sooting tendency of the different fuels. The measured LSSR signal depends on the maximum soot concentration, as well as other parameters such as soot temperature, air-to-fuel ratio, soot emissivity, and other scaling variables. Besides the soot concentration, these other parameters have a weak dependence on the type of dopant used at any given flame condition, and therefore cancel out when the LSSR signal is converted into YSI through Eq. (1).

For the LSSR measurements, the photodetector was set to obtain signal from the height above the burner (HAB) of the flame at which soot concentration peaks. This detection HAB changed based on the primary air and nitrogen levels, but was assumed to be independent of the choice of dopant for any given flame condition. The reliability of the LSSR technique in measuring YSI depends in part on the assumption that the maximum soot concentration occurs along the 2D-projection of the flame centerline and at the same HAB for different dopants under a particular set of flame conditions. To test this assumption, we used color-ratio pyrometry to obtain full 2D soot concentration maps for flames doped separately with hexane (YSI=0), benzene (YSI=100), and POSF 10264 (YSI=49.6) under four flame conditions $(T_{ad}, \lambda) = (2224K, 0), (2185K, 0), (2224K, 0.04), (2185K, 0.04)$ and determined the HAB where the soot concentration peaks for each doped flame. Representative results are shown in Figure 7-3. For a given set of flame conditions, for all three dopants, the soot concentrations peaked at the same flame height and the sootiest points of each flame (i.e. within the top 10th-percentile) were all

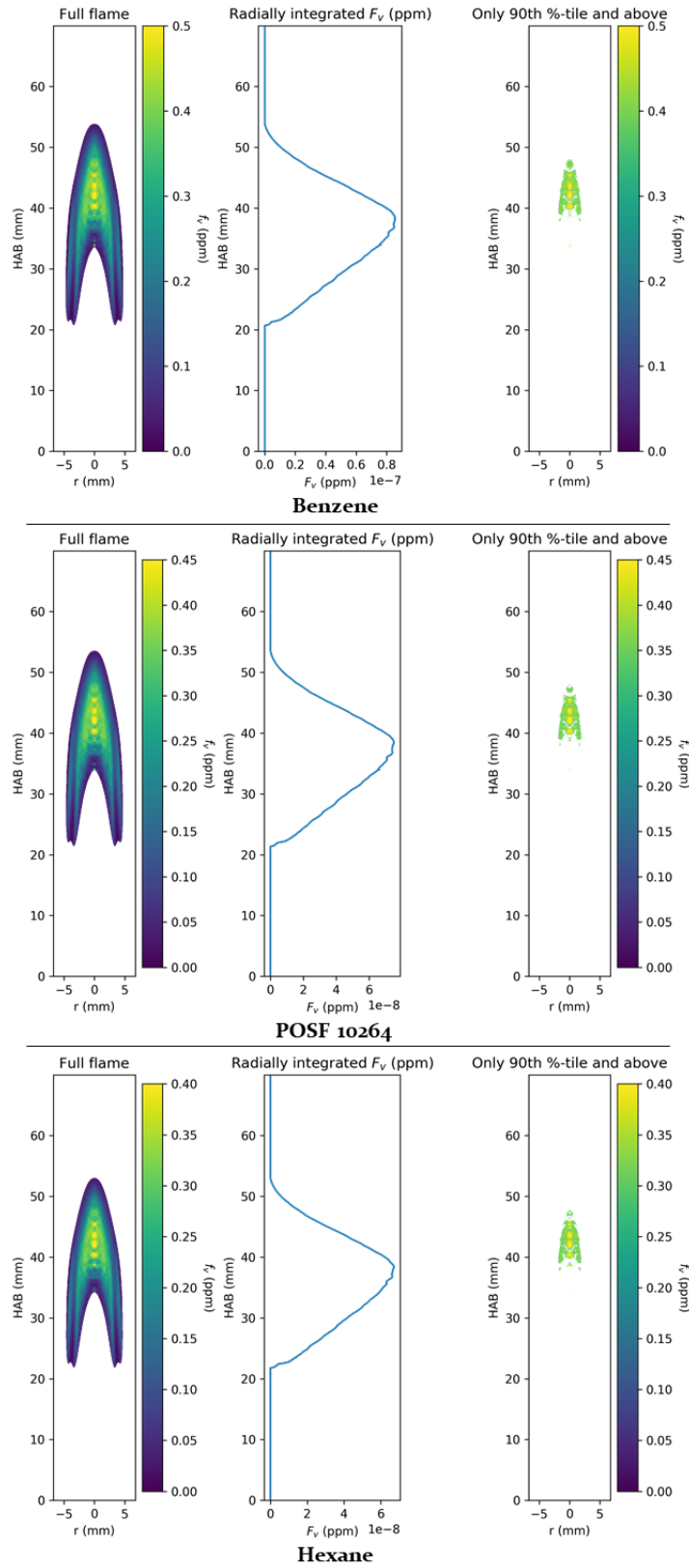


Figure 7-3: 2D Soot concentration profiles and radially integrated soot volume fractions vs. height above burner of doped methane flames (no premixed N₂/air)

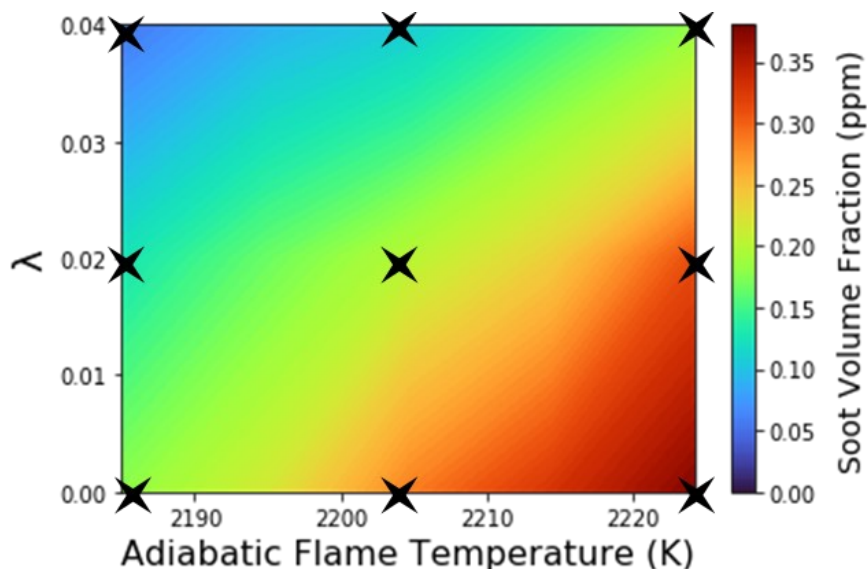


Figure 7-4: Soot concentration map of POSF 10264, demonstrating the range of conditions examined in this study

clustered around the centerline of the flame. The centerline in this case is that of the 3D axis, since color-ratio pyrometry images the whole flame and uses symmetry considerations to spatially resolve f_v as a function of HAB and radial position. This supported the applicability of the LSSR method in measuring relative differences in the sooting tendency, and yielded YSI results similar within experimental accuracy to those obtained using color-ratio pyrometry.

Nine different flame conditions were considered in this work. Figure 7-4 shows a 2D soot concentration map of POSF 10264 across the range of air-to-fuel ratios and adiabatic flame temperatures encountered in these experiments, with X's denoting the particular flame conditions analyzed for measurements used in Figure 7-5. The YSI of POSF 10264 has been previously measured to be 49.6 (280), which is almost exactly halfway between that of hexane (0) and benzene (100). It can be seen from Figure 7-4 that the range of flame conditions chosen were sufficient to span a wide range of sooting conditions for the POSF 10264-doped flames. The YSIs of all six hydrocarbons and fuels listed in Section 7.2.1 were then determined for each set of conditions and compared to a reference YSI. The results are summarized in Figure 7-5.

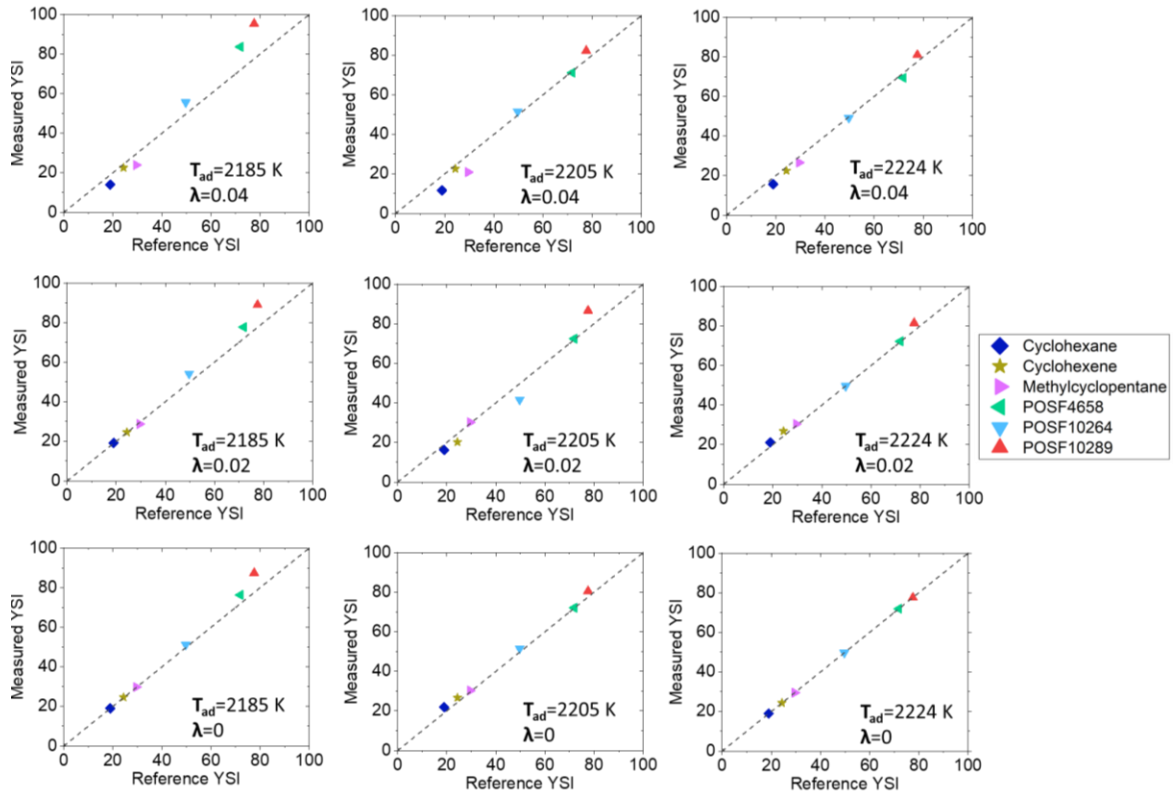


Figure 7-5: Reference YSI vs. experimentally measured YSI across various λ -values and adiabatic flame temperatures. The reference YSI for each fuel is that YSI computed under conditions $(\lambda, T_{ad}) = (0, 2224\text{K})$, and so for conditions $(\lambda, T_{ad}) = (0, 2224\text{K})$ all points in the scatter plot lie on the line $y=x$, denoted by the dashed line in each plot.

In Figure 7-5, the YSIs are compared as follows: a standard set of YSIs are measured under conditions $(T_{ad}, \lambda) = (2224\text{K}, 0)$ for each test compound and used as the reference YSI values on the horizontal axes of the nine plots. The YSIs measured for each of the nine chosen conditions are represented on the vertical axes of the nine plots. Thus, for conditions $(T_{ad}, \lambda) = (2224\text{K}, 0)$, all data points lie on the line $y=x$ (denoted in the plots by a dashed line) by definition. This mediates the problem of comparing the literature YSI of the test compounds, which were measured on either a mass or mole basis (130, 280), to the YSI measurements in these studies. As seen in Fig. 7-5, the YSIs of the various fuels measured across various λ values and adiabatic flame temperatures agree well with their corresponding reference YSI. The good agreement between the YSIs measured across the range of conditions examined in this study and their

reference YSIs suggests that the sooting tendency relationship between fuel compositions and structures holds across a range of air-to-fuel ratios and flame temperatures.

The three cyclic compounds were chosen for this study based on the hypothesis that the sooting behavior of cyclic compounds could be strongly impacted by the air-to-fuel ratio. Under oxygen-rich environments, O_2 can potentially extract protons from cyclic compounds, leading to the formation of cyclic alkenes, dienes, and eventually benzene (277, 278). This would manifest as a greater sooting propensity for cyclic compounds under increasing oxygen-rich conditions relative to the sooting propensity of hexane or benzene, thereby skewing the YSI value of these cyclic compounds at different air-to-fuel ratios. However, from Figure 7-5, it is evident that the YSI of the cyclic compounds did not deviate significantly from their reference YSI with changes in air-to-fuel ratio. This suggests that any increases in soot concentration through the H-abstraction pathway by O_2 are insignificant under the range of conditions examined. As the air-to-fuel ratios encountered in these studies led to practically no soot formation at higher flame temperatures and λ values (Fig. 7-4), it follows that these pathways would not contribute significantly to soot formation pathways at higher air-to-fuel ratios, as they would be outcompeted with hydrocarbon oxidation pathways to CO_2 and H_2O .

7.4 Conclusions

In this work, YSI measurements of various fuels doped into a nonpremixed and partially premixed methane/air co-flow flame under a range of flame temperatures and air-to-fuel ratios were reported and validated by two different techniques. Color-ratio pyrometry and LSSR were demonstrated to be feasible methods for determining the relative differences in maximum sooting tendency in doped methane flames. The relative differences in the maximum sooting tendencies of the various fuels were preserved across nine different combustion conditions, yielding YSI measurements which agreed well with their corresponding reference values. The

hypothesis that an increase in oxygen content would lead to an increase in the relative sooting tendency for the cyclic compounds was not realized, and is likely not to affect YSI measurements across a moderate range of air-to-fuel ratios. This work is expected to be of relevance to surrogate formulation applications, as well as in the design of practical devices since a wide range of conditions can be addressed.

8 Summary and Future Work

The research presented in this dissertation has elucidated the influence of fuel-nitrogen on soot formation. The results presented here show that nitrogen-containing compounds generally have lower sooting propensities than pure hydrocarbons and oxygenates, and that the relative differences in amines to form soot depends on their chemical structures. NH_3 was observed to have a strong suppressive effect on soot formation when co-fired with CH_4 , and comparisons to simulations highlight the need to improve detailed kinetic mechanisms to accurately predict soot emissions from NH_3 /hydrocarbon mixtures. The combined results suggest that nitrogen suppresses soot formation through carbon-nitrogen interactions, which competes with growth pathways to aromatic species. In addition, synchrotron X-ray fluorescence and scattering were found to be useful techniques for probing physical characteristics of sooting methane/air diffusion flames. The data provided by these techniques demonstrate that the model is capturing the physical characteristics of the flame well, and that future efforts should focus on identifying and including soot-relevant nitrogen-hydrocarbon interactions in the underlying chemical mechanism. Additionally, trends in sooting tendencies determined with the YSI metric were found to hold across a wide range of conditions relevant to soot formation. Should nitrogen-containing compounds find uses as fuels in the future, these results suggest that measured trends in their sooting tendencies may extend to other conditions.

While significant progress has been made in understanding the effect of fuel-nitrogen on soot formation, this research has also identified areas which could be explored in future investigations:

- Only a small range of nitrogen-containing compounds (unsaturated amines) were analyzed in this thesis. However, biomass, coals, and diesels can contain nitrogen in the form of various chemical motifs, including pyridinic, amide, and pyrrolic groups. To better understand the effect of different nitrogen-containing functional groups on

soot formation, the sooting tendencies of a larger number of nitrogen-containing hydrocarbons could be measured. If enough empirical measurements are taken, the data can be used to develop group additivity models for estimating sooting tendency based on chemical structure. Not only could this provide insights into the different effects of nitrogen functionalities on soot formation, but could also be used to estimate sooting tendencies for nitrogen-containing compounds for which measurements don't exist. This could be used to rationally select low-sooting nitrogen-containing compounds if they find uses as future fuels, and may also prove useful for predicting emissions from different biomass-compositions.

- The current results show a strong chemical influence of NH_3 on reducing soot formation when added to nonpremixed CH_4 flames. However, more work is required to determine the exact pathways that are affected by NH_3 . In addition, it is not clear whether the influence of NH_3 on soot formation is universal, or if it depends on the identity of the hydrocarbon it is co-fired with. Future studies should aim to collect detailed species profiles in NH_3 /hydrocarbon flames, and these results could be compared to DFT simulations to examine the most likely reaction pathways that need to be included and/or improved in chemical kinetic models.
- The results presented here suggest that NH_3 reduces benzene formation rates in CH_4 flames, while some literature studies using fuels other than CH_4 suggest benzene formation rates are largely unaffected by NH_3 . To understand how NH_3 may affect soot formation when fired with different hydrocarbons, future studies should analyze trends in soot formation and flame characteristics in nonpremixed flames containing NH_3 and other hydrocarbons, such as ethylene, acetylene, and propane.
- The synchrotron X-ray fluorescence and scattering techniques were successfully applied in sooting methane/air diffusion flames, and were found to be free from soot

interferences. The results presented here suggest that these X-ray techniques overcome issues faced when traditionally performing these measurements in heavily sooting flames. Future work could look to employ these techniques in ethylene, acetylene, or propane flames, which produce larger quantities of soot than methane flames. In addition, mixture fractions and temperatures in N_2/NH_3 -diluted fuel mixtures could be studied to provide stringent benchmarks for NH_3 -combustion models.

- While not addressed in this dissertation, potential fuel- NO_x emissions from nitrogen-containing hydrocarbons and NH_3 /hydrocarbon mixtures will certainly need to be considered if these become future fuels. Therefore, one potentially interesting avenue of research could be to explore the propensity of different compounds to form NO_x when co-fired with hydrocarbons. A measurement analogous to the YSI sooting tendency measurement could be developed to describe the relative propensities of different nitrogen-containing groups to form NO_x . These studies would help determine how strongly, if at all, chemical structure influences subsequent fuel- NO_x emissions, and could possibly inform the design of fuel mixtures and combustion technologies which aim to minimize both soot and NO_x emissions. Future efforts could also explore the role of unburned NH_3 in SCR-type reactions for eliminating NO_x formation.

9 References

1. US Energy Information Administration (Jan. 2021) Table 1.3. in *Monthly Energy Review*, p 7.
2. Smalley RE (2005) Future global energy prosperity: the terawatt challenge. *MRS Bull.* 30(6):412-417.
3. US Energy Information Administration (Jan. 2021) Table 2.1. in *Monthly Energy Reviews*, p 37.
4. US Energy Information Administration (Jan. 2021) Tables 2.4-2.6. in *Monthly Energy Reviews*, pp 43-47.
5. Davis SJ, *et al.* (2018) Net-zero emissions energy systems. *Science* 360(6396).
6. US Energy Information Administration (Oct. 2020) in *International Energy Outlook 2020 (IEO2020)*, p 4.
7. IEA (2020) CO2 Emissions from Fuel Combustion: Overview. (IEA, Paris).
8. Bond TC, *et al.* (2013) Bounding the role of black carbon in the climate system: A scientific assessment. *Journal of Geophysical Research: Atmospheres* 118(11):5380-5552.
9. Stocker T (2014) *Climate change 2013: the physical science basis: Working Group I contribution to the Fifth assessment report of the Intergovernmental Panel on Climate Change* (Cambridge university press).
10. Elrod MJ (1999) Greenhouse warming potentials from the infrared spectroscopy of atmospheric gases. *J. Chem. Educ.* 76(12):1702.
11. Bolin B & Doos BR (1989) Greenhouse effect.
12. Rodhe H (1990) A comparison of the contribution of various gases to the greenhouse effect. *Science* 248(4960):1217-1219.
13. Caldeira K, Jain AK, & Hoffert MI (2003) Climate sensitivity uncertainty and the need for energy without CO2 emission. *Science* 299(5615):2052-2054.
14. Sherwood S, *et al.* (2020) An assessment of Earth's climate sensitivity using multiple lines of evidence. *Rev. Geophys.* 58(4):e2019RG000678.
15. Archer D, *et al.* (2009) Atmospheric lifetime of fossil fuel carbon dioxide. *Annual review of earth and planetary sciences* 37.
16. US Environmental Protection Agency (2012) Report to Congress on Black Carbon (Figure A). p 4.
17. Nikula K, *et al.* (1995) Comparative pulmonary toxicities and carcinogenicities of chronically inhaled diesel exhaust and carbon black in F344 rats. *Fundam. Appl. Toxicol.* 25(1):80-94.
18. Valavanidis A, Vlachogianni T, Fiotakis K, & Loridas S (2013) Pulmonary oxidative stress, inflammation and cancer: respirable particulate matter, fibrous dusts and ozone as major causes of lung carcinogenesis through reactive oxygen species mechanisms. *Int. J. Env. Res. Public Health* 10(9):3886-3907.
19. Niranjana R & Thakur AK (2017) The toxicological mechanisms of environmental soot (black carbon) and carbon black: focus on oxidative stress and inflammatory pathways. *Frontiers in immunology* 8:763.
20. MacNee W & Donaldson K (2003) Mechanism of lung injury caused by PM10 and ultrafine particles with special reference to COPD. *Eur. Respir. J.* 21(40 suppl):47s-51s.
21. Lee JG, Noh WJ, Kim H, & Lee M-Y (2011) Generation of reactive oxygen species contributes to the development of carbon black cytotoxicity to vascular cells. *Toxicological research* 27(3):161-166.
22. Wittmaack K (2007) In search of the most relevant parameter for quantifying lung inflammatory response to nanoparticle exposure: particle number, surface area, or what? *Environ. Health Perspect.* 115(2):187-194.
23. Calderón-Garcidueñas L, *et al.* (2008) Air pollution, cognitive deficits and brain abnormalities: a pilot study with children and dogs. *Brain and cognition* 68(2):117-127.
24. Schraufnagel DE (2020) The health effects of ultrafine particles. *Experimental & molecular medicine* 52(3):311-317.
25. Heidari Nejad S, *et al.* (2015) The effect of diesel exhaust exposure on blood-brain barrier integrity and function in a murine model. *J. Appl. Toxicol.* 35(1):41-47.

26. Fraser M, Yue Z, Tropp R, Kohl S, & Chow J (2002) Molecular composition of organic fine particulate matter in Houston, TX. *Atmos. Environ.* 36(38):5751-5758.
27. Zheng M, *et al.* (2005) Seasonal trends in PM_{2.5} source contributions in Beijing, China. *Atmos. Environ.* 39(22):3967-3976.
28. Murray CJ, *et al.* (2020) Global burden of 87 risk factors in 204 countries and territories, 1990–2019: a systematic analysis for the Global Burden of Disease Study 2019. *The Lancet* 396(10258):1223-1249.
29. Matsui H, Hamilton DS, & Mahowald NM (2018) Black carbon radiative effects highly sensitive to emitted particle size when resolving mixing-state diversity. *Nature communications* 9(1):1-11.
30. Lohmann U, *et al.* (2020) Future warming exacerbated by aged-soot effect on cloud formation. *Nature Geoscience* 13(10):674-680.
31. Ramanathan V & Carmichael G (2008) Global and regional climate changes due to black carbon. *Nature geoscience* 1(4):221-227.
32. UNEP (2011) Integrated Assessment of Black Carbon and Tropospheric Ozone (UNEP). (Tech Rep).
33. Miller JA & Bowman CT (1989) Mechanism and modeling of nitrogen chemistry in combustion. *Progress in energy and combustion science* 15(4):287-338.
34. US Environmental Protection Agency (2018) Nitrogen Oxides Emissions. in *Report on the Environment*.
35. US Environmental Protection Agency (2020) Power Plant Emission Trends.
36. Wink DA, Ridnour LA, Hussain SP, & Harris CC (2008) The reemergence of nitric oxide and cancer. *Nitric oxide: biology and chemistry/official journal of the Nitric Oxide Society* 19(2):65.
37. Kampa M & Castanas E (2008) Human health effects of air pollution. *Environ. Pollut.* 151(2):362-367.
38. Boningari T & Smirniotis PG (2016) Impact of nitrogen oxides on the environment and human health: Mn-based materials for the NO_x abatement. *Current Opinion in Chemical Engineering* 13:133-141.
39. Rowland A, Murray A, & Wellburn A (1985) Oxides of nitrogen and their impact upon vegetation. *Reviews on environmental health* 5(4):295-342.
40. Etminan M, Myhre G, Highwood E, & Shine K (2016) Radiative forcing of carbon dioxide, methane, and nitrous oxide: A significant revision of the methane radiative forcing. *Geophys. Res. Lett.* 43(24):12,614-612,623.
41. Balmer E (Nov 2 2020) Japan carbon pledge boosts hopes of ammonia backers.
42. Crolius SH (Feb 6 2020) Korean Register Sees Ammonia as Preferred Alternative Maritime Fuel. ed Association AE.
43. Colthorpe A (Oct 26 2020) Australian government to fast-track 26GW hydrogen + ammonia 'Asian Renewable Energy Hub'. ed News ES.
44. Buckley AN (1994) Nitrogen functionality in coals and coal-tar pitch determined by X-ray photoelectron spectroscopy. *Fuel Process. Technol.* 38(3):165-179.
45. Chen S, Heap M, Pershing D, & Martin G (1982) Fate of coal nitrogen during combustion. *Fuel* 61(12):1218-1224.
46. Anonymous (2018) Shell Nitrogen Enriched Gasolines. (Shell).
47. Goldsborough S, Johnson M, Banyon C, Pitz W, & McNenly M (2015) Experimental and modeling study of fuel interactions with an alkyl nitrate cetane enhancer, 2-ethyl-hexyl nitrate. *Proceedings of the Combustion Institute* 35(1):571-579.
48. Demirbas A (2004) Combustion characteristics of different biomass fuels. *Prog. Energy Combust. Sci.* 30(2):219-230.
49. Parikka M (2004) Global biomass fuel resources. *Biomass Bioenergy* 27(6):613-620.
50. Chiesa S & Gnansounou E (2011) Protein extraction from biomass in a bioethanol refinery– Possible dietary applications: Use as animal feed and potential extension to human consumption. *Bioresour. Technol.* 102(2):427-436.
51. Stephanopoulos G, Aristidou AA, & Nielsen J (1998) *Metabolic engineering: principles and methodologies* (Elsevier).

52. Ahmed S, Mustafa G, Arshad M, & Rajoka MI (2017) Fungal biomass protein production from *Trichoderma harzianum* using rice polishing. *BioMed research international* 2017.
53. Piorreck M, Baasch K-H, & Pohl P (1984) Biomass production, total protein, chlorophylls, lipids and fatty acids of freshwater green and blue-green algae under different nitrogen regimes. *Phytochemistry* 23(2):207-216.
54. Vassilev SV, Baxter D, Andersen LK, & Vassileva CG (2010) An overview of the chemical composition of biomass. *Fuel* 89(5):913-933.
55. Usman M, *et al.* (2019) Characterization and utilization of aqueous products from hydrothermal conversion of biomass for bio-oil and hydro-char production: a review. *Green Chemistry* 21(7):1553-1572.
56. Wang S, Wang Q, Jiang X, Han X, & Ji H (2013) Compositional analysis of bio-oil derived from pyrolysis of seaweed. *Energy Convers. Manage.* 68:273-280.
57. Sanna A, Li S, Linforth R, Smart KA, & Andrésen JM (2011) Bio-oil and bio-char from low temperature pyrolysis of spent grains using activated alumina. *Bioresour. Technol.* 102(22):10695-10703.
58. Yu G, Zhang Y, Schideman L, Funk T, & Wang Z (2011) Distributions of carbon and nitrogen in the products from hydrothermal liquefaction of low-lipid microalgae. *Energy & Environmental Science* 4(11):4587-4595.
59. Toraman HE, Franz K, Ronsse F, Van Geem KM, & Marin GB (2016) Quantitative analysis of nitrogen containing compounds in microalgae based bio-oils using comprehensive two-dimensional gas-chromatography coupled to nitrogen chemiluminescence detector and time of flight mass spectrometer. *J. Chromatogr.* 1460:135-146.
60. Schnitzer MI, Monreal CM, & Jandl G (2008) The conversion of chicken manure to bio-oil by fast pyrolysis. III. Analyses of chicken manure, bio-oils and char by Py-FIMS and Py-FDMS. *Journal of Environmental Science and Health, Part B* 43(1):81-95.
61. Gaur RK (2014) Amino acid frequency distribution among eukaryotic proteins. *The IIOAB Journal* 5(2):6.
62. Yu Q, Brage C, Chen G, & Sjöström K (2007) The fate of fuel-nitrogen during gasification of biomass in a pressurised fluidised bed gasifier. *Fuel* 86(4):611-618.
63. Li Q, *et al.* (2000) Atmospheric hydrogen cyanide (HCN): Biomass burning source, ocean sink? *Geophys. Res. Lett.* 27(3):357-360.
64. Liu H & Gibbs BM (2003) Modeling NH₃ and HCN emissions from biomass circulating fluidized bed gasifiers☆. *Fuel* 82(13):1591-1604.
65. Hämäläinen JP, Aho MJ, & Tummavuori JL (1994) Formation of nitrogen oxides from fuel-N through HCN and NH₃: a model-compound study. *Fuel* 73(12):1894-1898.
66. Lucassen A, *et al.* (2012) Fuel-nitrogen conversion in the combustion of small amines using dimethylamine and ethylamine as biomass-related model fuels. *Combust. Flame* 159(7):2254-2279.
67. Lucassen A, Labbe N, Westmoreland PR, & Kohse-Höinghaus K (2011) Combustion chemistry and fuel-nitrogen conversion in a laminar premixed flame of morpholine as a model biofuel. *Combust. Flame* 158(9):1647-1666.
68. Sullivan N, *et al.* (2002) Ammonia conversion and NO_x formation in laminar coflowing nonpremixed methane-air flames. *Combust. Flame* 131(3):285-298.
69. Rawadieh SE, Altarawneh M, Altarawneh IS, Shiroudi A, & El-Nahas AM (2021) Exploring reactions of amines-model compounds with NH₂: In relevance to nitrogen conversion chemistry in biomass. *Fuel* 291:120076.
70. Plouffe J (Feb 7 2019) Renewable hydrogen power plant step closer in Port Lincoln. ed Economy R.
71. Suryanto BH, *et al.* (2019) Challenges and prospects in the catalysis of electroreduction of nitrogen to ammonia. *Nature Catalysis* 2(4):290-296.
72. Mehta P, *et al.* (2018) Overcoming ammonia synthesis scaling relations with plasma-enabled catalysis. *Nature Catalysis* 1(4):269-275.

73. Hu B, Hu M, Seefeldt L, & Liu TL (2019) Electrochemical dinitrogen reduction to ammonia by Mo₂N: catalysis or decomposition? *ACS Energy Letters* 4(5):1053-1054.
74. Reuters Staff (Feb 8 2021) Japan aims to boost ammonia fuel demand to 3 mln tonnes a year by 2030. ed Reuters.
75. Koch E (1945) Ammonia--a fuel for motor buses. *J. Inst. Pet* 31:213.
76. NASA (Feb 28 2014) NASA Armstrong Fact Sheet: X-15 Hypersonic Research Program.
77. Chen Z (2011) On the extraction of laminar flame speed and Markstein length from outwardly propagating spherical flames. *Combust. Flame* 158(2):291-300.
78. Hayakawa A, *et al.* (2015) Laminar burning velocity and Markstein length of ammonia/air premixed flames at various pressures. *Fuel* 159:98-106.
79. Dahoe A (2005) Laminar burning velocities of hydrogen-air mixtures from closed vessel gas explosions. *J. Loss Prev. Process Indust.* 18(3):152-166.
80. Pizzuti L, Martins CA, dos Santos LR, & Guerra DR (2017) Laminar burning velocity of methane/air mixtures and flame propagation speed close to the chamber wall. *Energy procedia* 120:126-133.
81. Okafor EC, *et al.* (2018) Experimental and numerical study of the laminar burning velocity of CH₄-NH₃-air premixed flames. *Combustion and Flame* 187:185-198.
82. Kurata O, *et al.* (2017) Performances and emission characteristics of NH₃-air and NH₃CH₄-air combustion gas-turbine power generations. *Proceedings of the Combustion Institute* 36(3):3351-3359.
83. Okafor EC, *et al.* (2019) Towards the development of an efficient low-NO_x ammonia combustor for a micro gas turbine. *Proceedings of the combustion institute* 37(4):4597-4606.
84. Okafor EC, *et al.* (2020) Control of NO_x and other emissions in micro gas turbine combustors fuelled with mixtures of methane and ammonia. *Combust. Flame* 211:406-416.
85. Iki N, *et al.* (2015) Micro gas turbine firing kerosene and ammonia. *ASME turbo expo 2015: turbine technical conference and exposition*, (American Society of Mechanical Engineers Digital Collection).
86. Okafor EC, *et al.* (2019) Measurement and modelling of the laminar burning velocity of methane-ammonia-air flames at high pressures using a reduced reaction mechanism. *Combust. Flame* 204:162-175.
87. Toland A & Simmie JM (2003) Ignition of alkyl nitrate/oxygen/argon mixtures in shock waves and comparisons with alkanes and amines. *Combust. Flame* 132(3):556-564.
88. Tanaka S, Ayala F, Keck JC, & Heywood JB (2003) Two-stage ignition in HCCI combustion and HCCI control by fuels and additives. *Combust. Flame* 132(1-2):219-239.
89. Ghosh P (2008) Predicting the effect of cetane improvers on diesel fuels. *Energy & fuels* 22(2):1073-1079.
90. Fuller ME & Goldsmith CF (2019) Shock Tube Laser Schlieren Study of the Pyrolysis of Isopropyl Nitrate. *The Journal of Physical Chemistry A* 123(28):5866-5876.
91. Clothier P, Aguda B, Moise A, & Pritchard H (1993) How do diesel-fuel ignition improvers work? *Chem. Soc. Rev.* 22(2):101-108.
92. Elishav O, *et al.* (2020) Progress and prospective of nitrogen-based alternative fuels. *Chem. Rev.* 120(12):5352-5436.
93. Lee KR, Song D, Park SB, & Han J-i (2014) A direct ammonium carbonate fuel cell with an anion exchange membrane. *RSC Advances* 4(11):5638-5641.
94. Troyan JE (1953) Properties, production, and uses of hydrazine. *Industrial & Engineering Chemistry* 45(12):2608-2612.
95. CHRISTOS T, MIRON Y, JAMES H, & PERLEE H (1967) Combustion characteristics of condensed-phase hydrazine-type fuels with nitrogen tetroxide. *Journal of Spacecraft and Rockets* 4(9):1224-1229.
96. Huang S, *et al.* (2016) Towards Safer Rocket Fuels: Hypergolic Imidazolylidene-Borane Compounds as Replacements for Hydrazine Derivatives. *Chemistry--A European Journal* 22(29):10187-10193.
97. Jos J & Mathew S (2017) Ammonium nitrate as an eco-friendly oxidizer for composite solid propellants: promises and challenges. *Crit. Rev. Solid State Mater. Sci.* 42(6):470-498.

98. Grinberg Dana A, Elishav O, Bardow A, Shter GE, & Grader GS (2016) Nitrogen-based fuels: a power-to-fuel-to-power analysis. *Angew. Chem. Int. Ed.* 55(31):8798-8805.
99. Bockhorn H (2013) *Soot formation in combustion: mechanisms and models* (Springer Science & Business Media).
100. Vander Wal RL, Tomasek AJ, Street K, Hull DR, & Thompson WK (2004) Carbon nanostructure examined by lattice fringe analysis of high-resolution transmission electron microscopy images. *Appl. Spectrosc.* 58(2):230-237.
101. Vander Wal RL, Yezerets A, Currier NW, Kim DH, & Wang CM (2007) HRTEM Study of diesel soot collected from diesel particulate filters. *Carbon* 45(1):70-77.
102. Cain JP, Gassman PL, Wang H, & Laskin A (2010) Micro-FTIR study of soot chemical composition—evidence of aliphatic hydrocarbons on nascent soot surfaces. *PCCP* 12(20):5206-5218.
103. Wang H (2011) Formation of nascent soot and other condensed-phase materials in flames. *Proceedings of the Combustion institute* 33(1):41-67.
104. Obaidullaha M, Brama S, & De Ruycka J (2020) Characteristics of particle mass concentrations from small scale biomass combustion: A review. *Small* 5:6.
105. Bockhorn H (1991) *Soot Formation in Combustion: Round Table Discussion.* (Springer Verlag, Heidelberg).
106. Wang Q, Legros G, Bonnetty J, & Morin C (2017) Experimental characterization of the different nitrogen dilution effects on soot formation in ethylene diffusion flames. *Proceedings of the Combustion Institute* 36(2):3227-3235.
107. Axelbaum R & Law CK (1991) Soot formation and inert addition in diffusion flames. *Symposium (International) on Combustion* 23(1):1517-1523.
108. Hunt RA (1953) Relation of smoke point to molecular structure. *Industrial & Engineering Chemistry* 45(3):602-606.
109. Gomez A, Sidebotham G, & Glassman I (1984) Sooting behavior in temperature-controlled laminar diffusion flames. *Combust. Flame* 58(1):45-57.
110. Anonymous (2015) ASTM D1322-15, Standard Test Method for Smoke Point of Kerosine and Aviation Turbine Fuel. (ASTM International, West Conshohocken, PA).
111. McEnally CS, Das DD, & Pfefferle LD (2017) Yield Sooting Index Database Volume 2: Sooting Tendencies of a Wide Range of Fuel Compounds on a Unified Scale Harvard (Harvard Dataverse).
112. Montgomery MJ, Das DD, McEnally CS, & Pfefferle LD (2019) Analyzing the robustness of the yield sooting index as a measure of sooting tendency. *Proceedings of the Combustion Institute* 37(1):911-918.
113. Lemaire R, Lapalme D, & Seers P (2015) Analysis of the sooting propensity of C-4 and C-5 oxygenates: Comparison of sooting indexes issued from laser-based experiments and group additivity approaches. *Combust. Flame* 162(9):3140-3155.
114. Xu L, Yan F, & Wang Y (2020) A comparative study of the sooting tendencies of various C5–C8 alkanes, alkenes and cycloalkanes in counterflow diffusion flames. *Applications in Energy and Combustion Science* 1:100007.
115. McEnally CS, Ciuparu DM, & Pfefferle LD (2003) Experimental study of fuel decomposition and hydrocarbon growth processes for practical fuel components: heptanes. *Combustion and flame* 134(4):339-353.
116. McEnally CS, Pfefferle LD, Atakan B, & Kohse-Höinghaus K (2006) Studies of aromatic hydrocarbon formation mechanisms in flames: Progress towards closing the fuel gap. *Prog. Energy Combust. Sci.* 32(3):247-294.
117. Mallard WG, Westley F, Herron J, Hampson RF, & Frizzell D (1992) *NIST chemical kinetics database* (National Institute of Standards and Technology).
118. Madden L, Moskaleva L, Kristyan S, & Lin M-C (1997) Ab initio MO study of the unimolecular decomposition of the phenyl radical. *The Journal of Physical Chemistry A* 101(36):6790-6797.
119. Westmoreland PR, Dean AM, Howard JB, & Longwell JP (1989) Forming benzene in flames by chemically activated isomerization. *The Journal of Physical Chemistry* 93(25):8171-8180.

120. Sharath N, Reddy K, & Arunan E (2014) Thermal decomposition of propargyl alcohol: single pulse shock tube experimental and ab initio theoretical study. *The Journal of Physical Chemistry A* 118(31):5927-5938.
121. Miller JA, *et al.* (2010) Reactions between resonance-stabilized radicals: propargyl+ allyl. *The Journal of Physical Chemistry A* 114(14):4881-4890.
122. Melius CF, Miller JA, & Evleth EM (1992) Unimolecular reaction mechanisms involving C₃H₄, C₄H₄, and C₆H₆ hydrocarbon species. *Symposium (International) on Combustion*, (Elsevier), pp 621-628.
123. Hwang J, Lee W, Kang H, & Chung SH (1998) Synergistic effect of ethylene–propane mixture on soot formation in laminar diffusion flames. *Combust. Flame* 114(3-4):370-380.
124. Yoon S, Lee S, & Chung SH (2005) Effect of mixing methane, ethane, propane, and propene on the synergistic effect of PAH and soot formation in ethylene-base counterflow diffusion flames. *Proceedings of the Combustion Institute* 30(1):1417-1424.
125. Chu H, Han W, Cao W, Gu M, & Xu G (2019) Effect of methane addition to ethylene on the morphology and size distribution of soot in a laminar co-flow diffusion flame. *Energy* 166:392-400.
126. Lee S, Yoon S, & Chung SH (2004) Synergistic effect on soot formation in counterflow diffusion flames of ethylene–propane mixtures with benzene addition. *Combust. Flame* 136(4):493-500.
127. Das DD, McEnally CS, & Pfefferle LD (2015) Sooting tendencies of unsaturated esters in nonpremixed flames. *Combust. Flame* 162(4):1489-1497.
128. Westbrook CK, Pitz WJ, & Curran HJ (2006) Chemical kinetic modeling study of the effects of oxygenated hydrocarbons on soot emissions from diesel engines. *The journal of physical chemistry A* 110(21):6912-6922.
129. Barrientos EJ, Lapuerta M, & Boehman AL (2013) Group additivity in soot formation for the example of C-5 oxygenated hydrocarbon fuels. *Combust. Flame* 160(8):1484-1498.
130. McEnally CS & Pfefferle LD (2011) Sooting tendencies of oxygenated hydrocarbons in laboratory-scale flames. *Environ. Sci. Technol.* 45(6):2498-2503.
131. Kim Y, *et al.* (2020) Investigation of structural effects of aromatic compounds on sooting tendency with mechanistic insight into ethylphenol isomers. *Proceedings of the Combustion Institute*.
132. Etz BD, *et al.* (2020) Elucidating the chemical pathways responsible for the sooting tendency of 1 and 2-phenylethanol. *Proceedings of the Combustion Institute*.
133. Kwon H, *et al.* (2020) Sooting tendencies of 20 bio-derived fuels for advanced spark-ignition engines. *Fuel* 276:118059.
134. Litzinger T, *et al.* (2011) Fuel additive effects on soot across a suite of laboratory devices, Part 2: Nitroalkanes. *Combust. Sci. Technol.* 183(8):739-754.
135. Duynslaegher C, Jeanmart H, & Vandooren J (2009) Flame structure studies of premixed ammonia/hydrogen/oxygen/argon flames: experimental and numerical investigation. *Proceedings of the Combustion Institute* 32(1):1277-1284.
136. Kohse-Höinghaus K, *et al.* (2010) Biofuel combustion chemistry: from ethanol to biodiesel. *Angew. Chem. Int. Ed.* 49(21):3572-3597.
137. Li S, Davidson DF, & Hanson RK (2014) Shock tube study of ethylamine pyrolysis and oxidation. *Combust. Flame* 161(10):2512-2518.
138. Bockhorn H, Fetting F, Meyer U, Reck R, & Wannemacher G (1981) Measurement of the soot concentration and soot particle sizes in propane oxygen flames. *Symposium (International) on Combustion* 18(1):1137-1147.
139. Haynes B, Jander H, Mätzing H, & Wagner HG (1982) The influence of gaseous additives on the formation of soot in premixed flames. *Symposium (International) on Combustion* 19(1):1379-1385.
140. Renard C, Dias V, Van Tiggelen P, & Vandooren J (2009) Flame structure studies of rich ethylene–oxygen–argon mixtures doped with CO₂, or with NH₃, or with H₂O. *Proceedings of the Combustion Institute* 32(1):631-637.

141. Bennett AM, *et al.* (2020) Soot formation in laminar flames of ethylene/ammonia. *Combust. Flame* 220:210-218.
142. Li Y, Zhang Y, Zhan R, Huang Z, & Lin H (2020) Effects of ammonia addition on PAH formation in laminar premixed ethylene flames based on laser-induced fluorescence measurement. *Energy* 213:118868.
143. Li Y, Zhang Y, Zhan R, Huang Z, & Lin H (2021) Experimental and kinetic modeling study of ammonia addition on PAH characteristics in premixed n-heptane flames. *Fuel Process. Technol.* 214:106682.
144. Boyette WR, *et al.* (2021) Soot formation in turbulent flames of ethylene/hydrogen/ammonia. *Combust. Flame* 226:315-324.
145. Das DD, St. John PC, McEnally CS, Kim S, & Pfefferle LD (2018) Measuring and predicting sooting tendencies of oxygenates, alkanes, alkenes, cycloalkanes, and aromatics on a unified scale. *Combust. Flame* 190:349-364.
146. Smooke M, *et al.* (1992) Computational and experimental study of OH and CH radicals in axisymmetric laminar diffusion flames. *Symposium (International) on Combustion*, (Elsevier), pp 813-821.
147. Gau J, *et al.* (2017) Yale Coflow Burner Information and CAD Drawings.
148. Design Institute for Physical Properties SbA ((2005; 2008; 2009; 2010; 2011; 2012; 2015; 2016; 2017; 2018; 2019) DIPPR Project 801 - Full Version. (Design Institute for Physical Property Research/AIChE).
149. Anonymous (2019) CRC Handbook of Chemistry and Physics. (CRC Press, Cleveland, Ohio).
150. McEnally CS, *et al.* (2019) Sooting tendencies of co-optima test gasolines and their surrogates. *Proceedings of the Combustion Institute* 37(1):961-968.
151. Montgomery MJ, Zhu J, Pfefferle LD, & McEnally CS (2021) Amines have lower sooting tendencies than analogous alkanes, alcohols, and ethers. *Combust. Flame* 227:335-345.
152. Köylü ÜÖ, McEnally CS, Rosner DE, & Pfefferle LD (1997) Simultaneous measurements of soot volume fraction and particle size/microstructure in flames using a thermophoretic sampling technique. *Combust. Flame* 110(4):494-507.
153. Holman J (1986) Heat transfer, 1986. *Mc Gran-Hill Book Company, Soythern Methodist University*.
154. Borch J, Lyne MB, Mark RE, & Habeger C (2001) *Handbook of Physical Testing of Paper: Volume 2* (Crc Press).
155. Schneider CA, Rasband WS, & Eliceiri KW (2012) NIH Image to ImageJ: 25 years of image analysis. *Nature methods* 9(7):671-675.
156. Abramoff MD, Magalhães PJ, & Ram SJ (2004) Image processing with ImageJ. *Biophotonics international* 11(7):36-42.
157. Roper F (1977) The prediction of laminar jet diffusion flame sizes: Part I. Theoretical model. *Combust. Flame* 29:219-226.
158. Gaydon A (2012) *The spectroscopy of flames* (springer science & business media).
159. Schuster G, Dubovik O, Arola A, Eck T, & Holben B (2016) Remote sensing of soot carbon-Part 2: Understanding the absorption Ångström exponent. *Atmospheric Chemistry & Physics* 16(3).
160. Calcote H & Manos D (1983) Effect of molecular structure on incipient soot formation. *Combust. Flame* 49(1-3):289-304.
161. Schmidt-Rohr K (2015) Why combustions are always exothermic, yielding about 418 kJ per mole of O₂. *J. Chem. Educ.* 92(12):2094-2099.
162. McEnally CS & Pfefferle LD (2007) Improved sooting tendency measurements for aromatic hydrocarbons and their implications for naphthalene formation pathways. *Combust. Flame* 148(4):210-222.
163. Kwon H, *et al.* (2020) Reactive Molecular Dynamics Simulations and Quantum Chemistry Calculations To Investigate Soot-Relevant Reaction Pathways for Hexylamine Isomers. *The Journal of Physical Chemistry A* 124(21):4290-4304.
164. Van Duin AC, Dasgupta S, Lorant F, & Goddard WA (2001) ReaxFF: a reactive force field for hydrocarbons. *The Journal of Physical Chemistry A* 105(41):9396-9409.

165. Chenoweth K, Van Duin AC, & Goddard WA (2008) ReaxFF reactive force field for molecular dynamics simulations of hydrocarbon oxidation. *The Journal of Physical Chemistry A* 112(5):1040-1053.
166. Kwon H, Jain A, McEnally CS, Pfefferle LD, & Xuan Y (2019) Numerical investigation of the pressure-dependence of yield sooting indices for n-alkane and aromatic species. *Fuel* 254:115574.
167. Burgess DR (2012) Thermochemical data. *NIST Chemistry WebBook, NIST Standard Reference Database* 69.
168. Kobayashi H, Hayakawa A, Somarathne KKA, & Okafor EC (2019) Science and technology of ammonia combustion. *Proceedings of the Combustion Institute* 37(1):109-133.
169. Gutkowski A (2006) Laminar burning velocity under quenching conditions for propane-air and ethylene-air flames. *Archivum combustionis* 26(3/4):163.
170. Rallis C, Garforth A, & Steinz J (1965) Laminar burning velocity of acetylene-air mixtures by the constant volume method: Dependence on mixture composition, pressure and temperature. *Combustion and Flame* 9(4):345-356.
171. Ciccarelli G, Jackson D, & Verreault J (2006) Flammability limits of NH₃-H₂-N₂-air mixtures at elevated initial temperatures. *Combustion and Flame* 144(1-2):53-63.
172. Spencer AB & Colonna GR (2002) *Fire protection guide to hazardous materials* (National Fire Protection Association Quincy).
173. Grcar JF, *et al.* (2005) Effects of mixing on ammonia oxidation in combustion environments at intermediate temperatures. *Proceedings of the Combustion Institute* 30(1):1193-1200.
174. Bell JB, *et al.* (2002) Detailed modeling and laser-induced fluorescence imaging of nitric oxide in a NH₃-seeded non-premixed methane/air flame. *Proceedings of the Combustion Institute* 29(2):2195-2202.
175. Tian Z, Li Y, Zhang L, Glarborg P, & Qi F (2009) An experimental and kinetic modeling study of premixed NH₃/CH₄/O₂/Ar flames at low pressure. *Combustion and Flame* 156(7):1413-1426.
176. Mendiara T & Glarborg P (2009) Ammonia chemistry in oxy-fuel combustion of methane. *Combustion and Flame* 156(10):1937-1949.
177. Xiao H, Howard M, Valera-Medina A, Dooley S, & Bowen P (2017) Reduced chemical mechanisms for ammonia/methane co-firing for gas turbine applications. *Energy Procedia* 105:1483-1488.
178. Konnov AA (2009) Implementation of the NCN pathway of prompt-NO formation in the detailed reaction mechanism. *Combustion and Flame* 156(11):2093-2105.
179. Glarborg P, Miller JA, Ruscic B, & Klippenstein SJ (2018) Modeling nitrogen chemistry in combustion. *Progress in Energy and Combustion Science* 67:31-68.
180. Smith GP, *et al.* (
181. Xuan Y & Blanquart G (2016) Two-dimensional flow effects on soot formation in laminar premixed flames. *Combustion and Flame* 166:113-124.
182. Smooke M, McEnally C, Pfefferle L, Hall R, & Colket M (1999) Computational and experimental study of soot formation in a coflow, laminar diffusion flame. *Combustion and Flame* 117(1-2):117-139.
183. ITS N (Thermocouple Database NIST Standard Reference Database 60, Version 2.0 (Web Version).
184. McEnally CS, Köylü ÜÖ, Pfefferle LD, & Rosner DE (1997) Soot volume fraction and temperature measurements in laminar nonpremixed flames using thermocouples. *Combustion and Flame* 109(4):701-720.
185. Bradley D & Entwistle A (1961) Determination of the emissivity, for total radiation, of small diameter Platinum-10% Rhodium wires in the temperature range 600-1450 C. *Br. J. Appl. Phys.* 12(12):708.
186. Acrivos A & Taylor TD (1962) Heat and mass transfer from single spheres in Stokes flow. *The Physics of Fluids* 5(4):387-394.
187. Lemmon E, McLinden M, & Friend D (2019) Thermophysical Properties of Fluid Systems in NIST Chemistry WebBook, NIST Standard Reference Database Number 69, ed. PJ Linstrom and WG Mallard, National Institute of Standards and Technology, Gaithersburg MD, 20899, 2011.

188. Walsh KT, Fielding J, Smooke MD, Long MB, & Liñán A (2005) A comparison of computational and experimental lift-off heights of coflow laminar diffusion flames. *Proceedings of the Combustion Institute* 30(1):357-365.
189. Dreyer JA, *et al.* (2019) Improved methodology for performing the inverse Abel transform of flame images for color ratio pyrometry. *Applied optics* 58(10):2662-2670.
190. Hickstein DD, Gibson ST, Yurchak R, Das DD, & Ryazanov M (2019) A direct comparison of high-speed methods for the numerical Abel transform. *Rev. Sci. Instrum.* 90(6):065115.
191. Das D (2017) Yale BASEX. (GitHub).
192. Kuhn PB, Ma B, Connelly BC, Smooke MD, & Long MB (2011) Soot and thin-filament pyrometry using a color digital camera. *Proceedings of the Combustion Institute* 33(1):743-750.
193. Das DD, Cannella WJ, McEnally CS, Mueller CJ, & Pfefferle LD (2017) Two-dimensional soot volume fraction measurements in flames doped with large hydrocarbons. *Proceedings of the Combustion Institute* 36(1):871-879.
194. Cignoli F, De Iulii S, Manta V, & Zizak G (2001) Two-dimensional two-wavelength emission technique for soot diagnostics. *Applied Optics* 40(30):5370-5378.
195. Krishnan S, Lin K-C, & Faeth G (2000) Optical properties in the visible of overfire soot in large buoyant turbulent diffusion flames. *Journal of Heat Transfer* 122(3):517-524.
196. Kempema NJ & Long MB (2018) Effect of soot self-absorption on color-ratio pyrometry in laminar coflow diffusion flames. *Optics letters* 43(5):1103-1106.
197. Jain A, Das DD, McEnally CS, Pfefferle LD, & Xuan Y (2019) Experimental and numerical study of variable oxygen index effects on soot yield and distribution in laminar co-flow diffusion flames. *Proceedings of the Combustion Institute* 37(1):859-867.
198. Mcenally CS, *et al.* (2000) Characterization of a coflowing methane/air non-premixed flame with computer modeling, rayleigh-raman imaging, and on-line mass spectrometry. *Proceedings of the Combustion Institute* 28(2):2063-2070.
199. Smyth KC, Miller JH, Dorfman RC, Mallard WG, & Santoro RJ (1985) Soot inception in a methane/air diffusion flame as characterized by detailed species profiles. *Combustion and Flame* 62(2):157-181.
200. Summers RL (1969) Empirical observations on the sensitivity of hot cathode ionization type vacuum gages.
201. Wallace WE (2019) Mass Spectrometry. in *NIST Chemistry WebBook, NIST Standard Reference Database Number 6 Eds. P.J. Linstrom and W.G. Mallard* (National Institute of Standards and Technology, Gaithersburg MD, 20899).
202. Desjardins O, Blanquart G, Balarac G, & Pitsch H (2008) High order conservative finite difference scheme for variable density low Mach number turbulent flows. *Journal of Computational Physics* 227(15):7125-7159.
203. Xuan Y & Blanquart G (2015) Effects of aromatic chemistry-turbulence interactions on soot formation in a turbulent non-premixed flame. *Proceedings of the Combustion Institute* 35(2):1911-1919.
204. Herrmann M, Blanquart G, & Raman V (2006) Flux corrected finite volume scheme for preserving scalar boundedness in reacting large-eddy simulations. *AIAA journal* 44(12):2879-2886.
205. Savard B, Xuan Y, Bobbitt B, & Blanquart G (2015) A computationally-efficient, semi-implicit, iterative method for the time-integration of reacting flows with stiff chemistry. *Journal of Computational Physics* 295:740-769.
206. Mueller ME, Blanquart G, & Pitsch H (2011) Modeling the oxidation-induced fragmentation of soot aggregates in laminar flames. *Proceedings of the Combustion Institute* 33(1):667-674.
207. Blanquart G, Pepiot-Desjardins P, & Pitsch H (2009) Chemical mechanism for high temperature combustion of engine relevant fuels with emphasis on soot precursors. *Combustion and Flame* 156(3):588-607.
208. Narayanaswamy K, Blanquart G, & Pitsch H (2010) A consistent chemical mechanism for oxidation of substituted aromatic species. *Combustion and Flame* 157(10):1879-1898.
209. Pepiot-Desjardins P & Pitsch H (2008) An efficient error-propagation-based reduction method for large chemical kinetic mechanisms. *Combustion and Flame* 154(1-2):67-81.

210. Bisetti F, Blanquart G, Mueller ME, & Pitsch H (2012) On the formation and early evolution of soot in turbulent nonpremixed flames. *Combustion and Flame* 159(1):317-335.
211. Attili A, Bisetti F, Mueller ME, & Pitsch H (2014) Formation, growth, and transport of soot in a three-dimensional turbulent non-premixed jet flame. *Combustion and flame* 161(7):1849-1865.
212. Attili A, Bisetti F, Mueller ME, & Pitsch H (2015) Damköhler number effects on soot formation and growth in turbulent nonpremixed flames. *Proceedings of the Combustion Institute* 35(2):1215-1223.
213. Blanquart G & Pitsch H (2009) Analyzing the effects of temperature on soot formation with a joint volume-surface-hydrogen model. *Combustion and Flame* 156(8):1614-1626.
214. Mueller ME, Blanquart G, & Pitsch H (2009) A joint volume-surface model of soot aggregation with the method of moments. *Proceedings of the Combustion Institute* 32(1):785-792.
215. Ju Y, Matsumi H, Takita K, & Masuya G (1999) Combined effects of radiation, flame curvature, and stretch on the extinction and bifurcations of cylindrical CH₄/air premixed flame. *Combustion and Flame* 116(4):580-592.
216. Chan S, Yin J, & Shi B (1998) Structure and extinction of methane-air flamelet with radiation and detailed chemical kinetic mechanism. *Combustion and Flame* 112(3):445-456.
217. Chatterjee P, de Ris JL, Wang Y, & Dorofeev SB (2011) A model for soot radiation in buoyant diffusion flames. *Proceedings of the Combustion Institute* 33(2):2665-2671.
218. Barlow R, Karpetis A, Frank J, & Chen J-Y (2001) Scalar profiles and NO formation in laminar opposed-flow partially premixed methane/air flames. *Combustion and flame* 127(3):2102-2118.
219. Caramunt K, Consul R, Pérez-Segarra C, & Oliva A (2004) Multidimensional mathematical modeling and numerical investigation of co-flow partially premixed methane/air laminar flames. *Combustion and Flame* 137(4):444-457.
220. Williams TC, Shaddix CR, Jensen KA, & Suo-Anttila JM (2007) Measurement of the dimensionless extinction coefficient of soot within laminar diffusion flames. *International Journal of Heat and Mass Transfer* 50(7-8):1616-1630.
221. McBride BJ & Gordon S (1996) Computer program for calculation of complex chemical equilibrium compositions and applications ii. users manual and program description. 2; users manual and program description.
222. Mckinnon JT & Howard JB (1992) The roles of PAH and acetylene in soot nucleation and growth. *Symposium (International) on Combustion* 24(1):965-971.
223. Kashif M, Guibert P, Bonnetty J, & Legros G (2014) Sooting tendencies of primary reference fuels in atmospheric laminar diffusion flames burning into vitiated air. *Combustion and Flame* 161(6):1575-1586.
224. Montgomery MJ, *et al.* (2020) Effect of ammonia addition on suppressing soot formation in methane co-flow diffusion flames. *Proceedings of the Combustion Institute*.
225. Betrancourt C, Mercier X, Liu F, & Desgroux P (2019) Quantitative measurement of volume fraction profiles of soot of different maturities in premixed flames by extinction-calibrated laser-induced incandescence. *Applied Physics B* 125(1):16.
226. Hansen N, *et al.* (2009) Benzene formation in premixed fuel-rich 1, 3-butadiene flames. *Proceedings of the Combustion Institute* 32(1):623-630.
227. Bartok W & Kuriskin R (1988) Formation of soot precursors in diffusion flames. *Combustion science and technology* 58(4-6):281-295.
228. Galli S (2014) X-ray crystallography: One century of nobel prizes. *Journal of Chemical Education* 91(12):2009-2012.
229. Bilderback DH, Elleaume P, & Weckert E (2005) Review of third and next generation synchrotron light sources. *Journal of Physics B: Atomic, molecular and optical physics* 38(9):S773.
230. Frank JH, *et al.* (2014) In situ soft X-ray absorption spectroscopy of flames. *Applied Physics B* 117(1):493-499.
231. Sakurai H, *et al.* (2016) Densitometry and temperature measurement of combustion gas by X-ray Compton scattering. *Journal of synchrotron radiation* 23(2):617-621.
232. Hansen N, *et al.* (2017) 2D-imaging of sampling-probe perturbations in laminar premixed flames using Kr X-ray fluorescence. *Combustion and Flame* 181:214-224.

233. Kastengren A, *et al.* (2008) Nozzle geometry and injection duration effects on diesel sprays measured by X-ray radiography. *Journal of fluids engineering* 130(4).
234. Als-Nielsen J & McMorrow D (2011) *Elements of modern X-ray physics* (John Wiley & Sons).
235. Kastengren A & Powell CF (2014) Synchrotron X-ray techniques for fluid dynamics. *Experiments in fluids* 55(3):1-15.
236. Jauncey G (1924) The scattering of x-rays and Bragg's law. *Proceedings of the National Academy of Sciences of the United States of America* 10(2):57.
237. Krause MO & Oliver J (1979) Natural widths of atomic K and L levels, K α X-ray lines and several KLL Auger lines. *Journal of Physical and Chemical Reference Data* 8(2):329-338.
238. Hubbell J & Seltzer S (2004) *Tables of X-ray mass attenuation coefficients and mass energy-absorption coefficients* (National Institute of Standards and Technology, Gaithersburg, MD).
239. Bearden J (1967) X-ray wavelengths and X-ray atomic energy levels. *NSRDS-NBS* 14:7.
240. Sahoo A & Narayanaswamy V (2019) Two-dimensional temperature field imaging in laminar sooting flames using a two-line Kr PLIF approach. *Applied Physics B* 125(9):168.
241. Gerig R, *et al.* (2011) Status of the Advanced Photon Source. *Nuclear Instruments and Methods in Physics Research Section A: Accelerators, Spectrometers, Detectors and Associated Equipment* 649(1):1-2.
242. Boigné E, *et al.* (2019) X-ray computed tomography for flame-structure analysis of laminar premixed flames. *Combustion and flame* 200:142-154.
243. Kempema NJ & Long MB (2016) Combined optical and TEM investigations for a detailed characterization of soot aggregate properties in a laminar coflow diffusion flame. *Combustion and Flame* 164:373-385.
244. Bodor AL, Franzelli B, Faravelli T, & Cuoci A (2019) A post processing technique to predict primary particle size of sooting flames based on a chemical discrete sectional model: Application to diluted coflow flames. *Combustion and Flame* 208:122-138.
245. Franzelli B, *et al.* (2019) Multi-diagnostic soot measurements in a laminar diffusion flame to assess the ISF database consistency. *Proceedings of the Combustion Institute* 37(2):1355-1363.
246. Botero ML, *et al.* (2019) Experimental and numerical study of the evolution of soot primary particles in a diffusion flame. *Proceedings of the Combustion Institute* 37(2):2047-2055.
247. Bartos D, Sirignano M, Dunn MJ, D'Anna A, & Masri AR (2019) Soot inception in laminar coflow diffusion flames. *Combustion and Flame* 205:180-192.
248. Carlson JS, *et al.* (2020) Biodiesel Ethers: Fatty Acid-Derived Alkyl Ether Fuels as Improved Bioblendstocks for Mixing-Controlled Compression Ignition Engines. *Energy & Fuels* 34(10):12646-12653.
249. Xuan Y, McEnally C, Jain A, Kwon H, & Pfefferle L (2018) Numerical investigation of pressure dependence of yield sooting tendencies. *2018 Spring Technical Meeting of the Eastern States Section of the Combustion Institute, ESSCI 2018*.
250. Deslattes R, *et al.* (2005) X-ray transition energies (version 1.2).[Online] Available: <http://physics.nist.gov/XrayTrans> [2009, October 20]. National Institute of Standards and Technology. Gaithersburg, MD.
251. Bergstrom Jr P & Pratt R (1997) An overview of the theories used in Compton scattering calculations. *Radiation Physics and Chemistry* 50(1):3-29.
252. Hasinoff SW (2014) Photon, Poisson Noise.
253. Smooke M, Long M, Connelly B, Colket M, & Hall R (2005) Soot formation in laminar diffusion flames. *Combustion and Flame* 143(4):613-628.
254. Bennett BAV, McEnally CS, Pfefferle LD, & Smooke MD (2000) Computational and experimental study of axisymmetric coflow partially premixed methane/air flames. *Combustion and Flame* 123(4):522-546.
255. Bennett BAV, McEnally CS, Pfefferle LD, Smooke MD, & Colket MB (2001) Computational and experimental study of axisymmetric coflow partially premixed ethylene/air flames. *Combustion and Flame* 127(1-2):2004-2022.

256. Bennett BAV, McEnally CS, Pfefferle LD, Smooke MD, & Colket MB (2009) Computational and experimental study of the effects of adding dimethyl ether and ethanol to nonpremixed ethylene/air flames. *Combustion and Flame* 156(6):1289-1302.
257. Kempema NJ & Long MB (2016) Boundary condition thermometry using a thermographic-phosphor-coated thin filament. *Applied optics* 55(17):4691-4698.
258. Gaffney JS & Marley NA (2009) The impacts of combustion emissions on air quality and climate—From coal to biofuels and beyond. *Atmospheric Environment* 43(1):23-36.
259. Jiaqiang E, *et al.* (2017) Effect of different technologies on combustion and emissions of the diesel engine fueled with biodiesel: A review. *Renewable and Sustainable Energy Reviews* 80:620-647.
260. Bennewitz JW, Schumaker SA, Lietz CF, & Kastengren AL (2020) Scaling of oxygen-methane reacting coaxial jets using x-ray fluorescence to measure mixture fraction. *Proceedings of the Combustion Institute*.
261. Doan NAK, Swaminathan N, & Minamoto Y (2018) DNS of MILD combustion with mixture fraction variations. *Combustion and Flame* 189:173-189.
262. Richardson DR, *et al.* (2017) Mixture-fraction imaging at 1 kHz using femtosecond laser-induced fluorescence of krypton. *Optics letters* 42(17):3498-3501.
263. Malbec L-M, Bruneaux G, Somers B, Rousselle C, & Pickett LM (2020) Identifying the Driving Processes of Diesel Spray Injection through Mixture Fraction and Velocity Field Measurements at ECN Spray A. (SAE Technical Paper).
264. Mueller ME (2020) Physically-derived reduced-order manifold-based modeling for multi-modal turbulent combustion. *Combustion and Flame* 214:287-305.
265. Hsu A, Narayanaswamy V, Clemens N, & Frank J (2011) Mixture fraction imaging in turbulent non-premixed flames with two-photon LIF of krypton. *Proceedings of the combustion institute* 33(1):759-766.
266. Gordon R, Heeger C, & Dreizler A (2009) High-speed mixture fraction imaging. *Applied Physics B* 96(4):745-748.
267. Park O, Burns RA, Buxton OR, & Clemens NT (2017) Mixture fraction, soot volume fraction, and velocity imaging in the soot-inception region of a turbulent non-premixed jet flame. *Proceedings of the Combustion Institute* 36(1):899-907.
268. Frank JH, Kaiser SA, & Long MB (2002) Reaction-rate, mixture-fraction, and temperature imaging in turbulent methane/air jet flames. *Proceedings of the Combustion Institute* 29(2):2687-2694.
269. Barlow R & Miles P (2000) A shutter-based line-imaging system for single-shot Raman scattering measurements of gradients in mixture fraction. *Proceedings of the Combustion Institute* 28(1):269-277.
270. Goix P, Leonard K, Talbot L, & Chen J (1993) Direct measurement of mixture fraction in reacting flow using Rayleigh scattering. *Experiments in fluids* 15(4):247-254.
271. Hubbell JH, *et al.* (1975) Atomic form factors, incoherent scattering functions, and photon scattering cross sections. *Journal of physical and chemical reference data* 4(3):471-538.
272. Duvauchelle P, Peix G, & Babot D (1999) Effective atomic number in the Rayleigh to Compton scattering ratio. *Nuclear Instruments and Methods in Physics Research Section B: Beam Interactions with Materials and Atoms* 155(3):221-228.
273. Wolfram S (1999) *The MATHEMATICA® book, version 4* (Cambridge university press).
274. Peters N (2001) *Turbulent combustion*. (IOP Publishing).
275. Kamimoto T & Bae M-h (1988) High combustion temperature for the reduction of particulate in diesel engines. *SAE transactions*:692-701.
276. Dempsey AB, Curran SJ, & Wagner RM (2016) A perspective on the range of gasoline compression ignition combustion strategies for high engine efficiency and low NO_x and soot emissions: Effects of in-cylinder fuel stratification. *International Journal of Engine Research* 17(8):897-917.
277. Zhang HR, Eddings EG, Sarofim AF, & Westbrook CK (2009) Fuel dependence of benzene pathways. *Proceedings of the Combustion Institute* 32(1):377-385.

278. Stuckey WK & Heicklen J (1967) Some Reactions of Oxygen Atoms. III. Cyclopropane, Cyclobutane, Cyclopentane, and Cyclohexane. *The Journal of Chemical Physics* 46(12):4843-4846.
279. Ben-Dor G, Sadot O, & Igra O (2017) *30th International Symposium on Shock Waves 1: ISSW30-Volume 1* (Springer).
280. Das DD, *et al.* (2017) Sooting tendencies of diesel fuels, jet fuels, and their surrogates in diffusion flames. *Fuel* 197:445-458.
281. Dooley S, *et al.* (2010) A jet fuel surrogate formulated by real fuel properties. *Combust. Flame* 157(12):2333-2339.
282. P.A.M Kalt MBL (2015) OMA – Image processing for Mac OS X.

ProQuest Number: 28321479

INFORMATION TO ALL USERS

The quality and completeness of this reproduction is dependent on the quality and completeness of the copy made available to ProQuest.



Distributed by ProQuest LLC (2021).

Copyright of the Dissertation is held by the Author unless otherwise noted.

This work may be used in accordance with the terms of the Creative Commons license or other rights statement, as indicated in the copyright statement or in the metadata associated with this work. Unless otherwise specified in the copyright statement or the metadata, all rights are reserved by the copyright holder.

This work is protected against unauthorized copying under Title 17, United States Code and other applicable copyright laws.

Microform Edition where available © ProQuest LLC. No reproduction or digitization of the Microform Edition is authorized without permission of ProQuest LLC.

ProQuest LLC
789 East Eisenhower Parkway
P.O. Box 1346
Ann Arbor, MI 48106 - 1346 USA